Origin, Evolution, and Control of Sidewall Line Edge Roughness Transfer During Plasma Etching

by

Stacy A. Rasgon

A.A. Liberal Arts
Los Angeles Pierce College, 1997

B.S. Chemical Engineering
University of California, Los Angeles, 1999

Submitted to the Department of Chemical Engineering
in Partial Fulfillment of the Requirements for the Degree of

DOCTOR OF PHILOSOPHY
in
CHEMICAL ENGINEERING

at the
MASSACHUSETTS INSTITUTE OF TECHNOLOGY
February 2005

© 2005 Massachusetts Institute of Technology
All rights reserved

Signature of Author.....
Department of Chemical Engineering
October 21, 2004

Certified By.....
Herbert H. Sawin
Professor of Chemical Engineering and
Electrical Engineering & Computer Science
Thesis Advisor

Accepted By.....
Daniel Blankschtein
Professor of Chemical Engineering
Chairman, Committee for Graduate Students

MASSACHUSETTS INSTITUTE OF TECHNOLOGY
DEC 2 2 2004
LIBRARIES

ARCHIVES

Origin, Evolution, and Control of Sidewall Line Edge Roughness Transfer During Plasma Etching

By
Stacy A. Rasgon

Submitted to the Department of Chemical Engineering on October 21, 2004 in Partial Fulfillment of the Requirements for the Degree of Doctor of Philosophy in Chemical Engineering

Abstract

For the patterning of sub 100 nm features, a clear understanding of the origin and control of line edge roughness (LER) is extremely desirable, both from a fundamental as well as a manufacturing perspective. Until recently, LER studies have focused on the analysis of top-down SEM micrographs of post-developed photoresist lines. However, the effect of plasma etch on sidewall roughness has not received sufficient attention. Plasma etching processes often roughen the feature sidewalls, leading to the formation of anisotropic striations. It is this post-etch sidewall roughness which will ultimately affect device performance.

Sidewall roughness transfer through all layers of a process stack (photoresist, ARC/hardmask, and oxide) was observed by cleaving dense line / space patterns parallel to the lines, and directly scanning the exposed sidewall with an atomic force microscope. This technique vividly highlighted the structural nature of the post – etch sidewall, and allowed the extraction of quantitative roughness data as a function of depth.

Sidewall roughness transfer can be improved through a variety of processing and material solutions. Maintaining a smooth sidewall immediately prior to the substrate etch (for example, through modulation of the ARC / hardmask open chemistry) leads to smoother sidewalls after oxide or polysilicon etch. However, smoothing must typically be balanced against critical dimension control. Additionally, the resist platform can add to roughness transfer. Thin and/or fluorinated photoresist can enhance roughness due to the poorer etch resistance of these materials.

Low – k (OSG) and porous low – k (MSQ) dielectrics can suffer from enhanced roughening during etching in fluorocarbon plasmas due to polymer – induced micromasking. Porous films seem especially prone, perhaps due to polymer diffusion into the pore structure. Control of polymerization during the etch through the use of lower – polymerizing fluorocarbons or the addition of oxygen was shown to effectively control excessive roughening on solid films, while porous dielectrics remain challenging.

Finally, an inductively-coupled plasma beam source was used to conduct a preliminary investigation into roughening of polysilicon in an HBr plasma beam. The initial polysilicon topography was shown to seed striation formation at glancing ion incident angles due to scattering and ion shadowing. These results indicate that, in a pure etching process (no deposition) the surface topography can be an important source of roughness and striation formation on sidewalls.

Thesis Supervisor:
Herbert H. Sawin
Professor of Chemical Engineering and Electrical Engineering & Computer Science

Acknowledgements

They say that no man is an island – indeed, I have discovered the truth of this statement during this long, utterly strange, yet ultimately fruitful journey. Thanks to everyone who traveled with me, especially the following:

First, foremost, and beyond all others, To my wife, Jung, for her incredible love and support during our time here. We made it, sweets!

To my advisor Herb for watching the map during the drive, and my committee members Karen and Bill for changing a tire or two along the way.

To my colleagues past – Brett, Steve, Brian, Weidong, and present – Ohseung, Bo, Yunpeng, Hiroyo, and Jujin (and James!), for making it fun.

To Peter and Glori, for easing the bumps in the road.

To Fred in the EC shop – for showing me something new every time.

To Libby and Tim in the CMSE – for your fine facilities and availability in a crunch!

To the folks at IBM – Arpan, Marie, Dario, Dirk, Bob, Peggy, Mark, Greg, Katia, the Karens P and T, the Burns Bros, Dakshi, Scott, George, and any others I might have missed, for providing the opportunity. This work wouldn't exist without you.

To the NSF, EPA, and SRC, for providing the moolah!

To my family – My mother Elois, and father Hermes. My brothers and sisters Jason, Nataly, and Hermes Jr. To my grandmother Irene, I wish you could have seen this day.

Table of Contents

List of Figures and Tables

Chapter 1 – Introduction

1.0. Integrated Circuit Manufacturing and Moore's Law

In 1965 Gordon Moore, the future founder of Intel, identified a trend for the continued scaling of integrated circuit technology that showed a doubling of the number of components on a chip roughly every two years[1], a proclamation known ever since as "Moore's Law." Since these early days, the microelectronics industry has maintained (and even exceeded) Moore's law through the advent of increasingly sophisticated materials selections and manufacturing techniques, enabling the fabrication of ever-smaller circuit features. Figure 1.1 shows data obtained from the International Technology Roadmap for Semiconductors (ITRS), a consortium of industrial, government, and academic entities that provides an assessment of the semiconductor industry technical requirements. Plotted are the DRAM ½ pitch and post – etch gate length forcasts as a function of the year of introduction[2]. Moore's law is indicated by the linear trends on the semi-log plot. Currently (in 2004), 90 nm DRAM features are in high volume production, and transistor gates are being fabricated with gate lengths less than 40 nm.

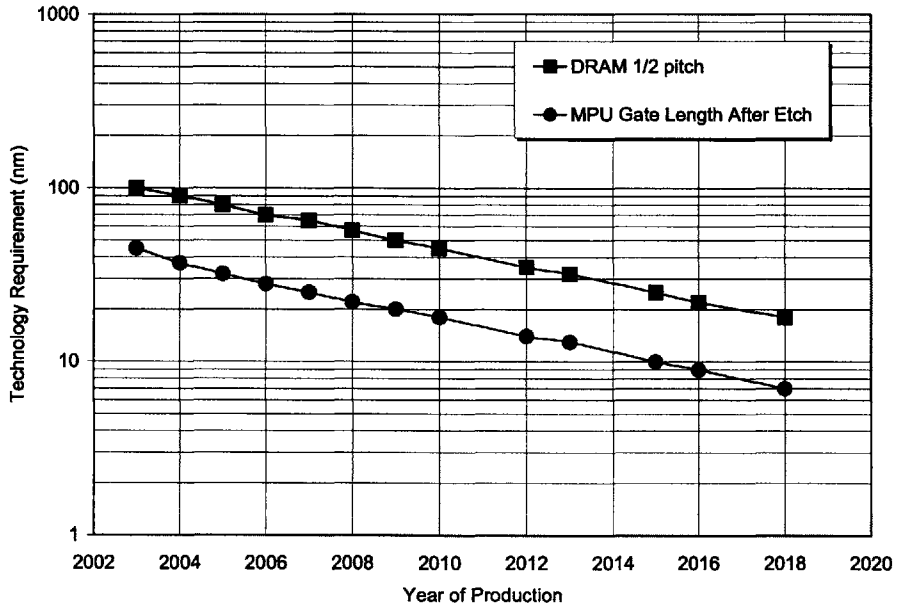

Figure 1.1 - Forecast of decreasing feature size as a function of the year of production, from the ITRS Roadmap.

1.1. Microelectronics Processing

The fabrication of integrated circuits involves a stepwise manufacturing process which is simplistically illustrated in figures 1.2 a – f. The film to be patterned is coated with a light – sensitive polymer material knows as photoresist. The photoresist is exposed to radiation through a mask. Exposed areas of the resist undergo a change in structure, and upon development, wash away (for a positive – tone resist). The remaining patterned resist on the wafer acts as a mask, protecting the underlying film material. This process is know as *lithography*. After patterning, the areas unprotected by photoresist are etched, typically via a plasma etching process. Following the etch, the remaining resist is stripped, leaving features remaining in the film. These steps (film deposition, lithography, and etch) are repeated over and over, with different imaging masks, in order to build up the many layers that make up the completed integrated circuit.

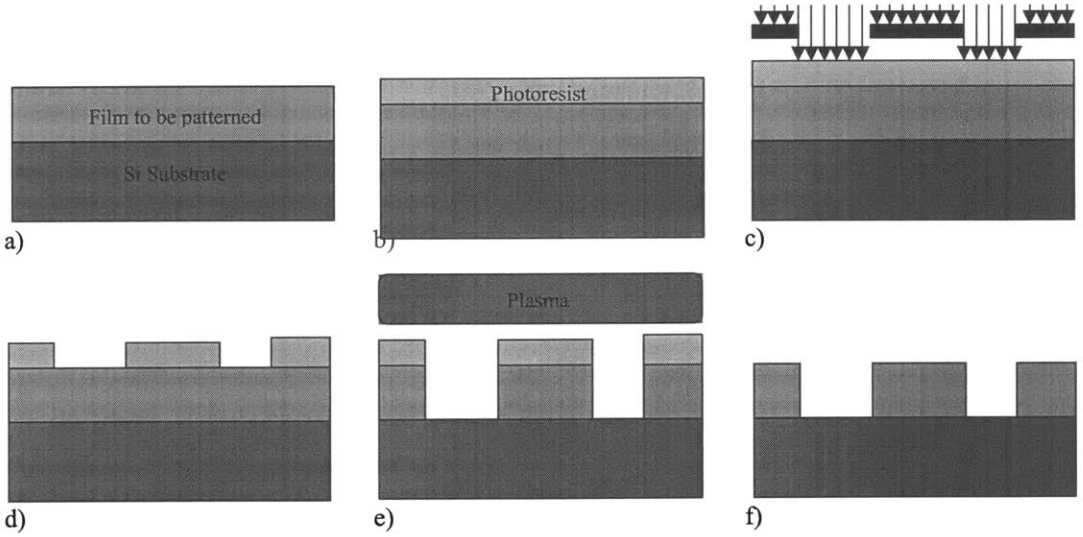

Figure 1.2 – a) Film to be patterned is deposited on a substrate. b) The film is coated with a light – sensitive polymer known as photoresist. c) The resist is exposed through a mask consisting of transparent and opaque regions defining the desired circuit features. d) After exposure, the resist is developed, leaving portions of the film masked by undissolved resist. e) The film is etched in a plasma process, leaving the areas protected by resist. f) The remaining resist is stripped, leaving a patterned film. These processes are then repeated over and over to build up the circuit layers.

While this thesis is concerned with feature roughness generated during the plasma etching steps, it was the lithography community that first recognized and studied the impact of feature roughness on microelectronics fabrication. As such, a brief review of

the history and causes of roughness during the lithographic process (as well as a short literature survey) should prove enlightening for the reader.

1.2. Lithography and Line Edge Roughness

One problem that can potentially limit the continued scaling predicted by Moore's law is feature roughness. This phenomenon has been studied extensively in the lithographic community as pertaining to the edge roughness of patterned photoresist features, and is referred to as *line edge roughness*, or LER. The moniker "line edge roughness" refers to the measurement method commonly used to observe it, in which printed photoresist lines are imaged top down via a scanning electron microscope (SEM). The digitized SEM images are then run through an algorithm that, based on the brightness of the image pixels, decides which elements lie on the line, and which do not. Thus, a representation of the pattern edge is extracted from the SEM micrograph (see Patsis et al[3]. for a nice discussion of profile extraction algorithms including both threshold and derivative techniques, and associated topics such as noise smoothing). Once the profile edge is obtained, the data is corrected for slope, and analyzed for roughness characteristics. The LER is typically defined to be the variation of the profile (in some fashion) from a straight line. While there are many ways to represent LER, the most common is to take the standard deviation of the profile edge, ie:

$$\mathrm{LER} = \sigma = \sqrt{\frac{1}{\mathrm{N}}\sum_i \left(z_i - \bar{z}\right)^2} \tag{1.1}$$

where z_i = position of the i'th data point, $\bar{z}$ = average of all data points, and N = total number of data points. Roughness analysis can additionally be performed on the line width data (LWR) as well as the line edge data. These concepts are demonstrated in figures 1.3 and 1.4. Figure 1.3 shows printed resist lines imaged as described above, with extracted profiles from the image demonstrated in figure 1.4 highlighting both the line width (LWR) and LER.

1.2.1. Lithographic LER as a Limiter of Moore's Law

Line edge roughness has been identified by the ITRS as one of the ten most difficult challenges facing ongoing lithography development as feature sizes continue to shrink. This is because, as patterned features become smaller, the associated LER takes up a correspondingly larger fraction of the total available critical dimension (CD) budget (the maximum amount that the critical dimension of the feature can vary from the des –

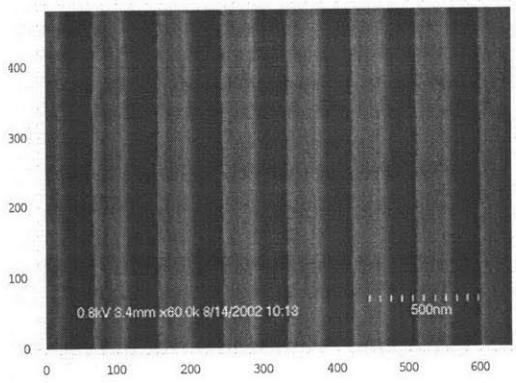

Figure 1.3 – Photoresist printed in a dense line/space pattern. The image was run through an analysis algorithm to extract the edge profiles for LER determination.

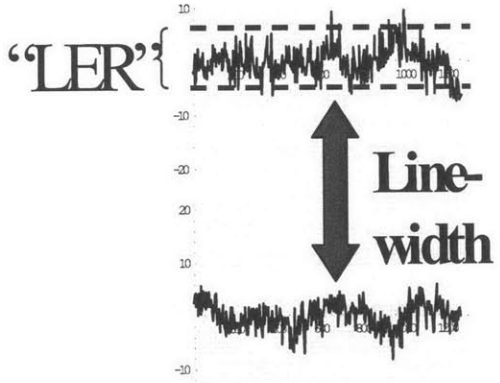

Figure 1.4 – Representative edge profiles extracted from one of the lines in figure 1.2 after slope correction. Roughness analysis can be performed on both the line width data (the difference between the two edge profiles) or the edges themselves. The LER is typically defined to be the variation of the edge profile, in some fashion, from a straight line.

ign). This is illustrated schematically in figure 1.5. For earlier technology nodes, the CD was so large that dimensional fluctuations from edge roughness could be adequately tolerated. As the designed CD shrinks, however, the magnitude of the resist roughness remained approximately constant, consuming an ever increasing fraction of the CD budget. Figure 1.6 shows ITRS LER requirement forecasts. At the current (90 nm) node, the 3σ LER requirement of ~2.1 nm is just barely tolerable. For future nodes, the ITRS lists LER requirements in red, indicating that no manufacturable solutions exist to reach the required LER levels. Unfortunately, the problem is growing worse by the year. By the year 2010 (upon reaching the 45 nm technology node) 3σ lithographic LER levels are anticipated to cross the 1 nm threshold, and will require levels approaching 5 angstroms by the year 2016. Therefore, unless implementable solutions to the LER problem can be

found, future scaling of feature sizes on integrated circuits will be impossible, and Moore's law will cease.

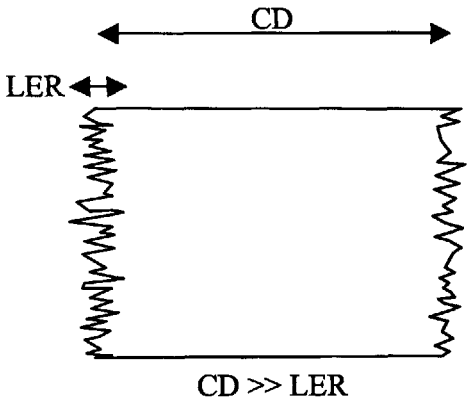

Figure 1.5a – When the CD is much larger than the LER magnitude, the LER takes up only a limited portion of the available CD budget.

Figure 1.5b – As the CD shrinks, the LER takes up an increasingly larger fraction of the available CD budget. Eventually, LER will limit the progression of Moore's law unless implementable solutions can be found.

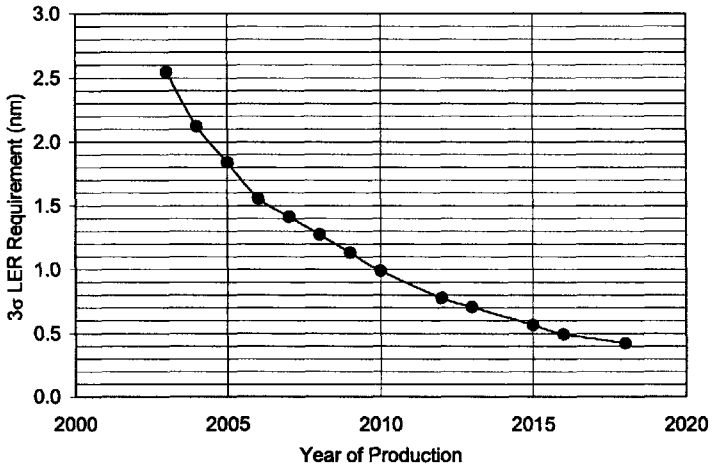

Figure 1.6 – Lithographic LER requirement forecasts from the ITRS. Currently (2004) the 90 nm node requires LER levels on the order of 2.1 nm. By 2010, LER requirements for lithography will cross the 1 nm level.

1.2.2. Causes of Lithographic LER

The potential troubles due to LER of lithographically patterned features have been evident for a number of years. As such, the causes and impact of LER in photoresists has

been a rich field of study. Some of the drivers of photoresist line edge roughness include the following:

1) Resist material properties such as photoacid diffusion (due to acid content or post exposure bake time/temperature), polymer size, aggregation, and molecular weight
2) Exposure factors such as aerial image contrast, shot noise, and mask imperfections
3) Process conditions such as dose, developer concentration, development time, or resist baking

1.2.2.1. Resist Material Effects

Development of chemically amplified photoresists relies on a solubility difference between exposed and unexposed regions. Exposure releases photoacid from photoacid generators (PAGs) that subsequently diffuses during a post – exposure bake (PEB). The photoacid deprotects the resist polymer, changing the solubility, additionally releasing more acid in a catalytic effect. The boundary between the developed and undeveloped resist is thus determined by the extent of photoacid diffusion.

Many researchers have examined the effect of photoacid concentration and diffusion on LER formation through both experiments and simulation. Experiments by Shiobara et al[4] showed that roughness improves with effective acid concentration. High concentrations of acid cause adjacent regions deprotected by each acid molecule to overlap, smoothing the profile. Henke et al[5] showed through modeling that increasing the acid diffusion length serves to homogenize the acid concentration, yielding lower roughness. Schmid et al[6] modeled acid diffusion during PEB, and found that higher acid concentration at feature edges yielded smoother features due to a smoother acid concentration gradient.

The effects of the PEB time on acid diffusion (and thus, roughness) have received much attention as well. Rau et al[7] showed that increasing acid diffusion by raising the PEB time led to smoother lines. Patsis et al demonstrated that increasing acid diffusion by increasing the dose or PEB time[8], or increasing acid content by higher photoacid generator concentration[9] yielded a smoother resist. Ocola et al[10] showed that a

percolation network formation model for acid diffusion/reaction could predict LER formation in a chemically amplified resist. However, Stewart et al[11] found an opposite result. Their simulations show an increase in roughness with increasing PEB time. They explain this by their finding that roughness seems to scale with the total developed distance, which increases with a longer PEB.

The polymer structure of the resist itself can lead to roughness. Yoshimura et al[12] demonstrated that a photoresist with aromatic rings in the main chain formed rougher patterns than one with aromatic rings in the side chains, due to steric effects. Ishida et al[13] used Fourier analysis to analyze rough profiles extracted from SEMs, and found that certain roughness spatial frequencies in the range of 10 – 100 nm depended on the molecular structure (specifically the number of monomers forming the cyclic molecule). Larger scale structural effects have also been examined. Rice et al[14] noted that line width roughness seemed to scale with the resist grain size. Yamaguchi et al[15-17] described a polymer aggregate extraction model to explain LER. They said that during development, the residual polymer surrounding polymer aggregates present in the resist dissolves, allowing the aggregates to float away. However, if the residual polymer only partially dissolves, the aggregates remain trapped, leading to LER formation.

1.2.2.3. Exposure Effects

Exposure anomalies including aerial image contrast, shot noise, and mask effects have been shown to affect roughness during lithography. Aerial image contrast (AIC) refers to the exposure intensity modulation between unexposed and exposed regions on the wafer. In a perfect world, exposed regions would receive a maximum, constant dose, and unexposed regions would receive no dose at all (100% AIC). However, in the real world this is not the case, and nominally unexposed regions receive some amount of dosing energy, partially exposing the resist. As such, the AIC is less than 100%. The role of AIC on LER has been explored. Sanchez et al[18] found that LER decreases with higher AIC. Additionally, they found a dependence of LER on the polymer molecular weight at low AIC conditions, with higher molecular weight polymers leading to higher LER values. Shin et al[19] investigated AIC effects using electron beam, X–ray, and extreme ultraviolet (EUV) exposures of several resists, and found that increasing AIC led to lower

LER for all cases. Ma et al[20] examined the effect of AIC on both dense and isolated line patterns. They found that while both types of patterns grew rougher as the AIC was decreased, the dense lines were rougher than the isolated at the same dose and nominal AIC modulation because the proximity effect lowers the true AIC modulation encountered by the dense patterns.

Shot noise refers to random dose fluctuations that lead to an undesired dosing variation on the exposed patterns. Eder-Kapl et al[21] used an ANOVA analysis and demonstrated that, on chemically amplified resists exposed with helium ion beams, shot noise seems to govern LER formation at low dose. However, at high dose the LER saturated, indicating that resist properties governed the LER at higher dose.

The effects of imperfections of the exposure mask itself on LER have also been investigated. Reynolds et al[22,23] demonstrated pattern transfer of mask profile defects into the resist. They showed that profile variations present on the mask sidewall were duplicated in the photoresist sidewall following development.

1.2.2.4. Process Effects

Different processing variables have been shown to affect LER in photoresist patterns. One important parameter is the exposure dose. He and Cerrina[24] showed that roughness typically scales with the extent of deprotection, but depends on the process history. The LER showed a maximum at intermediate dose levels. Flanagin et al[25] compared their simulation results to He and Cerrina's experiments, and predicted similar trends. Simulations by Patsis et al[9] also predicted an LER maximum at intermediate dose levels.

Development conditions can also play a role in LER formation. Reynolds et al[22] noted an increase in LER with both increasing developer concentration and increasing development time. Additionally, they found that the *rate* of roughness formation seemed to scale linearly with the development time. Stewart et al[11] found a similar result (increase in LER with increasing developer concentration) for resists with a poly 4-tertbutyloxycarbonyloxystyrene (TBOCST) resin, while an acrylic – based photoresist resin (ARP) showed a flat LER trend with increasing developer concentration. They attributed this to the different resin chemistries and deprotection mechanisms. Lowering

the developer concentration for the TBOCST film simply slows down the rate of deprotection and thus dissolution, yielding smoother surfaces. The ARP resin, however, generates a carboxylic acid when deprotected, a process that is insensitive to changes in developer concentration.

Rice et al[14] employed a six factor design of experiments to examine the effect of process conditions on LER. While it was easy to make the roughness worse, they found that improvements via process changes were difficult to achieve. However, they found that raising the hard bake (a bake performed after the development process is fully completed) temperature improved LER due to flowing of the photoresist.

1.3. Plasma Etching and Roughness

As the reader can see, a great deal of effort has been put into determining causes of and solutions for line edge roughness during lithographic processing. However, the role of the etching process on roughness has received comparably little attention. While obtaining smooth photoresist lines is undoubtedly important, from a manufacturing standpoint it is really the roughness of the final *etched* feature that will ultimately determine the electrical performance of the completed device, and will govern whether or not it will fail.

1.3.1. Surface Roughness Investigations on Blanket Films

Many researchers have investigated the surface roughening of blanket films during plasma etch processing. Potential roughening mechanisms include polymer deposition, ion bombardment, temperature effects, or selective etching of film components. Industrially relevant films include silicon, silicon oxide (SiO_2), silicon carbide (SiC), silicon nitride (Si_3N_4), and polymer films like polyimide or photoresists. A smattering of the available work is discussed below.

Zhao et al[26] investigated the roughening of Si surfaces in CF_4/O_2 plasmas. They used scaling theory and height-height correlation functions calculated from atomic force microscopy (AFM) images to determine how roughness develops during the etching process. They found that the surfaces tended to coarsen with increased etching time (with a shift to lower roughness spatial frequency and an increased interface width) but the

scaling remained constant. Drotar et al[27] confirmed these results later through simulations.

SiO_2 etching is typically performed in fluorocarbon plasmas. These chemistries produce fluorocarbon polymer that enhances selectivity and profile control. However, it can also play a role in roughening. In a series of papers, Min et al[28,29] investigated fluorocarbon particle redeposition from the bottom of a feature onto the sidewall during CF4 etching of SiO_2, and its role in roughening. They found that surfaces that experienced redeposition were significantly rougher than those without redeposition. Since surface analysis indicated a thick polymer film on the rough samples, they attributed the enhanced roughness to fluorocarbon polymer particles initiating the formation of rough polymerization. By adding O_2 to the etching chemistry, the roughening was reduced. Later in this thesis (Chapter 6) I will show my own investigation on the role of fluorocarbon polymerization in the roughening of SiO_2 and low – k dielectric films.

In several papers, Kim et al[30-32] examined the effects of processing parameters on the surface roughening of SiC in C_2F_6/O_2 inductively coupled plasmas. They asserted that changes in surface roughness were correlated to changes in the DC bias to the substrate as other parameters (such as the plasma source power and pressure) were changed. However, the surface roughness proved inversely correlated to the DC bias when other parameters (such as the O_2 concentration or gap spacing) were changed, so the true effects of the DC bias in their experiments are unclear. Jiang et al[33] investigated SiC roughening in SF_6/O_2 plasmas, and found no significant change with DC bias.

Massi et al[34] studied roughening of "diamond – like carbon" (DLC) films in Ar/O_2 plasmas as a function of source power and O_2 content. The etching rate and surface roughness both increased with increasing source power. The roughness also became extreme at higher O_2 fraction (with surface features beyond the vertical range of the AFM scanner), which the authors attributed to selective etching of DLC components by oxygen.

Ye et al[35] investigated roughening of Si_3N_4 in a variety of plasma chemistries for a local oxidation of silicon (LOCOS) process. After etching the Si_3N_4 in either a $CHF_3/CF_4/Ar$ or $CHF_3/CF_4/Ar/CO$ plasma, fluorocarbon polymer was left that roughened

the surface. After removing the polymer, the underlying surface of the sample etched with CO was rougher than the sample etched without CO. The addition of CO to the plasma resulted in a thicker polymer that led to the enhanced roughening.

Agarwal et al[36] examined roughness evolution in polyimide films during etching in O_2 plasmas. They found that the surface roughness scaled with the amount of material etched, independent of the power, etching rate, or gas composition. They also found that the roughness decreased at high pressure, which they attributed to collisional processes within the sheath at high pressure that make the incoming ions less directional.

Constantoudis et al[37] investigated photoresist roughening in O_2 plasmas. They found that processing in a high – density plasma (HDP) etcher gave smoother surfaces than a reactive ion etcher (RIE), probably due to the better temperature control in the HDP tool. As an aside, they also provide an illuminating discussion of various roughness parameters used to describe both the vertical and lateral surface structure including the RMS roughness (σ), the fractal dimension (D_F), and Fourier analysis (spatial frequency).

1.3.2. Plasma Roughening of Features and Sidewalls

During plasma etching, reactive neutral species and energetic ions impinging on the feature surface and sidewall impart morphological changes to the photoresist and the emerging etched substrate. These topographical changes typically take the form of "streaks" or "striations" that propagate down the etched sidewall, forming *anisotropic* roughness. In contrast, lithographic sidewall roughness is typically *isotropic* in nature, typified by a globular morphology.

Figures 1.7 and 1.8 show schematically what these different roughness types look like. These illustrations show an oxide substrate, coated with an anti – reflective coating (ARC) and patterned with photoresist lines. The photoresist isotropic roughness has become anisotropic after etching, with striations propagating down through the ARC layer into the underlying oxide substrate (figure 1.8).

Real examples of this are shown in figures 1.9 and 1.10, which show AFM images of both a patterned photoresist sidewall, and a sidewall following an oxide etch. The significance of these particular images will be discussed in (exhaustive) detail later, but for now, they are provided simply to give the reader a general idea of sidewall

roughness morphology. The photoresist shows a characteristic globular structure, without a significant directionality. However, the etched sample appears markedly different. The sample after etching is characterized by striations that traverse the entire length of the sidewall, and are correlated through all three different layers (photoresist, antireflective coating, and oxide).

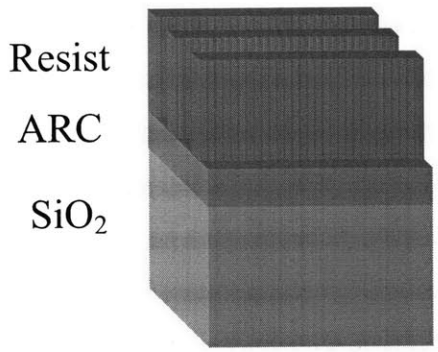

Figure 1.7 – Illustration showing patterned photoresist lines, with isotropic, globular sidewall roughness.

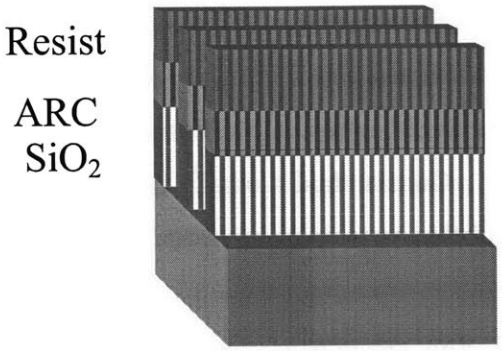

Figure 1.8 – Illustration showing how the preceding sample might appear following plasma etching. The isotropic roughness has become anisotropic, with correlated striations propagating down the length of the sidewall.

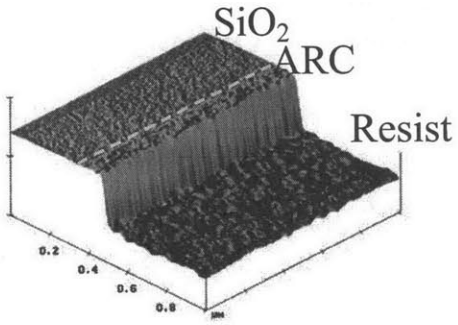

Figure 1.9 – Atomic force microscopy image of a photoresist sidewall after development. The isotropic, globular sidewall roughness is readily apparent.

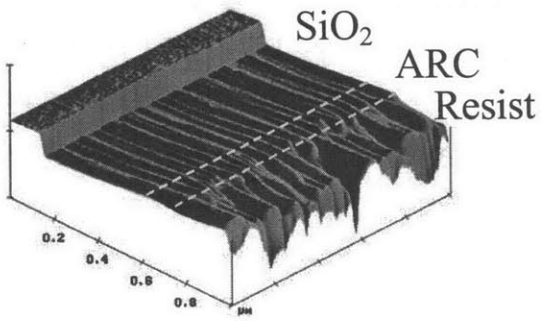

Figure 1.10 – Atomic force microscopy image of a similar sidewall after etching the oxide. Anisotropic etch striations are visible as described above.

It is apparent that roughness evolution on features and sidewalls occurs differently than on blanket films, and that the body of work described previously, while a decent starting point, cannot capture the phenomena governing sidewall roughness and anisotropic striation propagation. Unfortunately, the required investigations into feature

scale roughness evolution on sidewalls (similar to those studies performed in the lithography community) have received less attention.

Ren et al[38] examined striation formation during SiO_2 feature etching in CF_4 plasmas. They observed striations transferring from the photoresist into the oxide layer, and attributed the cause to polymer deposition and sputtering. Etching the oxide in SF_6 (without polymer deposition) resulted in smoother features.

Yahata et al[39] examined sidewall striation formation during Si trench etching in $HBr/SiF_4/O_2$. They observed that rougher photoresist patterns seemed to generate rougher sidewalls after etch. In another paper[40], they examined the effect of varying the O2 gas content. As the O_2 was increased, the roughness decreased, and then increased. While the increase at higher O_2 fraction was attributed to the oxidation of the sidewall, an explanation for the minimum was not offered. However, they did note that utilizing a sacrificial oxidation (oxidizing the surface, followed by a strip) could smooth the sidewall by 2/3.

Namatsu et al[41] also examined sidewall roughness during the etching of Si features, in this case in a chlorine electron cyclotron resonance (ECR) plasma source. They noted the presence of correlated roughness on the resist and Si sidewalls after etch, and attributed the striations on the Si to globular roughness in the initial resist structure. However, they did not observe the time evolution of the sidewall roughness, so it is unclear what the true source of the striations is.

Mahorowala et al[42] investigated transfer etching of bilayer resist systems in O_2 based plasmas. They found that the addition of SO_2 resulted in smoother sidewalls due to surface passivation by the sulphur compounds. Increasing the wafer temperature also allowed smoother etching.

Kim et al[43] examined the roughening of photoresists during nitride, oxide, and polysilicon plasma etching processes. They noted two types of resist morphology changes occurring, which they termed "striation" (our familiar etching streaks) and "wiggling," referring to a "zigzagged collapse of the photoresist during dry etching," as they so eloquently put it. They attributed striation formation in the resist to localized agglomeration and evaporation of components from the resist, ion bombardment, and fluorocarbon polymer deposition leading to microscopic variations in the etching rate.

They attributed wiggling of the resist lines to the differing thermal response of the photoresist and fluorocarbon polymers, eventually leading to collapse.

Rauf et al[44] modeled the effects of a photoresist trim process (an etching process used to reduce the size of patterned lines to enable the fabrication of smaller gates) on the photoresist roughness. They found that ion bombardment during the etching process preferentially etches asperities (high points) on the sidewall as opposed to cavities (low points), smoothing the surface. Their simulation highlighted the fact that high frequency roughness is more easily smoothed by plasma etching than low frequency roughness, a fact that was experimentally observed by Winkelmeier et al[45]. They patterned artificial LER into photoresists using direct write, and evaluated the spatial frequency of the roughness both after lithography and etch by using different measurement "box sizes" on digitized top – down SEMs. They determined that the LER reduction after etch was more profound at higher spatial frequency.

Researchers investigating optical channel waveguide fabrication have been aware of sidewall roughening during etch for a number of years, although their concerns are a bit different from those in the microelectronics field. Sidewall roughness on channel waveguides leads to propagation losses rather than device performance issues. Bazylenko et al[46] examined sidewall roughness transfer during silica based channel waveguide fabrication using both photoresist and silicon masks. They found that using a silicon mask led to smoother sidewalls than a photoresist mask due to less mask roughening during etch. Additionally, they found that increasing the temperature during the silica etch (in CHF_3/Ar) led to smoother sidewalls due to the reduced sticking probability of polymerization species, leading to lower polymer deposition during the etch. Lee et al[47] found that employing a sacrificial oxidation led to smoother sidewalls in Si/SiO_2 waveguide fabrication (similar to Yahata[40]). They also modeled the effects of sidewall roughness on waveguide losses[48].

1.3.3. Consequences of Post – Etch Line Edge Roughness

Post – etch LER is undesirable for many reasons. For front end processing, the LER present in the final etched gate can affect the implant profile of the source and drain regions of the transistor, changing the effective gate length. Charge carrier mobility can

also be degraded via scattering. On the back end, sidewall roughness can degrade the resolution of contacts, interfere with the deposition of conformal liner materials, and potentially lead to short circuits between adjacent metal lines or contacts (Figure 1.11).

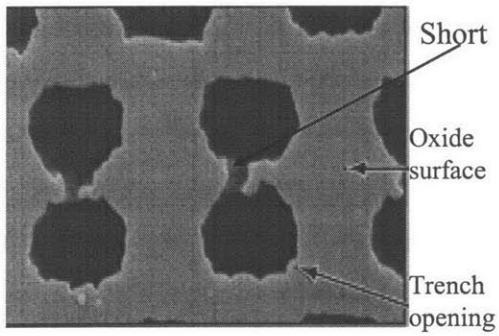

Figure 1.11 – Top down SEM of rough contact holes. "Mousebite" defects, corresponding to sidewall striations viewed on – end, are clearly visible. Additionally, the sidewall roughness has shorted out two adjacent contact holes, which would lead to device failure.

However, experimental evidence directly documenting the effect of edge and sidewall roughness on device performance is hard to come by, due to the difficulty of preparing etched samples with a highly controlled roughness level. Therefore, most of these insights have been accomplished through modeling and simulation. Diaz et al[49] developed an analytical model that represents the effects of LER on the off – state leakage current and drive current for sub – 100 nm devices. LER was found to greatly enhance the amount of leakage current, particularly as the device gate length shrank below 80 nm. Based on their model, they predicted that devices in the 0.1 μm node with gate lengths of 50 – 60 nm would require final a etched gate roughness less than 3 nm.

Oldiges et al[50] modeled a 3D rough polysilicon gate by assuming that it consisted of many 2D "slices," each of a fixed length. They calculated the current passing through each slice, added them up, and divided by the number of slices to obtain the average current through the device. They applied a monte carlo simulation to determine the effects of line edge roughness and nominal gate length on the transistor parameters. They found that while the average I_{on} and I_{off} current were relatively independent of the gate length, the variance of the parameters increased. Additionally, the I_{off} current average value rose with increasing LER due to short channel effects. They validated these results by comparing them to full 3 dimensional simulations.

1.4. Scope of This Thesis

As the reader can see, efforts to understand the impact of plasma etching on sidewall roughness have not received sufficient attention. While some studies exist, a comprehensive investigation on the effects of processing parameters on roughness transfer through all layers of a patterning scheme remains elusive. Work on industrially relevant patterning schemes including advanced resist systems, hardmasks, etc, has not been performed.

This thesis seeks to address some of these issues by providing an in – depth, comprehensive study of the causes of sidewall roughness transfer through all stages of patterning and processing (from the initial lithography, through the ARC etch, and through the substrate etch). Whenever possible, real, industrially relevant samples are examined, with some of the same resists, hardmasks, and substrates currently being used in advanced manufacturing. The contributions of different resist materials and compositions will be addressed, along with an exploration of the effects of various ARC or hardmask open plasma chemistries and substrate etch chemistries. Roughening of low – k dielectric films will be addressed, with caveats for successful integration. Most important for manufacturing, potential strategies for improving roughness transfer based on these results will be developed, both on back end (oxide) and front end (polysilicon) processing. Finally, a new apparatus is described that will enable a fundamental study of roughness development and striation formation by allowing a decoupling of processing parameters impossible to achieve in a conventional plasma etcher.

I hope you find the following work as enlightening and thought provoking as I do. Please read on, and enjoy!

1.5. References

1 G. E. Moore, Electronics **38** (1965).

2 International Technology Roadmap For Semiconductors, Semiconductor Industry Association, San Jose, CA (2003).

3 G. P. Patsis, V. Constantoudis, A. Tserepi, E. Gogolides, and G. Grozev, Journal of Vacuum Science & Technology B **21,** 1008-1018 (2003).

[4] E. Shiobara, D. Kawamura, K. Matsunaga, T. Koike, S. Mimotogi, A. Onishi, and Y. Onishi, Proc. SPIE **3333,** 313-323 (1998).

[5] W. Henke and M. Torkler, Journal of Vacuum Science & Technology B **17,** 3112-3118 (1999).

[6] G. M. Schmid, M. D. Stewart, V. K. Singh, and C. G. Willson, Journal of Vacuum Science & Technology B **20,** 185-190 (2002).

[7] N. Rau, F. Stratton, C. Fields, T. Ogawa, A. Neureuther, R. Kubena, and G. Willson, Journal of Vacuum Science & Technology B **16,** 3784-3788 (1998).

[8] G. P. Patsis, N. Glezos, I. Raptis, and E. S. Valamontes, Journal of Vacuum Science & Technology B **17,** 3367-3370 (1999).

[9] G. P. Patsis and E. Gogolides, Microelectronic Engineering **57-8,** 563-569 (2001).

[10] L. E. Ocola, P. A. Orphanos, W. Y. Li, W. Waskiewicz, A. E. Novembre, and M. Sato, Journal of Vacuum Science & Technology B **18,** 3435-3440 (2000).

[11] M. D. Stewart, D. L. Goldfarb, M. Angelopoulos, and C. G. Willson, Proc. SPIE **5039,** 415-422 (2003).

[12] T. Yoshimura, H. Shiraishi, J. Yamamoto, and S. Okazaki, Applied Physics Letters **63,** 764-766 (1993).

[13] M. Ishida, K. Kobayashi, J. Fujita, Y. Ochiai, H. Yamamoto, and S. Tono, Japanese Journal of Applied Physics Part 1 **41,** 4228-4232 (2002).

[14] B. J. Rice, H. Cao, M. Chandhok, and R. Meagley, Proc. SPIE **5039,** 384-392 (2003).

[15] T. Yamaguchi, H. Namatsu, M. Nagase, K. Yamazaki, and K. Kurihara, Applied Physics Letters **71,** 2388-2390 (1997).

[16] T. Yamaguchi, H. Namatsu, M. Nagase, K. Kurihara, and Y. Kawai, Proc. SPIE **3676,** 617-624 (1999).

[17] T. Yamaguchi, K. Yamazaki, M. Nagase, and H. Namatsu, Japanese Journal of Applied Physics Part 1 **42,** 3755-3762 (2003).

[18] M. I. Sanchez, W. D. Hinsberg, F. A. Houle, J. A. Hoffnagle, H. Ito, and C. Nguyen, Proc. SPIE **3678,** 160-171 (1999).

[19] J. Shin, G. Han, Y. Ma, K. Moloni, and F. Cerrina, Journal of Vacuum Science & Technology B **19,** 2890-2895 (2001).

[20] Y. S. Ma, G. Tsvid, and F. Cerrina, Journal of Vacuum Science & Technology B **21,** 3124-3130 (2003).

[21] S. Eder-Kapl, H. Loeschner, M. Zeininger, W. Fallmann, O. Kirch, G. P. Patsis, V. Constantoudis, and E. Gogolides, Microelectronic Engineering **73-74,** 252-258 (2004).

[22] G. W. Reynolds and J. W. Taylor, Journal of Vacuum Science & Technology B **17,** 334-344 (1999).

[23] G. W. Reynolds, J. W. Taylor, and C. J. Brooks, Journal of Vacuum Science & Technology B **17,** 3420-3425 (1999).

[24] D. He and F. Cerrina, Journal of Vacuum Science & Technology B **16,** 3748-3751 (1998).

[25] L. W. Flanagin, V. K. Singh, and C. G. Willson, Journal of Vacuum Science & Technology B **17,** 1371-1379 (1999).

[26] Y. P. Zhao, J. T. Drotar, G. C. Wang, and T. M. Lu, Physical Review Letters **82,** 4882-4885 (1999).

[27] J. T. Drotar, Y. P. Zhao, T. M. Lu, and G. C. Wang, Physical Review B **61,** 3012-3021 (2000).

[28] J. H. Min, S. W. Hwang, G. R. Lee, and S. H. Moon, Journal of Vacuum Science & Technology A **20,** 1574-1581 (2002).

[29] J. H. Min, S. W. Hwang, G. R. Lee, and S. H. Moon, Journal of Vacuum Science & Technology B **21,** 1210-1215 (2003).

[30] B. Kim, H. J. Choi, and B. T. Lee, Journal of Vacuum Science & Technology A **20,** 424-429 (2002).

[31] B. Kim and B. T. Lee, IEEE Trans. Plasma. Sci **30,** 2074-2077 (2002).

[32] B. Kim, K. Kim, and B. T. Lee, Applied Surface Science **217,** 261-267 (2003).

[33] L. D. Jiang, N. O. V. Plank, R. Cheung, R. Brown, and A. Mount, Microelectronic Engineering **67-8,** 369-375 (2003).

[34] M. Massi, J. M. J. Ocampo, H. S. Maciel, K. Grigorov, C. Otani, L. V. Santos, and R. D. Mansano, Microelectronics Journal **34,** 635-638 (2003).

[35] J. H. Ye and M. S. Zhou, Journal of the Electrochemical Society **147,** 1168-1174 (2000).

[36] N. Agarwal, S. Ponoth, J. Plawsky, and P. D. Persans, Applied Physics Letters **78,** 2294-2296 (2001).

[37] V. Constantoudis, E. Gogolides, G. P. Patsis, A. Tserepi, and E. S. Valamontes, Journal of Vacuum Science & Technology B **19,** 2694-2698 (2001).

[38] F. Ren, S. J. Pearton, J. R. Lothian, C. R. Abernathy, and W. S. Hobson, Journal of Vacuum Science & Technology B **10,** 2407-2411 (1992).

[39] A. Yahata, S. Urano, and T. Inoue, Japanese Journal of Applied Physics Part 1 **36,** 6722-6723 (1997).

[40] A. Yahata, S. Urano, T. Inoue, and T. Shinohe, Japanese Journal of Applied Physics Part 1 **37,** 3954-3955 (1998).

[41] H. Namatsu, M. Nagase, T. Yamaguchi, K. Yamazaki, and K. Kurihara, Journal of Vacuum Science & Technology B **16,** 3315-3321 (1998).

[42] A. P. Mahorowala, K. Babich, Q. Lin, D. R. Medeiros, K. Petrillo, J. Simons, M. Angelopoulos, R. Sooriyakumaran, D. Hofer, G. W. Reynolds, and J. W. Taylor, Journal of Vacuum Science & Technology A **18,** 1411-1419 (2000).

[43] J. Kim, Y. S. Chae, W. S. Lee, J. W. Shon, C. J. Kang, W. S. Han, and J. T. Moon, Journal of Vacuum Science & Technology B **21,** 790-794 (2003).

[44] S. Rauf, P. J. Stout, and J. Cobb, Journal of Vacuum Science & Technology B **21,** 655-659 (2003).

[45] S. Winkelmeier, M. Sarstedt, M. Ereken, M. Goethals, and K. Ronse, Microelectronic Engineering **57-8,** 665-672 (2001).

[46] M. V. Bazylenko, M. Gross, and M. Faith, Applied Physics Letters **69,** 2178-2180 (1996).

[47] K. K. Lee, D. R. Lim, L. C. Kimerling, J. Shin, and F. Cerrina, Optics Letters **26,** 1888-1890 (2001).

[48] K. K. Lee, D. R. Lim, H. C. Luan, A. Agarwal, J. Foresi, and L. C. Kimerling, Applied Physics Letters **77,** 1617-1619 (2000).

[49] C. H. Diaz, H. J. Tao, Y. C. Ku, A. Yen, and K. Young, IEEE Electron Device Letters **22,** 287-289 (2001).

[50] P. Oldiges, Q. Lin, K. Petrillo, M. Sanchez, M. Leong, and M. Hargrove, Proc. Int. Conf. SISPAD 2000, 131-134 (2000).

Chapter 2 – Experimental Equipment

2.0. Introduction

This chapter will provide a brief discussion of the various experimental processing apparatus, diagnostics, and analytical techniques used in this thesis. Experimental processing equipment includes various industrial and home – built plasma etchers, lithographic photomasks, and a home – built realistic plasma beam source. Diagnostics on the beam source include an attached ion flux analyzer and ion energy analyzer. Analytical techniques include atomic force microscopy (AFM), scanning electron microscopy (SEM), X–ray photoelectron spectroscopy (XPS), and variable angle spectroscopic ellipsometry (VASE).

2.1. Processing Apparatus

2.1.1. Plasma Etchers

A plasma is a partially ionized gas with a sufficient charge density such that the charged particles interact with coulombic forces coupling charged particles to neighbors, creating a fluid – like behavior. A plasma etcher typically uses RF energy to dissociate a reactant gas into reactive ions and neutral radical species. The ions directionally impinge on the sample surface due to the formation of a plasma sheath, allowing directional etching of features.

Four different plasma etchers were used for various experiments in this thesis. A home – build inductively coupled etcher located in the Sawin laboratory at MIT was used for blanket film etching. Patterned samples were etched on one of three industrial etchers. A LAM 9400SE and LAM 4520XL (LAM Research) were located at the IBM TJ Watson Research Center in Yorktown Heights, NY. Additionally, a TEL DRM (Tokyo Electronics) was located in the IBM Advanced Semiconductor Technology Center (IBM ASTC) in East Fishkill, NY.

The home – built inductively coupled etcher is shown schematically in figure 2.1. It consists of a 10" diameter stainless steel reactor pumped by a Leybold Turbovac 361C corrosive service turbomolecular pump. 4" wafers can be loaded through an integral load lock. The chamber base pressure is monitored with an ionization gauge and is typically

maintained at 10^{-6} torr. The chamber is topped with a quartz plate. A 3 – turn planar copper coil is placed on the plate, and is powered at 13.56 MHz (Comdel CPS-500A RF power supply) via a matching network. The bottom electrode is independently powered at

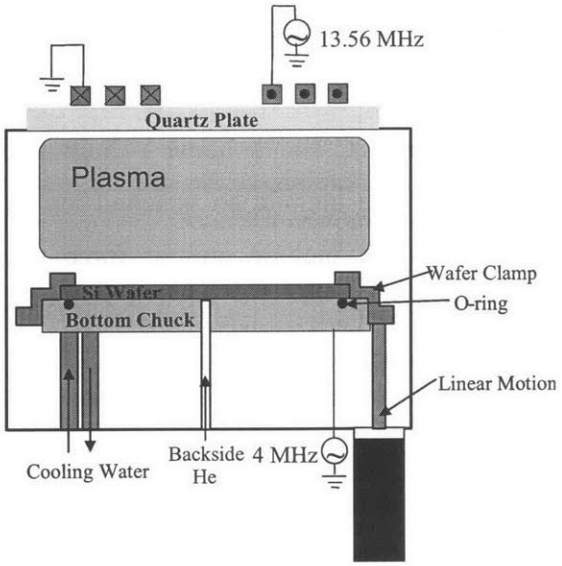

Figure 2.1 – Schematic of home – built inductively – coupled plasma etcher used in this work.

4 MHz (Comdel CX-2000 RF power supply) to minimize cross – talk with the upper power supply via a second matching network, to control the ion bombardment energy to the wafer. The bottom power and matching are varied to achieve the desired wafer bias. Circulating cooling water at approximately 15 °C through the electrode controls the temperature. Wafers are mechanically clamped using a heavy clamping ring that can be raised and lowered with a linear motion feedthrough. He gas is supplied to the wafer backside (10 – 20 torr) to enhance thermal contact with the cooled electrode. Wafers typically experience a temperature rise to approximately 50 °C during processing.

The LAM 9400SE etcher is an inductively – coupled tool typically used for polysilicon etch. It is very similar in configuration to the home – built etcher (many of the parts were originally salvaged from an older LAM Rainbow TCP tool). The main differences (besides such niceties as computerized touch – screen controls and robotic wafer handling) include the wafer size and clamping mechanism. The LAM 9400 etches 8" wafers, and has electrostatic (rather than mechanical) clamping.

The LAM 4520XL etcher is a capacitively – coupled parallel plate tool typically used for oxide etch. The TEL DRM is similar, but uses a magnetic field to enhance the plasma density. The field is set up by permanent magnets, which are rotated at ~ 1/3 Hz to improve the uniformity.

2.1.2. Realistic Inductively Coupled Plasma Beam Chamber

The realistic plasma beam chamber allows for the independent control of ion bombardment energy and ion impingement angle with any desired sample type and plasma chemistry, enabling a decoupling of parameters impossible to achieve in a conventional plasma etcher. It is described in detail in Chapter 7, section 7.2

2.1.3. Lithographic Photomasks

The basic lithographic process was outlined in Chapter 1. Incident radiation is passed through a photomask with opaque and transparent regions outlining the desired circuit features to be patterned onto a light sensitive polymer layer called photoresist. Exposed areas undergo a chemical deprotection and/or crosslinking that changes the solubility characteristics of the resist. After a subsequent (typically wet) development step, either the exposed areas (for a positive – tone resist) or the unexposed areas (for a negative – tone resist) wash away, leaving areas masked for the following etching step. Figure 2.2 shows a schematic of lithographic patterning via both positive and negative tone resist processing.

Two different photomasks were used to produce patterns of various dimensions for experiments in this thesis. The first is referred to herein as the "ARPAN" mask. This was a chrome – on – glass reticle with four different fields, with the following patterns:

1) Dense (1:1 pitch) lines / spaces, 150 nm wide
2) Isolated (1:8 pitch) lines / spaces, 150 nm wide
3) Dense (1:1 pitch) contact holes, 150 nm diameter
4) Isolated (1:8 pitch) contact holes, 150 nm diameter

A schematic of the mask is shown in figure 2.3. In this work, only the dense lines / spaces were used.

Unfortunately, this photomask only has a single feature size available (150 nm). In order to produce patterns with a smaller dimension, a second mask was fabricated. This new mask, referred to as the "DARPA" mask, was also chrome – on – glass. It had sixteen 4 mm x 4 mm fields with line / space patterns and contact holes of various pitches and dimensions and is illustrated in figure 2.4.

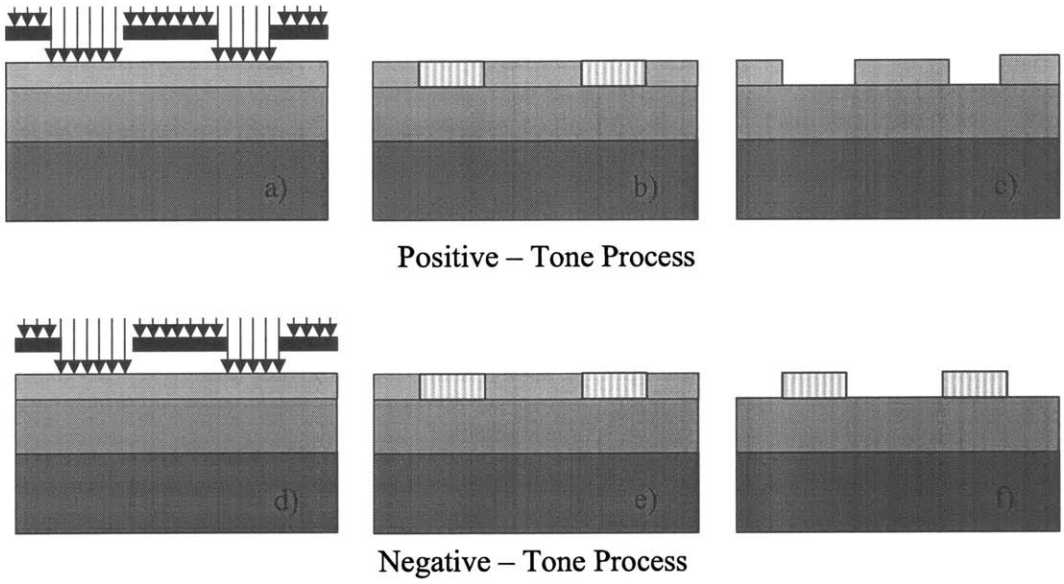

Figure 2.2 – Illustration of positive tone (a-c) and negative tone (d-f) lithographic patterning process. a) A positive tone resist is exposed through a photomask. b) The exposed areas undergo deprotection, becoming soluble in the developer. c) After development, a positive (same as the mask) image is patterned .d) A negative tone resist is exposed through a photomask. e) The exposed areas crosslink, becoming insoluble in the developer. f) After development, a negative (opposite of the mask) image is patterned.

It should be noted that the line/space patterns on the DARPA were reversed when fabricated, with opaque regions in place of transparent, and vice – versa, resulting in a negative image produced in the resist. For the dense (1:1) lines, this makes no difference, but for the isolated patterns, it resulted in the production of "isolated spaces" rather than isolated lines (see figure 2.5). For this thesis, only dense patterns were used (150 nm and 110 nm), but any future users of this mask who are interested in isolated patterns should pay careful attention when using it. Both the ARPAN and DARPA photomasks currently reside at either the IBM TJ Watson Research Center in Yorktown Heights, NY, or the IBM ASTC in East Fishkill, NY.

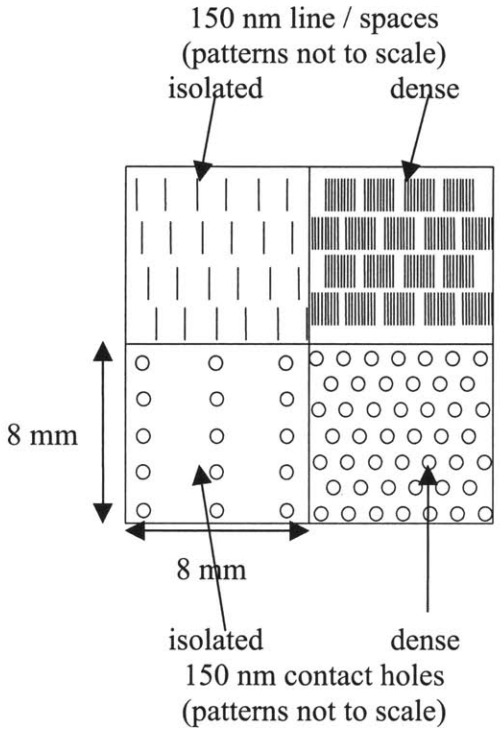

Figure 2.3 – Schematic of the "ARPAN" photomask. The four printed fields were approximately 12 mm square, with 150 nm features in dense and isolated lines / spaces and contact holes, as indicated. The patterns in the figure are for illustrative purposes only, and are not to scale. In this work, only the dense line / space quadrant was used.

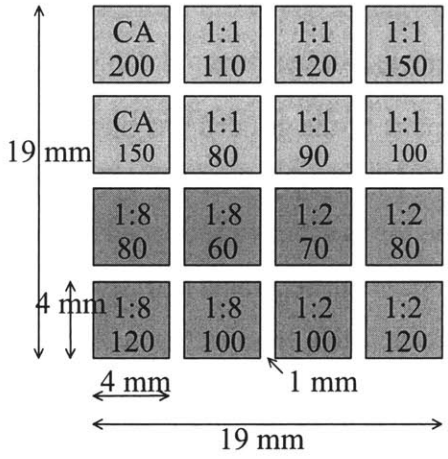

Figure 2.4 – Schematic of the "DARPA" photomask. The upper numbers in each field refer to the pattern pitch (1:1, 1:2, or 1:8). The lower number refers to the line width or hole diameter in nanometers. CA refers to contact holes. In this work, both the 1:1 150 nm and 1:1 110 nm line /space patterns were used.

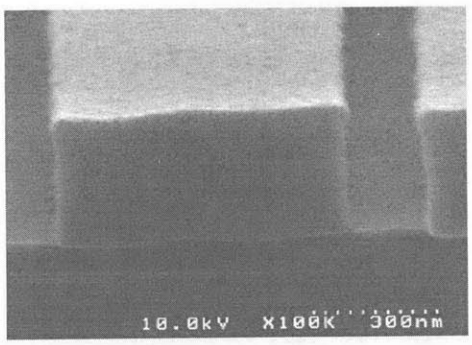

Figure 2.5 –120 nm isolated space produced with DARPA mask due to a mask printing error.

The ARPAN mask was used for 248 nm (KrF) lithography, and was exposed on an ASML 0.63 numerical aperture (NA) stepper with annular illumination located at IBM in Yorktown Heights. The DARPA mask was used for both 248 nm and 193 nm (ArF) lithography. The 193 nm stepper was an ASML 0.75 NA with annular illumination, located at the IBM ASTC in East Fishkill, NY.

2.2. Diagnostics

Both a gridded ion energy analyzer (IEA) and an ion flux analyzer (IFA) were used to characterize the plasma beam. They are described below

2.2.1. Gridded Ion Energy Analyzer

A section – view schematic of the gridded ion energy analyzer is shown in figure 2.6. It was designed in a similar fashion to the one described by Vitale[1]. A stainless steel can with a 0.375" orifice on the top is acts as a grounded shield. Inside the can, there are two grid plates and a collector plate, all separated and isolated from the ground shield by alumina washers (Superior Technical Ceramics, 2-56 Al_2O_3 washer, 0.25" diameter, 0.032" thick). The grid plates each have a 0.5" orifice, covered with stainless steel mesh (Buckbee Mears 5-1-4, 0.005" holes, 0.006" thick, 27% open area), while the collector plate is a solid stainless steel disk. Ceramic screws (Superior Technical Ceramics 2-56 Al_2O_3 screw) are used to assemble the parts together. Electrical contact to the grid plates and collector is made by 4 BNC electrical vacuum feedthroughs with kapton coated vacuum wire. The entire assembly is mounted on a linear motion feedthrough to allow it

to be moved into the beam at the chamber center, and backed out of the way when not in use.

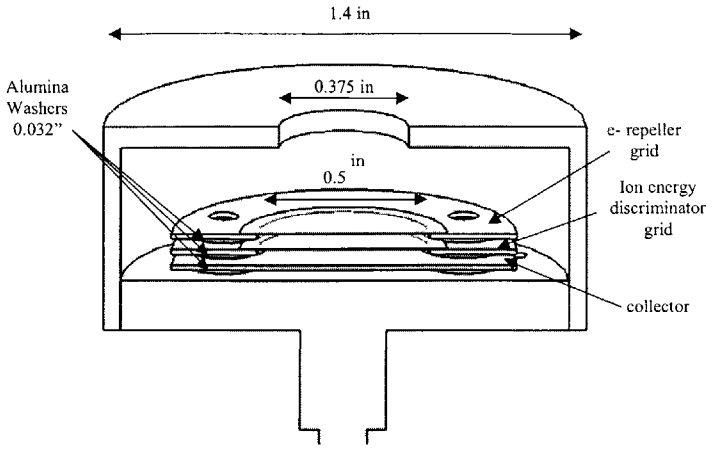

Figure 2.6 – Section view of the gridded ion energy analyzer. It consists of a stainless steel ground shield containing 3 grid plates and a collector plate. The upper grid is biased at –25 V to repel electrons The second grid voltage is swept, setting up a potential energy barrier. Only ions with an energy greater than the sweep voltage will pass through to be measured at the collector. By measuring the ion current as a function of the sweep voltage on grid # 2, the ion energy distribution is determined.

The upper grid is connected to a DC power supply, and biased slightly negative (-25 V) to repel electrons. Ions enter the orifice of the ground shield, and pass through the upper grid. The lower grid is connected to a second DC power supply and biased positively with a sweeping voltage. This sets up a potential barrier to the incoming ions. Only ions with an energy greater than the sweep voltage on grid # 2 will pass through to be measured at the collector, which is connected to a picoammeter (Keithley model 485).

The ion energy distribution function (IEDF) is determined by measuring the collected current as a function of the sweep voltage on the second grid. The measured I-V characteristic is equivalent to the integrated IEDF, ie:

$$I(V) = \int_0^V f(E)dE \qquad (2.1)$$

where f(E) is the IEDF. Thus, the IEDF can be obtained by differentiating the measured I-V curve. Figure 2.7 shows a representative I-V characteristic and IEDF obtained with the IEA.

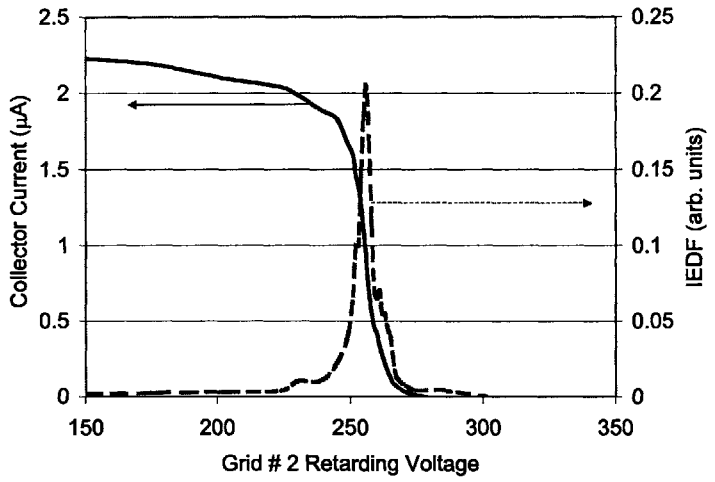

Figure 2.7 – Characteristic I-V curve of Ar plasma beam with 250 V DC bias applied to the plasma. The peak position is slightly higher than the applied DC bias due to the plasma self – biasing.

2.2.2. Ion Flux Analyzer

A section – view schematic of the ion flux analyzer (IFA) is shown in figure 2.8. It consists of a grounded stainless steel top plate with a 1 mm orifice, and collector plate that is electrically isolated from the IFA via ceramic washers and nylon 0-80 screws. A grounded aluminum shield surrounds the IFA to prevent ion flux from the sides to be measured at the collector. The entire assembly is held together by four 8-32 screws. A kapton coated vacuum wire is spot welded to the collector, and is electrically connected to a picoammeter via a floating BNC electrical feedthrough. The picoammeter is connected to a DC power supply and floated with a –25 V potential to repel electrons.

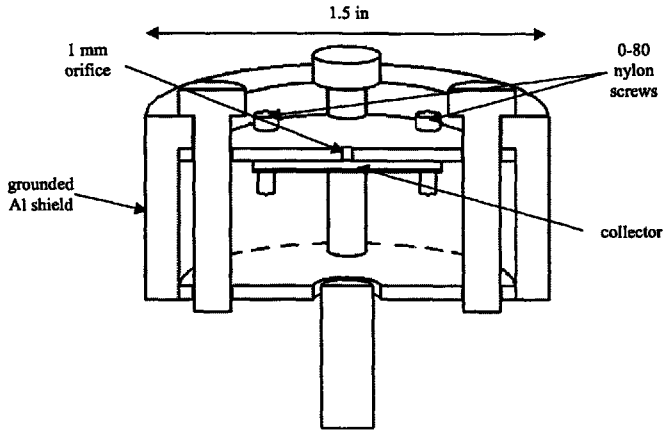

Figure 2.8 – Section view of the ion flux analyzer. The ion current passing through the orifice is measured at the collector via a floating picoammeter. By dividing the measured current by the orifice area, the ion flux is determined.

The ion flux is directly measured by dividing the measured beam ion current by the orifice area.

The IFA is mounted on an XYZ stage. This enables the IFA to be moved to the side when not in use. Additionally, since the orifice diameter is much smaller than the beam diameter, spatially resolved beam current uniformity maps can be collected. Examples are shown in Chapter 7.

2.3. Analytical Techniques

A variety of analytical techniques were used to collect the data in this thesis. They include Atomic Force Microscopy (AFM) for roughness measurements, X – ray Photoelectron Spectroscopy (XPS) for surface composition measurements, Variable Angle Spectroscopic Ellipsometry (VASE) for film thickness measurement, and Profilometry for step height measurements.

2.3.1 Atomic Force Microscopy

Several atomic force microscopes (Digital Instruments / Veeco 3100) located both at IBM in Yorktown Heights, NY, and at the MIT Center for Materials Science and Engineering, were used to collect surface roughness measurements.

A schematic of the 3100 AFM operation is shown in figure 2.9 (adapted from the Veeco Scanning Probe Microscopy Training Notebook[2]). Piezoelectric scanners in X, Y, and Z maneuver a micromachined silicon cantilever with a sharp tip over a sample. The cantilever is oscillated at or near its resonance frequency, typically in the range of 200 – 400 kHz at an amplitude of ~ 20 – 100 nm. By reflecting a laser off the oscillating cantilever onto a photodiode, the amplitude is monitored. As the tip interacts with the sample surface, the amplitude changes. By setting a desired cantilever amplitude, the photodiode signal acts as an input to a feedback loop that actuates the Z – scanner to keep the amplitude constant, moving the tip nearer or farther away from the sample as needed. Thus, by recording the Z – scanner height as a function of the position, the local topography of the surface can be measured with great precision and resolution, allowing quantitative analysis of the surface roughness.

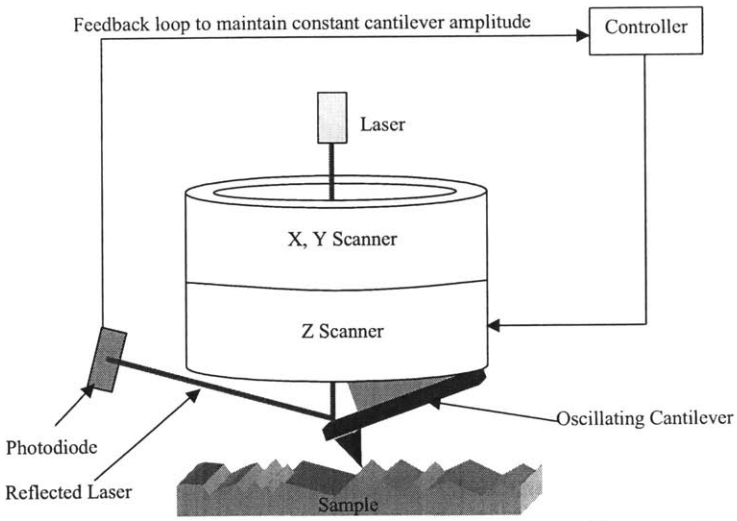

Figure 2.9 – Digital Instruments 3100 Tapping Mode AFM operation. A silicon cantilever with a sharp tip is oscillated at or near its resonance frequency (200 – 400 kHz) at a desired oscillation amplitude, "tapping" the sample surface. As the tip interacts with the surface, the amplitude will change. The amplitude is monitored by reflecting a laser beam off the cantilever onto a photodiode. The photodiode signal is used as the input to a feedback loop that actuates the Z – scanner, continually adjusting the height of the tip above the sample such as to keep the amplitude constant. By recording the Z – scanner height as a function of position, the topography of the sample is measured.

While several different varieties of cantilevers are available, Tapping – Mode Etched Silicon Probes (TESPs) were used for data collection. These cantilever probes are etched from single crystal silicon and have a regular, controlled tip geometry, with a tip radius of curvature of approximately 10 nm. Having a sharp tip is important as it ultimately limits the resolution of the AFM, since the images obtained are actually a superposition of the tip geometry and the local sample topography (figure 2.10). See chapter 3 for a more thorough discussion of tip size effects on AFM images.

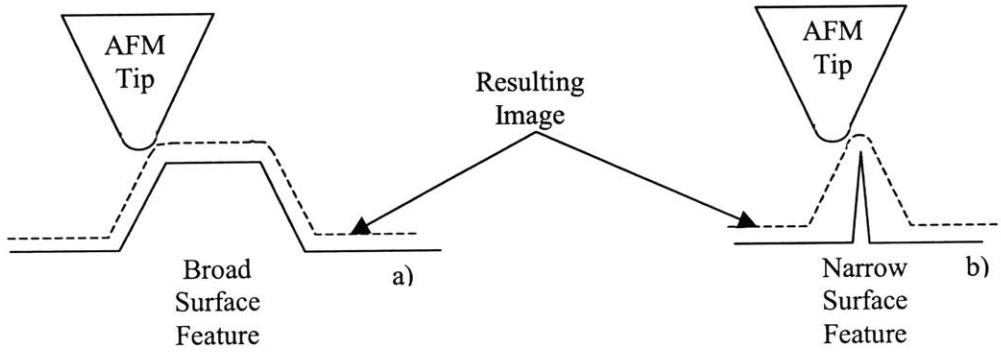

Figure 2.10 – AFM images are a convolution of the local sample topography and tip geometry. If the surface feature is larger than the tip (a), the image is dominated by the sample, although tip features appear (for example, the rounded corners at the top). If, however, the sample feature is narrower than the tip point (b), the result will be an image mainly of the tip itself, rather than showing the true sample surface.

2.3.2. X–Ray Photoelectron Spectroscopy (XPS)

XPS is a sensitive analytical technique that characterizes a sample's surface composition by irradiating it with X–rays and analyzing the kinetic energy of photoelectrons emitted. The binding energy of the electrons is related to the kinetic energy by:

$$KE = h\upsilon - BE \tag{2.2}$$

where KE = measured kinetic energy of the photoelectrons, BE = binding energy of the photoelectrons, and hν = energy of the incident X–rays (ignoring work function effects). Thus, if the energy of the X–rays is known, the binding energy of the electrons and hence, the chemical identity of the surface species, can be identified. Typically AlKα (1486.6 eV) or MgKa (1253.6 ev) X – rays are used. For an excellent resource on XPS, see Perkin – Elmer's Handbook[3].

A schematic of a typical XPS setup is is shown in figure 2.11. X – rays from a source impinge on a sample, releasing photoelectrons from the surface. An electron energy analyzer measures the kinetic energy of the electrons. Typically, the sample can be rotated to change the take – off angle θ between the sample surface and the electron energy analyzer, allowing the acquisition of depth–dependent compositional information.

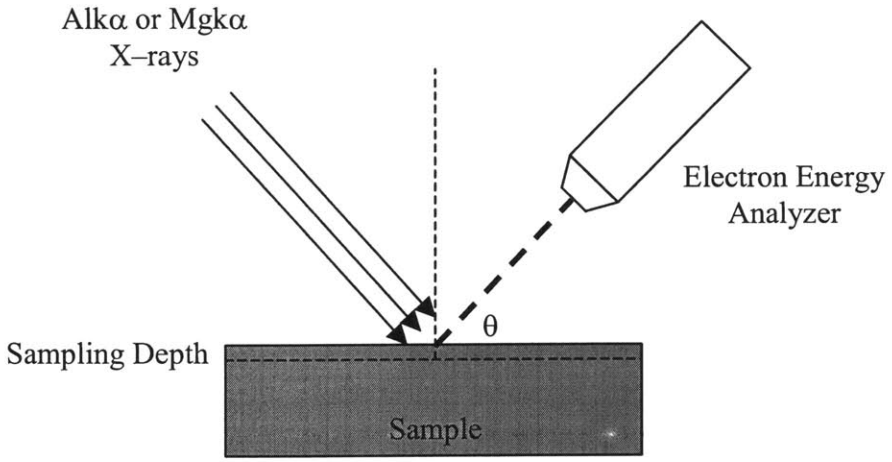

Figure 2.11 – Schematic of typical XPS operation. X – rays impinge on a sample surface, releasing photoelectrons that are detected by an electron energy analyzer. By measuring the kinetic energy of the electrons, the chemical composition of the surface can be determined.

While the Sawin Laboratory does possess an XPS apparatus, the instrument used in this thesis was a Kratos AXIS Ultra Imaging XPS located in the MIT Center for Material

Science and Engineering. This was for the purpose of enhanced throughput, since the Kratos possesses automation enabling the rapid acquisition of data from up to 15 samples sequentially.

2.3.3. Variable Angle Spectroscopic Ellipsometry (VASE)

Ellipsometry uses the change in the polarization of light reflected from a sample surface to determine the optical constants or thickness (or both) of the film. Typically, the ellipsometric parameters measured are Ψ and Δ, which are related to the Fresnel reflection coefficients $\tilde{R}_p$ and $\tilde{R}_s$ for p– and s– polarized light, respectively, by the following equation:

$$\frac{\tilde{R}_p}{\tilde{R}_s} = \tan(\Psi)e^{i\Delta} \tag{2.3}$$

Once Ψ and Δ are measured as a function of wavelength, an optical model is constructed to fit the data. This model contains such parameters as the light wavelength, polarization state, angle of incidence, the film optical constants, and the film thickness. If the optical constants are already known, the film thickness can be determined with great accuracy by fitting the model to the measured Ψ and Δ.

Film thickness was measured with a J.A. Woollam M2000 Spectroscopic Ellipsometer with Variable Angle Stage, equipped with WVASE32 software. The system consisted of a light source, monochromator, collimating optics, polarizer, sample stage, rotating analyzer, and a detector. It acquired data with light wavelengths from 2600 to 7200 angstroms at 20 angstrom intervals, at 65°, 70°,and 75° incident angles. A Cauchy model for the film optical constants was developed for each film by fitting the data for a sample with a known film thickness. Once determined, the optical constant models were fixed, and films with unknown thickness (for example, after etching) could be analyzed. J.A. Woollam's "A Short Course in Ellipsometry[4] contains a very nice primer on VASE.

2.4. References

1 S. A. Vitale, Ph.D. Thesis, Massachusetts Institute of Technology, 2001.

2 *SPM Training Notebook* (Digital Instruments Veeco Metrology Group, 2001).

[3] C. D. Wagner, W. M. Riggs, L. E. Davis, J. F. Moulder, and G. E. Muilenberg, *Handbook of X-Ray Photoelectron Spectroscopy* (Perkin-Elmer Corporation, Eden Prarie, Minnesota, 1979).

[4] in *Guide to Using WVASE32* (J.A. Woollam Co. Inc).

Chapter 3 – Observation and Quantification of Depth – Dependent Sidewall Roughness Transfer During Antireflective Coating / Hardmask Open and Oxide Etch.

3.0. Abstract and Introduction

In this chapter, an atomic force microscopy (AFM) technique is described, that allows the quantification of sidewall roughness on a feature, after any stage in processing, as a function of depth. Thermal oxide wafers are coated with various antireflective coating (ARC) or hardmask films, and then patterned with either a 248 nm (KrF), or 193 nm (ArF) resists (a 193 nm bilayer system is investigated as well). The depth dependent SWR is quantified after each stage in the processing (initial lithography, ARC/hardmask/underlayer etch, and oxide etch). The initial 248 nm lithography sidewall morphology is isotropic in nature with a 3-5 nm 1-σ RMS roughness, and is relatively constant as a function of depth. After the ARC/hardmask etch, however, the sidewall morphology takes on an anisotropic characteristic, with striations created by ion bombardment. During a subsequent oxide etch, these striations transfer into the oxide sidewall, the anisotropic topography created during the ARC/hardmask etch casting the morphology of the oxide layer beneath.

While all resist systems are about equivalent from a roughness standpoint after the ARC/hardmask etch, they show variation after oxide etch. On the 248 nm resist platforms, hardmask and Si containing ARC samples allow more roughness transfer during an aggressive oxide etch than organic ARC samples, perhaps due to the polymerizing nature of the Si ARC / hardmask open chemistry, or to compositional differences between these films as compared to the organic ARC. On the 193 nm resist platforms, a less aggressive (higher pressure, lower ion bombardment) oxide etch was required due to the lower etch resistance versus 248 nm systems. However, this gentler oxide etch allowed the oxide to be opened relatively smoothly regardless of the resist type, leaving the post – etch oxide SWR comparable to that obtained with 248 nm organic resist/ARC. These results indicate that the SWR on the oxide substrate can be maintained within reasonable limits, as long as the increasing resist/ARC roughness does not extend to the oxide interface.

3.1. Atomic Force Microscopy of Sidewall Roughness

A methodology consisting of directly scanning the sidewall of a patterned trench was used to quantify the magnitude and extent of SWR in on the feature as a function of depth. This technique, used previously to quantify sidewall roughness in chemically amplified photoresists[1,2], vividly highlights the structural nature of the post-etch sidewall allowing any potential spatial correlations between different layers to be identified. In this study, it enabled a simultaneous calculation of the two – dimensional SWR of the resist, ARC/hardmask layer, and oxide substrate surfaces. The evolution of the SWR of the patterned structures was followed throughout consecutive etch processes, and morphological changes to the resulting topographies were analyzed.

3.1.1. AFM Methodology

With the current photomask configuration (non-offset patterns), the AFM technique can only be applied to a dense (1:1) line / space pattern, because there is no way to guarantee that the cleave will be near enough to an isolated line to allow analysis via AFM (the photomasks used in this work are described in chapter 2). The line / space field, after any stage in processing, is scribed and cleaved by eye (parallel to the pattern) to expose the sidewall surface (figure 3.1). The sample is then carefully turned "on end"

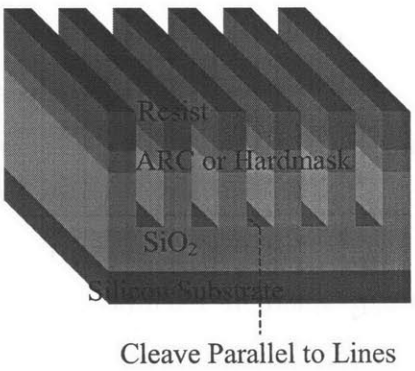

Figure 3.1 - Schematic of dense line/space pattern after final oxide etch. The sample is carefully cleaved parallel to the pattern, exposing the sidewall for analysis

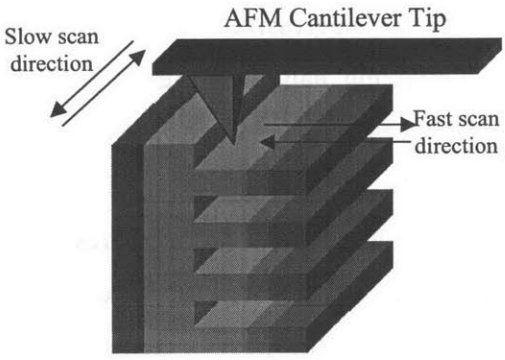

Figure 3.2 - The cleaved sample is turned 90° on end. The AFM cantilever can then image the exposed sidewall.

in a special sample holder to expose the sidewall. Using extreme caution, the AFM cantilever tip is brought down on the cleaved sample surface, and then slowly offset to access the exposed sidewall surface. The AFM fast scan is performed from the top of the line to the bottom, while it is slowly rastered laterally across the line, eventually producing an image of the sidewall (figure 3.2).

Due to the shape of the AFM tip, the bottom of the line feature may be "shadowed," where the solid angle of the tip prevents access. A schematic of this is shown in figure 3.3. Therefore, a 10° sample tilt was used to access more of the sidewall bottom (figure 3.4). Greater sample tilting is inadvisable, as sample tilt beyond 10° can introduce artifacts into the image such as inflated roughness values and enhancement of higher frequency roughness components at the expense of lower frequency components[3]. However, due to the pyramidal shape of the AFM tip in excess of 10°, it was not possible to eliminate all tip shadowing from these results, and the extreme bottom of the sidewalls could not be accessed (~50-100 nm, depending on where the sample cleaved).

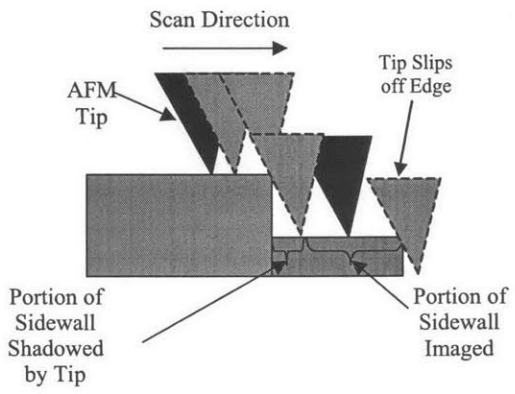

Figure 3.3 - Schematic of AFM tip "shadowing" effect at the bottom of the sidewall. Note that the solid angle of the tip cone, coupled with the height of the cleaved portion, prevents the extreme bottom of the sidewall to be imaged.

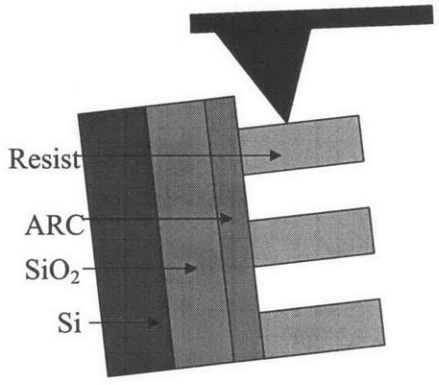

Figure 3.4 - Tilting the sample can allow greater AFM tip access to the sidewall bottom

Figure 3.3 also shows that the AFM tip can "slip" off the line edge. This will lead to artificially enhanced roughness measurements near the top of the line. To avoid it, the datasets were carefully observed and truncated so that only areas truly imaged by the tip were included in the analysis.

At various stages in processing (post-litho, post-ARC/HM open, and post oxide etch), the samples were cleaved and analyzed on a Digital Instruments Dimension 3100 AFM in tapping mode. Figure 3.5 shows the process stages where analysis was performed. Instruments were located both at the IBM TJ Watson Research Center in Yorktown Heights, NY, and at the MIT Center for Materials Science and Engineering in Cambridge, MA. Commercially available Tapping-Mode Etched Silicon Probes (TESPs) were used. These tips have a standard, controlled tip geometry, with a tip radius of curvature of ~10 nm. A new tip was employed before each AFM session, and used to analyze between 1-4 samples. Tip wear was monitored by visually examining successive images from the samples and in general, was not a concern. Damage did occur on occasion, primarily from accidental contact with the surface. In these cases, the tip was changed, and a new portion of the sample was imaged.

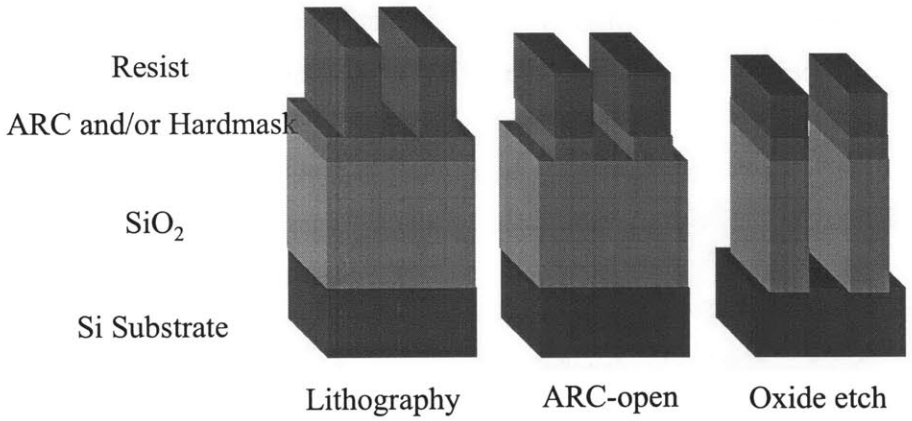

Figure 3.5 - Process flow. AFM roughness measurements were taken after each step.

Each image was 1 μm x 1 μm, and consisted of 256 linescans, each containing 256 data points for a minimum pixel – to – pixel distance of ~3.9 nm. Planefitting was applied to the sidewall portion of the images to correct for tilt and offset. A 1st order planefit was applied in the fast scan direction (down the sidewall) to correct for the sample tilting, while either a 2nd or 3rd order planefit was applied in the slow scan direction (across the sidewall) to correct for piezo and thermal drift effects.

After planefitting, the root–mean square (RMS) roughness was calculated for each line profile along the sidewall, yielding information on the SWR magnitude as a function of depth. The RMS roughness was calculated as:

$$RMS=\left[\frac{1}{n}\sum_{i}^{n}(z_i-\bar{z})^2\right]^{\frac{1}{2}} \quad (3.1)$$

where n = # of data points in profile or surface (256 in each profile across the feature), z_i = height of i^{th} data point, and $\bar{z}$ = average height of all data points. It is quite easily seen that the RMS roughness is simply the standard deviation of the heights of the data points, and can be applied to both line profiles and 2-D surfaces.

3.1.2. AFM Tip Filtering Effects[4]

The image produced by the AFM is actually a convolution of both the sample topography and the tip geometry. The finite tip curvature will limit the ultimate resolution of any topographical features on a smaller scale (see Villarrubia[5] for a thorough discussion of AFM tip convolution effects). A simple example of this can be observed by convolving a sinusoidal surface with a spherical tip (figure 3.6). The tip represented by the small circle can fully access the sample topography. However, a tip represented by the larger circle cannot fully describe the sample, and will filter the image to some extent. Figure 3.7 shows the effect of increasing the tip radius of curvature on the resulting

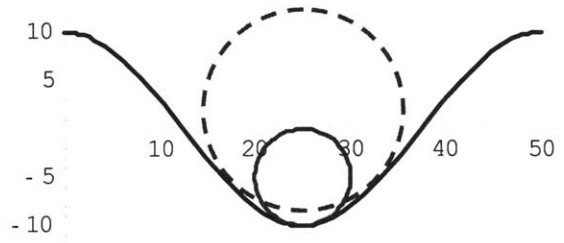

Figure 3.6 - Illustration of AFM tip filtering. The small tip (solid circle) can fully access the sample topography, while the larger tip (dotted circle) cannot.

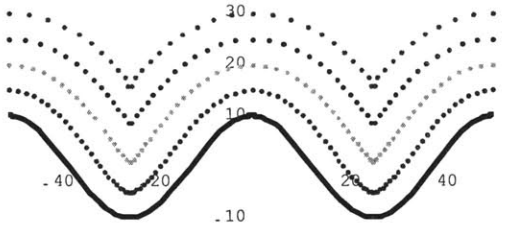

Figure 3.7 - Effect of increasing the tip radius of curvature. Traces closer to the sample surface correspond to smaller tip sizes

image, showing that filtering increases with increasing tip radius. Sample valley regions take on "inverted" peak shapes, while asperities become round protrusions. For the case of a spherical tip of radius R imaging a sinusoidal surface, we can describe the form of the filter function. In the valley region, the shape of the sinusoid y is given by :

$$y=A\frac{1}{2}\left(\frac{2\pi x}{P}\right)^2 \quad (3.2)$$

where A = amplitude, and P = period. The circle shape is given by:

$$y=\left(\frac{x^2}{2R}\right) \tag{3.3}$$

By equating the circle curvature with the sample shape, we arrive at:

$$A=\frac{1}{(2\pi f)^2 R} \tag{3.4}$$

where f = frequency = 1/P. Finally, the power spectrum filtering can be obtained via:

$$|A|^2=\frac{1}{(2\pi f)^4 R^2} \tag{3.5}$$

The extent of filtering can be determined by performing a spatial frequency analysis of the topographical AFM image. Typically, the power spectrum density (PSD) coefficients are plotted as a function of spatial frequency on a log – log plot (the PSD coefficients are simply the square of the Fourier coefficients). The filtering threshold (or cut – off) frequency can thus be identified by the point at which the slope of the PSD plot approaches –4, beyond which the finite tip size begins to distort the image. In this work, 1-D PSD plots generated from sidewalls typically showed strong contributions to the SWR from low – frequency components (~1 – 30 cycles/μm), with a cut – off frequency of ~ 30 cycles/μm. This indicates that surface feature with a periodicity below 33 nm were filtered to some extent.

The determination and consequences of tip filtering are best demonstrated by example. Figure 3.8 shows a representative sidewall line profile (measured across the sidewall surface). A visual examination reveals a partially filtered morphology characterized by inverted peaks and rounded protrusions (cross sections of striations traversing down the sidewall). This profile was taken from an etched sample, and has an RMS roughness of 3.56 nm. The data is discretized into 256 data points over a 1μm length, for a sampling rate of 256/μm. The highest frequency available to analyze is the nyquist frequency, equal to one-half the sampling rate, or 128 cycles/μm.

Figure 3.9 shows the PSD calculated for this profile. Note that at low frequencies, the PSD is relatively flat, indicating that no tip filtering is occurring. The cut – off frequency is clearly visible around 30 cycles/μm, beyond which the PSD falls of with a

slope of –4 (shown by the solid line). This indicates that, for features with a spatial periodicity smaller than ~33 nm, tip filtering occurs.

We can get a further estimate for the impact of filtering by examining the contribution of each spatial frequency to the RMS roughness measurement. We make use of Parseval's theorem, which demonstrates the equivalence of the RMS value of a signal in either the spatial or frequency domain. For our purposes, we can write Parseval's theorem as:

$$\sqrt{\frac{1}{N}\sum_{n=0}^{N-1}|x_n|^2} = \sqrt{\sum_{k=0}^{N/2} P_k \Delta f} \tag{3.6}$$

where N = total # of data points in the profile, n = n^{th} data point, x_n = height corresponding to the n^{th} data point, k = k^{th} frequency component with k = N/2 = nyquist frequency, P_k = PSD value at k^{th} frequency, and Δf = frequency resolution.

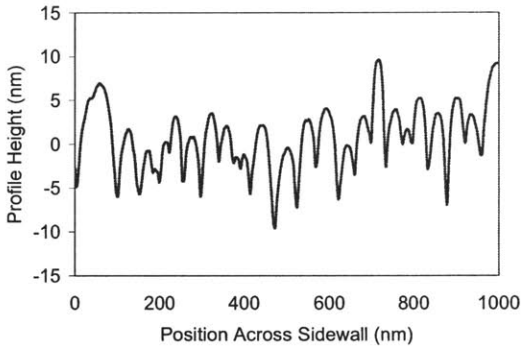

Figure 3.8 – Representative AFM profile taken across an etched sample. Note the filtered morphology characterized by inverted peaks at the low points, and rounded protrusions at the high points.

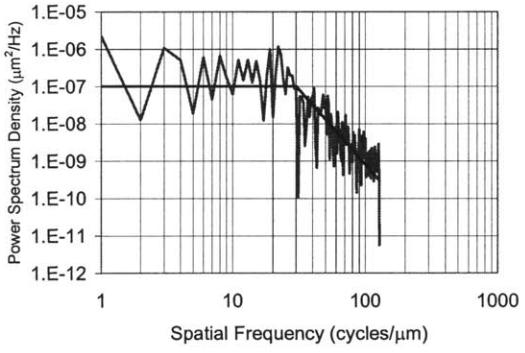

Figure 3.9 – Power spectrum density of the profile in figure 3.8. The PSD is flat at spatial frequencies below ~ 30 cycles/mm (features > 33 nm). However, at higher spatial frequencies, tip filtering is evident as shown by the –4 slope of the plot.

The term on the left is simply the RMS roughness (assuming the profile is mean – centered about zero). Therefore, by changing the limits of the summation on the right hand term, we can calculate the cumulative contribution of each frequency component to the total RMS roughness:

$$RMS_k = \sqrt{\sum_{i=0}^{k} P_i \Delta f} \tag{3.7}$$

where RMS_k = cumulative RMS roughness corresponding to the frequency components from 0 to k. Figure 3.10 shows the cumulative RMS roughness as a function of spatial frequency for the profile shown in figure 3.8. We see that the vast majority (over 96%) of the measured RMS roughness is accounted for by the lower frequency components (below 30 cycles/μm). This demonstrates that, as long as our main sidewall features are below the cut – off frequency, we should be able to capture their impact in the RMS roughness. However, features with a spatial periodicity greater than the cut – off frequency are suppressed.

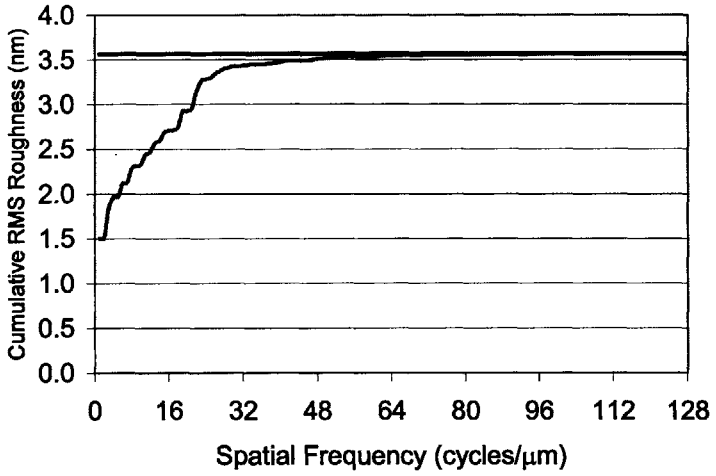

Figure 3.10 – Cumulative RMS roughness as a function of spatial frequency for the profile shown in figure 3.8. The flat line shows the total RMS roughness of the sample (3.56 nm). We see that the majority of the RMS roughness (96%) is accounted for by the lower frequency components (below 30 cycles/μm).

Now that the extent of tip filtering can be quantified, we would like to know how much of a concern it actually is. Fortunately, it is generally found that features with a high spatial frequency (small features) tend to be of smaller amplitude than low frequency features. This is shown conceptually in figure 3.11. If this were not the case, we would observe closely spaced, thin, fin – like protrusions traversing down the

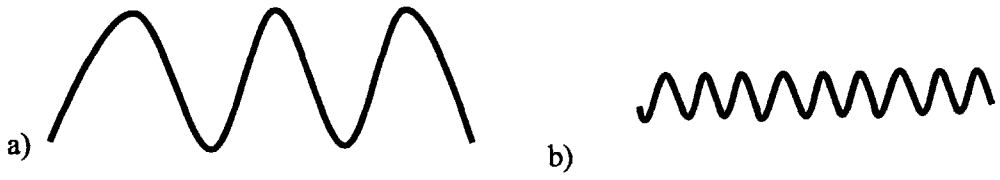

Figure 3.11 – Low frequency features (a) tend to have larger amplitude, while high frequency features (b) tend to have smaller amplitude.

sidewall, which would be unphysical and does not occur. Therefore, even though tip filtering limits the observation of high – frequency roughness components, due to this amplitude variation they tend to be unimportant anyway. Additionally, the major features generated during the etching processes described in this thesis tend to be at spatial frequencies smaller than the cut – off, in the range of 20 – 10 cycles/μm (50 – 100 nm). Based on this, we conclude that, though unavoidable, tip filtering does not greatly influence results obtained via AFM of feature sidewalls.

3.2. Roughness Transfer on 248 nm Positive Tone Resist/ARC platforms

Image formation of a positive tone chemically amplified resist structure is based on dissolution rate differences between exposed (deprotected) and unexposed (protected) regions. All physical changes occur in a spatially isotropic fashion, and therefore the topography associated with the sidewall of a developed resist line does should not show any preferential orientation. An exception to this can occur under conditions in which the ARC layer thickness is non-optimized, leading to the formation of standing waves in the resist line that will show up as ripples traversing across (rather than down) the sidewall.

Thermal oxide substrates were coated with various ARC or hardmask films, and then patterned with ~600 nm of a 248 nm environmentally stable chemically amplified photoresist (ESCAP) in a nominal 150 nm dense (1:1) line/space pattern on 8" wafers, using the "ARPAN" chrome – on – glass photomask described in chapter 2. The samples were exposed using a KrF 0.63 NA ASML stepper with annular illumination. Exposures were performed at the IBM TJ Watson Research Center in Yorktown Heights, NY. Exposure doses ranged from 22 – 24 mJ/cm^2 depending on the ARC or hardmask used.

3.2.1. Organic ARC

Antireflective coatings (ARCs) are typically highly absorbing polymeric films, coated underneath the photoresist layer. These films minimize reflection of the exposure radiation, which if left unchecked can interfere with the incident radiation within the resist film, leading to standing wave formation[6]. The ARC thickness must be carefully tuned to the resist type and exposure wavelength, with a non-optimized ARC thickness creating standing waves. The thickness tuning is accomplished by investigating the reflective properties of the resist/ARC system as a function of the ARC thickness.

Figure 3.12 shows typical reflectance curves for an ARC as a function of thickness on both Si and SiO_2 substrates. The reflectance varies with the ARC thickness, reaching several minimums (the "interference" mode), and finally approaches a low constant value when the thickness gets very large (the "matched" mode). While a thick ARC might be desirable from an optical properties standpoint, from an etch perspective we would like to keep the film as thin as possible. Therefore, for processing the ARC thickness is generally chosen in the interference region, at the point of the second minimum in the curve.

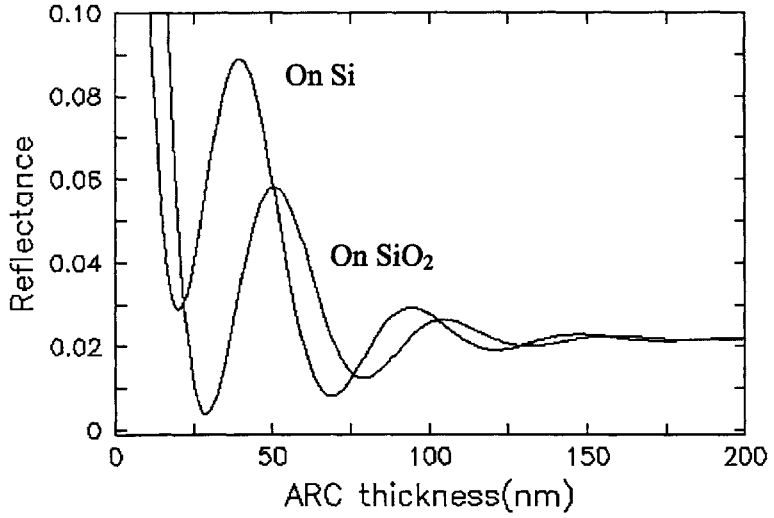

Figure 3.12 – Reflectance curves for an ARC film on Si and SiO_2 substrates. Note the reflectance varies greatly as a function of ARC thickness. The appropriate thickness is generally chosen at the point of the second minimum in the curve.

3.2.1.1 – Organic ARC, initial Lithography

90 nm of an organic ARC material was coated onto thermal oxide wafers, and then patterned with a 248 ESCAP resist as described above with a dose of 22.5 mJ/cm^2. Figures 3.13 and 3.14 show a cross sectional SEM of the patterned resist line/space pattern, and a sidewall AFM image, respectively. A slight standing wave can be observed in both the cross section and the AFM image, indicating a non-optimized ARC thickness. Discounting this irregularity, the remaining roughness is indeed isotropic and globular, without a preferential *vertical* orientation (i.e., no striations). The AFM captures approximately 490 nm of the resist sidewall (~125 linescans), leaving ~100 nm shadowed by the AFM tip (indicated on figure 3.13). Using all points imaged on the sidewall, the

RMS roughness of the whole surface is ~3.9 nm (slightly elevated due to the presence of the standing wave).

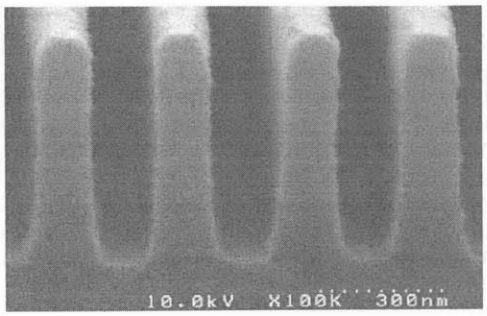

Figure 3.13 – Cross sectional AFM of initial 248 lithography on organic ARC. Note the presence of a slight standing wave, indicating a non-optimized ARC thickness.

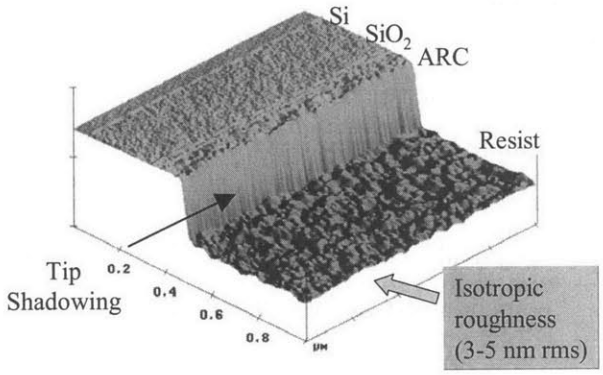

Figure 3.14 – Sidewall AFM image of initial 248 lithography. The SWR is isotropic in nature, with an RMS value of 3-5 nm, depending on location. Note the tip shadowing at the base of the sidewall

Figure 3.15 shows the RMS roughness for each linescan traversing down the sidewall. We see that it fluctuates between 3-5 nm, but aside from this variation remains fairly constant as a function of depth.

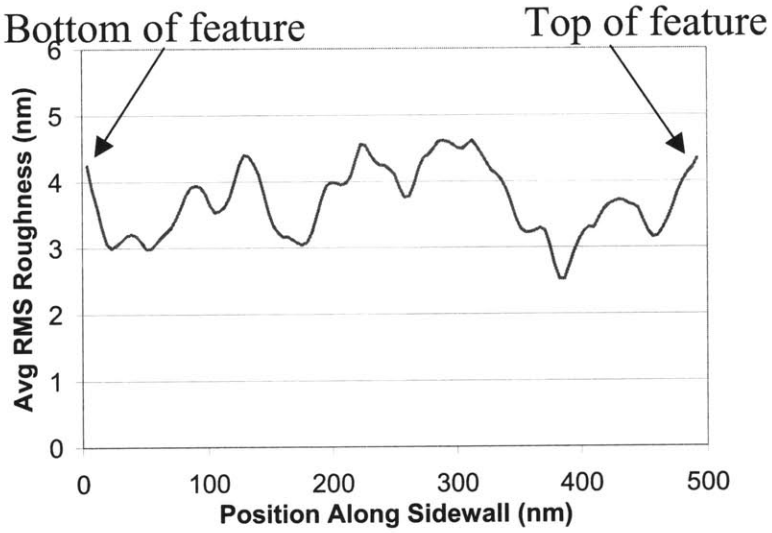

Figure 3.15 – RMS roughness as a function of depth for the resist line. The top of the feature is to the right of the plot, while the bottom is to the left. The RMS roughness fluctuates between 3-5 nm, and remains fairly constant down into the feature.

3.2.1.2. Organic ARC Open

After patterning, an etching step is required to open the ARC layer and expose the underlying oxide substrate (see figure 3.5). To enhance the etching rate and selectivity, and to control the critical dimension (CD) and profile, a sizeable bias voltage to the sample is typically used. The bias imparts directional ion bombardment, which assists in rapid, direct etching and the formation of perpendicular profiles. However, this very "physical" etching process also leads to the formation of striations on the sidewall, perpendicular to the substrate plane.

A N_2/H_2 based plasma, with ion bombardment, was used to etch the organic ARC film. The etch was performed on a LAM 4520-XL500 etcher located at IBM TJ Watson Research Center in Yorktown Heights, NY. The etching conditions are listed in Table 3.1, row 1.

Figure 3.16 shows an SEM cross – sectional micrograph of the line features after the organic ARC open etch. Faceting due to ion bombardment is clearly visible at the top of the resist (indicated by the sloped profile at the top of the line). We might expect, therefore, that the sidewall will be rougher at the top than at the bottom, taking on a depth-dependent characteristic.

Figure 3.17 shows an AFM sidewall image of a feature after the organic ARC open etch. Again, the facet is visible at the line top (to the right of the AFM image). We

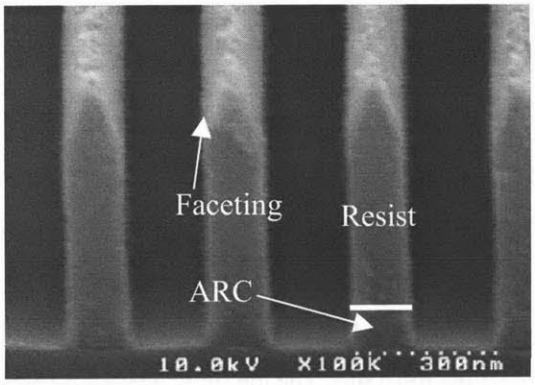

Figure 3.16 – Cross sectional SEM of sample after N_2-H_2 organic ARC open. Note the resist faceting at the feature top due to ion bombardment.

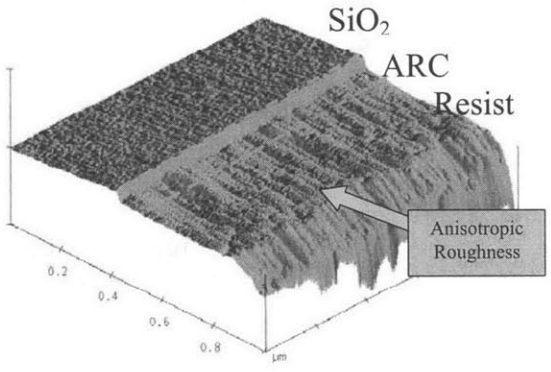

Figure 3.17 – Sidewall AFM image after N_2 – H_2 organic ARC open. The morphology of the sidewall has been transformed during the etching process, with anisotropic etch streaks now present.

observe that the morphological structure of the sidewall has been transformed. The isotropic structure that was present post-litho has been eliminated, with ion bombardment during the ARC open imparting striations, perpendicular to the sample sidewall.

Figure 3.18 shows the RMS roughness calculated as a function of depth for the sidewall shown in figure 3.17. It confirms the supposition of a depth – dependent roughness, with the top of the line rougher than the bottom due to ion bombardment. The sidewall grows smoother as the depth increases, leveling off at a fairly constant value of ~2 nm RMS. By comparison to figure 3.14, we see that, although the sidewall is now anisotropic, it is actually smoother than the initial resist sidewall (2 nm vs. 3-5 nm RMS). This is due to the fact that, with enhanced exposure to energetic ions high points on the surface etch preferentially to low points, where shadowing of etchant species can reduce the etch rate[7].

Table 3.1 – Etch conditions

Etch	Process	Pressure (mT)	Top Power (W)	Bottom Power (W)	Etch Time (s)	Gas Flow rates (sccm)	Etcher
1	N_2-H_2 ARC Open	40	500	500	15	200 N_2, 200 H_2	LAM 4520 XL
2	248 Oxide Etch	60	600	600	45 or 90	60 CF_4, 20 CHF_3, 450 Ar	LAM 4520 XL
3	"Thick" Hardmask Open	30	1000	2000	42	30 CHF_3, 150 N_2, 100 Ar, 5 O_2	LAM 4520 XL
4	"Thin" Hardmask Open	30	1000	2000	15	30 CHF_3, 150 N_2, 100 Ar, 5 O_2	LAM 4520 XL
5	Si Containing ARC Open	30	1000	2000	15	30 CHF_3, 150 N_2, 100 Ar, 5 O_2	LAM 4520 XL
6	193 Oxide Etch	100	600	300	90	60 CF_4, 20 CHF_3, 450 Ar	LAM 4520 XL
7	Bilayer Transfer Etch	10	260	80	57	20 SO_2, 40 O_2	LAM 9400

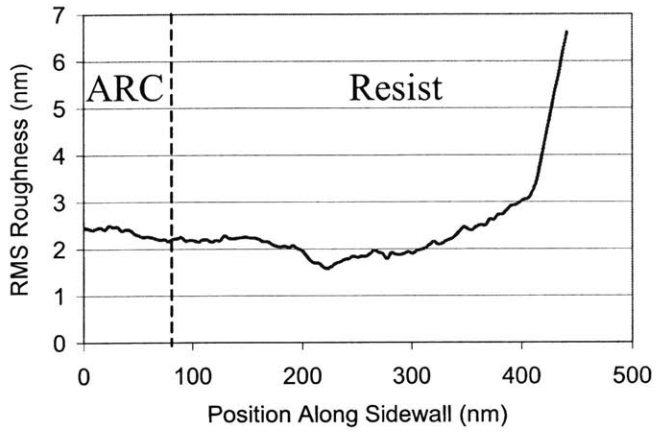

Figure 3.18 – RMS roughness as a function of depth after N_2 – H_2 ARC open. Note the depth – dependent trend, with a rougher surface near the top of the feature. The roughness decreases, finally leveling off to a fairly constant value of ~ 2 nm. Additionally, although the surface morphology has changed, it is smoother than the post – litho sidewall. High points on the surface have been smoothed by the etching process.

3.2.1.3. "Partial" (45 s) Oxide Etch

Once the ARC is opened, the remaining mask is used to pattern the underlying oxide substrate. Fluorocarbon chemistries are typically used to etch oxide, which make use of atomic fluorine and CF_x etching species, coupled with a fluorocarbon polymer deposition to control the feature profile. High ion bombardment on the feature top and bottom with deposition on the sidewall can yield vertical sidewalls[8]. However, the ion bombardment can also cause a transfer of the anisotropic roughness down the feature.

After the N_2-H_2 ARC open, a 45s fluorocarbon plasma was used to pattern the oxide. Table 3.1 row 2 gives the etching conditions. Figure 3.19 shows SEM micrographs of the post-oxide etch lines in a cross sectional, top – down, and sidewall orientation.

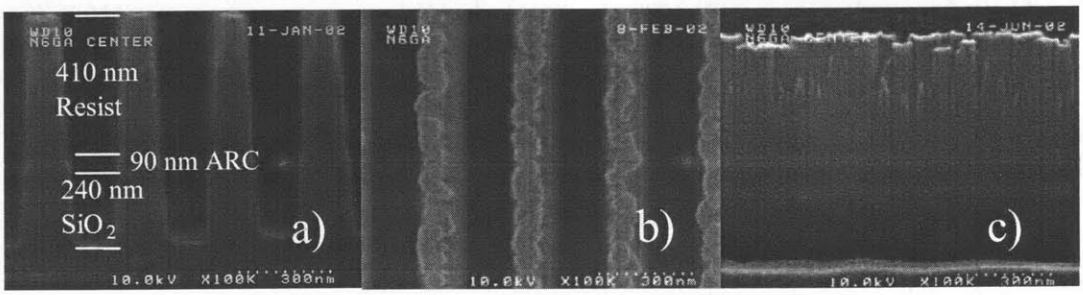

Figure 3.19 – Cross sectional (a), top down (b), and sidewall (c) SEM micrographs after a 45 s oxide etch. The top down and sidewall pictures show a large amount of "cratering" at the top of the line due to ion bombardment, leaving extremely deep, broad grooves in the sidewall.

The cross sectional image shows that ~410 nm of photoresist remains after the 45 s (240 nm) oxide etch, for an oxide/resist selectivity of ~2. However, a glance at the top – down picture shows the top of the resist is extremely roughened. Ion bombardment during the oxide etch has "cratered" the resist, particularly at the edges. The sidewall SEM image shows this effect clearly, with deep, broad striations near the top of the line.

The resulting nature of the sidewall roughness is clearly illustrated in figures 3.20 and 3.21, which show the AFM image after the 45 s oxide etch and the RMS roughness as a function of depth, respectively. It is clear that resist faceting induced during the ARC open is maintained during the oxide etch. The resist roughness now shows a depth – dependent profile, being rougher at the top. Striations formed on the resist layer now serve as a template for the emerging oxide sidewall. In other words, the existing resist topography is transferred into the silicon oxide. This behavior is partially tempered by the

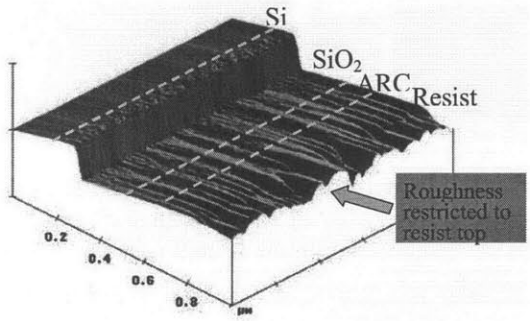

Figure 3.20 – Sidewall AFM image after 45s oxide etch. The top of the remaining resist is heavily roughened. However, the majority of the excessive roughening is confined to the mask layer, and the oxide sidewall remains relatively smooth.

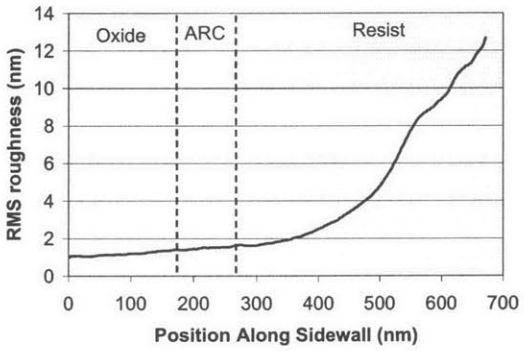

Figure 3.21 – RMS roughness after 45s oxide etch as a function of depth. The roughness shows a depth – dependent characteristic, very rough at the top of the resist, and decreasing as the depth increases. The oxide sidewall, however, remains smooth, with only shallow striations, and an RMS roughness of ~ 1 nm.

fact that, as previously mentioned, protruding features are more rapidly etched than the recessed ones, so the oxide surface is partially smoothed with respect to the resist topography. This is supported by the etch selectivity, since the resist is consumed at a slower rate compared to the oxide.

An examination of the AFM data indicates that the majority of the heavy roughening is confined to the mask layer (remaining ARC and photoresist). While there are striations in the oxide, they are relatively shallow, yielding a smooth oxide sidewall (~ 1 nm RMS). It appears that resist consumption and striation formation near the *mask / underlayer* interface might determine the extent of anisotropic roughness created on the underlayer sidewalls. By completing only a partial etch, extreme roughening of the oxide has been prevented.

This can be seen by stripping the remaining ARC and photoresist using an O_2 plasma, and imaging the etched oxide lines via top down SEM (figure 3.22). Any deep striations present on the oxide sidewall will show up as "mousebites" on the line edge.

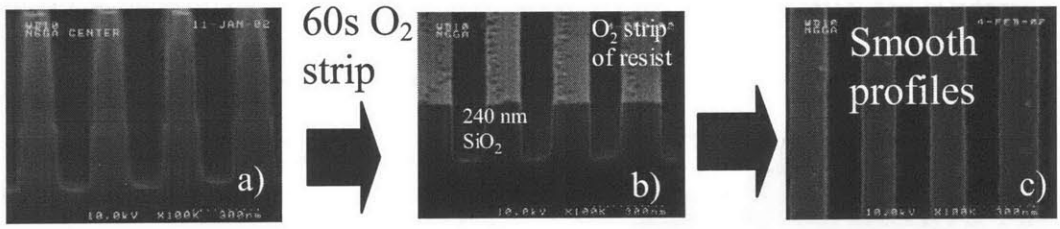

Figure 3.22 – a) Patterns after 45s oxide etch. b) Remaining ARC and photoresist is stripped in an O_2 plasma. The remaining oxide profiles appear smooth, with a sharp edge. c) The stripped profiles, when viewed top down are smooth and sharp, with no sign of "mousebites" on the feature edge that would indicate the presence of deep striations on the oxide sidewall.

However, we see that this is not the case. The oxide remaining after resist strip looks smooth, with a sharp edge devoid of striations. The top – down SEM of the stripped sample is smooth, with no signs of "mousebites" that would indicate the presence of deep striations on the oxide sidewall. Thus, by confining the roughness transfer above the ARC / oxide interface, we have prevented anisotropic roughness from reaching the substrate.

3.2.1.4. "Complete" (90 s) Oxide Etch

To examine this phenomenon further, a sample was etched for twice as long (90 s). The ARC open and oxide etch plasma chemistries were identical to those in the previous section; only the oxide etch time was changed. Figure 3.23 shows SEM

micrographs of the features after the 90 s etch from cross sectional, top down, and sidewall viewpoints. The same trends are evident – heavy cratering of the resist tops, with broad striations traversing down the sidewall.

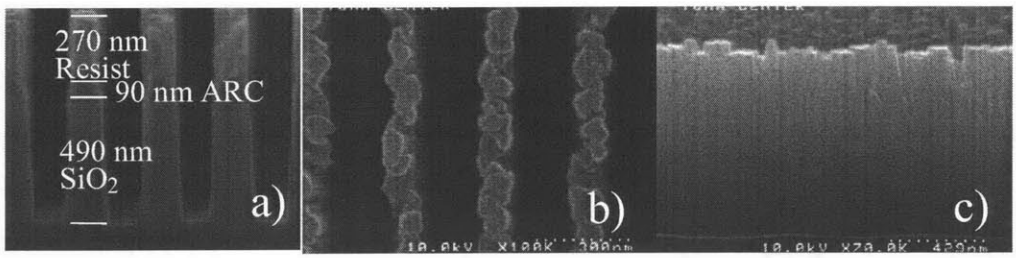

Figure 3.23 – Cross sectional (a), top down (b), and sidewall (c) SEM micrographs of organic ARC sample after a 90 s oxide etch. As with the partial etch, the top down and sidewall pictures show a large amount of "cratering" at the top of the line leaving extremely deep, broad grooves in the sidewall.

Figures 3.24 and 3.25 show the AFM of the 90 s etched sample, and the RMS roughness as a function of depth, respectively. From the AFM image, it is clear that incipient striations generated at early stages of the etch process became fully developed oxide crevices, whose origin can be traced back to the remaining ARC and resist layer. The SWR is depth dependent, with extreme values (~17 nm) near the top of the line. The SWR on the oxide is larger in magnitude than that left after the partial oxide etch (~ 2 nm vs. 1 nm RMS) as the grooves had the opportunity to etch deeper.

From the AFM image it appears the anisotropic striations have penetrated the ARC/oxide interface, allowing the grooving of the sidewall. This was verified by, as before, stripping the remaining ARC and photoresist with an O_2 plasma, and imaging the oxide features via a top down SEM (figure 3.26). After the complete 90 s oxide etch, mousebites are visible on the stripped oxide lines (corresponding to the sidewall striations viewed end – on). Therefore, it does indeed seem that in this case, resist consumption and striation formation near the ARC/oxide interface determines the extent of anisotropic roughness created on the oxide.

3.2.1.5. Comparison of Surface Profiles from Partial and Complete Oxide Etch Samples

In order to better compare and quantify the depth dependence of the SWR on both the partial and complete oxide etch samples, surface profiles were generated and the associated LER calculated. Figures 3.27 and 3.28 show these surface profiles generated

from the AFM images for the partial and complete oxide etch samples, respectively, at 5 locations along the sidewall: near the resist top (a), in the middle of the remaining resist

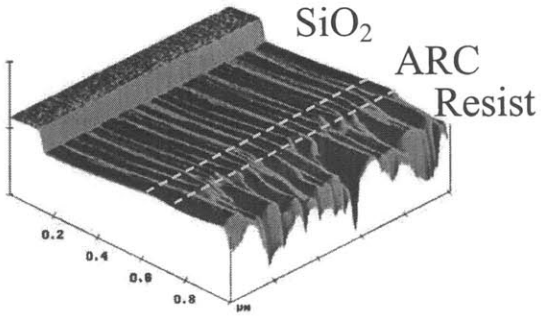

Figure 3.24 – Sidewall AFM image after 90s oxide etch. Again, the top of the remaining resist is heavily roughened. However, the SWR has penetrated the ARC/oxide interface, creating fully developed anisotropic striations along the oxide sidewall.

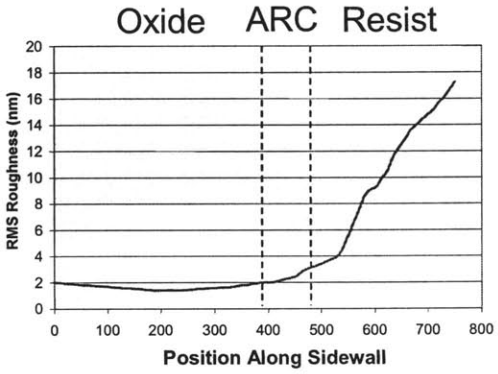

Figure 3.25– RMS roughness after 90s oxide etch as a function of depth. The roughness shows the familiar depth – dependent characteristic. The oxide sidewall is rougher than that left after the partial etch (2 nm vs. 1 nm RMS)

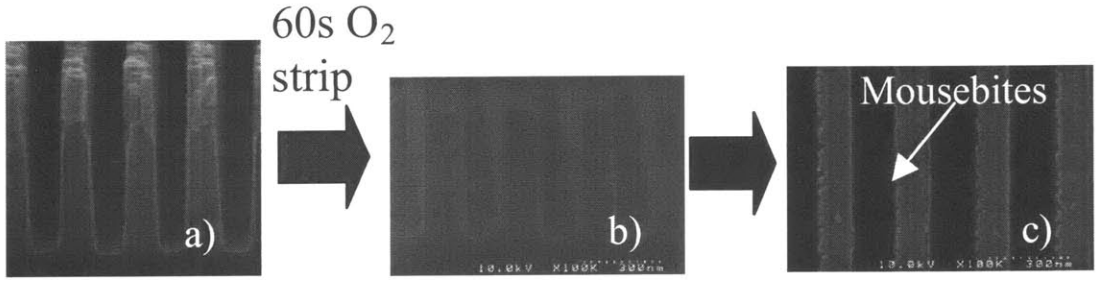

Figure 3.26 – a) Patterns after 90s oxide etch. b) Remaining ARC and photoresist is stripped in an O_2 plasma. c) Mousebites can be seen on the stripped profile edge when viewed top down, indicating the presence of deep striations on the oxide sidewall.

(b), at the resist/ARC interface (c), at the ARC/oxide interface (d), and near the bottom of the oxide (e). The RMS roughness of the partial etch profiles are 8.4, 3.7, 1.6, 1.4, and 1.0 nm, respectively. Looking at figure 3.27, we see that the large striations present on the resist and ARC have died out by the time the ARC/oxide interface was reached (d), yielding smooth oxide sidewalls. The spatial periodicity of any remaining roughness has increased as well, as evidenced by the decrease in observed tip filtering from the resist

profiles to the ARC and oxide profiles. In comparison, the 90 s etched sample (figure 3.28) shows extreme cratering at the top of the resist, with striations that remain spatially correlated to the line profile at the ARC/oxide interface (d). These features are still traceable even on the oxide layer itself (e), but their amplitude has decreased. We note that tip filtering is evident at the ARC/oxide interface as well, indicating the presence of deep grooving and giving rise to the mousebites observed in figure 3.26c. The magnitude of the roughness on the oxide layer is approximately twice that observed on the partially etched sample (~ 2 nm vs. 1 nm RMS), indicating that the longer etch has allowed the development of deeper sidewall striations.

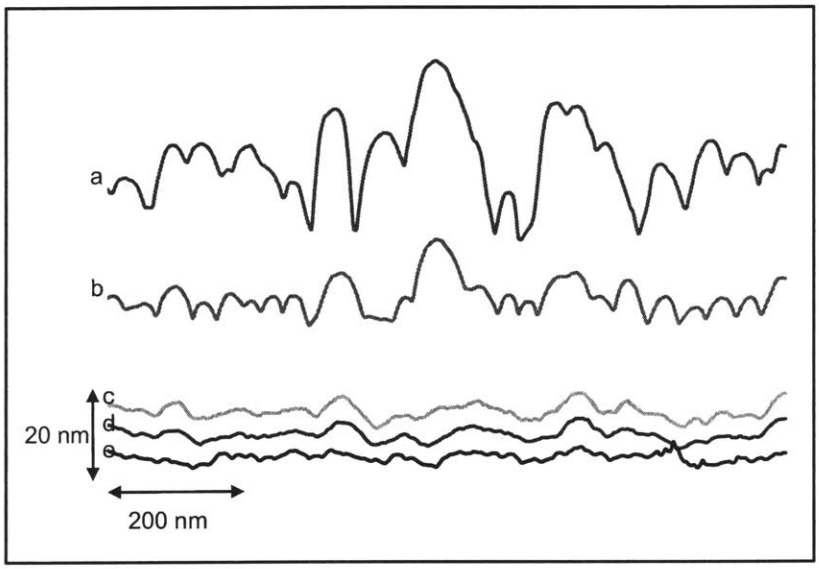

Figure 3.27 – Surface profiles generated for the partial oxide etch sample at 5 locations: (a) Near the top of the resist (σ=8.4 nm), (b) in the middle of the remaining resist (σ=3.7 nm), (c) at the resist/ARC interface (σ=1.6 nm), (d) at the ARC/oxide interface (σ=1.4 nm), and (e) near the bottom of the oxide (σ=1.0 nm). The profiles have been offset for clarity. We note that striations present on the resist have for the most part, died out at the ARC/oxide interface (as has evidence of tip filtering), yielding smooth oxide sidewalls.

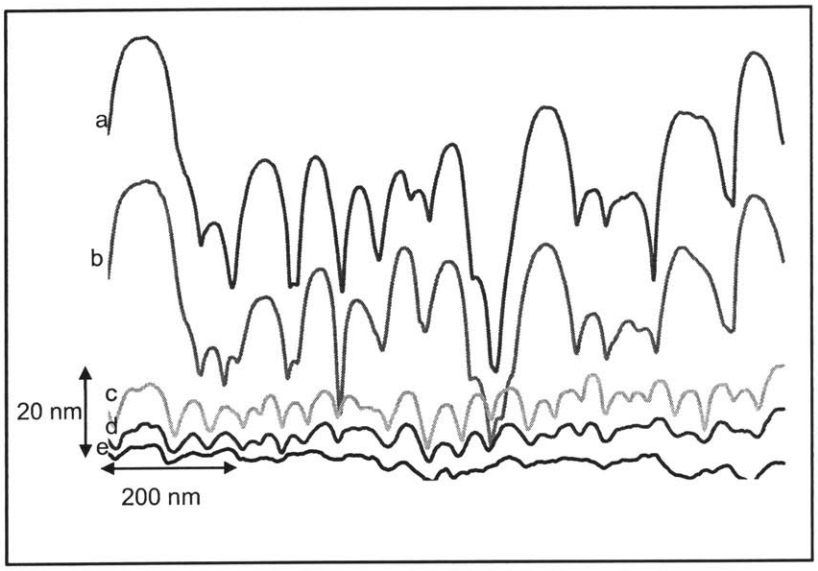

Figure 3.28 – Surface profiles generated for the complete oxide etch sample at 5 locations: (a) Near the top of the resist (σ=15.2 nm), (b) in the middle of the remaining resist (σ=12.7 nm), (c) at the resist/ARC interface (σ=3.1 nm), (d) at the ARC/oxide interface (σ=2.0nm), and (e) near the bottom of the oxide (σ=2.0nm). Now, striations present on the resist sidewall can be spatially correlated all the way to the ARC/oxide interface, creating the mousebites observed on the stripped oxide sample.

3.2.2. Hardmask

Organic ARC materials suffer from poor etch selectivity to photoresist (often less than 1), as they are compositionally very similar. With the advent of thin film imaging (where the resist layer may be on the order of 100 – 200 nm), the bulk of the resist may be consumed during the ARC open etch, leaving inadequate mask material remaining to etch the substrate to the required depth.

This problem can be addressed by incorporating ARC properties into an underlying hardmask (HM), designed to have a high etch selectivity to both the overlying photoresist and the underlying substrate. IBM has accomplished this via the invention of Si based materials, deposited by plasma – enhanced chemical vapor deposition (PECVD) that perform both as an ARC and a hardmask, enabling the use of thin resists for device fabrication[9-12]. These materials act as ARCs at both 248 and 193 nm wavelengths (although the 248 nm and 193 nm versions differ compositionally from each other). The index of refraction (n) and extinction coefficient (k) can be tuned by varying the

deposition parameters, with substrate temperature and deposition bias having the most effect[10].

Because the chemical composition of this HM material is significantly different from typical photoresists (unlike organic ARCs) its etch selectivity is much higher, on the order of ~2-4 depending on etch chemistry (compared with a typical selectivity for organic ARC of ~0.7 - 1), enabling thicker HM films with thinner resists. Additionally, the selectivity over oxide can exceed 10, allowing the etching of deep oxide trenches even after the remaining photoresist is completely lost. The HM has been used to etch deep contact structures into 1.8 μm borosilicate glass (BSG)[9].

The optical constants of the hardmask material can be graded by continually varying the deposition parameters, yielding a reflectance curve free of interference fringes like those seen in figure 3.12. If a tuned HM is not used, the HM thickness is chosen at the second minimum in the interference mode (a "thin" HM); however, this can create problems when attempting to pattern over existing topography, or if the HM thickness varies over the wafer (similar to problems seen with organic ARCs). Fortunately, the enhanced etch resistance of the HM compared with organic ARC enables the deposition of a "thick" HM if desired, chosen to operate in the matched mode where the reflectance is independent of the HM thickness.

To examine the roughness transfer characteristics of the IBM HM material, samples were patterned similar to figure 3.5, with the same photoresist as used on the organic ARC samples, and either a "thin" (100 nm) or "thick" (300 nm) HM replacing the organic ARC layer. The hardmask was opened in a fluorocarbon plasma chemistry, with the resulting patterns used to transfer the trenches into the underlying oxide substrate via a 90 s etch. AFM sidewall images and roughness data were calculated after the HM open and oxide etch for both the "thin" and "thick" HM samples (the initial lithography was similar to that obtained on the organic ARC samples).

3.2.2.1. "Thick" Hardmask Open

After lithographic patterning, 300 nm of HM was etched in a highly physical fluorocarbon plasma (the etch conditions are given in table 1, row 3). The large bottom power (2000 W) and polymerization (CHF_3 chemistry) enabled highly selective etching

over the photoresist (selectivity ~ 2.6). Figure 3.29 shows SEM micrographs of the "thick" HM sample after the HM open in a cross sectional, top down, and sidewall perspective.

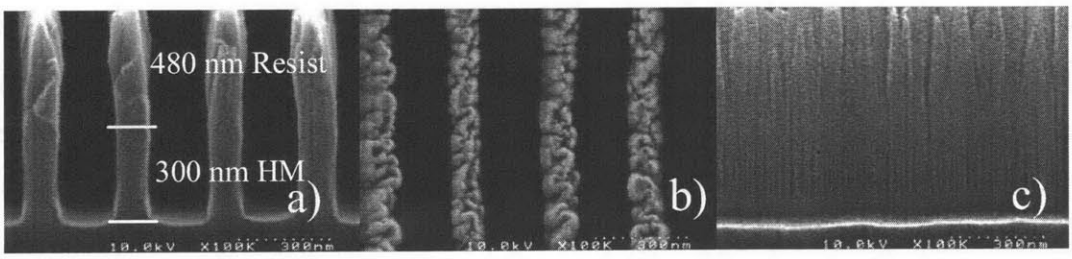

Figure 3.29 – Cross sectional (a), top down (b), and sidewall (c) SEM micrographs after a 42 s "thick" HM open. A large amount of resist remains due to the enhanced etch selectivity the HM possesses. However, the extreme physical nature of the HM open has left the tops of the lines cratered, and the sidewall striated.

From these pictures, we see that the physical etch characteristics that enabled selective etching have also created heavy cratering and striation formation on the top and sidewall of the etched lines.

Figures 3.30 and 3.31 show the AFM sidewall image and the calculated RMS depth dependent SWR, respectively, for the "thick" HM sample. The AFM image confirms the details observed in the sidewall SEM image, with large, apparently deep striations particularly visible on the resist sidewall. A particle or other protrusion is observable near the resist top, and yields an enhanced RMS roughness measurement at that depth observed on the plot. The SWR shows the (by now) familiar depth - dependent roughness characteristic, with excessive roughness at the top of the line, decreasing as the depth is increased. Note that ~ 85 nm at the bottom of the line is shadowed by the AFM tip.

The SWR on the bulk of the HM sidewall is slightly larger in magnitude than that observed on the organic ARC sample (3-4 nm vs. 2 nm), indicating that a subsequent oxide etch might be rougher as well. The roughness at the resist/HM interface is ~ 4 nm, creating mousebites on the HM top that can be observed by stripping the remaining photoresist (figure 3.32).

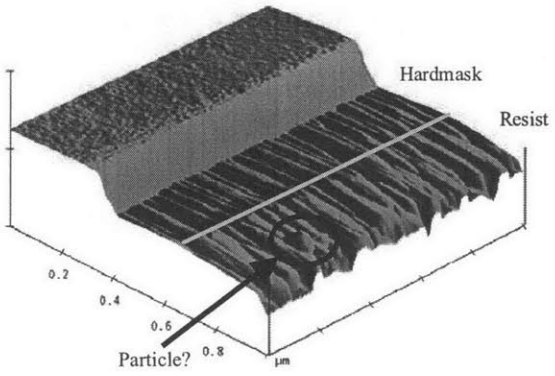

Figure 3.30 – Sidewall AFM image "thick" hardmask open. The sidewall surface is heavily striated, with extreme roughness at the top of the line due to the large bottom power (2000 W) and ion bombardment during the etch. Note the presence of a particle that increases the local roughness at that depth.

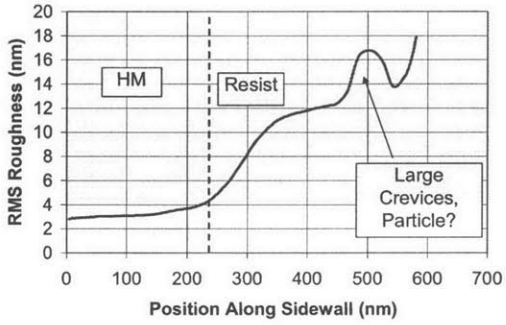

Figure 3.31 – RMS roughness after "thick" hardmask open as a function of depth. The roughness shows the familiar depth – dependent characteristic, very rough at the top of the resist, and decreasing as the depth increases. The hardmask sidewall is rougher than the organic ARC (~3 – 4 nm RMS). Note the increased roughness on the resist line due to the particle.

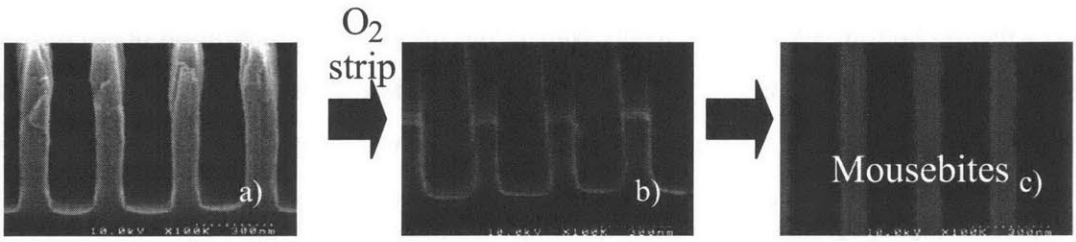

Figure 3.32 – a) Patterns after "thick" hardmask open. b) Remaining photoresist is stripped in an O_2 plasma, leaving the trenches etched in the hardmask. c) Mousebites can be seen on the stripped profile edge when viewed top down, indicating the presence of deep striations on the hardmask sidewall.

3.2.2.2. "Thin" Hardmask Open

Similar to the above, samples were created with a 100 nm hardmask layer ("thin" HM). After lithography, the same high power fluorocarbon etch was used to open the hardmask (with an etch time of 14 s rather than 42 s). The etch conditions are detailed in table 1, row 4.

Figure 3.33 shows SEM micrographs of the samples after the "thin" HM open. They look similar to the "thick" HM samples, with striations traversing down the sidewall, and deep cratering at the top of the line. The HM/resist selectivity is about the same as expected (~2.5). However, a comparison of the depth – dependent SWR between the "thick" and "thin" HM open samples reveals differences due to the shorter etch time.

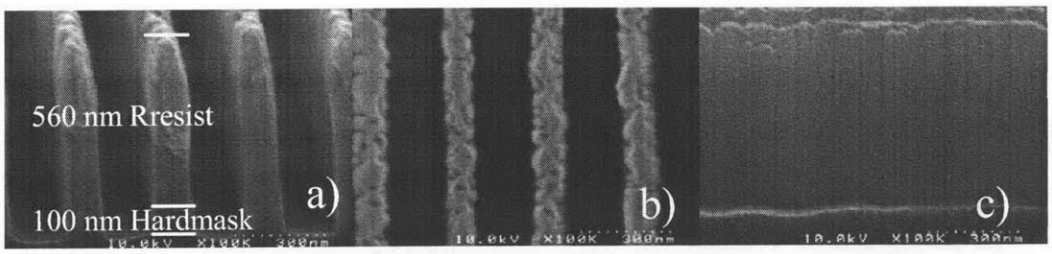

Figure 3.33 – Cross sectional (a), top down (b), and sidewall (c) SEM micrographs after a 42 s "thin" HM open. Similar to the "thick" HM sample, a large amount of resist remains due to the enhanced etch selectivity the HM possesses, and the sidewall is striated.

Figure 3.34 shows the AFM image of the "thin" HM sample sidewall. It confirms the sidewall SEM image, showing correlated striations traversing down due to ion bombardment during the etch. However, differences in the SWR due to the shorter etch time can be seen in figure 3.35, which shows the depth dependent SWR of both the "thick" and "thin" HM open samples for comparison. The "thin" sample, with a shorter required etch, yields a larger fraction of relatively smooth sidewall, leveling out at ~ 3 nm RMS for the bottom 300 nm of the sidewall in the image. The penetration depth of deep striations can be determined by observing the inflection point on each curve. On the "thin" HM sample, deep striations traverse down approximately 250 nm from the top of the line. The longer etch on the "thick" HM sample, in contrast, yielded a larger SWR on the bulk of the sidewall, and allowed deep striations to penetrate all the way to the resist/HM interface. This leads to a rougher sidewall at that location than on the "thin" sample (4 nm vs. 3 nm RMS). However, a glance at the SWR magnitude at the bottom of the sidewall (near the HM/oxide interface) for both the "thick" and "thin" HM samples is approximately the same (~3 nm RMS), indicating that, as long as the deeper striations can be confined to the mask layers and kept away from the oxide, the sidewalls on the oxide substrate after oxide etch might be of comparable roughness on both types of sample.

3.2.2.3. "Thick" Hardmask Oxide Etch

After opening the 300 nm hardmask as described above, the samples underwent the same 90 s oxide etch performed on the organic ARC samples (etch conditions given in table 1, row 2). Figure 3.36 shows SEM micrographs of the etched samples. After the oxide etch, only about 120 nm of resist remains. However, the entire 300 nm thick HM

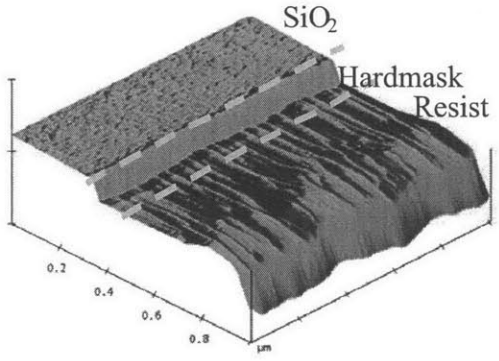

Figure 3.34 – Sidewall AFM image of "thin" hardmask open.

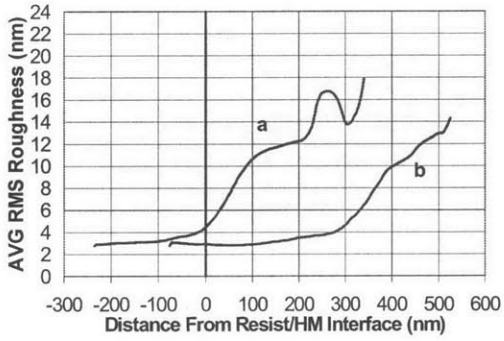

Figure 3.35 – Depth – dependent SWR of both "thick" (a) and "thin" (b) hardmask open samples, plotted vs. distance from the resist/HM interface. The much longer etch time on the "thick" HM sample has created a much rougher sidewall, with deep striations penetrating almost to the interface. The "thin" HM sample, in contrast, is smoother near the top of the line, and deep striations do not penetrate as far down the sidewall.

is still untouched, leaving 420 nm of remaining mask available to continue the etch if desired. Contrast this with the organic ARC sample, where 270 nm of mask remained after the 90 s oxide etch.

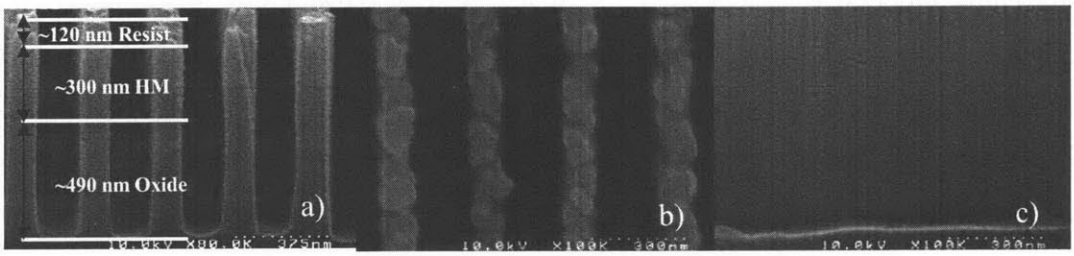

Figure 3.36 – Cross sectional (a), top down (b), and sidewall (c) SEM micrographs after 90 s oxide etch on "thick" HM open. Most of the resist has been consumed, but due to the thickness of the HM approximately 420 nm of masking material remains, demonstrating the applicability of HM materials when etching deep trenches.

Figures 3.37 and 3.38 show the sidewall AFM and depth dependent SWR, respectively, of the post – oxide – etch "thick" hardmask sample. Some sort of particulate or other contaminant can be observed in the AFM image, which leads to a slightly irregular (bumpy) SWR plot. Nevertheless, correlated striations can be seen traversing

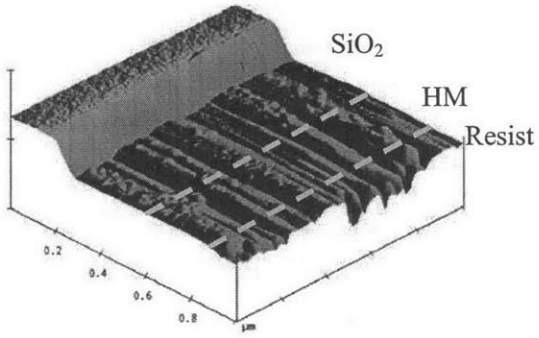

Figure 3.37 – Sidewall AFM image of "thick" hardmask sample after 90 s oxide etch. There is some sort of particulate contamination on the sidewall. Nonetheless, deep correlated striations are observable, transferring through all the layers

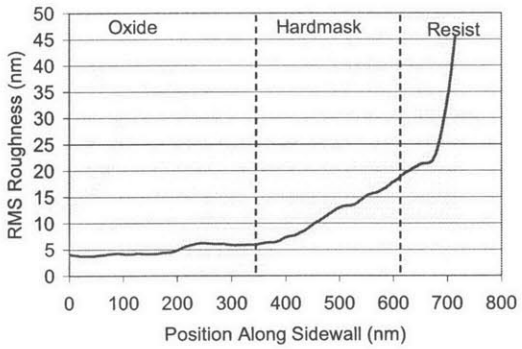

Figure 3.38 – Depth dependent RMS roughness of "thick" hardmask sample after 90 s oxide etch. The resist and hardmask are extremely roughened. However, the bulk of the oxide sidewall ranges from 4 – 6 nm RMS

the entire sidewall, from the photoresist straight down to the bottom of the oxide, unlike the comparable organic ARC sample after oxide etch (figure 3.24) that showed large striations within the resist layer, and higher frequency striations through the ARC and oxide. The hardmask therefore seems to allow more SWR transfer into the emerging oxide sidewall than the organic ARC in this particular oxide etch chemistry, indicating that the hardmask material has been optimized for selectivity purposes rather than for roughening propensity. The oxide etch chemistry may transfer roughness through the hardmask easier than through the organic ARC because this fluorocarbon chemistry tends to be more selective to organic materials than inorganic materials. It is also possible that the highly polymerizing fluorocarbon chemistry used to open the hardmask left a residual polymer on the sidewall, creating the larger striations observed during the oxide etch. We will investigate this point more closely in chapter 4.

The hardmask material seems to allow not only a more spatially correlated SWR transfer, but also permits a larger magnitude roughness transfer as well during oxide etch. A comparison of the SWR magnitude on the organic ARC and HM samples after oxide etch bears this out as well. Recall from figure 3.18 that the SWR at the ARC/oxide interface after organic ARC open was ~2.5 nm RMS. This compares reasonably well with the SWR after the thick HM open (about 3 nm RMS as shown in figure 3.31). The post – oxide etch SWR, however, is markedly different for the organic ARC and thick HM samples (2 nm vs. 4.5 nm RMS, respectively, from figures 3.25 and 3.38). So, even

though the post ARC/HM open SWR was comparable for both samples, the post oxide etch SWR is higher in magnitude for the HM than for the organic ARC.

3.2.2.4. "Thin" Hardmask Oxide Etch

Similar to the "thick" (300 nm) hardmask sample, after hardmask open the "thin" (100 nm) HM sample underwent the same 90 s oxide etch (etch conditions detailed in table 1, row 2). Figure 3.39 shows SEM micrographs of the etched samples.

Figure 3.39 – Cross sectional (a), top down (b), and sidewall (c) SEM micrographs after 90 s oxide etch on "thin" HM open. More resist remain than on the "thick" sample (~200 nm vs. ~120 nm) as less was consumed during the shorter required hardmask etch.

More resist remains than on the "thick" HM sample as less was consumed during the shorter hardmask etch (14 s vs. 42 s). However, the sidewall itself looks very similar. Again, striations correlated down the entire sidewall (through all three layers) can be observed on the sidewall SEM figure.

Figure 3.40 shows the sidewall AFM image of the "thin" HM sample after oxide etch. It is free of the particulate contamination observed on the previous sample, and looks quite similar to it, confirming the SWR structure observed in the SEM. Again, the hardmask has allowed a more correlated SWR (as compared to organic ARC) to transfer through to the oxide.

Recall our hypothesis that, for a given material, the SWR at the ARC (or HM) / oxide boundary, after ARC/HM, open casts the SWR transfer into the emerging sidewall during a subsequent oxide etch. Therefore, both the "thick" and "thin" HM samples should yield similar SWR magnitudes on the post – etch oxide, as the SWR magnitude at the HM/oxide interface after HM open was approximately the same for both the "thick" and "thin" samples even though the "thick" sample had a larger amount of roughness on the bulk sidewall due to the longer required hardmask etch (figure 3.35). This supposition is borne out in figure 3.41, which shows the depth dependent SWR after oxide etch for

both the "thick" and "thin" HM samples, plotted from the hardmask/oxide interface. Accounting for the slight irregularities in the "thick" HM curve due to the presence of contamination on the sidewall, the two curves lie almost on top of one another at the level of the oxide. Additionally, the increased roughening at the top of the line on the "thick" sample due to the longer HM etch is captured as well.

3.2.3. Silicon – Containing Spin – On ARC

While the above PECVD hardmask material possesses the etch selectivity required for thin film imaging, from a process integration perspective it is less than ideal. First, an extra processing step is required to deposit the hardmask on the substrate, which limits throughput of wafers. Additionally, the hardmask material cannot be removed as easily as an organic ARC, necessitating extra strip processes.

It would be desirable to incorporate etch selectivity into a polymer formation that can be spun – on the wafers during the photoresist application and exposure, eliminating

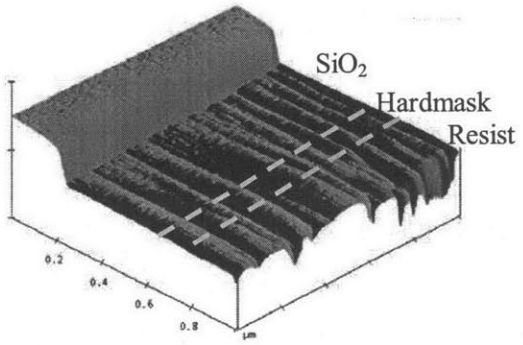

Figure 3.40 – Sidewall AFM image of "thin" hardmask sample after 90 s oxide etch

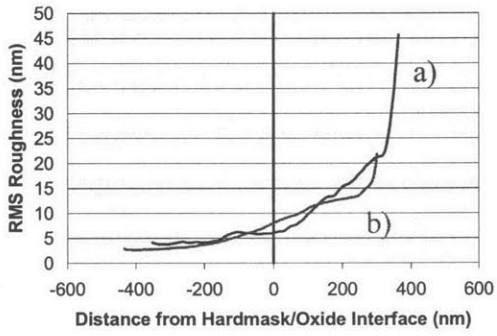

Figure 3.41 – Depth dependent SWR of both "thick" (a) and "thin" (b) hardmask open samples after 90 s oxide etch, plotted vs. distance from the hardmask/oxide interface. Both curves lie almost on top of each other, bolstering the hypothesis that the SWR at the HM/oxide boundary after HM open serves to cast the underlying SWR transfer during the subsequent oxide etch.

the need for an extra deposition step. To this end, IBM has invented a novel class of silicon – containing polymers that can be spin applied, allowing their integration in a fashion similar to standard organic ARC materials[13]. They function as ARC layers at 248 and 193 nm wavelengths. The silicon content gives the polymer an inorganic characteristic, leading to etch selectivity on the order of ~2-3:1 over photoresist in

fluorocarbon based plasma chemistries. Additionally, the Si – containing ARC can planarize the surface over topography[14].

To examine the roughness transfer characteristics of the IBM Si – containing ARC, samples were patterned similar to figure 3.5, with the same photoresist as used on the organic ARC samples, with a 160 nm layer of Si ARC replacing the organic ARC. The Si ARC was opened in a fluorocarbon plasma chemistry (the same chemistry used to open the hardmask material), with the resulting patterns used to transfer the trenches into the underlying oxide substrate via a 90 s etch. AFM sidewall images and roughness data were calculated after the Si ARC open and oxide etch. Again, the initial lithography was similar to that obtained on the organic ARC samples, and for brevity is not shown.

3.2.3.1. Si – Containing ARC Open

After lithographic patterning, 160 nm of Si ARC was etched in the same highly physical fluorocarbon plasma used to open the hardmask (the etch conditions are given in table 1, row 5). A selectivity over the photoresist of approximately 2:1 was obtained. Figure 3.42 shows the by-now familiar SEM micrographs of the Si ARC sample after the ARC open in a cross sectional, top down, and sidewall perspective.

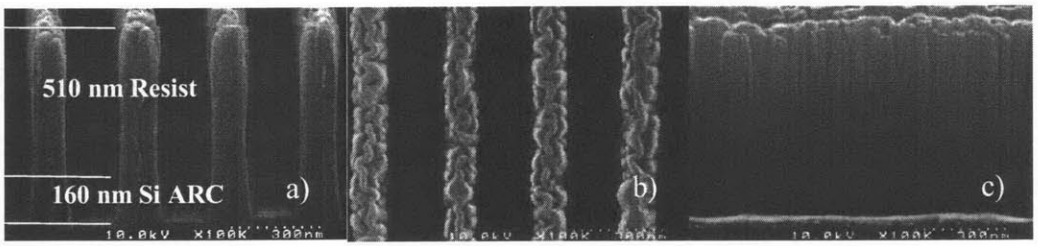

Figure 3.42 – Cross sectional (a), top down (b), and sidewall (c) SEM micrographs after a 15 s Si ARC open.

Figure 3.43 shows the sidewall AFM image of the Si ARC sample after ARC open. Note that ~ 50 nm at the bottom of the line is shadowed by the AFM tip. Additionally, a glance at figure 3.42c will show large, low-frequency striations that are not observed on the AFM image in figure 3.43. This is due to a measurement error (the top ~ 70 nm of the sidewall was not imaged during the AFM scan). Nevertheless, the higher frequency striations observed in the SEM in the middle of the sidewall are clearly visible in the AFM image.

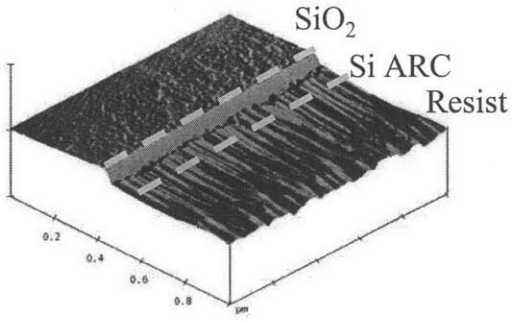

Figure 3.43 – Sidewall AFM image of Si ARC sample after ARC open. Approximately 50 nm at the bottom of the ARC layer is shadowed by the AFM tip, and the top ~ 70 nm of the resist was not imaged. Nevertheless, correlated striations are observed traversing down the sidewall into the ARC layer, confirming the sidewall SEM image.

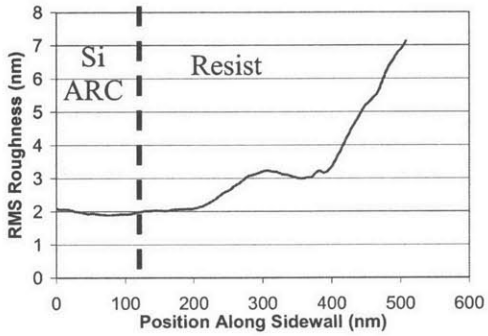

Figure 3.44 – Depth – dependent SWR of Si ARC sample after ARC open. The roughness in the ARC layer is comparable to the organic ARC sample (~ 2 nm RMS).

Figure 3.44 shows the depth dependent SWR calculated from the AFM image. We see the familiar characteristic of the sidewall, rough at the top with decreasing amplitude as the depth is increased. Interestingly, the roughness magnitude in the Si ARC layer after ARC open is comparable to the organic ARC sample (~ 2 nm RMS). Therefore, if the Si ARC were to etch the same as the organic ARC during the subsequent oxide etch we would expect the final oxide SWR to be comparable on both samples. If they are not, material differences between the Si and organic ARC might be responsible, or the highly polymerizing fluorocarbon nature of the ARC open might be to blame (similar to the trends observed on the hardmask samples).

3.2.3.2. Si – Containing ARC Oxide Etch

The Si ARC samples, after ARC open, underwent the same 90 s oxide etch used on all the samples (table 1, row 2). Figure 3.45 shows SEM micrographs of the etched samples. Immediately apparent from figure 3.45a is that the oxide did not etch as deeply as on the other samples (330 nm vs. 490 nm). Additionally, the profiles are much more tapered. The tapering may be due to polymer deposition left on the sidewall during the ARC open, narrowing the feature during oxide etch. The etching rate difference may be due to a loading effect, where the Si-O moieties in the exposed Si ARC sidewall create a larger active etching area, consuming etchant species and/or evolving product species,

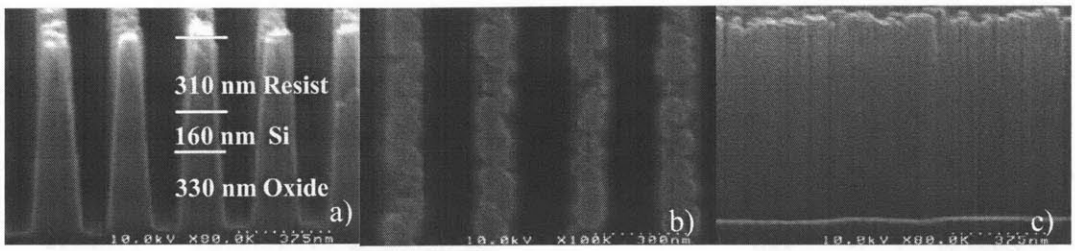

Figure 3.45 – Cross sectional (a), top down (b), and sidewall (c) SEM micrographs of Si ARC sample after 90 s oxide etch. Note the tapered profiles and the fact that only ~ 330 nm of oxide was etched (in contrast to the 490 nm etched in 90s on the other samples). It is possible that the Si ARC material caused loading from the sidewall during processing, changing the etch rate and tapering the features.

depressing the etch rate[15].

Figure 3.46 shows the sidewall AFM image of the Si ARC sample after oxide etch. Approximately 80 nm at the bottom of the sidewall is shadowed by the AFM tip, and not imaged. Similar to the hardmask samples, we see broad, correlated striations traversing right through the ARC layer into the underlying oxide, which could be due to the inorganic nature of the Si ARC material, or due to the depositing fluorocarbon chemistry used to open it.

Figure 3.47 shows the depth – dependent SWR roughness calculated from the AFM image. Here also, the roughness magnitude on the oxide sidewall more closely resembles that found on the inorganic hardmask sample rather than the organic ARC sample. The SWR is about 5 nm RMS on the oxide sidewall, and at the Si ARC/oxide interface. This large roughness magnitude at the interface yields mousebites on the oxide lines, which can be observed by stripping the remaining resist and Si ARC material (figure 3.48).

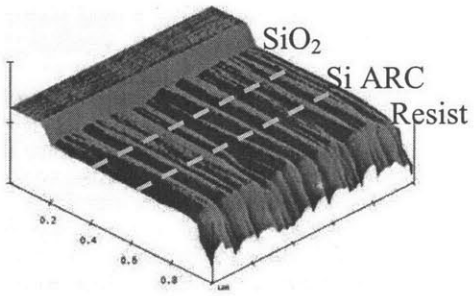

Figure 3.46 – Sidewall AFM image of the Si ARC sample after 90s oxide etch. Broad striations traverse the entire length of the sidewall, similar to the hardmask samples. Again, the depositing fluorocarbon chemistry used to open the ARC may be to blame.

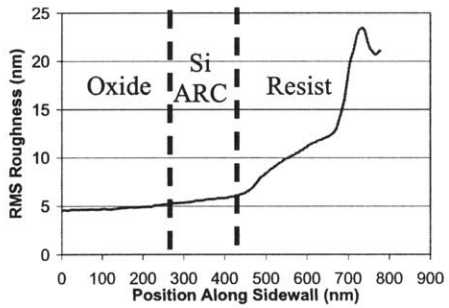

Figure 3.47 – Depth – dependent SWR of Si ARC sample after oxide etch. The roughness magnitude on the oxide is higher than that obtained on the organic ARC sample, and is similar to the hardmask results (~ 5 nm RMS).

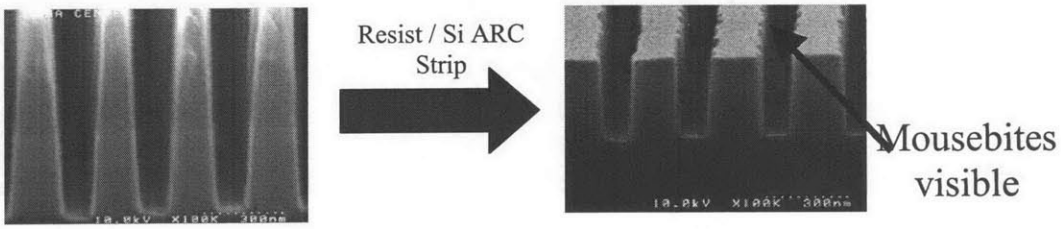

Figure 3.48 – After stripping the remaining photoresist and Si ARC, mousebites are observed at the top of the oxide lines.

3.2.4 – Summary of 248 nm Resist System Results

We have seen how the structural morphology of a feature sidewall can change during a plasma etching process. After lithography, the SWR is isotropic in nature as the main roughening mechanisms of developing photoresists typically occur without any spatial orientation (except for the occurrence of standing waves, which typically appear parallel to the substrate plane). After lithography with a typical ESCAP 248 nm photoresist, we observed isotropic SWR that was approximately constant as a function of depth, with a value of 3-5 nm RMS.

However, ion bombardment and other processes that occur during etching can result in the loss of the original morphological information, incorporating an anisotropic component to the roughening of the sidewall and creating striations that propagate perpendicular to the substrate plane. We observed on organic ARC samples that striations formed during ARC open can act as physical templates for subsequent image transfer into an underlying oxide substrate. Additionally, the nature of the ARC material, and its interaction with the etching chemistry can determine the amount and structural nature of the SWR transfer process.

Table 3.2 shows a summary of the 248 system results, in conjunction with figures 3.49 and 3.50. Figure 3.49 and shows the depth – dependent SWR of all samples (organic ARC, thin and thick hardmask, and Si ARC) after ARC open, calculated from the AFM images, and plotted as a distance from the resist/ARC interface. From the plot, we observe that near the bottom of the feature (closest to the oxide substrate) all samples have approximately the same SWR magnitude (~2-3 nm RMS). The thick hardmask sample has a slightly elevated SWR at the resist/ARC interface due to the longer etch

Table 3.2 – Summary of 248 results.

Sample Type	Process	Chemistry	RMS Roughness	Striations	Notes
Organic ARC	Litho	N/A	3-5 nm	Isotropic	Roughness relatively constant
Organic ARC	ARC Open	N_2/H_2	2 nm	Narrow	Faceting and streaking
Organic ARC	45s Oxide Etch	FC	1 nm	Narrow	Streaks do not penetrate oxide interface
Organic ARC	90s Oxide Etch	FC	2 nm	Narrow	Oxide interface penetrated, roughening oxide sidewall
Thick HM	HM Open	FC	3 nm	Narrow	Long etch excessively roughens top of line
Thin HM	HM Open	FC	3 nm	Narrow	Top smoother due to shorter etch
Si ARC	ARC Open	FC	2 nm	Narrow	Looks similar to Organic ARC
Thick HM	90s Oxide Etch	FC	4-5 nm	Broad	Broad striations due to FC left on sidewall during HM open?
Thin HM	90s Oxide Etch	FC	3-5 nm	Broad	Broad striations due to FC left on sidewall during HM open?
Si ARC	90s Oxide Etch	FC	5 nm	Broad	Broad striations due to FC left on sidewall during ARC open?

time required to open the hardmask, but it levels out eventually. A visual examination of all four AFM images (figures 3.17, 3.30, 3.34, and 3.43) shows a very similar morphology, with striations of approximately the same width traversing down the sidewall. Therefore, since all samples used the same photoresist, have the same oxide etch chemistry, and look approximately the same after ARC open, we would expect that any differences noted after oxide etch be due either to the differences in ARC open plasma chemistry, or the ARC materials' differing interactions with the oxide etch chemistry.

Figure 3.50 shows the depth-dependent SWR of all samples after 90 s oxide etch (with the organic ARC sample after 45 s oxide etch shown as well), plotted as a distance from the ARC(HM)/oxide interface. An examination of the 90 s and 45 s organic ARC sample shows the increased mask roughening due to the longer etch time on the 90 s etched sample, and a corresponding rougher SWR on the oxide surface (2 vs. 1 nm RMS). We also saw how correlated striations traverse down to the ARC/oxide interface on the 90 s sample, yielding mousebites on the top of the oxide lines, yet not observed on the 45 s etched sample. The spatial frequency of the roughness after ARC open is comparable

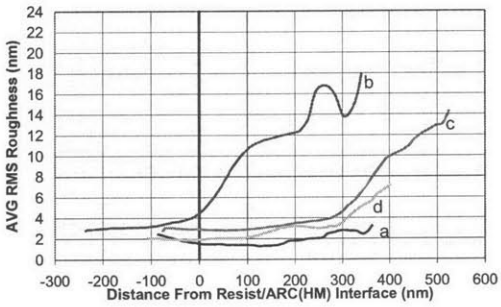

Figure 3.49 – Comparison of all samples after ARC/HM open, plotted as a distance from the resist/ARC interface. a) Organic ARC, b) "thick" Hardmask, c) "thin" Hardmask, d) Si ARC. Note that the SWR magnitude near the bottom of the feature is approximately the same for all sample types (2-3 nm RMS). However, the fluorocarbon nature of the ARC/HM open for the hardmask and Si ARC samples

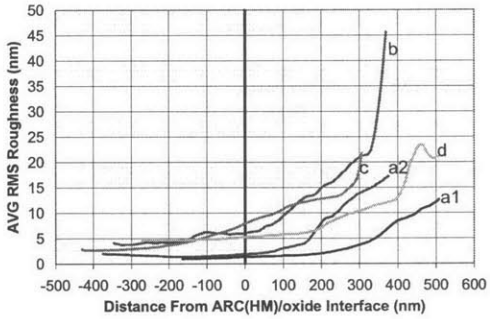

Figure 3.50 – Comparison of all samples after oxide etch, plotted as a distance from the ARC(HM)/oxide interface. a1) Organic ARC, 45s etch, a2) Organic ARC, 90s etch, b) "thick" Hardmask, c) "thin" Hardmask, d) Si ARC. The hardmask and Si ARC samples are approximately equivalent to each other, and rougher on the oxide sidewall than the organic ARC, probably due to either compositional differences between these films and the organic ARC, or to the depositing fluorocarbon ARC open chemistry.

to that seen after oxide etch, indicating that the structure of the roughness post – ARC open casts the morphology of the emerging oxide sidewall.

Both the hardmask and Si ARC samples are rougher after oxide etch than the organic ARC sample, with a SWR magnitude of ~4-5 nm RMS (compared with 2 nm RMS for the organic ARC). Additionally, an examination of the AFM images shows that the spatial structure of the post – etch sidewalls is different as well. The organic ARC oxide sidewall is characterized by a higher spatial frequency roughness, while on the hardmask and Si ARC the lower frequency roughness seen on the resist portion of the sidewall extends down all the way to the bottom of the oxide. This may be due either to

compositional differences between the organic ARC and the inorganic films, or to the heavily depositing fluorocarbon nature of the ARC open used on these two samples. It is possible that fluorocarbon polymer left on the sidewall after ARC/HM open, with a high selectivity to the oxide, casts the lower spatial frequency roughness that develops on the HM/Si ARC samples during oxide etch.

3.3. Roughness Transfer on 193 nm Resist Systems.

Lithography resolution is defined by:

$$R=\frac{k_1\lambda}{NA} \tag{3.8}$$

where R = resolution, k_1 = constant, λ = exposure wavelength, and NA = numerical aperture. We see that a decrease in the exposure wavelength and/or increased NA gives a corresponding decrease in the resolution of the lithographic process. Therefore, in order to achieve sub – 100 nm patterning the industry has undertaken a move to photoresists imaged with 193 nm radiation (ArF exposure) on high NA tools.

However, the move to 193 nm resists is not without its problems. First, most of these films have a higher etching rate in most chemistries than 248 nm resists (a good rule of thumb is to assume they will etch ~30% faster[16]). Even more important, 193 nm resists are typically coated much thinner than corresponding 248 nm resists due to both 1) depth of focus and 2) pattern collapse concerns. The depth of focus (DOF) is given by :

$$DOF=\frac{\lambda}{2NA^2} \tag{3.9}$$

which is contradictory for robust processing at high resolution. Therefore, as λ decreases and the NA increases, thinner resist must be used to account for the lower DOF. Pattern collapse occurs when capillary forces present in the developer solution pull on patterned line features. The capillary force is given by[17] :

$$\Delta P=\frac{\gamma\cos\theta}{d} \tag{3.10}$$

where ΔP = capillary force, γ = surface tension, θ = contact angle of rinse fluid with sidewall, and d = line spacing. If the aspect ratio of the lines is too large, the capillary forces will collapse the lines. The typical critical aspect ratio to avoid pattern collapse is approximately 3:1, meaning that to pattern a dense 100 nm line – space pattern, the 193

resist should be no thicker than ~300 nm. This combination of poorer etch resistance and thinner initial thickness of single layer 193 nm photoresists provides many integration challenges from an etch perspective.

Some of these issues can be addressed through the use of bilayer resists[18,19]. Bilayer patterning schemes involve coating the substrate with a thick, planarizing organic underlayer, followed by a thin imaging resist. The imaging resist usually contains silicon, either through a post-patterning silyation step (typically seen in "top surface imaging", or TSI[20]), or through the inclusion of silicon – containing moieties within the resist structure itself, to provide etch resistance to the organic underlayer. After patterning the Si containing etch resistant imaging layer, a selective plasma etch is used to transfer the pattern to the underlayer. Finally, the finished stack (remaining imaging resist and underlayer) is used to pattern the substrate. The advantages of bilayer patterning include true thin film imaging, and the ability to be patterned over existing topography. However, sidewall roughness is known to be a problem. Not only are bilayer and TSI resists typically rougher than standard single layer resists[21] , but observed sidewall roughness transfer can be an issue[22,23].

In order to investigate their roughness transfer characteristics, single layer 193 nm photoresists consisting of either a methyl adamantine acrylate–co–lactone acrylate resin (referred to herein as the "methacrylate" resist), or a cyclo–olefin–maleic anhydride based resin (referred to as the "cyclic olefin" resist) were used to print nominal 1:1 100 – 150 nm line/space features patterned in ~ 300 nm thick films. ArF exposures were made on a 0.75 NA ASML stepper with annular illumination using the DARPA mask described in Chapter 2. Similar to the 248 nm samples, an organic ARC appropriate for each wavelength was used when patterning the single–layer resists in order to suppress standing waves. Additionally, roughness transfer on a 193 bilayer resist system was examined. The imaging resist was a silane containing norbornene–maleic anhydride terpolymer[24], while the underlayer was based on a styrene–acrylate copolymer. As before, 8 inch thermally grown SiO_2 substrates were used for resist pattern transfer.

3.3.1. 193 nm Lithography Results

From sidewall AFM images, the calculated RMS roughness of the methacrylate and cyclic olefin resists was 3.3 nm and 2.9 nm, respectively. Both were smoother than

the 248 nm resist (3.9 nm RMS) as the ARC thickness was better optimized, eliminating the standing waves observed previously. The initial roughness of the bilayer imaging resist was rougher than the single layer resists, with a value of 4.4 nm RMS, probably due to the silicon content. Figure 3.51 shows the depth – dependent SWR of each 193 resist. The 248 organic resist is also shown for comparison. Note the reduced thickness of the 193 resists in comparison to the 248. In particular, observe the extremely thin bilayer imaging resist, a "true" thin film imaging technology at only ~140 nm thick.

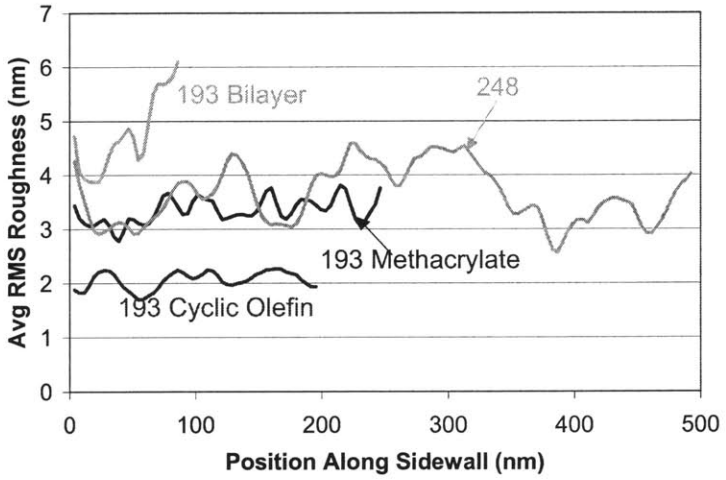

Figure 3.51 – Depth – dependent SWR of 193 nm resists, with the 248 resist included for comparison. Both the methacrylate and cyclic olefin resists are smoother than the 248 resist due to a better optimized ARC thickness that eliminated standing waves in the patterns, while the bilayer imaging resist is rougher. Note that the 248 resist is approximately twice the thickness of the 193 single layer resists, and about 5 times the bilayer imaging resist thickness.

3.3.2. 193 nm N_2/H_2 ARC Open

After development of the resists and etching of the ARC in N_2/H_2, sidewall surfaces on the single layer resists showed similar morphological changes comparable to the 248 nm resist processing, in that the isotropic nature of the developed resist became striated. The tops of the lines also became faceted in a similar fashion. The methacrylate system after N_2/H_2 ARC open is shown in figures 3.52 (SEM) and 3.53 (AFM). The cyclic olefin result was similar.

3.3.3. SO_2/O_2 Bilayer Underlayer Etch

To achieve transfer of the thin imaging layer patterns to the underlayer, extreme selectivity of the resist to the underlayer is required. The high silicon content of the

imaging layer makes this possible through the use of an SO_2/O_2 based transfer etch. The oxygen reacts with the Si in the imaging resist, converting it to SiO_2, in essence changing

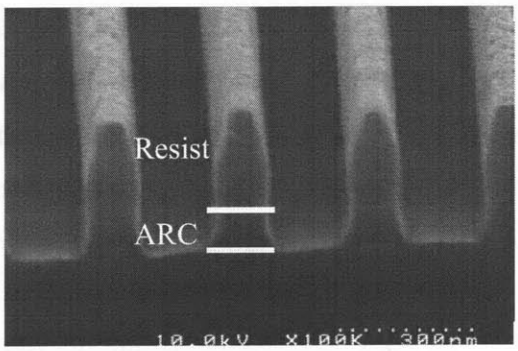

Figure 3.52 – Cross sectional SEM of 193 nm methacrylate resist after N_2/H_2 ARC open. Similar morphological changes as observed on the 248 system can be seen (faceting, etc).

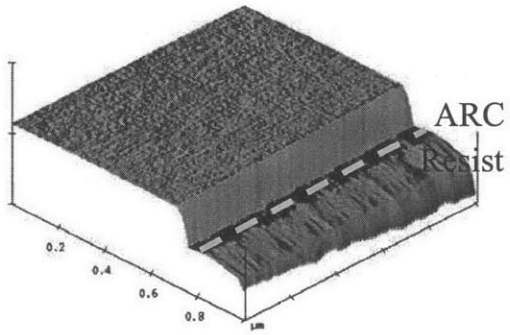

Figure 3.53 – Sidewall AFM of 193 nm methacrylate resist after N_2/H_2 ARC open. The process has striated the sidewall similar to the 248 nm sample.

the resist to an oxide – like hardmask. Additionally, profile control is obtained through the addition of SO_2, which acts as a passivation agent[25] through the formation of S, C-S and C-S-O species[26,27]. Figures 3.54 and 3.55 show the bilayer resist after lithography and underlayer transfer etch, respectively. Note the excellent profile control generated by the passivating underlayer etch (table 3.1, row 7), and a resist to underlayer selectivity exceeding 10:1. The remaining resist/underlayer thickness is over 450 nm, illustrating the capability of bilayer resists to pattern very deep substrate trenches.

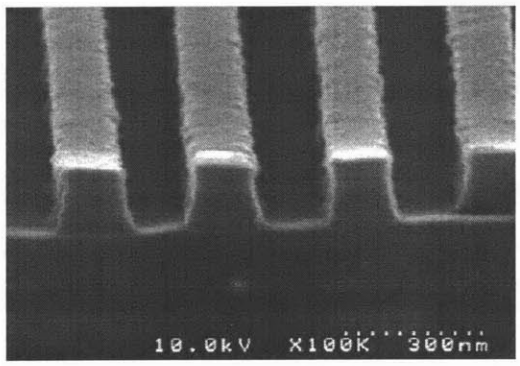

Figure 3.54 – Cross sectional SEM of 193 nm bilayer imaging resist lithography. The resist is only ~130 nm thick.

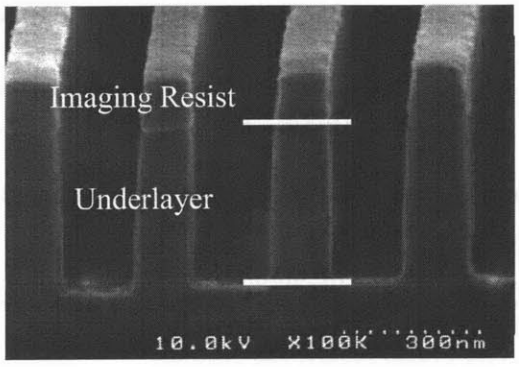

Figure 3.55 – Cross sectional SEM after underlayer transfer etch in SO_2/O_2. The oxygen has changed the Si in the imaging resist to SiO_2, forming a hardmask with excellent selectivity over the organic underlayer (>10:1). SO_2 sidewall passivation leads to very straight profiles.

The sidewall roughness of the imaging resist was shown in figure 3.51. The corresponding AFM image and depth – dependent SWR after the transfer etch are shown in figures 3.56 and 3.57. Immediately apparent on the sidewall are the presence of large agglomerations, or "bumps," in the AFM image that enhance the measured SWR (the "hump" observed in figure 3.57). These agglomerations are believed to be caused by reaction of the sulphurous passivation layer with atmospheric moisture[22], and only form if the wafer is taken out of the etcher. This makes an accurate determination of the post – transfer etch SWR difficult. However, wafers that undergo oxide etch immediately after the transfer etch (without removing them from the vacuum system) do not suffer from this problem, and the SWR measurement post-oxide etch therefore are not affected. Our best estimate of the SWR at the bottom of the feature after transfer etch ranges from 3 – 4.5 nm RMS, rougher than that observed on the single layer resists.

3.3.4. "Gentler" Oxide Etch Chemistry for 193 nm Resists

As mentioned previously, 193 nm resists typically have poorer etch resistance than 248 nm resists. On our samples, this fact of life was immediately borne out when the 248 nm oxide etch chemistry was used with the 193 nm methacrylate resist. Rather than etching cleanly, the resist patterns showed severe erosion and "twisting" (figure 3.58). Therefore, the oxide etch chemistry was made gentler by raising the pressure (from 60 mT to 100 mT) and lowering the ion bombardment (from 600 W to 300 W). The conditions are listed in table 3.1, row 6. This change allowed the resists to withstand the etching process, at the cost of reduced etch selectivity and oxide etch rate (figure 3.59).

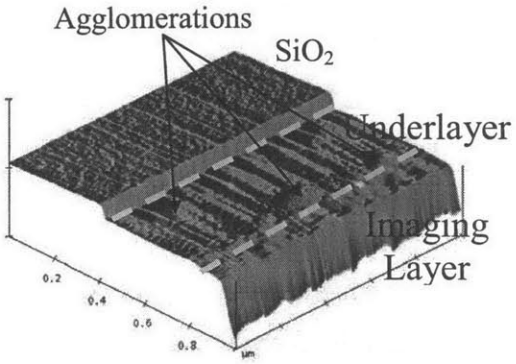

Figure 3.56 – Sidewall AFM image of 193 bilayer resist after underlayer transfer etch. Large agglomerations due to atmospheric moisture can be observed.

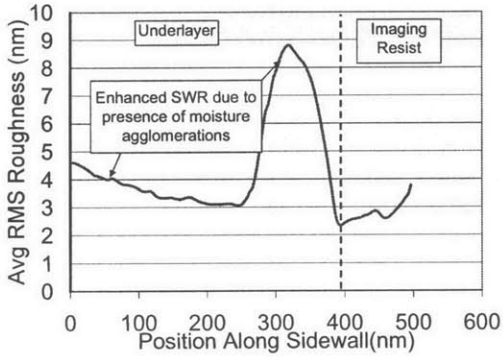

Figure 3.57 – Depth dependent SWR calculated from the AFM image. The SWR is enhanced due to the agglomerations, making an accurate roughness determination difficult.

3.3.5. 193 nm Oxide Etch Results

The required change in oxide etch chemistry, while initially viewed as unfortunate, actually allowed us a glimpse at the smoothing capabilities of the oxide etch itself. We will see in chapter 4 that using a more "chemical" type ARC open (Cl_2/O_2) can yield smoother post – oxide etch lines than "physical" N_2/H_2 or fluorocarbon ARC/HM etches, when paired with the highly physical 248 nm oxide etch previously described. However, when paired with the gentler 193 nm oxide etch chemistry, roughness transfer on the 193 nm resist systems was fairly independent of ARC open chemistry and etch time, suggesting that the gentler oxide etch itself imparted a smoothing characteristic to the sidewall. This can be seen by plotting the depth – dependent SWR after oxide etch of all the 193 nm resist systems, with the 248 result included for comparison (figure 3.60). The plots show the familiar shape (rough at the top, smoother with increasing depth) again supporting the idea that the anisotropic topography created on the upper layer during plasma etching helps to cast the morphology of the emerging sidewall. The SWR at the oxide/ARC interface ranges from ~ 1.5 – 2.5 nm RMS, regardless of resist type, ARC open chemistry, or oxide etch time, suggesting that the oxide etch itself may be

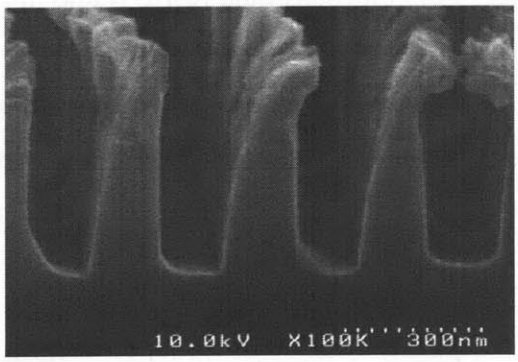

Figure 3.58 – 193 nm methacrylate resist after oxide etch for 45 s in the 248 nm etch chemistry. The lower etch resistance of the photoresist has created severe erosion and twisting.

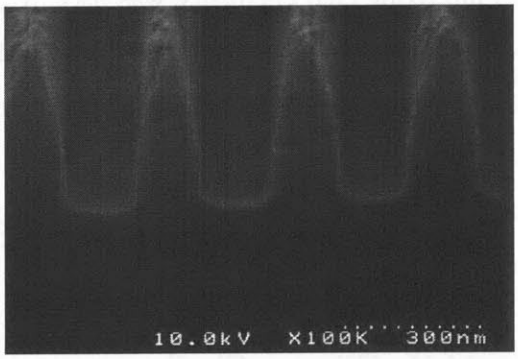

Figure 3.59 – The same resist after a 45 s oxide etch in the "gentler" 193 nm etch chemistry. The photoresist lines have withstood the etch, at the cost of a lower oxide etch rate.

imparting a smoothing characteristic. Since the extreme roughness does not penetrate to the oxide/ARC interface, the oxide sidewalls remain smooth, in each case comparable to the results found for the 248 nm resist / organic ARC system. These results demonstrate that it is indeed possible to maintain roughness transfer on 193 nm resist systems at a

level comparable to that found on typical 248 nm resists, with careful selection of processing conditions. It is, however, important to keep in mind that we are playing etch selectivity over roughness transfer (unfortunately, there is no free lunch!), and a balance must be struck to ensure that enough resist remains during the etch to completely pattern the substrate. The relevance of bilayer lithography to this goal is thus immediately apparent. More on this topic will be discussed in Chapter 5, which investigates the role of photoresist fluorine content on etch selectivity and roughness transfer.

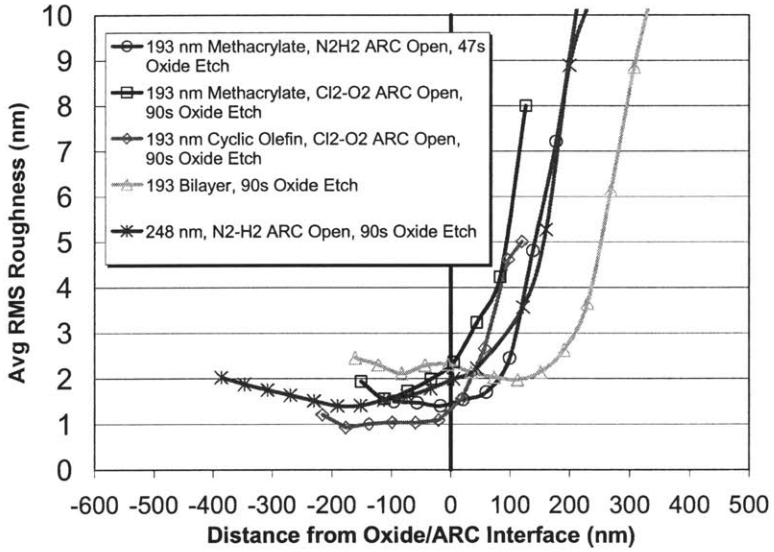

Figure 3.60 – Depth dependent SWR of 193 methacrylate, cyclic olefin, and bilayer resist systems (the 248 nm result is also shown for comparison). The roughness levels range from ~1.5 – 2.5 nm at the oxide/ARC interface for all samples, regardless of resist type, ARC open chemistry, or oxide etch time, suggesting that the "gentler" oxide etch chemistry used on the 193 nm samples has a smoothing characteristic. The roughness transfer for all the 193 samples is comparable to the 248 nm organic ARC sample, demonstrating that the sidewall roughness on 193 nm resist samples can be maintained within reasonable limits with careful selection of processing conditions.

3.4. Summary

In this chapter, an AFM technique was described that allows the determination of sidewall roughness as a function of depth on an etched feature. The evolution of SWR during processing (lithography, ARC/HM open, and oxide etch) was investigated for a variety of 248 nm and 193 nm resist systems with an assortment of organic and Si – containing ARCs, inorganic hardmasks, and bilayers. The initial lithography sidewall morphology was isotropic in nature with a 3-5 nm 1-σ RMS roughness, and relatively constant as a function of depth. After the ARC/hardmask etch, however, the sidewall

morphology takes on an anisotropic characteristic, with striations created by ion bombardment. During a subsequent oxide etch, these striations transfer into the oxide sidewall, the anisotropic topography created during the ARC/hardmask etch casting the morphology of the oxide layer beneath. The roughness typically takes on a depth – dependent characteristic (rougher at the top, smoother as the depth increases).

While all samples appeared relatively equivalent after ARC/HM open, the roughness transfer on 248 nm hardmask or Si ARC samples after oxide etch was greater than on organic ARC samples, at a lower spatial frequency. This was attributed to the fact that the Si ARC and HM samples underwent a depositing fluorocarbon etch to open the ARC/HM layer, potentially leaving polymer on the surface that casts the lower frequency roughness during a subsequent oxide etch. The organic ARC sample underwent a non – depositing N_2/H_2 ARC open, allowing relatively smooth roughness transfer at a higher spatial frequency. This point will be examined a bit closer in the next chapter, in which the effect of opening the hardmask in a non-polymerizing, "chemical" Cl_2/O_2 plasma is investigated.

On the 193 nm samples, a "gentler" oxide etch was required due to the excessive resist twisting observed under the 248 nm oxide etch condition. The SWR after oxide etch was comparable to the 248 nm organic ARC results, and was independent of resist type, ARC open chemistry, and oxide etch time. This suggests that the "gentle" oxide etch itself possessed smoothing characteristics, and demonstrated that 193 nm resist systems can be etched with a roughness comparable to 248 nm systems with careful selection of processing conditions. However, this must be balanced against a reduction in etch rate and selectivity, illustrating the relevance of bilayer resist technologies.

These results indicate that SWR transfer on the oxide substrates can be maintained within reasonable limits, as long as the increasing resist/ARC roughness does not extend to the oxide/ARC interface.

3.5. References

1 G. W. Reynolds, J. W. Taylor, and C. J. Brooks, Journal of Vacuum Science & Technology B **17**, 3420-3425 (1999).

[2] G. W. Reynolds and J. W. Taylor, Journal of Vacuum Science & Technology B **17,** 334-344 (1999).

[3] G. W. Reynolds and J. W. Taylor, Journal of Vacuum Science & Technology B **17,** 2723-2729 (1999).

[4] D. L. Goldfarb, A. P. Mahorowala, G. M. Gallatin, K. E. Petrillo, K. Temple, M. Angelopoulos, S. Rasgon, H. H. Sawin, S. D. Allen, M. C. Lawson, and R. W. Kwong, Journal of Vacuum Science & Technology B **22,** 647-653 (2004).

[5] J. S. Villarrubia, Journal of Research of the National Institute of Standards and Technology **102,** 425-454 (1997).

[6] S. Wolf and R. N. Tauber, *Silicon processing for the VLSI era* (Lattice Press, Sunset Beach, Calif., 1986).

[7] S. Rauf, P. J. Stout, and J. Cobb, Journal of Vacuum Science & Technology B **21,** 655-659 (2003).

[8] O. Kwon, Ph.D Thesis, Massachusetts Institute of Technology, 2004.

[9] A. P. Mahorowala, K. Babich, K. Petrillo, J. Simons, and M. Angelopolous, Proc. SPIE **4343,** 306-316 (2001).

[10] K. Babich, A. P. Mahorowala, D. Medeiros, D. Pfeiffer, K. Petrillo, M. Angelopolous, A. Grill, and V. Patel, Proc. SPIE **5039,** 152-165 (2003).

[11] M. Angelopolous, K. Babich, A. Grill, S. D. Halle, A. P. Mahorowala, and V. Patel, US Patent # 6,316,167 (Intenational Business Machines Corporation, United States, 2001).

[12] M. Angelopolous, K. Babich, A. Grill, S. D. Halle, A. P. Mahorowala, and V. Patel, US Patent # 6,514,667 (International Business Machines Corporation, United States, 2003).

[13] D. Pfeiffer, M. Angelopolous, K. Babich, P. Brock, W. S. Huang, A. P. Mahorowala, D. Medeiros, and R. Sooriyakumaran, US Patent # 6,730,454 (International Business Machines Corporation, United States, 2004).

[14] D. Pfeiffer, A. P. Mahorowala, K. Babich, D. Medeiros, K. Petrillo, and M. Angelopolous, Proc. SPIE **5039,** 136-143 (2003).

[15] C. J. Mogab and H. J. Levinstein, Journal of Vacuum Science & Technology **17,** 721-730 (1980).

[16] A. Mahorowala, IBM, Personal Communication.

[17] T. Tanaka, M. Morigami, and N. Atoda, Japanese Journal of Applied Physics Part 1 **32,** 6059-6064 (1993).

[18] Q. Lin, K. Petrillo, K. Babich, D. La Tulipe, and D. Medeiros, Proc. SPIE **3678,** 241-250 (1999).

[19] R. Kwong, P. R. Varanasi, M. C. Lawson, T. Hughes, G. Jordhamo, M. Khojasteh, A. Mahorowala, R. Sooriyakumaran, P. Brock, C. Larson, D. Fenzel-Alexander, H. Truong, and R. Allen, Proc. SPIE **4345,** 50-57 (2001).

[20] T. Sugihara, F. Van Roey, A. M. Goethals, K. Ronse, and L. Van den hove, Microelectronic Engineering **46,** 339-343 (1999).

[21] V. Rao, J. Hutchinson, S. Holl, J. Langston, C. Henderson, D. R. Wheeler, G. Cardinale, D. O'Connell, J. Goldsmith, J. Bohland, G. Taylor, and R. Sinta, Journal of Vacuum Science & Technology B **16,** 3722-3725 (1998).

[22] A. P. Mahorowala, K. Babich, Q. Lin, D. R. Medeiros, K. Petrillo, J. Simons, M. Angelopoulos, R. Sooriyakumaran, D. Hofer, G. W. Reynolds, and J. W. Taylor, Journal of Vacuum Science & Technology A **18,** 1411-1419 (2000).

[23] C. Y. Lee, S. Das, J. Yang, T. Weidman, D. Sugiarto, M. Nault, D. Mui, and Z. Osborne, Proc. SPIE **3333,** 625-633 (1998).

[24] R. Kwong, M. Khojasteh, P. Lawson, T. Hughes, P. R. Varanasi, and B. Brunsvold, Proc. SPIE **4690,** 403-409 (2002).

[25] M. Pons, O. Joubert, C. Martinet, J. Pelletier, J. P. Panabiere, and A. Weill, Japanese Journal of Applied Physics Part 1 **33,** 991-996 (1994).

[26] J. H. Ha, D. H. Yi, and J. J. Kim, Vacuum **51,** 519-524 (1998).

[27] C. Monget and O. Joubert, Journal of Vacuum Science & Technology B **17,** 1406-1412 (1999).

Chapter 4 – Improvement of Sidewall Roughness Transfer Through the Variation of ARC/Hardmask Open Plasma Chemistry

4.0. Abstract and Introduction

In the previous chapter, we observed how the interaction of different etch chemistries with existing sidewall profiles can result in the loss of the original morphological information and the creation of new spatial frequency domains that act as physical templates for subsequent image transfer processes. The isotropic sidewall roughness present on a lithographic feature can become anisotropic during a subsequent ARC/hardmask etch, leading to striations that propagate down the feature sidewall. We saw how excessive roughness transfer into the underlying substrate could originate from striation propagation from the resist layer, and varied depending on the ARC/hardmask material, ARC open chemistry, and/or the interaction between the two.

In this chapter, methods for modulating (and potentially improving) the transfer of post–etch sidewall roughness to the underlayer, by varying the nature of the ARC/hardmask open plasma chemistry, are discussed. It was found that, on the 248 nm organic ARC system from Chapter 3, opening the ARC in a Cl_2/O_2 plasma chemistry (or "chemical" ARC open) enabled an isotropic SWR to be maintained, at the cost of reduced selectivity to resist. A subsequent oxide etch resulted in smoother sidewalls than the samples with a "physical" N_2/H_2 ARC open, as no post ARC open striations were present to transfer into the oxide.

It was also possible to etch the hardmask material in a Cl_2/O_2 "chemical" HM open, again resulting in an isotropic sidewall. After a subsequent oxide etch, the sidewall roughness underwent a vast improvement over the hardmask samples opened with the "physical," highly depositing fluorocarbon chemistry described previously, with an RMS roughness decrease of ~60% at the top of the oxide line (from 8 nm to 3.3 nm RMS).

Finally, a similar methodology was applied to the post – etch roughness of polysilicon gate lines, patterned with a TEOS oxide hardmask. Varying the hardmask etch conditions highlighted a roughness improvement mechanism driven by polymerization during the hardmask open. Fluorocarbon polymer (formed on the gates during the hardmask etch) filled in imperfections in the gate line, allowing a smoother

transfer to the underlying polysilicon. However again the roughness improvement came at a cost. The increased polymerization grew the width of the line during the hardmask open, creating a "fatter" mask that resulted in wider gates than originally patterned.

These results indicate several methods by which modulating the ARC/HM open chemistry can improve roughness transfer, and illustrates some of the tradeoffs (reduced selectivity, CD shift, etc) involved.

4.1. Roughness Transfer via "Templating"

Recall from Chapter 3 that the state of the sidewall immediately prior to the substrate etch was of critical importance in determining the final substrate SWR. It seemed that faceting or striations formed during the ARC/HM open acted as "templates," transferring the roughness into the oxide. Neglecting for the moment any possibly effects due to ARC open deposition, we might represent the templating process conceptually as shown in figure 4.1. It schematically illustrates the process by which striations formed during a "physical" type ARC open begin at the top of the resist line, and propagate down the sidewall. By the time the ARC open is completed, the mask layer contains microfeatures that can maintain themselves during the subsequent oxide etch, replicating the streaked sidewall in the oxide substrate.

4.2. "Physical" vs. "Chemical" ARC/HM Open, 248 nm oxide samples

To investigate the role of striation formation during ARC/HM open on the final post – etch oxide SWR, two categories of ARC/HM open plasma chemistry were examined. The first is loosely defined as "physical," characterized by large ion bombardment. Both the N_2/H_2 organic ARC open and polymerizing fluorocarbon hardmask open described in the preceding chapter fall into this category, in both cases performed on a capacitively coupled LAM 4520XL etcher, with applied bottom power to the wafer imparting an appreciable bias across the plasma sheath and inducing ion bombardment. The physical nature of these etches offers good selectivity toward photoresist and enhances the etch rate of the ARC or hardmask material, but facets the resist corners and striates the sidewall.

The second category of ARC/HM open we have classified as "chemical." These etches were performed in a Cl_2/O_2 etching chemistry on a high density inductively cou –

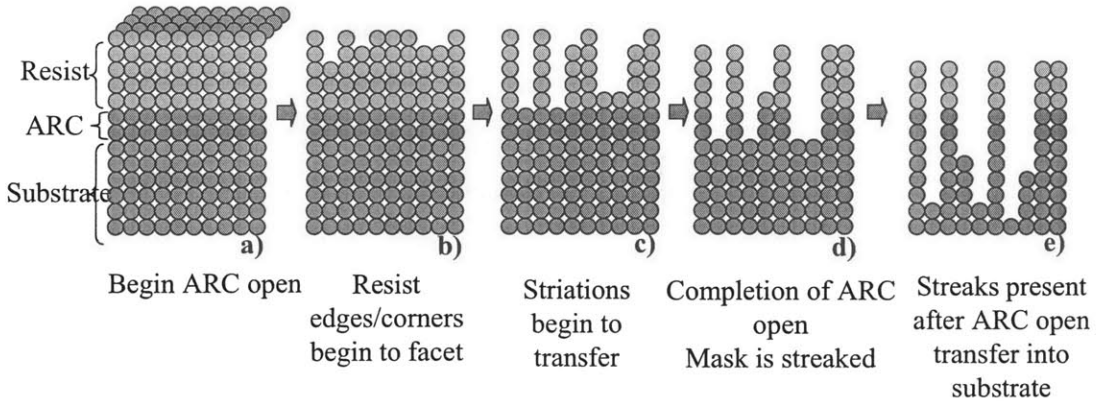

Figure 4.1 – Concept of ARC "templating." At the beginning of the ARC open, the sidewall is smooth and isotropic (a). However, a physical type etching process involving ion bombardment can create resist faceting at the top of the line (b). These facets can develop into full striations that propagate the length of the sidewall (c,d). Finally, the striations themselves act as templates that transfer the anisotropic microstructure into the underlying substrate during a subsequent oxide etch (e).

pled LAM 9400 etcher with very little applied bias, allowing etching of the features without imparting an anisotropic character to the sidewall structure. There is, unfortunately, a trade–off (no free lunch!) in that etch selectivity between the ARC or hardmask and photoresist is poor (~1:1) in the "chemical" ARC/HM open. Additionally, since the Cl_2/O_2 plasma tends to etch more isotropically, one must be wary of CD narrowing. This occurs because photoresist lines can etch laterally as well as vertically in the Cl_2/O_2, yielding final structures that are narrower than those originally patterned. The trade-off between smoother sidewalls (desirable) and CD variation (undesirable) must be carefully considered. It should be noted that the Cl_2/O_2 etching conditions varied slightly between the organic ARC and hardmask ; all etching conditions are detailed in table 4.1.

4.3. Organic ARC

Similar to the previous chapter, 8 inch Si wafers with ~10,000 Å thermally grown SiO_2 were coated with ~90 nm organic ARC. The samples were then spun coated with ~600 nm thick layer of the previously used 248 nm ESCAP chemically amplified photoresist, and patterned with a dense (1:1 pitch) 150 nm line/space array using the ARPAN mask described in Chapter 2. The samples were exposed using a KrF 0.63 NA ASML stepper with annular illumination. Exposures were performed at the IBM TJ Watson Research Center in Yorktown Heights, NY. Exposure doses ranged from 22 – 24 mJ/cm^2.

Table 4.1- Etch conditions for organic ARC and hardmask samples.

Etch	Process	Pressure (mT)	Top Power (W)	Bottom Power (W)	Etch Time (s)	Gas Flow rates (sccm)	Etcher
1	"Physical" ARC Open	40	500	500	15	200 N_2, 200 H_2	LAM 4520 XL
2	"Chemical" ARC Open	5	350	55	40	45 Cl_2, 15 O_2	LAM 9400
3	"Physical" HM Open	30	1000	2000	15	30 CHF_3, 150 N_2, 100 Ar, 5 O_2	LAM 4520 XL
4	"Chemical" HM Open	3	400	50	50	60 Cl_2, 3 O_2	LA 9400
5	Oxide Etch	60	600	600	90	60 CF_4, 20 CHF_3, 450 Ar	LAM 4520 XL

Following patterning, the organic ARC was opened in either the same N_2/H_2 "physical" etch (table 4-1, row 1), or a Cl_2/O_2 "chemical" etch (table 4.1, row 2). The SWR on each sample was measured as described previously via AFM, and the sidewall structural morphology was compared. Finally, all samples received the same highly physical 90 s oxide etch (table 4.1, row 5). Differences in the post – etch SWR were thus attributable to the differences in ARC open chemistry used.

4.3.1. Sidewall Morphology Differences due to "Physical" vs. "Chemical" ARC Open

Figures 4.2 and 4.3 show cross sectional SEM images of the organic ARC line patterns after both "physical" and "chemical" ARC open, respectively (the "physical" sample is the same one described in chapter 3). Again, note the faceting due to ion bombardment at the top of the "physical" sample. Also note the isotropic etching of the ARC in the "chemical" ARC open, the rounded line tops, and the slightly higher amount of resist loss.

Figure 4.4 shows an AFM image of the organic ARC sample sidewall after "physical" ARC open, and is the same sample as described in chapter 3. To reiterate, the large amount of ion bombardment present during this etch process has faceted the top of

the resist, and striated the sidewall. We have already seen how these striations can "template" themselves, casting the morphology of the oxide sidewall during a subsequent

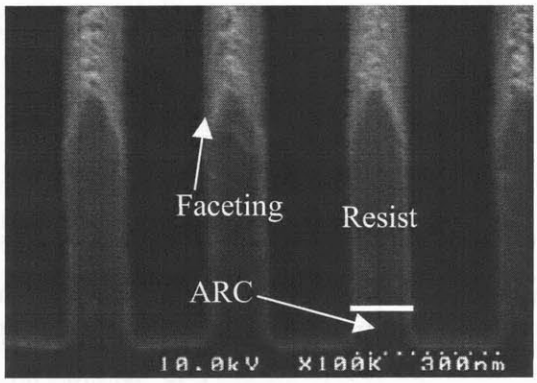

Figure 4.2 – Cross sectional SEM image of the organic ARC sample after a "physical" ARC open. Note the faceting at the top of the feature due to ion bombardment.

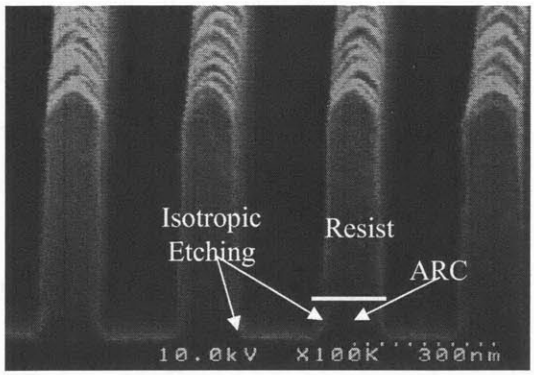

Figure 4.3 – Cross sectional SEM image of the organic ARC sample after a "chemical" ARC open. Isotropic etching can be observed in the ARC layer (lateral rounding), and slightly more resist has been lost than in the "physical" case.

oxide etch. To investigate this phenomenon further, it was desired to open the ARC in a chemistry that would not leave striations, and was accomplished with the Cl_2/O_2 "chemical" ARC open. Figure 4.5 shows the corresponding AFM sidewall image of the "chemical" organic ARC sample.

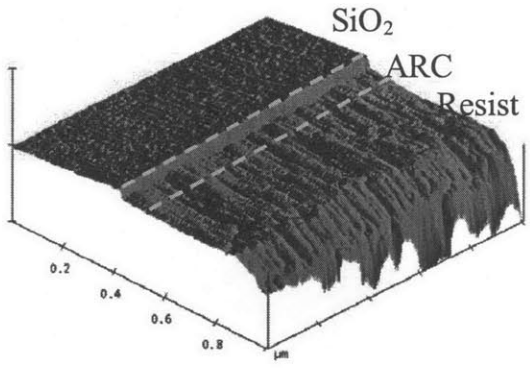

Figure 4.4 – Sidewall AFM image of the organic ARC sample after "physical" ARC open. Ion bombardment has faceted the top of the resist, and striated the sidewall.

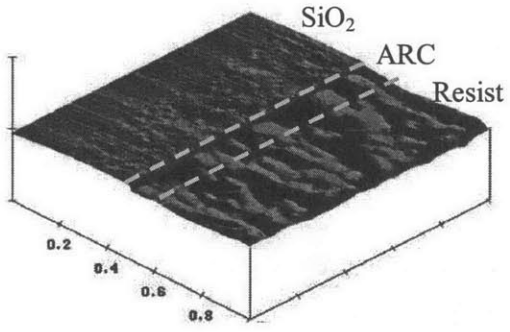

Figure 4.5 – Sidewall AFM image of the organic ARC sample after "chemical" ARC open. No striations are observable, instead, an isotropic morphology is obtained.

The difference in sidewall morphology between the "physical" and "chemical" samples is rather stunning. No striations are observable – instead, the surface is isotropic, similar to

the photoresist sidewall observed in the previous chapter. The surface itself has been smoothed by the etch. Recall that the resist surface had an RMS roughness of ~4 nm. In contrast, the sidewall after "chemical" ARC open has a roughness of ~2.5 nm. The high points on the sidewall have been smoothed by the isotropic nature of the Cl_2/O_2 plasma chemistry, in a manner similar to that described by Rauf[1].

The advantages of beginning the underlying oxide etch with a smooth sidewall are apparent. According to our very simple, conceptual picture of the templating process, striations present on the sidewall immediately prior to etching the substrate will maintain themselves, duplicating the anisotropic morphology. However, if no striations are present, it might be possible to open the oxide in a smoother fashion, as striations will have to propagate from the top of the resist line rather than from the ARC/oxide interface.

4.3.2. "Physical" vs. "Chemical" SWR Comparison After Oxide Etch, Organic ARC

To test this hypothesis, organic ARC samples were subjected to either a "physical" or "chemical" ARC open as described above, and then underwent a 90 s oxide etch. The oxide etch conditions were the same as those described in Chapter 3, and are detailed again in table 4-1, row 5.

Figures 4.6 and 4.7 show the resulting sidewall AFM images of both samples. We can observe immediately that our hypothesis is correct. The post – etch "physical" sample (the same one from Chapter 3) shows the familiar striations propagating down the whole of the sidewall. In contrast, the oxide sidewall surface on the "chemical" ARC open sam–

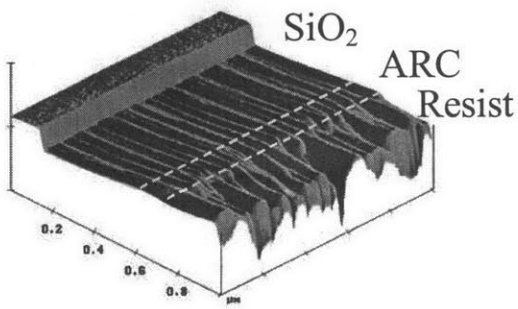

Figure 4.6 – Sidewall AFM image of "physical" ARC open sample after 90 s oxide etch. The striations present after ARC open have templated, transferring the anisotropic morphology into the oxide sidewall.

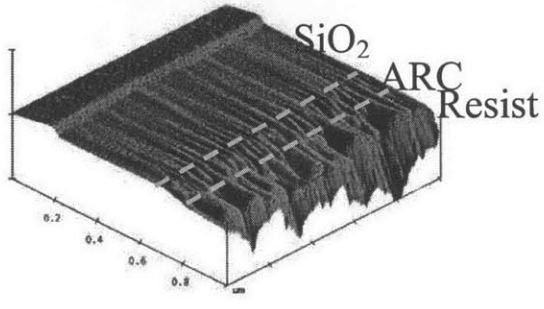

Figure 4.7 – Sidewall AFM image of "chemical" ARC open sample after 90 s oxide etch. The oxide sidewall is visually much smoother on the bulk of the oxide sidewall as no striations were left after ARC open.

ple is visually much smoother. Striations present on the bulk of the oxide sidewall are relatively shallow. It can be inferred from these results that, indeed, the state of the resist/ARC sidewall after ARC open does greatly affect the final post – etch SWR of the substrate. Carefully tuning the ARC open chemistry to a more "chemical" type etch offers one way to improve SWR transfer, as long as the lower etch selectivity and CD bias inherent with these chemistries can be tolerated.

Further evidence of the lower SWR transfer obtained with a "chemical" ARC open can be obtained by stripping the remaining photoresist and ARC from the post – etch samples, and observing the lines top – down via SEM. Recall that, on the "physical" ARC open sample, "mousebites" were observed at the top of the oxide as deep striations penetrated the ARC/oxide interface during the etch. The image is repeated in figure 4.8. However, fewer mousebites are observable on the "chemical" ARC open sample (figure 4.9), indicating that, as believed, striation transfer through the ARC/oxide interface is lessened through the use of a smoother ARC open chemistry.

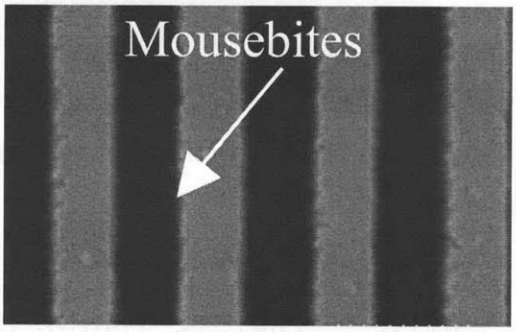

Figure 4.8 – Top down SEM of "physical" ARC open sample after oxide etch, with remaining resist/ARC stripped. "Mousebites" are observable on the line edges, indicating striation penetration through the ARC/oxide interface.

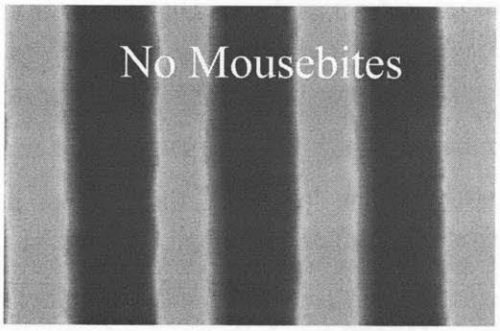

Figure 4.9 – Top down SEM of "chemical" ARC open sample after oxide etch, with remaining resist/ARC stripped. No mousebites are visible, demonstrating that smoother oxide lines can be obtained through the use of a smoother ARC open chemistry.

4.4. Hardmask

Since the results seemed very successful on the organic ARC samples, we investigated using a similar approach to improve SWR transfer on hardmask samples as well. Recall that the hardmask material was opened in a highly physical depositing fluorocarbon chemistry. It was also possible to open it in a "chemical" Cl_2/O_2 chemistry

similar to that used on the organic ARC. The etching conditions were slightly different (lower pressure, more Cl_2, less O_2) and are detailed in Table 4-1, row 4.

4.4.1. "Chemical" Hardmask Open

After lithography, a "thick" hardmask sample was etched in the Cl_2/O_2 chemistry described above (for 95 s) to elucidate the resulting sidewall roughness morphology. A "thick" sample was used at this stage to ensure that some of the hardmask surface would be visible in the AFM; on a corresponding "thin" hardmask sample the entire hardmask layer was shadowed by the AFM tip and was not visible. The cross sectional SEM and the sidewall AFM image of the "thick" hardmask sample after the "chemical" hardmask open are shown in figures 4.10 and 4.11, respectively. Note that the hardmask material has only been partially etched through (the 95 s etch time was not sufficient to clear the hardmask layer), and that much of the hardmask is shadowed at the bottom. Nevertheless, the structure of the sidewall on both the resist and hardmask is visible.

A comparison of figure 4.11 with figure 3.30 shows a similar trend as that observed on the organic ARC. The "chemical" hardmask open enabled the hardmask material to be etched while maintaining a smooth, isotropic surface, devoid of etch striations. It was hoped that, similar to the organic ARC, this smoother sidewall immediately prior to oxide etch would enable a smoother oxide sidewall, with less SWR transfer than the "physical" fluorocarbon hardmask open chemistry.

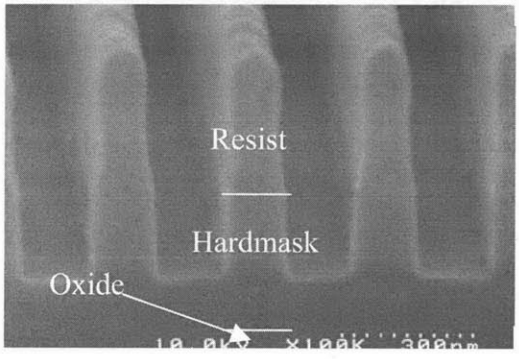

Figure 4.10 – Cross sectional SEM of "thick" hardmask sample after "chemical" hardmask open. The hardmask has only been partially etched.

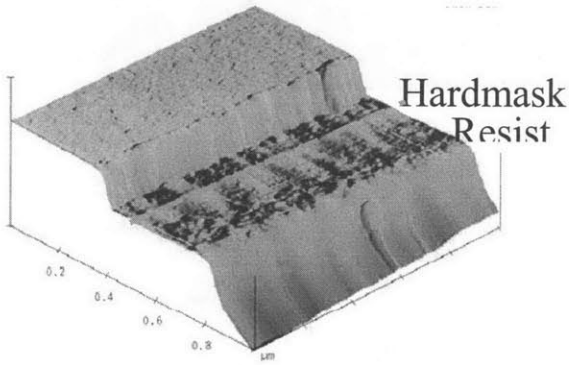

Figure 4.11 – Sidewall AFM image of the "thick" hardmask sample after "chemical" hardmask open. Even though the majority of the hardmask surface is shadowed at the bottom, the isotropic sidewall morphology can be observed. The surface is free of striations, and is smooth.

4.4.2. "Physical" vs. "Chemical" SWR Comparison After Oxide Etch, Hardmask

A 150 s "chemical" hardmask open was required to completely clear the hardmask layer on the "thick" hardmask samples. Because a Cl_2/O_2 etch of this length left only ~200 nm of resist, the oxide etch comparison was performed using "thin" hardmask samples that required only a 50 s "chemical" hardmask open. An AFM image of the "thin" hardmask sample after "chemical" hardmask open is, unfortunately, unavailable. However, the sidewall morphology is essentially the same as that found on the "thick" hardmask sample described above.

Figures 4.12 and 4.13 show the post-oxide-etch sidewall AFM images of "thin" hardmask samples with "physical" fluorocarbon and "chemical" Cl_2/O_2 hardmask opens, respectively. The "physical" image is the same one as in chapter 3. Recall, this surface was characterized by broad, deep striations that propagated from the top of the resist, through the hardmask, and traversed all the way down to the bottom of the oxide. In

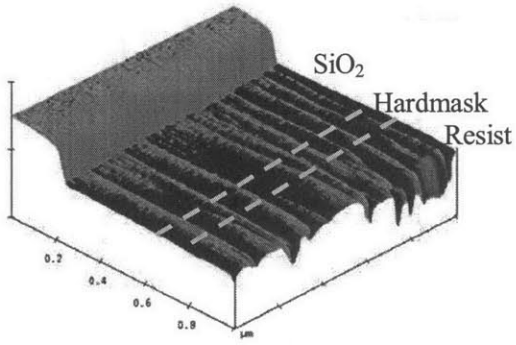

Figure 4.12 – Sidewall AFM image of "thin" hardmask sample with "physical" ARC open after oxide etch. The surface is characterized by broad, deep striations that traverse the length of the sidewall.

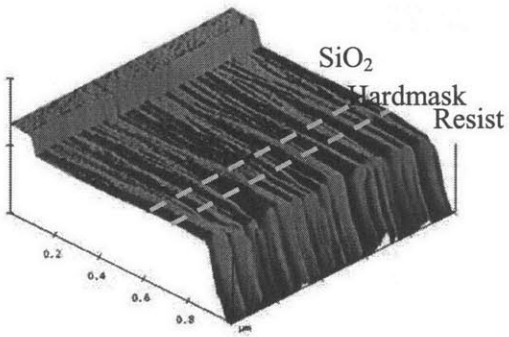

Figure 4.13 – Sidewall AFM image of "thin" hardmask sample with "chemical" hardmask open after oxide etch. In comparison, the sidewall is much smoother. The broad striations present on the "physical" hardmask open sample are not seen. The surface is flat and smooth, with only shallow striations.

contrast, the "chemical" hardmask open sample, after oxide etch, is significantly smoother. The surface is flat, with shallow striations on the resist that mostly die out by the time the oxide is reached. The extremely broad surface striations observed on the previous sample are not seen even on the slightly striated resist surface, where the streaks that are present are rather narrow. It is this result that we believe indicates the role of fluorocarbon deposition during the ARC open as the source of the broad striations. Since

there is no deposition during the "chemical" hardmask open process, the raw nature of the sidewall surface is preserved.

The immense degree of SWR improvement observed on the hardmask samples by using a "chemical" etch to open the hardmask material can be quantified by plotting the depth – dependent SWR of both samples. Figure 4.14 shows the graph, plotted as a distance from the hardmask / oxide interface. The "physical" hardmask open sample had an RMS roughness of ~ 8 nm at the interface. In contrast, however, roughness on the sidewall of the "chemical" hardmask open sample at the same location was improved by almost 60%, with a value of ~3.3 nm RMS.

Results of these experiments are summarized in table 4.2.

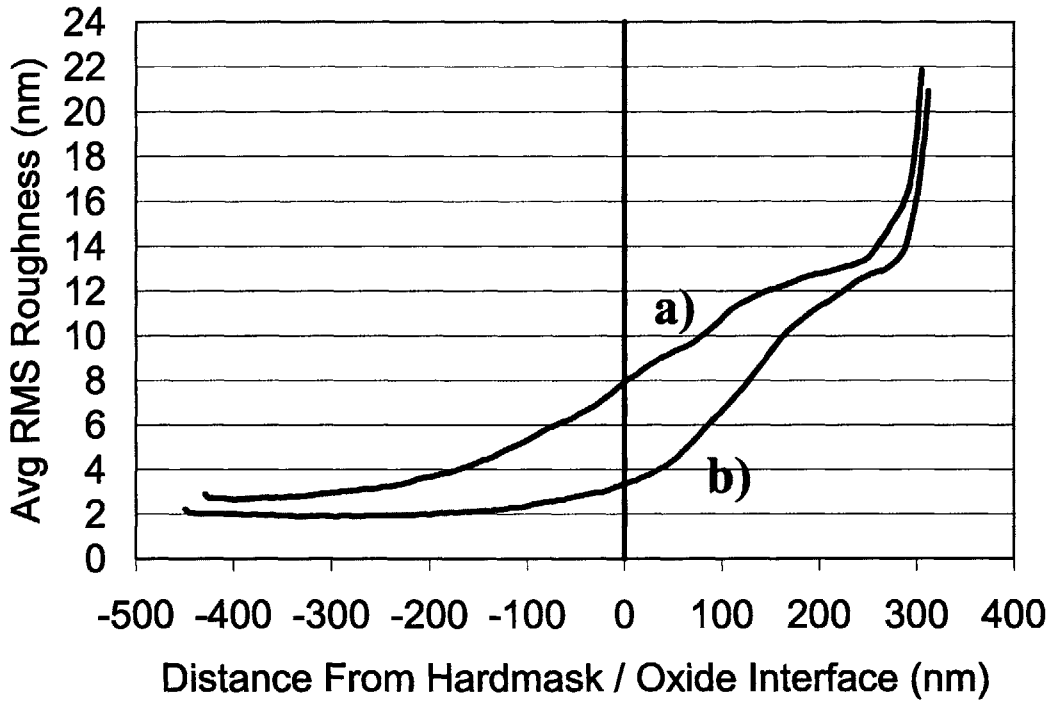

Figure 4.14 – Depth dependent SWR after oxide etch for "physical" hardmask open samples (a) and "chemical" hardmask open samples (b), both plotted vs the distance from the hardmask/oxide interface. Note that using a smoother hardmask open has significantly improved the SWR on the entire oxide sidewall, and has reduced the roughness at the interface by almost 60% (from 8 nm to 3.3 nm RMS).

Table 4.2 – Summary of ARC Open Effect

Sample Type	ARC Open Chemistry	Sidewall After ARC Open	Sidewall after 90s Oxide Etch	Comments
Organic ARC	Physical N_2/H_2	Striated	Striated	Striations left after ARC open transfer down into oxide
Organic ARC	Chemical Cl_2/O_2	Isotropic	Slightly Striated, Smoother	No striations after ARC open, oxide sidewall smoother
Hard Mask	Physical Fluorocarbon	Striated	Broad Striation	Broad striations may be due to FC deposition during ARC open
Hard Mask	Chemical Cl_2/O_2	Isotropic	Smoother, Narrow Striation	Non – depositing ARC open yields smoother sidewall without broad striations

4.5. Roughness Modulation via Hardmask Etch Variation for Polysilicon Gate Etch Processing

Similar to the back – end processing scheme described in Chapter 3 and above, the implications of varying etch processing parameters on roughness transfer during a front – end polysilicon gate etch process was investigated.

Previous researchers have investigated roughening of polysilicon gates via simulation, showing that gate LER affects both the transistor off current I_{off} and V_{tsat}. Additionally, the variance of both V_{tlin} and I_{on} scale with the gate line edge roughness[2]. The effects of processing on the gate LER profile have been previously studied via both experiments and simulation for resist trim[3], mask open selectivity and gate etch[4], and through simulation to identify the effect of gate LER on the device drive current and leakage current[5,6]. However, a detailed study of the effects of the hardmask open chemistry has not been performed.

4.5.1. Experimental

The gates stack consisted of a 220 nm thick methyl adamantine-co-lactone acrylate-based 193 nm resist, 90 nm organic ARC, 50 nm oxide hardmask, and 150 nm undoped polysilicon. The organic ARC was etched and the resist was trimmed simultaneously in a CF_4-O_2 plasma. The hardmask were then etched in a CHF_3-CF_4-based plasma. Finally, the polysilicon was etched in an HBr/O_2 plasma. The resist was patterned with a production mask, with nominal 80 nm gate features. The wafers were run in a production environment at IBM's Advanced Semiconductor Technology Center in East Fishkill, NY. Since the patterning, tooling, and etch processing was production level, further specifics cannot be released. Figure 4.15 shows the processing scheme to form the polysilicon gates.

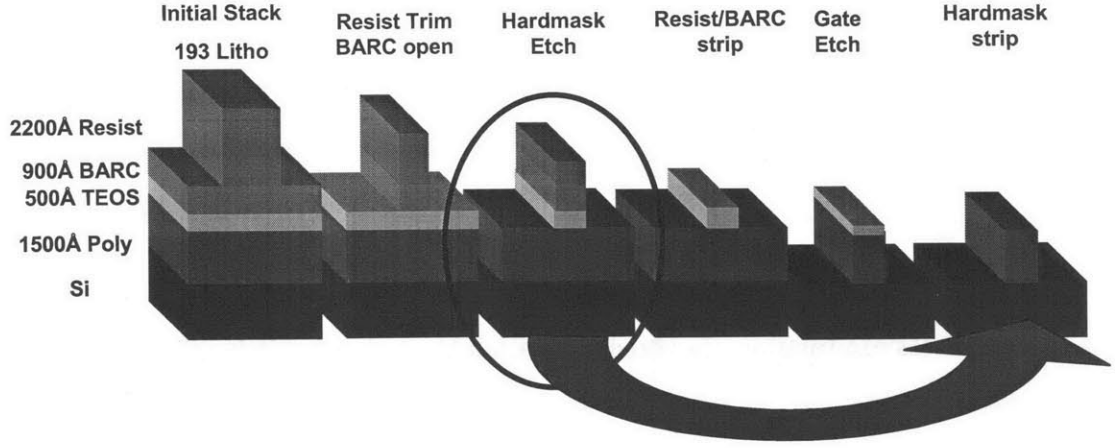

Figure 4.15 – Processing scheme to form polysilicon gate features. A simultaneous ARC open / resist trim in CF_4/O_2 was followed by a CHF_3/CF_4 oxide hardmask open. After stripping the remaining resist and ARC, the etched hardmask was used to pattern the polysilicon gates in an HBr/O_2 chemistry. The hardmask open chemistry was varied, and the effect on the LER of the final etched polysilicon gates was observed.

Recalling our contention that it is the state of the sidewall immediately prior to the final substrate etch that is critical in modulating the final SWR of the etched feature, we systematically varied the hardmask open plasma chemistry, and observed any resulting changes in the roughness of the final resulting polysilicon gate lines.

A full 2^3 two – level design of experiments (DOE) was performed[7], varying the hardmask open etch conditions. The factors varied were the pressure, bottom power, and CHF_3/CF_4 gas ratio, yielding eight wafer splits. A ninth split was run at the midpoint condition, and represented the baseline process currently used in production. Table 4.2

lists the levels and etching conditions for each run. Each wafer underwent the standard ARC open / resist trim, then was processed with its assigned hardmask open chemistry. Finally, all received the same, standard gate etch. Thus, any differences in the line profiles are directly attributable to the hardmask etch chemistry modulation.

Recall from section 3.1.1 that the sidewall AFM technique requires dense lines and spaces to ensure that the cleave is close enough to a line to allow analysis. Since the gates patterned and etched in this experiment were isolated lines, using AFM to determine the gate roughness was not possible. Therefore, we used edge extraction analysis of top-down SEM images acquired via a VERASEM. While not as visually appealing and lacking in depth-dependent information, this method had the advantage of rapid, multiple data collection from many points on the wafer simultaneously, and allowing us to apply statistics to the results. 23 – 27 lines were analyzed on each wafer as follows : each gate line edge was extracted from the image, and the linewidth was measured at several hundred locations on the gate, yielding raw line width data. The VERASEM algorithm then distinguished between high frequency roughness and low frequency roughness by passing the line width data through a 15 point moving average window (which acts as a low – pass filter), yielding both a smoothed line width profile and a profile of the residuals. The average of the residuals was defined as the "high frequency line width roughness," or HFLWR, and was the roughness statistic monitored for each gate line measured on each wafer. The average of the line widths measured for each line was also tracked as the line critical dimension, or CD. The effect of varying the hardmask open chemistry on both the HFLWR and the CD was monitored for the experiment. It should be noted that the roughness data was calculated for the line width rather than the line edge. For uncorrelated edges (meaning the roughness on one side of the line has no spatial relationship to the roughness on the other side) the numbers calculated by performing the analysis on the line width or the line edge should be equivalent within a factor of $\sqrt{2}$ [8].

4.5.2. AFM Measurements for Pre-Gate Etch Samples, Baseline Process

Since the production samples did not allow AFM results to be obtained, parallel samples were prepared in a dense line/space pattern. The same gate stack shown in figure

4.15 was patterned in 110 nm dense lines using the DARPA mask, and etched similarly to the isolated gate samples. The dense samples were stopped at intermediate stages in the processing to allow AFM images to be taken at each etch step (after litho, ARC open/trim, hardmask open, and gate etch). Cross sectional SEMS were examined to determine if the dense patterns etched similarly to the isolated gates, and they did up through the hardmask etch. The gate etch, unfortunately, created severe pitting on the dense samples, preventing AFM imaging. However, sidewall AFM images were obtained for 110 nm dense line/space samples after lithography, ARC open/trim, and hardmask open (with the baseline process outlined in table 4.3, row 9). They are shown in figures 4.16 – 4.18, below. Figure 4.19 shows the corresponding cross sectional SEMS.

Table 4.3 – 2^3 two – level factorial DOE for hardmask open etch on polysilicon gate samples

Wafer	Bottom Power Level	Pressure Level	CHF_3/CF_4 Ratio Level	Bottom Power (W)	Pressure (mtorr)	CHF_3/CF_4 Ratio (sccm/sccm)
1	-	-	-	60	20	15/25
2	+	-	-	140	20	15/25
3	-	+	-	60	60	15/25
4	+	+	-	140	60	15/25
5	-	-	+	60	20	25/15
6	+	-	+	140	20	25/15
7	-	+	+	60	60	25/15
8	+	+	+	140	60	25/15
9 (baseline)	0	0	0	100	40	20/20

The initial lithography, similar to before, was isotropic in nature. The sidewall had an RMS roughness of ~3.9 nm. The elevated value is again due to a slightly non – optimized ARC thickness, which produced a standing wave in the resist sidewall visible in figure 4.19a. The CF_4/O_2 ARC open / trim striated the sidewall, but the non-polymerizing, slightly "chemical" nature of the etch yielded a significant smoothing as compared to the initial resist (with a reduction in RMS roughness from 3.9 nm to 1.8

nm). The baseline TEOS hardmask open left the sidewall slightly striated, with a further small reduction in roughness to 1.5 nm RMS.

4.5.3. Polysilicon Gate Results

After etching each wafer, top down SEMs of gate lines at various locations were imaged, and both the HFLWR and CD were calculated for each line as described above. Table 4.4 shows the results for each experimental condition, and lists the experimental condition, number of gates, average HFLWR and CD, and standard deviations for both

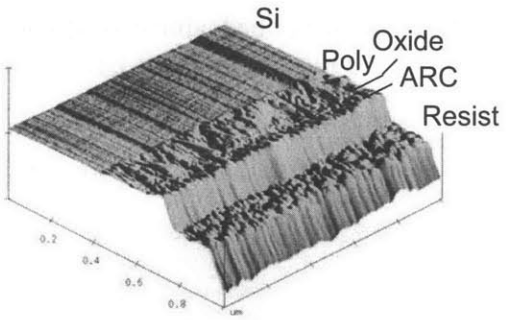

Figure 4.16 – Sidewall AFM image of gate stack, post litho. The sidewall is isotropic, with an RMS roughness of ~3.9 nm.

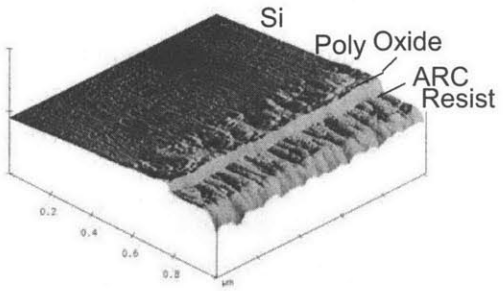

Figure 4.17 – Sidewall AFM image of gate stack, post ARC open / resist trim. The process has striated the sidewall, but reduced the RMS roughness to ~1.8 nm.

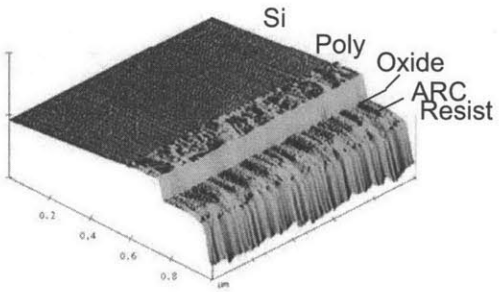

Figure 4.18 – Sidewall AFM image of gate stack, post hardmask open (baseline process). The striations have maintained themselves, but the sidewall is again slightly smoother, with an RMS roughness of ~1.5 nm.

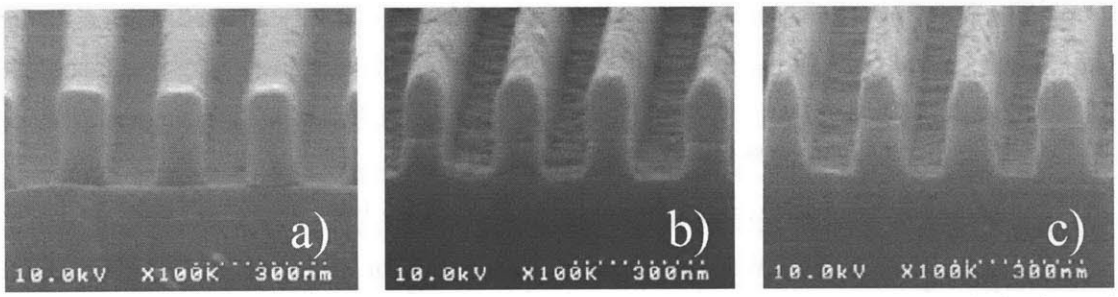

Figure 4.19 – Cross sectional SEMs of dense gate stack after lithography (a), ARC open / trim (b), and hardmask open (c). Note the slight standing wave present in (a) due to a non – optimized ARC thickness.

quantities. Figure 4.20 shows representative SEMs of gate lines (from wafer 9 : baseline, wafer 3 : -+-, and wafer 6 : +-+) that were analyzed as described above, and show differences in roughness and line width.

Table 4.4 - Results from Polysilicon Gate Experiment

Wafer	Condition (Pressure, Bottom Power, CHF_3/CF_4)	Number of Gates analyzed per wafer	Avg HFLWR	StDev HFLWR	Avg CD	StDev CD
1	---	25	5.8	0.52	88.8	2.5
2	--+	27	6.4	0.58	80.4	2.2
3	-+-	23	10.7	2.35	80.8	3.6
4	-++	26	5.9	0.40	82.0	2.4
5	+--	25	6.3	0.55	90.2	2.0
6	+-+	26	5.6	0.44	100.2	1.8
7	++-	27	5.9	0.41	87.6	2.5
8	+++	27	5.6	0.49	96.4	2.9
9	000 (baseline)	27	5.8	0.41	81.6	3.0

A paired t-test was performed to compare the difference of the means between each experimental run (wafers 1-8) and the baseline (wafer 9) against the estimated standard error of each difference in means. For each comparison, the t statistic is given by:

$$t = \frac{(\bar{y}_i - \bar{y}_{baseline}) - \eta_0}{\sqrt{s^2\left(1/N_i + 1/N_{baseline}\right)}} = \frac{(\bar{y}_i - \bar{y}_{baseline})}{estimated\ std\ error} \tag{4.1}$$

where t = t statistic, $\bar{y}_i$ = mean of wafer i, $\bar{y}_{baseline}$ = mean of wafer 9, N_i = # of gate lines

for wafer i, $N_{baseline}$ = # of lines for wafer 9 (in this case, 27 lines), and s^2 = pooled variance of wafers i and 9, as calculated by the following:

$$s^2 = \frac{\sum_{i=1}^{8} \nu_i s_i^2}{\sum_{i=1}^{8} \nu_i} \tag{4.2}$$

where i = wafer number, s_i = standard deviation calculated from wafer i, and ν_i = degrees of freedom of wafer i and is equal to N_i-1. η_0 is the null hypothesis, in this case, that $\overline{y}_i - \overline{y}_{baseline} = 0$. The quantity in the denominator of equation 4.1 is the estimated standard error of the difference in the means. Once the t statistic is calculated for each pairing, the significance level is obtained by calculating the probability given by a one – tailed t distribution with ($N_i + N_{baseline} - 2$) degrees of freedom.

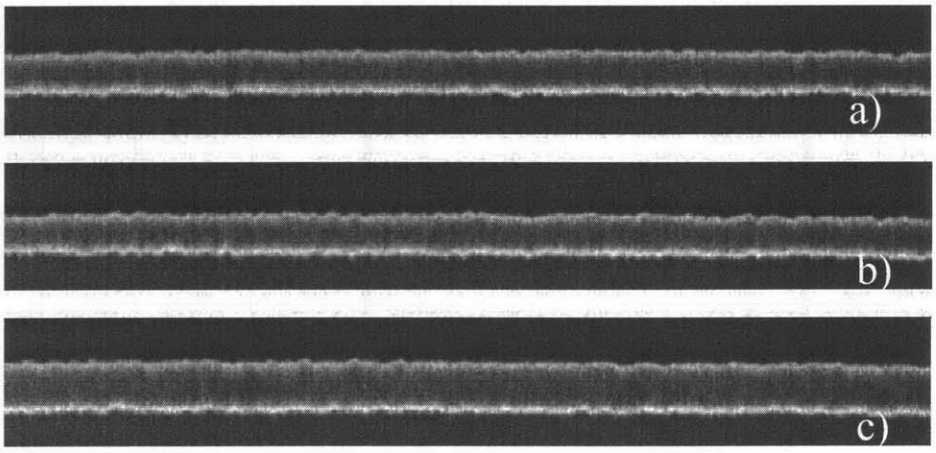

Figure 4.20 – Representative SEMs of polysilicon gates processed with 3 different hardmask open chemistries, showing differences in roughness and line width. a) baseline process. b) -+- process, roughest lines, but no CD growth. C) +-+ process, smoother lines, but large CD growth.

Table 4.5 lists the estimated standard error, t value, and significance level for both the HFLWR and CD results, for each wafer as compared to the baseline run. Results with significance levels of 5% or lower are highlighted.

Many of the treatments appear to be statistically significantly different from the baseline hardmask open, both for roughness and line width. We further can verify these results through the use of an analysis of variance (ANOVA) for the treatments (for both HFLWR and CD). The results are listed in table 4.6. The between – treatment mean

square (s_T^2) is much larger than the within – treatment mean square (s_R^2) for both quantities, verifying that there is a significant difference between some of the treatments. We can get a quick, visual determination of which treatments differ from which by plotting the treatment means beneath a t-distribution, centered over the baseline treatment mean, and scaled by the factor:

$$t\text{-}scale = \frac{s_R^2}{\bar{N}} \tag{4.3}$$

Table 4.5 – Results of paired t-tests for treatments vs. baseline.

Wafer	HFLWR				CD			
	$y_i - y_{baseline}$	Est. Std Error	t	Sig. Level	$y_i - y_{baseline}$	Est. Std Error	t	Sig. Level
1 (---)	-0.04	0.129	0.32	37.58%	7.21	0.772	9.34	0.00%
2 (--+)	0.41	0.133	3.07	0.17%	8.66	0.719	12.04	0.00%
3 (-+-)	4.85	0.459	10.5	0.00%	-0.74	0.942	0.78	21.86%
4 (-++)	0.08	0.111	0.73	23.35%	5.98	0.756	7.90	0.00%
5 (+--)	0.54	0.136	3.96	0.01%	-1.15	0.715	1.61	5.71%
6 (+-+)	-0.24	0.116	2.10	2.06%	18.63	0.683	27.26	0.00%
7 (++-)	0.01	0.111	0.11	45.65%	0.46	0.746	0.62	26.83%
8 (+++)	-0.23	0.122	1.90	3.17%	14.81	0.811	18.26	0.00%

where $\bar{N}$ = average number of samples per treatment (in our case, 25.8), and s_R^2 = within – treatment mean square. The results are plotted in figures 4.21 (HFLWR) and 4.22 (CD). The treatment means located far from the center of the distribution indicate a statistically significant deviation from those located underneath the distribution. The significant differences identified by ANOVA are identical to those indicated by the paired t-tests, providing a convenient check on the statistical analysis.

Complex interactions are apparent by the numerous treatments that possess a statistically significant difference in mean from the baseline, and the analysis shows us that indeed, modulating the hardmask open plasma chemistry does have an effect on the resulting roughness of the etched polysilicon gates. While interesting, however, we would like some insight into the mechanism behind the line roughening and CD variation, which

the t-tests and ANOVA do not provide. To understand the mechanism, it is necessary to decouple the effects of the process variables.

To accomplish this, a factor analysis was performed on wafers 1-8 for both the HFLWR and CD results to elucidate both the individual and combined contribution of the three experimental variables, and to understand the mechanism by which modifying the hardmask open chemistry influences the gate roughness transfer (the analysis is equivalent to a regression). The factors have been coded as : Pressure = 1, Bottom Power

Table 4.6 - Results of ANOVA analysis.

	HFLWR	CD
Within - Treatment Mean Square (s_R^2)	0.75	6.74
Between - Treatment Mean Square (s_T^2)	61.08	1330.96
$F_{7,201}$ (s_T^2/s_R^2)	81.56	197.43
Significance Level	0.000%	0.000%

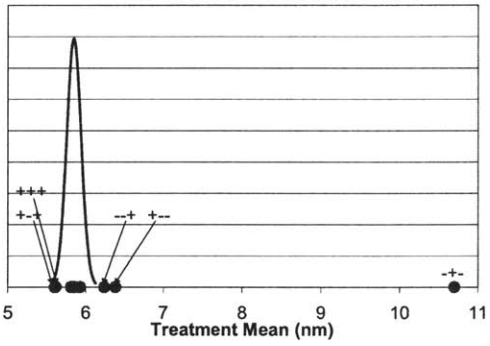

Figure 4.21. HFLWR treatment means plotted with a scaled t-distribution centered over the baseline mean. The same treatments (--+, -+-, +--, +-+, and +++) identified as significantly different from the baseline by a paired t-test are identified by the ANOVA.

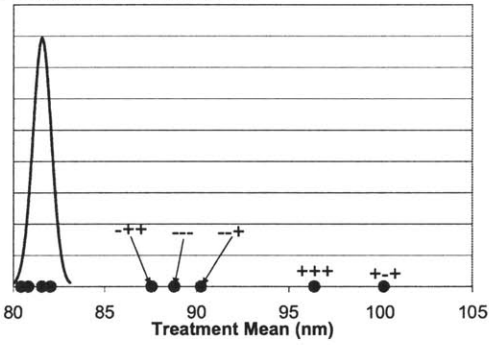

Figure 4.22. CD treatment means plotted with a scaled t-distribution centered over the baseline mean. The same treatments (---, --+, -++, +-+, and +++) identified as significantly different from the baseline by a paired t-test are identified by the ANOVA.

= 2, CHF_3/CF_4 ratio = 3. After application of Yates' algorithm[7], the first, second, and third order interactions (describing the individual and combined contributions of each experimental variable) and an estimate for the standard error of each factor is calculated as shown in table 4.7. The standard error estimates are calculated by first obtaining a pooled variance (equation 4.2, using the standard deviation and number of samples from

all wafers 1-8. Application to the HFLWR and CD data yields pooled variances of: $s^2_{HFLWR} = 0.91$, $s^2_{CD} = 2.54$).

Next, the estimates for the variance of the mean and the factors are given by:

$$V(mean) = \frac{s^2}{N} \tag{4.4}$$

$$V(effect) = \frac{4}{N} s^2 \tag{4.5}$$

where s^2 = pooled variance, and N = total number of gates on all wafers 1-8 (in this data set, 198 gates). Finally, the standard error is calculated by taking the square root of the variance, ie:

$$\text{std error(mean or effect)} = \sqrt{\text{V(mean or effect)}} \tag{4.6}$$

Table 4.7 - Results of factor analysis

Factor	HFLWR		CD	
	Estimate	Std. Error	Estimate	Std. Error
Mean	6.52	0.19	88.31	0.31
1	-1.31	0.13	2.91	0.35
2	1.01	0.13	-3.21	0.35
12	-1.27	0.13	2.11	0.35
3	-1.34	0.13	10.57	0.35
13	0.82	0.13	6.49	0.35
23	-1.17	0.13	-0.04	0.35
123	1.44	0.13	-2.67	0.35

Applying equations 4.2, and 4.4 – 4.6 to the HFLWR and CD results, we arrive at the standard errors listed in table 4.7.

To observe which factors significantly impact the HFLWR and CD, we can again utilize the concept of a representative t-distribution, this time centered at zero and appropriately scaled by the factor standard error. The results for both statistics are shown

in figure 4.23 (HFLWR) and 4.24 (CD). Since the total DOF is high (190) a normal distribution is plotted rather than the t distribution. These figures summarize the tabular data in an easy – to – interpret fashion, and provide for an immediate assessment of the important factors and interactions. Factor values that lie far outside the distribution can be taken as contributing in a statistically significant fashion.

A glance at the two plots reiterates our previous finding that there exist complex interactions between all three process variables for both roughness and line width. However, the data can be interpreted together in such a way as to highlight the probable mechanism of roughness modulation in this process.

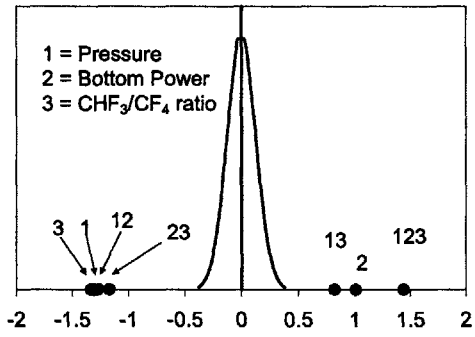

Figure 4.23 – Factors and interactions contributing to HFLWR modulation, plotted under a scaled t-distribution. All individual and higher – order interactions fall outside the distribution, suggesting that all have a statistically significant effect on HFLWR.

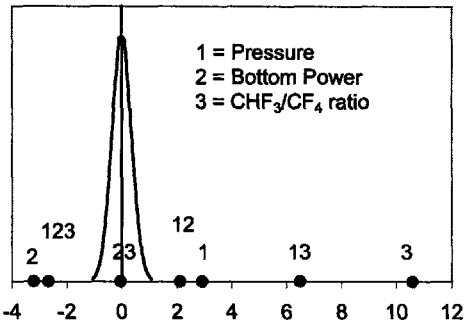

Figure 4.24 – Factors and interactions contributing to CD modulation, plotted under a scaled t-distribution. Except for the 23 interaction (Bottom Power x gas ratio), all individual and higher – order interactions fall outside the distribution.

Let us first examine the individual (first – order) factors for both the HFLWR and CD modulation. They are:

Factor	**HFLWR**	**CD**
Pressure (1)	-1.31 nm	+2.91 nm
Bottom Power (2)	+1.01 nm	-3.21 nm
CHF_3/CF_4 (3)	-1.34 nm	+10.57 nm

These should be read as *"Raising pressure from the low condition (20 mT) to the high condition (60 mT) decreases HFLWR by –1.31 nm, and increases the line CD by +2.91*

nm," and so forth. We see that the roughness and CD effects are opposite in magnitude, meaning that to first order, every decrease in roughness in accompanied by an increase in the line width. Roughness goes down with increasing pressure, decreasing ion bombardment, and increasing CHF_3, with the opposite trend for the CD. The smoother lines accompanied by a CD growth are highly suggestive of a polymerization mechanism for the line roughness modulation. Conditions that increase polymerization (ie high pressure, low power, high CHF_3) lay down polymer on the lines during the hardmask open. The polymer tends to fill imperfections in the line edge, yielding a smoother line after gate etch. However, the deposition grows the line during the hardmask open, resulting in a "fatter" mask used to etch the polysilicon, and creating wider gates. The raw data backs this hypothesis up. The sample with the hardmask opened under the least polymerizing condition (wafer 3, -+-) was the roughest by far (10.7 nm HFLWR) without showing CD growth. The sample with the hardmask opened under the most polymerizing condition (wafer 6, +-+) was the smoothest (5.6 nm HFLWR), but had a 25% CD growth, the most of all the samples (100.2 nm CD). As on the oxide samples, where we gained smoother lines at a cost (decreased selectivity), this is another example of "no free lunch," where the requirements of line smoothness and line width must be balanced against each other.

Figures 4.23 and 4.24 show that most of the 2-factor interactions are significant as well. However, they must be analyzed jointly. Table 4.8 shows the 12, 23, and 13 joint interaction squares for both the HFLWR and the CD. The bold numbers show the effect on the HFLWR or CD by moving from one condition to the other for one variable, while leaving the other constant. They should be read as: *"HFLWR 12 interaction. At the low power condition (60 W), an increase in the pressure from the low condition (20 mT) to the high condition (60 mT) yields an 0.04 nm decrease in the HFLWR. Conversely, at the high power condition (140 W), an increase in the pressure from the low condition to the high condition decreases the HFLWR by 2.58 nm."* The interaction squares can be read across as well as down, ie: *"HFLWR 12 interaction. At the low pressure condition (20 mT), increasing the power from the low condition (60 W) to the high condition (140 W) yields a 2.28 increase in the HFLWR. Conversely, at the high pressure condition (60 mT), increasing the power from the low to the high condition yields a 0.26 nm decrease in the*

HFLWR.." Note that not all variations are significant, those that are (defined as a change of more than 3X the effect standard error) are highlighted. Also note the 23 interaction for CD, which shows no difference in effect regardless of level (confirming the factor calculation that showed this interaction to be statistically insignificant).

The analysis of the 2-factor interactions provide more detail into the CD/roughness trade – off, illustrating the rather complex interplay of the experimental variables. Still, the second order effects mirror those discovered through our analysis of the first order, and seems to confirm the hypothesis of a polymerization driven smoothing. Increasing the power (ion bombardment) at all conditions, roughens the lines

Table 4.8 - Joint factor interactions (12, 23, and 13) .

HFLWR	12 interaction		
+	5.99	**-0.26**	5.74
Pressure	**-0.04**		**-2.58**
-	6.03	**2.28**	8.31
	-	Power	+

CD	12 interaction		
+	90.32	**-1.10**	89.22
Pressure	**0.81**		**5.02**
-	89.51	**-5.31**	84.20
	-	Power	+

HFLWR	23 interaction		
+	8.28	**-2.51**	5.77
Power	**2.18**		**-0.16**
-	6.09	**-0.17**	5.93
	-	CHF_3	+

CD	23 interaction (insignificant)		
+	81.44	**10.53**	91.97
Power	**-3.17**		**-3.25**
-	84.61	**10.61**	95.22
	-	CHF_3	+

HFLWR	13 interaction		
+	6.12	**-0.51**	5.61
Pressure	**-2.13**		**-0.48**
-	8.25	**-2.16**	6.09
	-	CHF_3	+

CD	13 interaction		
+	81.24	**17.06**	98.30
Pressure	**-3.58**		**9.40**
-	84.81	**4.08**	88.89
	-	CHF_3	+

Increasing the CHF_3 flow (and thus, the polymerization of the hardmask open chemistry), under all conditions, smooths the lines. Increasing the pressure at high power, and all CHF_3 flow, smooths the lines. Therefore, under any combination of variables that

increases the polymerization of the etch, smoother gates result, and are almost always accompanied by a growth in the line width.

The third order interaction can be analyzed in a similar fashion (by forming joint interaction squares of 12 vs. 3, 13 vs. 2, and 23 vs. 1). These are omitted for simplicity, as they show similar interactions to the first and second order effects, again indicating a polymerization induced smoothing with associated CD gain.

It should be noted that the gate smoothing induced by polymerization during the hardmask etch is opposite to the trend noticed on the oxide samples, where excess polymerization during the hardmask open seemed to increase the final oxide sidewall roughness. This may be due to either fact that the oxide samples were etched without a resist strip, or to differences in the substrate etch chemistries. First, etching the oxide samples without a resist strip allows the polymer deposited during the hardmask open to remain, potentially leading to the observed increase in post – etch oxide roughness as previously described. The polysilicon samples, on the other hand, underwent a resist strip, and used only the remaining hardmask to etch the gates. The resist strip may have removed the residual polymer from the hardmask sidewall, preventing excessive roughening during the etch. Second, the oxide substrate was etched in a fluorocarbon chemistry, while the polysilicon was etched in HBr/O_2. The latter chemistry is probably an effective remover of residual polymer, while the oxide etch chemistry promotes further deposition.

4.6. Summary

In this chapter we have observed how maintaining the state of the feature sidewall immediately prior to the substrate etch is of critical importance in determining roughness transfer to the substrate. Several examples of modulating roughness through modifying the ARC/hardmask open were shown. On oxide samples with organic ARC or an inorganic hardmask, using a Cl_2/O_2 "chemical" ARC/hardmask open chemistry allowed a smoother sidewall to be maintained, providing less roughness transfer than using "physical," high ion bombardment chemistries (with an almost 60% improvement on the hardmask samples). However, the roughness improvement came at the cost of decreased selectivity over resist during the hardmask open. For polysilicon gate etching with an

oxide hardmask, modulating the hardmask open also proved to effect the roughness of the final etched gates. The mechanism was shown to be due to polymerization forming on the gates during the fluorocarbon hardmask etch. Greater polymerization filled in imperfections in the gate line, allowing a smoother transfer to the underlying polysilicon. However, again the roughness improvement came at a cost. The increased polymerization grew the width of the line during the hardmask open, creating a "fatter" mask that resulted in wider gates than originally patterned.

4.7. References

[1] S. Rauf, P. J. Stout, and J. Cobb, Journal of Vacuum Science & Technology B 21, 655-659 (2003).

[2] Q. Lin, C. Black, L. G. Detavernier, K. Guarini, B. Herbst, H. Kim, P. Oldiges, K. Petrillo, and M. Sanchez, Proc. SPIE 5039, 1076 - 1085 (2003).

[3] J. Cobb, S. Rauf, A. Thean, S. Dakshina-Murthy, T. Stephens, C. Parker, R. Peters, and V. Rao, Proc. SPIE 5039, 376 - 383 (2003).

[4] T. Chowdhury, R. Bamnolker, R. K. Chan-Lon Yang, and H. C. L, Proc. SPIE 5039, 240 - 248 (2003).

[5] P. Oldiges, Q. Lin, K. Petrillo, M. Sanchez, M. Leong, and M. Hargrove, Proc. Int. Conf. SISPAD 2000, 131-134 (2000).

[6] C. H. Diaz, H. J. Tao, Y. C. Ku, A. Yen, and K. Young, IEEE Electron Device Letters 22, 287-289 (2001).

[7] G. P. Box, W. G. Hunter, and J. S. Hunter, Statistics for Experimenters : An Introduction to Design, Data Analysis, and Model Building (Wiley, New York, 1978).

[8] L. H. A. Leunissen, R. Jonckheere, K. Ronse, and G. B. Derksen, Journal of Vacuum Science & Technology B 21, 3140-3143 (2003).

Chapter 5 – Impact of Thin Resist Processes on Post–Etch Line Edge Roughness Transfer : Influence of Photoresist Thickness and Fluorine Content

5.0. Abstract and Introduction

Requirements of the sub – 70 nm technology nodes limit resist film thicknesses to less than 150 nm for critical circuit levels, for the reasons described previously (pattern collapse[1], etc), creating challenging conditions for etch processing. Much of the resist layer can be consumed during the ARC open, leaving insufficient masking material remaining to pattern the substrate and creating excess roughness transfer. Additionally, with conventional lithography techniques these nodes will require a shift to even shorter exposure wavelengths than 193 nm, namely 157 nm (F_2) and EUV (extreme ultraviolet, 13 nm). Current photoresists are highly absorbing at these wavelengths, rendering them useless as lithographic systems. Consequently, the incorporation of fluorine into the resist structure is required to obtain transparency at the new exposure wavelength[2-4]. This added fluorine can yield lower etch selectivity to the underlying ARC, causing the resist to etch faster than a similar non-fluorinated material[5,6], and potentially creating roughness.

In this chapter, the impact of employing thin and/or fluorinated photoresists on the post etch line edge roughness transfer into oxide substrates was investigated. First, a non-fluorinated, very thin (130 nm) resist was investigated. It was found that almost half of the resist thickness was consumed during the ARC open, leaving inadequate masking material remaining to properly etch the oxide. At the feature edges, all the resist and ARC was consumed during a 0.6 μm oxide etch, leaving the substrate exposed and causing mousebite formation. Next, blanket etch rates of fluorinated 193 resists with varying fluorine content were measured in both halogen and fluorocarbon plasma chemistries. The dependence of the etching rate on resist fluorine content showed a "threshold" behavior in both chemistries. Resists with fluorine content below the threshold showed no significant etch rate enhancement. However, once the fluorine content of the resist increased beyond the threshold, etching rates increased monotonically. Sidewall roughness transfer was compared on 3 different resist systems: 1) non-fluorinated, 2) sub – threshold fluorine content, and 3) super-threshold fluorine content. Roughness transfer

on the sub-threshold resist was only slightly higher than the control. However, the super-threshold system showed severe roughening during etch accompanied by extreme resist consumption, faceting at the resist corners, and large mousebites left on the oxide lines.

These results have important implications for the success of 157 nm lithography. Because 157 nm resists are expected to be heavily fluorinated and extremely thin, it may become impossible to pattern certain levels using the conventional single layer resist / organic ARC approach that works well for 248 and 193 nm systems. These levels will require the use of alterative patterning schemes such as hard mask and / or bilayer approaches, which are expected to gain importance as the industry migrates to sub-70 nm nodes.

5.1. Non-Fluorinated 193 nm Resist ("Methacrylate")

The same 193 nm adamantine–co–lactone acrylate based resin examined in Chapters 3 and 4 ("methacrylate" resist) was used as a control to compare to the fluorinated resist systems. Thermal oxide substrates were spun coated with ~90 nm of organic ARC, and patterned in a 260 nm thick, 150 nm dense line/space pattern using the DARPA mask. Exposures were performed on a 0.75 NA ASML stepper with annular illumination (as were all the resists discussed in this chapter). Figures 5.1 and 5.2 show the cross sectional patterns and sidewall AFM image (repeated from chapter 3). The resist sidewall has an RMS roughness of ~3.6 nm (smoother than the 248 nm system) with no evidence of a standing wave, indicating a better optimized ARC thickness.

5.1.1. ARC Open

The ARC was opened in a CF_4/O_2 plasma chemistry (30s, 300 W, 40 mT, 90 sccm CF_4, 10 sccm O_2, 160 sccm Ar) in a TEL DRM etcher. Approximately 120 nm of resist was consumed during the ARC open. Additionally, the slight overetch resulted the consumption of ~30 nm of the oxide substrate, due to the fluorocarbon nature of the etch. A cross sectional SEM of the etched profiles is shown in figure 5.3.

This ARC open shares characteristics of both the "physical" N_2/H_2 and "chemical" Cl_2/O_2 chemistries investigated previously. The sidewall is striated due to the significant physical nature of the etch, owing to the high DC bias generated in the

capacitively coupled etcher. However, the RMS on the bulk of the sidewall is < 2 nm indicating relatively shallow striations, probably due to the etching by the oxygen and

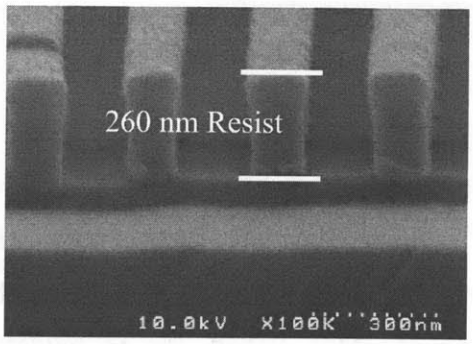

Figure 5.1 – Cross sectional SEM of methacryate resist patterns.

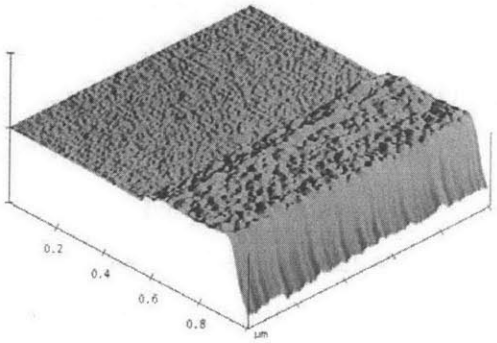

Figure 5.2 – Sidewall AFM image of the methacrylate resist. The surface has an RMS roughness of ~3.6 nm. No standing waves are evident, indicating a properly optimized ARC thickness.

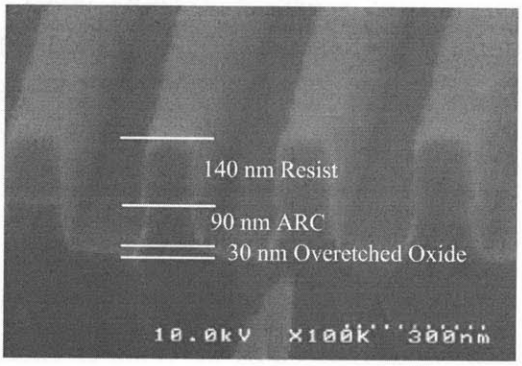

Figure 5.3 – Cross sectional SEM of Methacrylate resist sample after CF_4/O_2 ARC open. A slight overetch has consumed ~30 nm of the underlying oxide substrate.

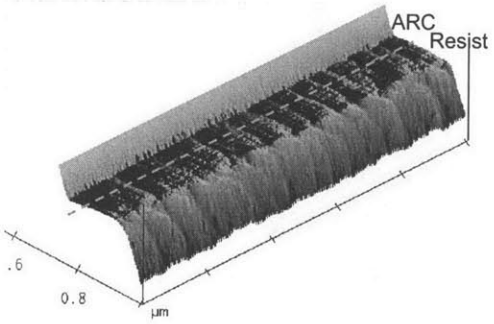

Figure 5.4 – Sidewall AFM image of methacrylate resist sample after CF_4/O_2 ARC open. The sidewall is slightly striated due to the high DC bias developed during the etch.

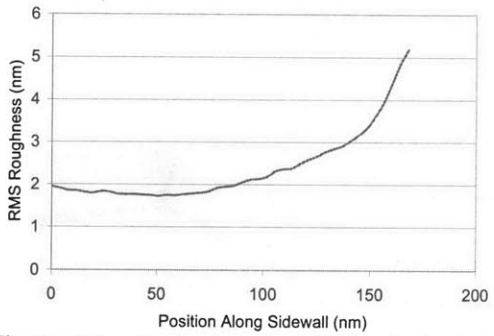

Figure 5.5 – Depth dependent SWR calculated from the AFM image. Note that the striations are relatively shallow (~2 nm) due to the oxygen and fluorine radicals that impart a "chemical" nature to the ARC open.

fluorine radicals formed. Note that CF_4 does not deposit significant amounts of polymer[7]. Figures 5.4 and 5.5 show the sidewall AFM and depth – dependent SWR of the methacrylate resist sample after ARC open.

5.1.2. Oxide Etch

After the ARC open, the patterns were transferred into the oxide substrate via a C_4F_6/O_2 etch, again on a TEL DRM etcher (90 s, 1500 W, 50 mT, 9 sccm C_4F_6, 6 sccm O_2, 500 sccm Ar). Figure 5.6 shows the cross sections of the etched features. Only 30 nm of resist remains, however, 600 nm of oxide has been etched, for an oxide/resist selectivity of more than 5:1, probably due to the excess fluorocarbon (3:2 FC/O_2 ratio in the gas feed). This is also borne out by the CD gain of the lines. The etched features are approximately 195 nm wide, for a gain of 45 nm in width during the etch due to the excess polymerization. Still, the profiles look square and even, with little resist loss at the corners. The sidewall AFM image (figure 5.7) shows broad but shallow striations. Stripping the remaining resist and ARC, and imaging the oxide lines via a top – down SEM shows small mousebites (figure 5.8), with an average RMS roughness of 3.3 nm determined by edge analysis of the digitized SEM data.

5.2. Non-Fluorinated "Thin" Resist

The advanced 193 nm and 157 nm resists being developed for sub-70 nm nodes are expected to be less than 200 nm thick after developing. Therefore, it is important to study the impact that extremely thin resists might have on roughness transfer. Similar patterns were generated using another 193 nm resist with a post – develop thickness of

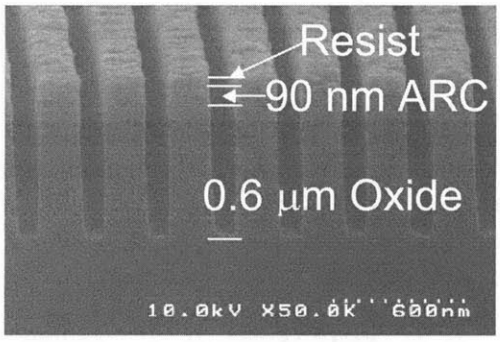

Figure 5.6 – Cross sectional SEM of methacrylate resist patterns after 90s oxide etch.

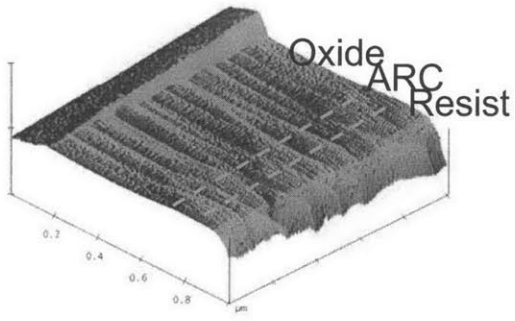

Figure 5.7 – Sidewall AFM image of methacrylate resist sample after 90s oxide etch. Broad but shallow striations are observable on the oxide sidewall.

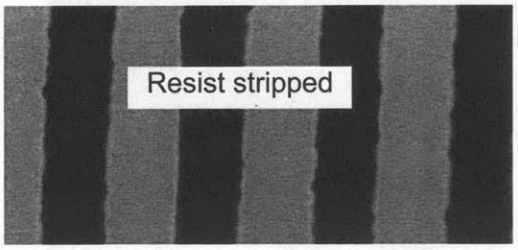

Figure 5.8 – Top down SEM of oxide lines after stripping the remaining resist and ARC in an O_2 plasma. Small mousebites corresponding to the striations seen in the AFM are observable on the sides of the line. Threshold analysis of the SEM indicates an RMS roughness of ~3.3 nm at the line edges.

only ~130 nm (½ the thickness of the methacrylate resist) over organic ARC, and the same processing was employed for ARC open and oxide etch. Figure 5.9 shows SEM results of the patterning using the thin resist after lithography, ARC open, and oxide etch. It can be seen in figure 5.9b that more than half of the resist has been consumed just during the ARC open, leaving limited masking material to etch the oxide. This unhappy result is borne out in figure 5.9c, which shows the line profiles after a 90s, 600 nm oxide etch. All the resist and the majority of the ARC has been lost. Indeed, at the feature corners, no masking material remains at all, leaving the bare oxide open to attack during the end of the etching process. Stripping what little ARC is left, and imaging the lines via top down SEM shows severe mousebites at the edges of the lines corresponding to the exposed areas observed in the cross sections (figure 5.10). Obviously, these results show that single layer resists with non-selective ARC opens cannot be expected to perform adequately for deep trench etches, due to insufficient masking material remaining to pattern the underlying substrate.

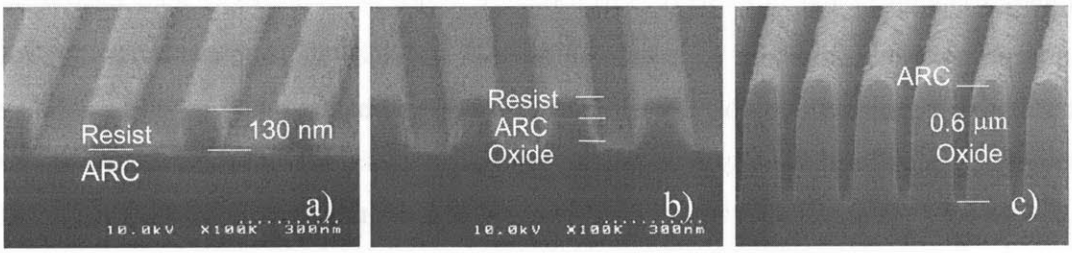

Figure 5.9 – a) Lithographic patterning of 150 nm line/space pattern using 130 nm thin photoresist. b) Line patterns after ARC open. More than ½ of the resist has been consumed. c) Line patterns after 90s 600 nm oxide etch. All of the remaining masking material has been consumed during the etch, especially at the feature edges, leaving the oxide exposed to the plasma.

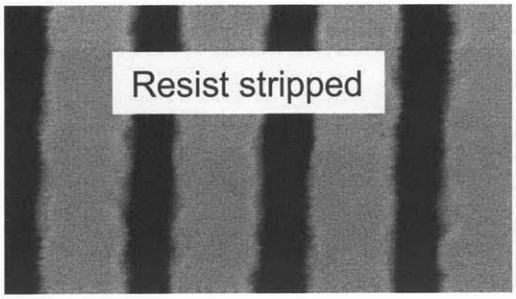

Figure 5.10 – After stripping the remaining resist and ARC, large mousebites can be seen at the line edges due to the inadequate mask thickness provided by the thin resist.

5.3. Fluorinated Resists

To investigate the role of resist fluorination on roughness transfer, photoresist formulations with varying fluorine contents were etched. Blanket films elucidated the effect of fluorination on the resist etching rate, the results of which were correlated with roughness development on patterned features.

5.3.1. Effect of Resist Fluorine Content on Blanket Etch Rates

Figure 5.11 shows the dependence of resist blanket etch rates on the extent of polymer fluorination in both halogen (Cl_2) and fluorocarbon ($CHF_3/CF_4/Ar$) plasma chemistries. It can be seen that low concentrations of fluorine do not result in a significant etching rate increase. However, the fluorinated resist systems seem to exhibit a "threshold" like behavior. Once the threshold fluorine concentration is crossed, the etching rate of the resist increases monotonically. It should be noted that the exact threshold fluorine content and the slope of the curve beyond the threshold are expected to depend the specific polymer platform, as well as other factors such as the resist oxygen content[8].

To examine the role of resist fluorination on sidewall roughness transfer, two fluorinated resists were compared to the non-fluorinated methacrylate resist discussed in section 5.1. The fluorinated systems were chosen on either side of the threshold indicated in figure 5.11. The sub-threshold resist contained approximately 8 wt% fluorine, while the higher fluorine content resist contained ~13 wt%.

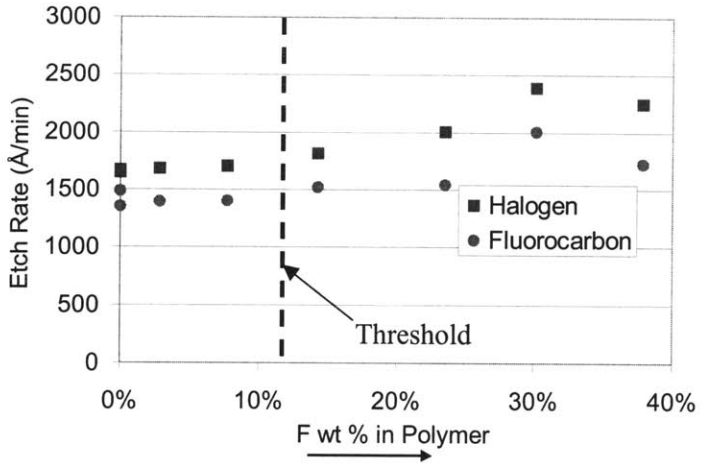

Figure 5.11 – Resist etch rate as a function of polymer fluorine content in both halogen and fluorocarbon etch chemistries. Note the "threshold" behavior. Resists with low fluorine content show no significant etch rate enhancement. However, at higher fluorination the etching rate increases monotonically.

5.3.2. Sidewall Roughness for Resist with Sub-Threshold Fluorination

Dense 150 nm lines and spaces were patterned in a 230 nm thick sub – threshold fluorinated resist, with an organic ARC to minimize standing wave formation (figure 5.12). At this time we are unable to release compositional information. The sidewall roughness was isotropic, with an RMS value of 3.2 nm calculated from the AFM image (figure 5.13). The ARC was opened in the same $CF_4/O_2/Ar$ plasma used previously on the methacrylate system, and the patterns underwent the same $C_4F_6/O_2/Ar$ 90 s oxide etch, in order to enable a direct comparison with the non – fluorinated system. Very little masking material remained after completion of the oxide etch. However, the profiles remained square, with no excessive resist loss at the feature corners (figure 5.14). Since the fluorine content of the resist was sub – threshold, no etch rate enhancement was either expected or seen. A sidewall AFM (figure 5.15) shows broad but shallow striations comparable to those seen on the non-fluorinated sample. After stripping the remaining ARC, a top down SEM shows small mousebites on the oxide surface (figure 5.16). The average roughness calculated via edge analysis on the SEM image is 4.0 nm RMS, slightly higher than the methacrylate resist (3.3 nm). This are attributable to the fact that the initial thickness of the sub – threshold fluorinated resist was 30 nm less than the non – fluorinated resist (230 nm vs. 260 nm).

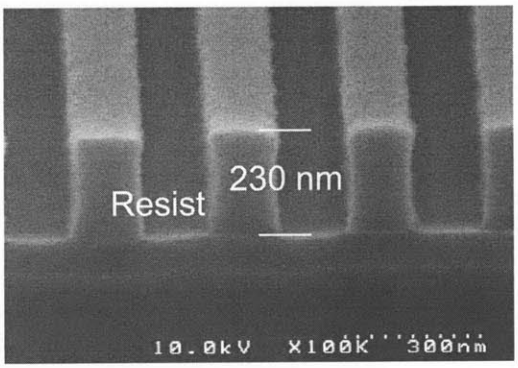

Figure 5.12 – Sub–threshold fluorinated resist printed in a 230 nm thick, 150 nm wide dense line/space pattern

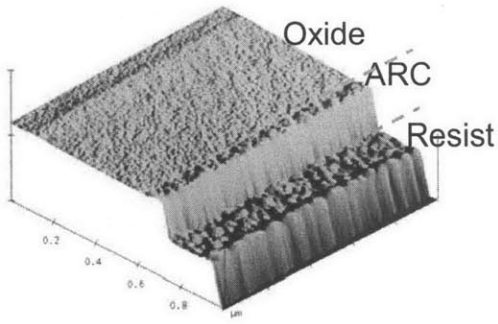

Figure 5.13 – Sidewall AFM image of sub–threshold fluorinated resist. The SWR is isotropic, with an RMS value of 3.2 nm.

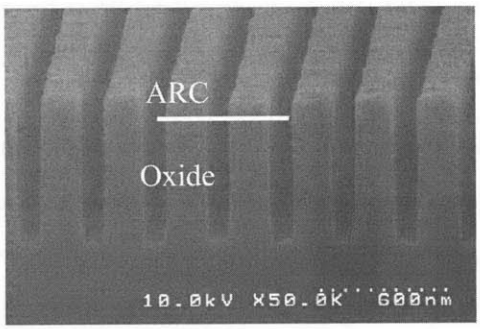

Figure 5.14 – Cross sectional SEM of patterns after 90 s oxide etch. While only residual resist and ARC remain, there has been no excessive masking material lost at the feature edges, leaving square profiles. No etch rate enhancement of the resist is observed due to the sub – threshold fluorine content.

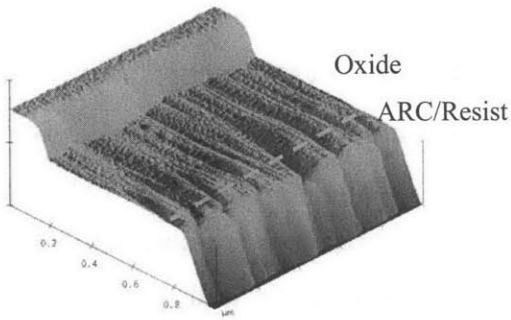

Figure 5.15 – Sidwall AFM image of the etched line. Broad but shallow striations are present on the sidewall, but appear comparable to those seen with the non – fluorinated methacrylate resist used previously.

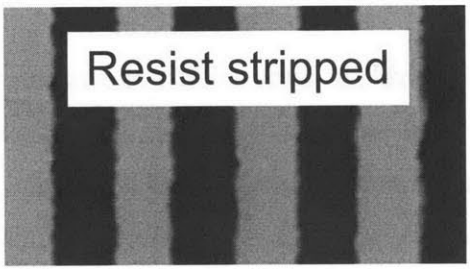

Figure 5.16 – After stripping the remaining ARC and resist in an O_2 plasma, small mousebites are observable on the oxide lines. Analysis of the SEM data yields an average RMS roughness of 4.0 nm for the line edges. This is slightly rougher than that seen on the methacrylate resist system (4.0 nm vs. 3.3 nm), but not excessively so, and is attributed to the fact that the initial thickness of the sub – threshold fluorinated resist was 30 nm less than the non fluorinated resist (230 nm vs. 260 nm).

5.3.3. Sidewall Roughness Transfer for Super - Threshold Fluorinated Resist

Dense 150 nm lines and spaces were patterned in a resist with a super–threshold fluorine content (~13 wt%) It consisted of a poly – norbornene backbone bearing a hexafluoroalcohol functionality and an alicyclic protecting group[9]. The resist was spun on to a thickness of 290 nm (this time, slightly greater than the non – fluorinated resist). The patterns were slightly t – topped (figure 5.17) and no attempt was make to optimize the profiles. The sidewall roughness calculated from the AFM image (figure 5.18) was ~2.4 nm after ignoring the t – top profile artifact at the top of the line. As before, the ARC was opened in a $CF_4/O_2/Ar$ plasma, and the patterns underwent the same $C_4F_6/O_2/Ar$ 90 s oxide etch.

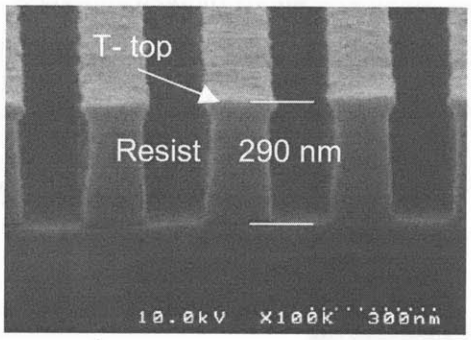

Figure 5.17 – Super–threshold fluorinated resist patterned in 290 nm thick, 150 nm dense line/space profiles. No attempt has been made to optimize the t–topped patterns. Note that the thickness is greater than the non–fluorinated resist.

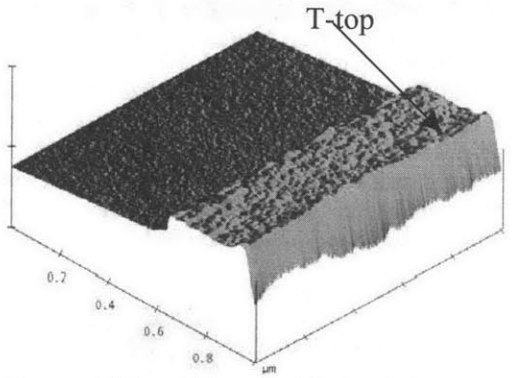

Figure 5.18 – Sidewall AFM of the super – threshold fluorinated resist patterns. The t – top is clearly visible in the AFM. The SWR is isotropic, with a calculated value of ~2.4 nm after discounting the profile artifact.

Figure 5.19 show a cross sectional SEM of the etched profiles. The high fluorine content of the resist has indeed led to excessive resist consumption (~130 nm/min) and severe faceting. Recall that this resist was thicker than both the sub – fluorinated resist and the non – fluorinated resist (290 nm vs. 230 nm vs. 260 nm, respectively). However, the thicker mask was more than offset by the etch rate increase caused by the high amount of incorporated fluorine. Resist loss is heavy especially at the feature edges, leading to deep, crevice – like striations that extend through the entire oxide layer as observed on the AFM image (figure 5.20). These crevices correlate well with the appearance of severe mousebites observed after stripping the remaining resist/ARC

(figure 5.21). These SEM profiles are so rough it is impossible to reliably extract the line edge for analysis. However, they are visually rougher by far than any of the other systems. These results indicate that the reduced etch selectivity due to excessive fluorination of photoresist polymers can indeed cause an enhancement in sidewall roughness transfer during etch. Table 5.1 summarizes the results of these experiments.

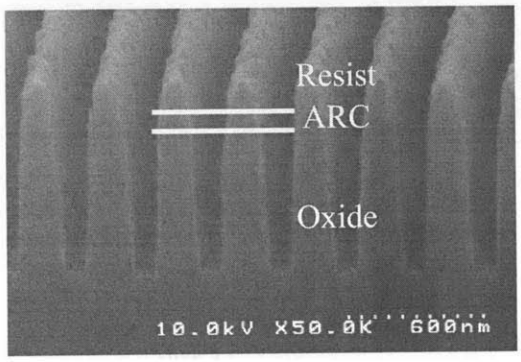

Figure 5.19 – Cross sectional SEM of super – threshold fluorinated resist system after 90 s oxide etch. Even though the resist began thicker than either the sub – threshold fluorinated or non – fluorinated resists, excessive resist loss at the edges of the feature due to the excess fluorine content leads to enhanced roughness transfer.

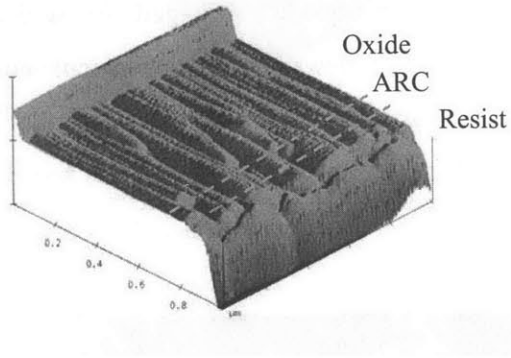

Figure 5.20 – Sidewall AFM image of super – threshold fluorinated resist system after 90 s oxide etch. Deep, crevice – like striations are observed through the entire oxide layer.

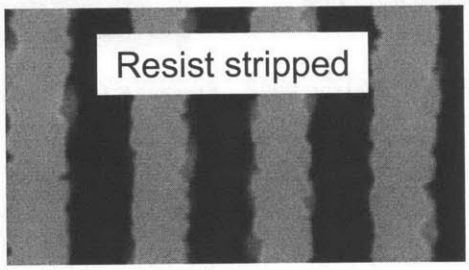

Figure 5.21 – After stripping the remaining ARC and resist in an O_2 plasma, severe mousebites can be seen at the line edges, correlating well with the crevices observed via AFM. The profiles are much rougher than the others, indicating that excess resist fluorination can indeed lead to enhanced roughness transfer.

5.4. Implications for 157 nm Resist Systems

As previously discussed, 157 nm resists are expected to etch even faster than those described here, due to the even higher anticipated fluorine content. In addition, the resists will be thinner due to d depth of focus issues. The combination of these two factors suggests that it might become impossible to successfully pattern certain levels

Table 5.1 – Results Summary

Resist Type	Thickness	Sidewall After Oxide Etch	Mousebites?
Non - Fluorinated	260 nm	Shallow striations	Few mousebites
Non – Fluorinated	130 nm	N/A	Large mousebites due to total resist loss
Sub – Threshold Fluorination	230 nm	Shallow striations, comparable to non - fluorinated	Slightly larger mousebites than non – fluorinated case due to thinner initial resist
Super – Threshold Fluorination	290 nm	Crevice – like striations	Severe mousebites due to high resist fluorination

using conventional single layer resist / organic ARC lithographic approaches due to the excessive sidewall roughness generated during the etching process. Therefore, successful patterning will require alternative schemes such as fast etching ARCs with enhanced selectivity[10], hardmasks with built – in ARC characteristics[11], or bilayer approaches[12,13].

5.5. Summary

In this chapter we have observed how thin and/or fluorinated resist can lead to enhanced sidewall roughness transfer during plasma etching, when the masking material proves inadequate to fully pattern the underlying substrate. Investigation of a thin, non – fluorinated single layer resist demonstrated that, once the masking material is removed, exposure of the substrate to the etching process allows more roughness to propagate through as compared to a thicker non – fluorinated methacrylate resist, leaving mousebites on the top of the lines.

The dependence of resist etching rate on the extent of fluorination showed a threshold behavior. Photoresists with a fluorine content below the threshold value did not exhibit an etching rate enhancement. However, once the fluorine content increased beyond the threshold value, etching rates increased monotonically. These results were correlated with roughness transfer during etch on both sub – threshold and super – threshold fluorinated resist systems. Roughness propagation during pattern transfer with the sub – threshold fluorinated resist was comparable to the non – fluorinated case, with the slightly higher roughness attributable to the fact that the fluorinated resist was 30 nm thinner. However, the super – fluorinated resist allowed extreme roughness transfer into

the underlying oxide due to the high fluorine content, even though the resist was spun on thicker than all the other resist systems.

These results were shown to have implications for advanced 157 nm lithography. 157 nm resists that are thin and fluorinated are likely to be inadequate for pattern transfer to certain critical levels, necessitating the use of alternative patterning schemes for sub – 70 nm manufacturing nodes.

5.6. References

1 T. Tanaka, M. Morigami, and N. Atoda, Japanese Journal of Applied Physics Part 1 **32,** 6059-6064 (1993).

2 M. Toriumi, T. Ishikawa, T. Kodani, M. Koh, T. Moriya, T. Yamashita, T. Araki, H. Aoyama, T. Yamazaki, T. Furukawa, and T. Itani, Journal of Vacuum Science & Technology B **22,** 27-30 (2004).

3 M. Toriumi, T. Yamazaki, T. Furukawa, S. Irie, S. Ishikawa, and T. Itani, Journal of Vacuum Science & Technology B **20,** 2909-2912 (2002).

4 N. Fender, P. J. Brock, W. Chau, S. Bangsaruntip, A. Mahorowala, G. M. Wallraff, W. D. Hinsberg, C. E. Larson, H. Ito, G. Breyta, K. Burnham, H. Truong, P. Lawson, and R. D. Allen, Proc. SPIE **4345,** 417-427 (2001).

5 T. H. Fedynyshyn, R. R. Kunz, R. F. Sinta, M. Sworin, W. A. Mowers, R. B. Goodman, and S. P. Doran, Proc. SPIE **4345,** 296-307 (2001).

6 T. Itani, M. Toriumi, T. Naito, S. Ishikawa, S. Miyoshi, T. Yamazaki, and M. Watanabe, Journal of Vacuum Science & Technology B **19,** 2705-2708 (2001).

7 G. S. Oehrlein and H. L. Williams, Journal of Applied Physics **62,** 662-672 (1987).

8 F. Watanabe and Y. Ohnishi, Journal of Vacuum Science & Technology B **4,** 422-425 (1986).

9 W. Li, P. R. Varanasi, M. C. Lawson, R. Kwong, K. Chen, H. Ito, H. Truong, R. D. Allen, M. Yamamoto, E. Kobayashi, and M. Slezak, Proc. SPIE **5039,** 61-69 (2002).

10 D. Pfeiffer, A. P. Mahorowala, K. Babich, D. Medeiros, K. Petrillo, and M. Angelopolous, Proc. SPIE **5039,** 136-143 (2003).

[11] A. P. Mahorowala, K. Babich, K. Petrillo, J. Simons, and M. Angelopolous, Proc. SPIE **4343,** 306-316 (2001).

[12] Q. Lin, K. Petrillo, K. Babich, D. La Tulipe, and D. Medeiros, Proc. SPIE **3678,** 241-250 (1999).

[13] R. Kwong, P. R. Varanasi, M. C. Lawson, T. Hughes, G. Jordhamo, M. Khojasteh, A. Mahorowala, R. Sooriyakumaran, P. Brock, C. Larson, D. Fenzel-Alexander, H. Truong, and R. Allen, Proc. SPIE **4345,** 50-57 (2001).

Chapter 6 – Polymer Micromask – Induced Surface Roughening During Fluorocarbon Plasma Etching of Low-k and Porous Low-k Dielectric Films

6.0. Abstract and Introduction

To further reduce interconnect delay and enable higher device speeds (especially as the critical dimensions are lowered below 0.13 μm), it becomes advantageous to reduce the dielectric constant of the interlevel dielectric material between the metal lines[1]. Low-k films containing carbon[2] and/or pores[3] in the matrix are candidates to meet this objective. While there has been research focusing on the material characterization of porous low-k films[3,4], and some attention to the etching characteristics of both solid[5,6] and porous[7,8] low-k dielectrics, little attention has been paid the surface roughening of these films during plasma etch processing. Roughness present after dielectric etch can cause problems during subsequent processing, for example by interfering with the deposition of conformal liner materials or barrier layers prior to copper metallization[9]. Therefore, an understanding of surface roughening mechanisms of low-k and porous low-k materials during plasma etching is extremely desirable.

Three dielectric films: 1) thermal oxide, 2) organosilicate glass (OSG), and 3) a methylsilsequioxane porous low-k film (PLK), were etched in various fluorocarbon plasma chemistries, while varying ion bombardment energy. Etch rates and surface roughnesses were measured. Polymer – induced micromasking was identified as a roughening mechanism. During the etching process, under certain conditions multiple surface steady states develop on the films, creating regions with both net etching and net fluorocarbon polymer deposition. Once the dual regions form, etch selectivity between the low-k substrate and the polymer leads to the formation surface roughness.

On the solid films, the roughness formation shows a threshold behavior in relation to ion bombardment, with a transition from roughening to smooth etching as the ion bombardment energy is increased. Moreover, on the solid dielectrics roughness formation can be prevented through polymerization control, for example by the addition of oxygen to the etching gases. However, roughness formation on the porous films was greater due to fluorocarbon diffusion into the pore structure, which seeded the formation of micromasks at conditions at which they do not form on the solid films. Therefore, the

successful integration of porous low-k dielectrics will require very careful control of polymerization to prevent unacceptable roughness formation during fluorocarbon etching.

6.1. Experimental

The homemade inductively coupled plasma etcher used in this work is shown schematically in figure 6.1. It consists of a 10" diameter stainless steel reactor pumped by a Leybold Turbovac 361C turbomolecular pump. 4" wafers can be loaded through an integral load lock. The chamber base pressure is monitored with an ionization gauge and is typically maintained at 10^{-6} torr. The chamber is topped with a quartz plate. A 3 turn planar copper coil is placed on the plate, and is powered at 13.56 MHz (Comdel CPS-500A RF power supply) via a matching network. The bottom electrode is independently powered at 4 MHz (Comdel CX-2000 RF power supply) via a second matching network, and has a V_{pp} sensor to provide a measure of the applied DC bias to the sample (assumed to be ½ V_{pp})[10]. The bottom power and matching are varied to achieve the desired wafer bias. Circulating cooling water at approximately 15 °C through the electrode controls the temperature. Wafers are mechanically clamped using a heavy clamping ring that can be raised and lowered with a linear motion feedthrough. He gas is supplied to the wafer backside to enhance thermal contact with the cooled electrode[11]. Wafers typically experience a temperature rise to approximately 50 °C during processing.

Thermal oxide, OSG, and porous MSQ low-k films were etched at MIT in the above reactor. The OSG is a spin-on carbon – doped oxide – like film, with k~2.8. The PLK has a solid phase composition similar to the OSG (determined via XPS), with approximately 30% porosity, and has a dielectric constant of ~2.2. The films were diced into ¼" x ¼" samples, and adhered to dummy silicon wafers with either thermally conductive silver paint (Ernest F. Fullam, P/N 14811) or vacuum grease (Apiezon type H) to assure thermal contact to the electrode. Each Si wafer had 3 such samples mounted (1 from each film type) allowing simultaneous etching of all films at each processing condition to minimize variation due to run-to-run process fluctuations. After etching, the etching rate and surface roughness were determined for all three films as a function of ion bombardment energy.

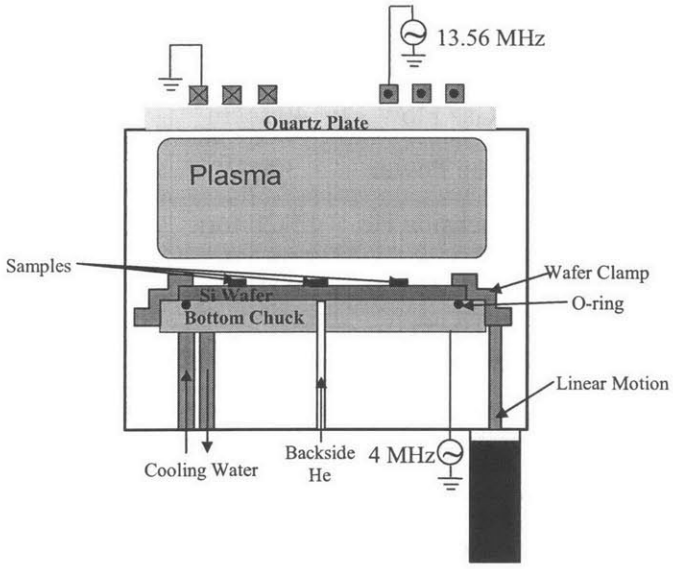

Figure 3.1 – Schematic of home – built inductively – coupled plasma etcher used in this work. 1 sample of each film type was adhered to a dummy silicon wafer, so all three films were processed identically at each experimental condition.

6.2. Etch Rate Results

Etch rates of thermal oxide and OSG were determined using variable angle spectroscopic ellipsometry. Pre and post-etch film thicknesses were measured on a J.A. Woollam M-2000 ellipsometer by measuring the ellipsometric parameters ψ and Δ at ~ 200 wavelengths (from 350-700 nm) and 3 angles (65 °, 70 °, and 75 °) and fitting an appropriate model to the data[12]. The etching conditions are given in table 6.1. Post-etch ellipsometry on the PLK film, however, proved unreliable (high mean squared error in the model fit). Therefore, etch rates of PLK were determined by masking ½ of the sample before etch with a piece of silicon, and measuring the resulting step height after etching using a Tencor P-10 profilometer. Figure 6.2 shows a representative step height measurement on PLK after etch, with a step height of approximately 1300 Å. Figures 6.3 and 6.4 show measured etch rates for all three films as a function of applied DC bias in 10% C_4F_8/Ar and C_2F_6, respectively.

Figure 6.3 shows that processing in C_4F_8/Ar below 150V results in net deposition on all films. Additionally a fluorocarbon layer on the surface was maintained at higher ion bombardment energies, and was thick enough that it needed to be accounted for in the

Table 6.1–Etching Conditions

Pressure	20 mTorr
Gas Flow	40 sccm
Top Power	300 W
Backside He	15-20 torr
DC Bias	varied
Etch Time	3 minutes

ellipsometric fit to obtain accurate post – etch thickness measurements (the presence of a steady state fluorocarbon layer is well known in oxide etching[13]). Optical constants for the fluorocarbon film were obtained by depositing a thick layer of polymer onto a silicon wafer, measuring the thickness using profilometry via a scratch test, and then fitting the measured ellipsometric data to an appropriate model. C_2F_6 has no net deposition regime at these conditions, and the inclusion of a fluorocarbon film layer was unnecessary to obtain accurate post – etch thickness measurements via ellipsometry. In both plasma chemistries the etching rate of the three films follow the same descending order ($ER_{PLK} > ER_{OSG} > ER_{SiO2}$). The two low-k films etch faster than thermal oxide, probably due to their less dense structure. Additionally, the PLK etches faster than OSG due to the porous nature of the film.

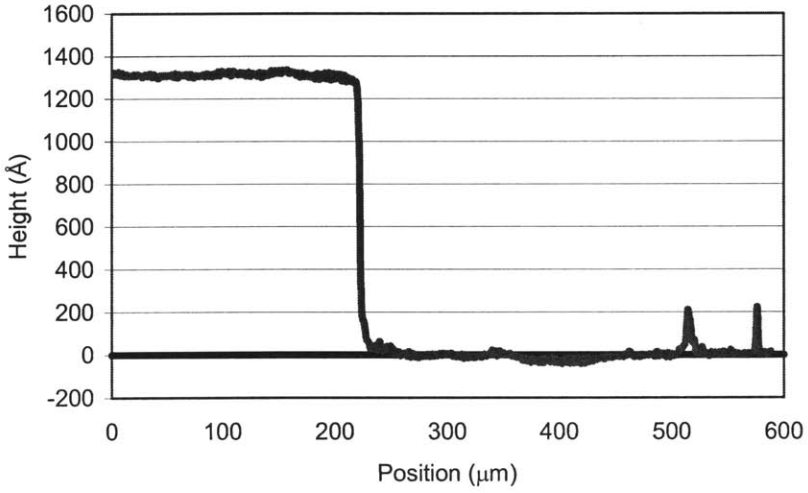

Figure 6.2 - Representative profilometery measurement after etching of a PLK sample. The sample shows ~ 1300 nm etched in 3 minutes, for an etch rate of ~430 nm/min.

In fact, as the solid phase of the PLK is chemically similar to the solid OSG, we would expect the porosity-corrected PLK etch rate to be similar to OSG as well. The porosity-corrected etch rate is given by[7]:

$$ER_{corrected} = ER_{porous}(1-\Pi) \tag{6.1}$$

where Π = porosity (30% for PLK). Figures 6.5 and 6.6 show the porosity corrected etching rate of PLK compared to OSG as a function of DC bias in both 10% C_4F_8/Ar and C_2F_6 plasma chemistries. The C_4F_8/Ar results have been plotted for the net etching regime only (≥ 150 V). These results indicate that, at least to first order, porosity alone can explain the differences in etching rate between OSG and PLK.

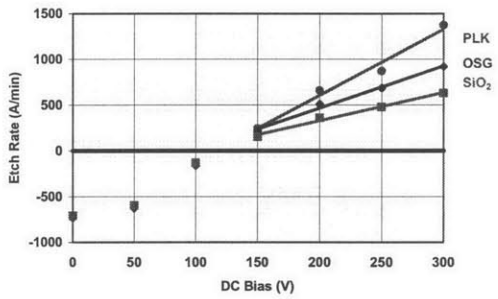

Figure 6.3 - Etch rates in 10% C_4F_8 / 90% Ar plasma. Note that below 150 V, net deposition occurs on all three films.

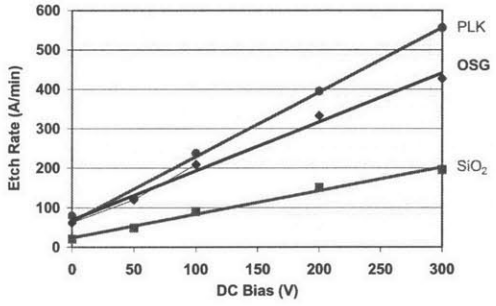

Figure 6.4 - Etch rates in C_2F_6 plasma. Net etching occurs at all DC bias conditions. The etch rate, however, is less than in C_4F_8/Ar.

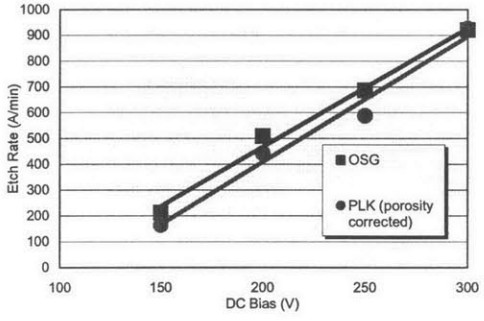

Figure 6.5 - Etch rate comparison of OSG to 30% porosity – corrected PLK in 10% C_4F_8 / Ar plasma (in the net etching regime, 150 V – 300 V). Since the PLK solid phase is similar to the OSG, porosity alone seems to explain the etching rate difference.

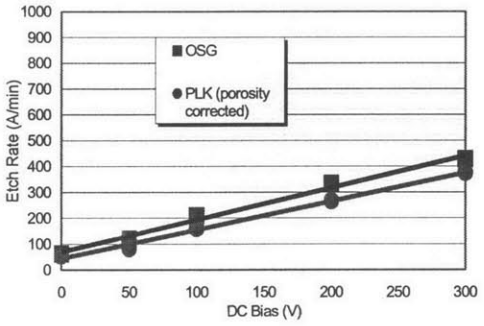

Figure 6.6 - Etch rate comparison of OSG to 30% porosity – corrected PLK in C_2F_6 plasma. Again, Since the PLK solid phase is similar to the OSG, porosity alone seems to explain the etching rate difference.

6.3. Surface Roughness

Surface roughness was measured with a Digital Instruments 3100 atomic force microscope (AFM) in tapping mode. Standard TESP (tapping-mode etched silicon probes) tips were used to image the surfaces. All images were 1 μm x 1 μm, 256 linescans, with 256 pixels/linescan. After data collection, and prior to any analysis, 3rd order polynomials in both the x and y directions were subtracted to correct for sample tilt and scanner nonlinearities. Then, a flatten operation was performed to correct any residual line-to-line offsets. Finally, the root-mean squared (RMS) roughness of each image was calculated. On each sample, 2 images were taken from each of 3 locations (6 images in total per sample), and averaged to obtain the reported RMS value.

6.3.1. Pre –Etch Surface Roughness

Prior to etching, the RMS roughness of the unprocessed films was determined. Figure 6.7 shows AFM images of the unetched films, with corresponding RMS roughness values. All three images have a 20 nm vertical scale, enabling direct visual comparison between them. The thermal oxide is the smoothest, with a RMS roughness below 2 Å over the 1 μm^2 surface. The OSG and PLK films, being spin-ons, are markedly rougher, with RMS values of 1 and 1.2 nm, respectively. The porous nature of the PLK probably accounts for the increase in roughness over the OSG, although it should be noted the radius of curvature of the AFM tip (nominally 10 nm) is too large to actually image the pore structure. Still, prior to etch, all surfaces are relatively smooth and flat.

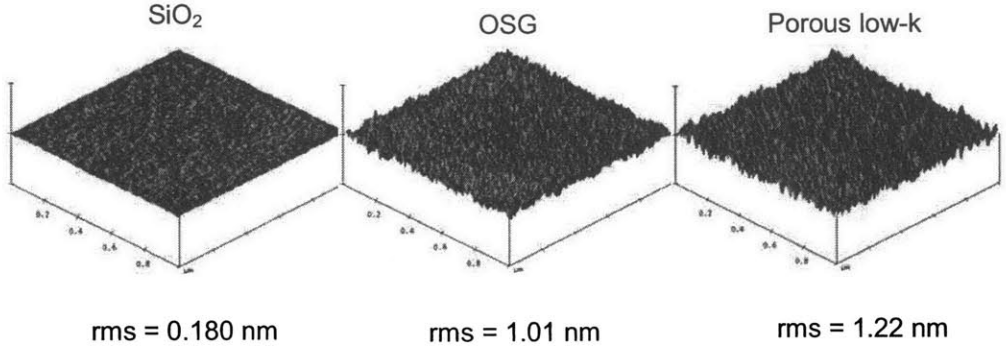

Figure 6.7 - AFM images of unetched dielectric films. All three images are on a 20 nm vertical scale. The thermal oxide is extremely smooth, while the OSG and PLK films are rougher (due to the fact that both are spun – on). The porous nature of the PLK may account for its added roughness compared to the OSG, although it should be noted that the AFM tip cannot access the pore structure.

6.3.2. Surface Roughening in 10% C_4F_8/ Ar Plasma

Surface roughening during etching in a 10% C_4F_8 / Ar plasma chemistry (etch conditions given in table 6.1) as a function of ion bombardment energy was investigated. Figure 6.8 shows AFM images of all three films, as a function of DC bias, after a 3 minute etch. The images are shown in 3 different vertical scales in this figure to better highlight relevant features (20 nm for thermal oxide, 50 nm for OSG, and 100 nm for PLK). Figure 6.9 shows a plot of the rms roughness of the sample surfaces, with the RMS values of the unetched samples included as a reference.

At low ion bombardment energy (100 V), the surface roughness on all three films is identical. As ion bombardment energy is increased, however, the surfaces roughen. A visual examination of the roughened surfaces reveals the formation of a "peaks and valley" morphology. Very interestingly, and initially unexpectedly, the solid films (oxide and OSG) show a roughness maximum at a threshold DC bias level as ion bombardment is increased (although the threshold is different for each film). As the threshold is exceeded, the surfaces of the thermal oxide and OSG become smooth. The jump between roughened and smoothed surfaces is highly evident on the OSG sample, with the surface roughness changing from 7.9 nm to 1.4 nm between 250 and 300 V.

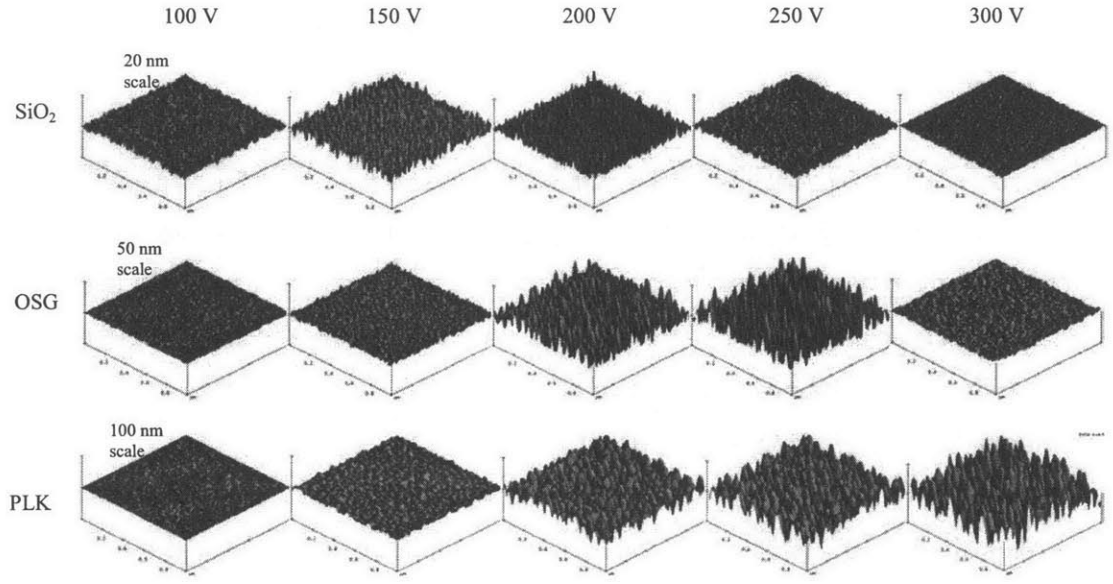

Figure 6.8 – AFM images of thermal oxide, OSG, and PLK after 3 minute etch in 10% C_4F_8/Ar plasma. The three films are shown in different vertical scales as labeled to better highlight the relevant features. Note the "peaks and valleys" shape of the roughness features, especially on the roughened OSG and PLK samples.

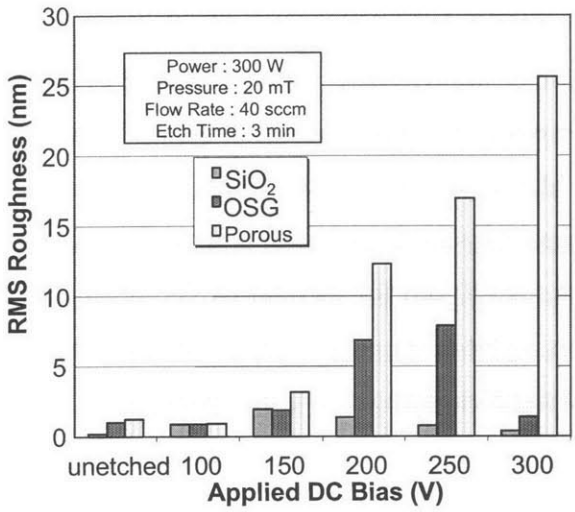

Figure 6.9 – RMS roughness of thermal oxide, OSG, and PLK in 10% C_4F_8/Ar plasma corresponding to the AFM images in figure 6.8. At low ion bombardment (100 V) the roughness on all three films is identical due to uniform polymer deposition. As the ion bombardment energy is raised, the films roughen. The solid films (oxide and OSG) show a threshold behavior, smoothing after the threshold is attained (~175 V for oxide, and 275 V for OSG). The jump between roughened and smoothed surfaces is highly evident on the OSG sample, with the surface roughness changing from 7.9 nm to 1.4 nm between 250 and 300 V. The PLK, on the other hand, increasingly roughens to extreme values.

The PLK, on the other hand, exhibits a different behavior. Rather than showing a roughness maximum in C_4F_8/Ar, the surface roughness increases monotonically with increasing DC bias, becoming severe at high ion bombardment (reaching levels exceeding 25 nm RMS).

6.3.2.1. Polymer – Induced Micromasking as a Roughness Formation Mechanism

The observed features (identical roughness on all films at low ion bombardment, roughness maximums on solid films, and severe roughening of the porous film) can be explained by postulating a *polymer – induced micromasking* mechanism for roughness formation, with a competition between deposition and etching yielding smooth or rough surfaces depending on ion bombardment.

In a well – known paper, Coburn and Winters[14] qualitatively plotted the etching vs. deposition characteristics for fluorocarbon etching of substrates as a function of the fluorine to carbon (F/C) ratio of the chemically active plasma species, and the ion bombardment to the wafer. They found that a transition from fluorocarbon polymer deposition to etching occurs as both the ion bombardment energy and the F/C ratio

increased. The F/C ratio could also be influenced by the addition of additional gases. For example, oxygen addition forms CO or CO_2, consuming carbon containing etching species and thereby increasing the F/C ratio, while addition of hydrogen has the reverse effect through the consumption of fluorine.

We might generate our own qualitative plot by collapsing all factors influencing the etching and deposition on a substrate into a very general "polymerization propensity" of the system. This plot is illustrated in figure 6.10. A sample that is "substrate rich" will undergo net etching, with a decreasing etch rate as the polymerization is increased, until finally etching stops. A sample that is "polymer – rich," however, will undergo increasing polymer deposition as the polymerization propensity of the system is increased.

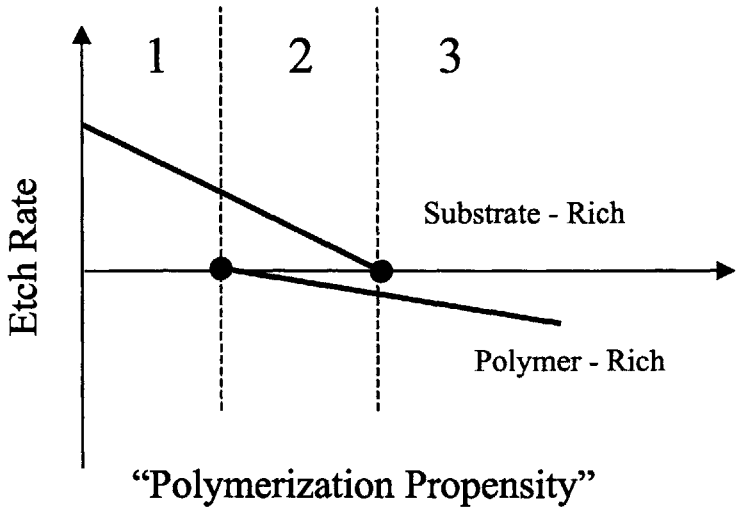

Figure 6.10 – Illustrative plot of etching and deposition on substrate – rich and polymer – rich sample areas as a function of the system polymerization. Substrate – rich areas undergo decreasing etching as polymerization is increased, while polymer – rich areas undergo increasing deposition. This allows for three regimes. Regions 1 and 3 are characterized by smooth uniform substrate etching and polymer deposition, respectively. However, in the transition region (2) we believe that multiple steady states (etching and deposition) can occur simultaneously on different areas of the sample, leading to micromask formation and surface roughening.

Thus, the plot yields three regimes, labeled 1,2, and 3 in the figure. Region 1 is characterized by rapid substrate etching, with no areas of net polymer deposition. In our experiment, this region would correspond to etching under high ion bombardment conditions, yielding smooth samples. In region 3, the polymerization is so high that no etching takes place, leaving only uniform smooth polymer deposition. An examination of our samples etched at 100 V shows this type of behavior. Net deposition yielded film surfaces completely covered with a thick uniform layer of fluorocarbon polymer.

Ellipsometry measurements on oxide and OSG at this condition suggested a polymer thickness of about 45 nm present after the 3 minute etch (see figure 6.3), which should be thick enough to planarize the surface. Additionally, XPS analysis verifies the similarity of the polymer deposited on all three films etched at 100V in 10% C_4F_8/Ar, as shown in figure 6.11.

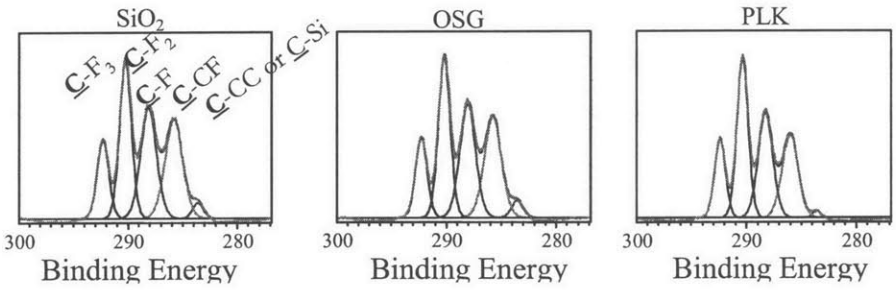

Figure 6.11 - C 1(s) XPS spectra of oxide, OSG, and PLK after etching at 100 V in 10% C_4F_8/Ar plasma. All three spectra are identical, indicating the polymerization on all three films is the same at this condition.

The intermediate region 2 is interesting. In this regime, we believe that certain areas of the substrate that are polymer deficient can undergo net etching, while others that are polymer rich undergo net deposition. In other words, multiple steady states can form on the surface, leading to surface inhomogeneity where polymer islands form in some regions. These polymer islands develop into polymer *micromasks*. Once formed, etch selectivity between the deposited polymer and the underlying substrate leads to the formation of a "peaks and valleys" morphology that roughens the surface. Figure 6.12 shows a schematic of how this process might occur. The transition from region 2 (micromasking) to region 1 (smooth etching) would therefore be very dependent on the local polymer formation on the surface. This may explain why the transition on OSG occurs at a higher ion bombardment energy than on the SiO_2, as the carbon content in the OSG would be expected to enhance the deposition of fluorocarbon polymer.

Micromasking as a roughening mechanism has been observed before. Fukasawa et al[15] attributed the formation of "conelike" defects during quartz etching to micromasking caused by particles generated in the plasma. Kawanishi et al[16] noticed roughening during Cl_2 chemically assisted ion beam etching of GaAs/AlGaAs due to the formation of Al_2O_3 micromasks. Kong et al[17] encountered micromask roughness from

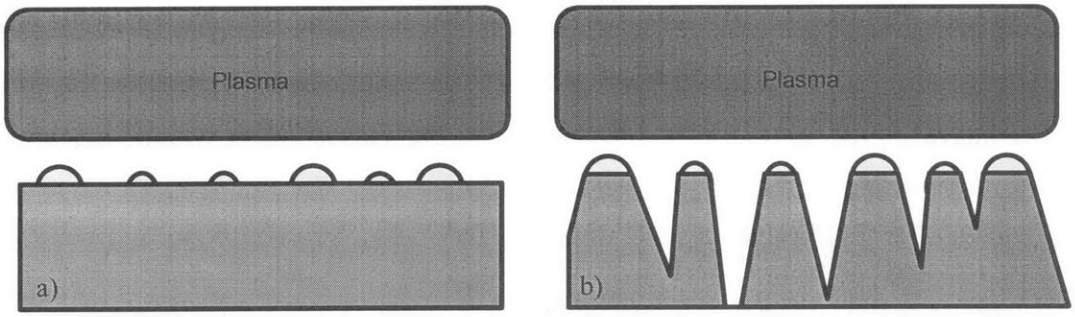

Figure 6.12 - a) Polymer micromasks form. b) Selectivity between deposited polymer and substrate roughens the surface.

sputtering of a stainless steel electrode during C_2F_6/O_2 etching of SiC. Richter[18] discussed the formation of silicon needles due to micromasking in cyclic ASE processes with enhanced deposition. A few odder examples include Perera's[19] investigation into micromasking from bacteria left on wafers occurring in ultrapure water systems, and Schroder's[20] work on micromask roughening when etching Si (100) surfaces in *liquid* KOH due to the formation of H_2 bubbles. Micromask induced roughening has even been exploited as a method to form controllably rough SiC surfaces for enhanced LED performance[21] and to form textured silicon surfaces for cell attachment[22-24].

6.3.2.2. Enhanced Micromask Roughening on Porous Low–k

The porous low-k film shows a different roughening characteristic than the solid oxide and OSG samples. Once micromasking occurs, there is no threshold exhibited. Instead, the surfaces grow increasingly rougher as the ion bombardment energy increases. We believe pore-filling is seeding the formation of polymer micromasks even at higher ion bombardment energies under conditions in which they do not appear on solid films. During the etching process, fluorocarbon can diffuse into the porous matrix of the PLK. (figure 6.13a) As the solid matrix etches around the filled pores, it exposes the polymer (figure 6.13b), which can agglomerate and form micromasks (figure 6.13c). This mechanism can occur even under conditions of high ion bombardment, as the polymer within the pores is shielded from the incoming ion flux. According to our simple model, this has the property of "pushing" the polymer – rich line to the left on the plot, eliminating region 1, explaining why there is no transition from micromasking to smooth etching of the porous substrate (figure 6.14). Additionally, as the etch rate of PLK is very

large at high DC bias, micromask formation can lead to extreme values for surface roughness under conditions of high ion bombardment. This explains why the PLK surface increasingly roughens to large values as the DC bias is raised, with no maximum observed.

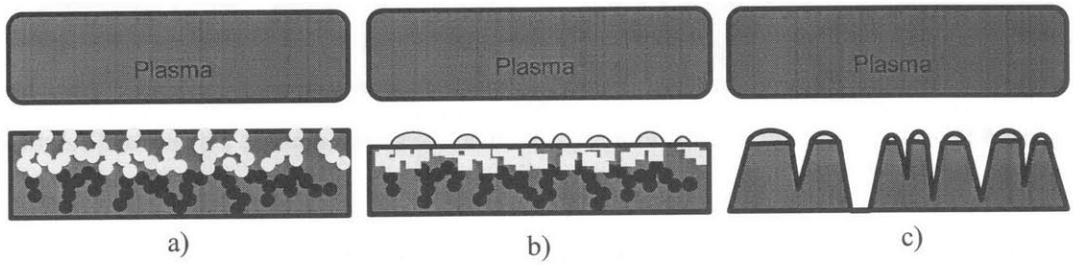

Figure 6.13 - Pore filling seeds micromask formation on PLK. a) Fluorocarbon diffuses into the pore structure. b) Simultaneous etching of the PLK forms polymer micromasks even under conditions of high ion bombardment. c) Selectivity between the deposited polymer and the substrate roughens the surface.

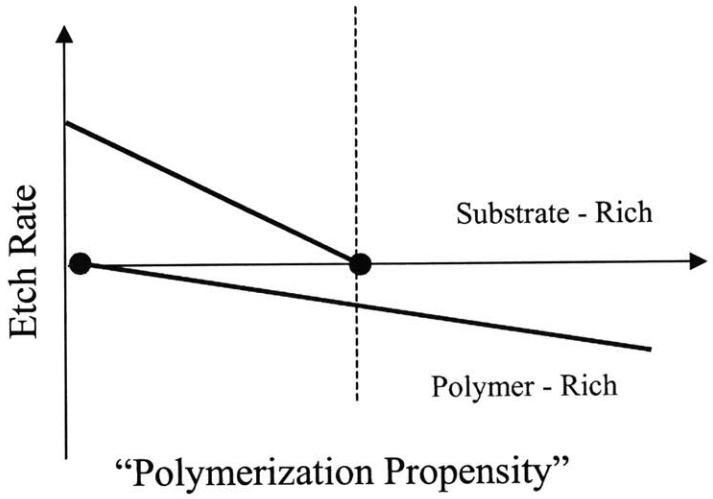

Figure 6.14 – Illustrative plot of etching and deposition on substrate – rich and polymer – rich sample areas as a function of the system polymerization on PLK surface. Fluorocarbon diffusion into the pore structure enhances deposition, effectively "pushing" the polymer – rich line to the left. This effectively eliminates the smooth etching regime and expands the micromasking regime, explaining why no transition is observed.

6.3.3. Surface Roughening in C_2F_6 Plasma

If the above mechanism is correct, it is natural to postulate a surface roughness improvement by controlling polymerization during etch. To this end, we investigated the roughening of our three dielectric films in a pure C_2F_6 plasma chemistry. Etching in C_2F_6 produces much less polymerization, due to the much higher amount of fluorine generated in the discharge in comparison to C_4F_8/Ar[25]. Figure 6.15 shows C 1(s) XPS data of our

three films after etching in C_2F_6 at the conditions outlined in table 6.1, at 0V, 100V, and 300V applied DC bias. While all films have fluorocarbon deposition, the solid films (oxide and OSG) lose fluorocarbon as the ion bombardment is increased. The PLK, however, retains fluorocarbon even at high DC bias, giving further evidence that polymer can diffuse into the pore structure. This polymer forms even though C_2F_6 is a low-polymerizing discharge. Therefore, we have evidence that the pore structure can indeed shield polymer as postulated. Based on the XPS results, if polymer – induced micromasking is the dominant roughness mechanism, we would expect our solid films to remain smooth when etching in C_2F_6 as ion bombardment energy is increased as there is no gross polymer deposition at intermediate ion bombardment (although we may see a slight roughening due to deposition at 0V). However, we would expect the PLK to exhibit the same trend as in 10% C_4F_8/Ar, as there is still polymer shielding within the pore structure.

This is indeed exactly what is observed. Figure 6.16 shows AFM images of all three films etched in C_2F_6 at 0, 50, 100, 200, and 300 V. All images share a 10 nm vertical scale to enable direct comparison between them. Figure 6.17 shows a surface roughness plot of these images. At 0 V, the oxide film is slightly roughened due to the

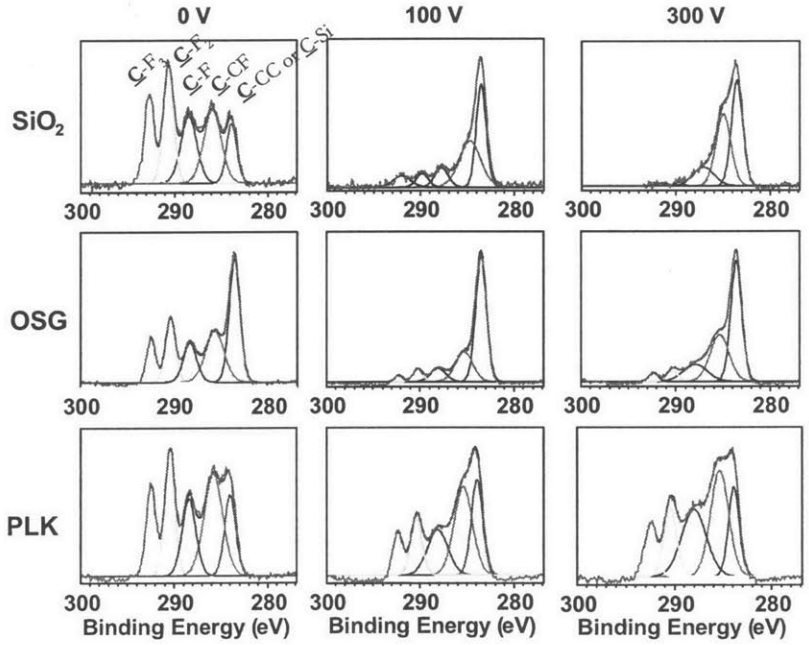

Figure 6.15 - C 1(s) XPS of all three films after etching in C_2F_6 plasma. All surfaces have fluorocarbon deposition at 0V Bias. As ion bombardment increases, the solid films lose fluorocarbon. However, the PLK retains fluorocarbon in the pore structure, even at high ion bombardment energies.

polymer deposition, but the surface roughness levels out to about 4 Å RMS as the DC bias is increased to 300 V. The OSG also remains smooth, with a roughness of ~8 Å RMS, independent of bias voltage. A visual examination of the images shows no evidence of a "peaks and valleys" morphology on the solid films. These results indicate that indeed, no micromasking is occurring on the solid films when etched in C_2F_6.

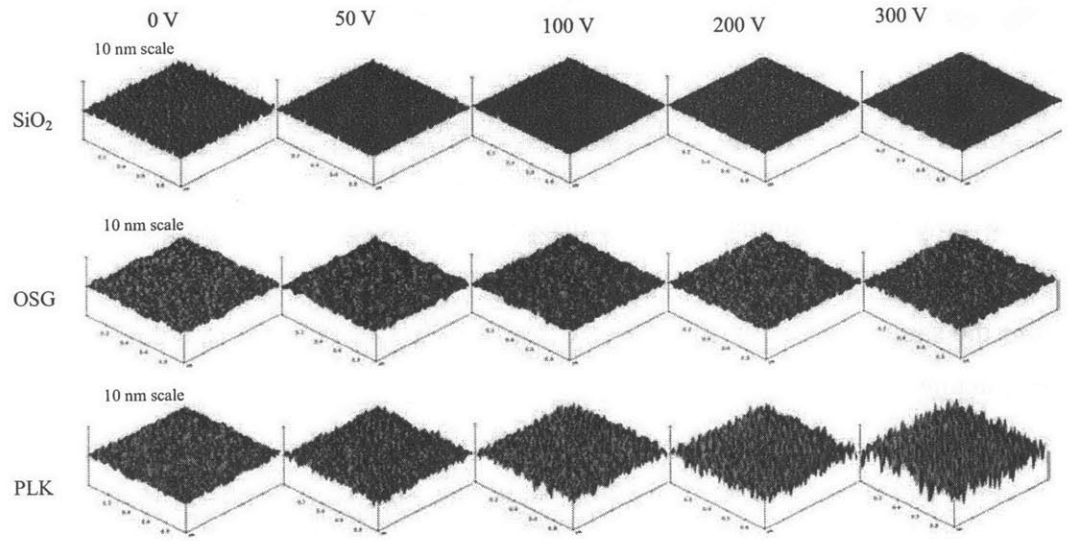

Figure 6.16 - AFM images of all three films after etching in C_2F_6 plasma. All have the same 10 nm vertical scale. The solid films remain smooth at all bias conditions, as gross polymer deposition is prevented due to increasing ion bombardment. The PLK film, however, shows the same trend as seen in 10% C_4F_8 / Ar due to the formation of micromasks caused by polymer diffusion into the pore structure.

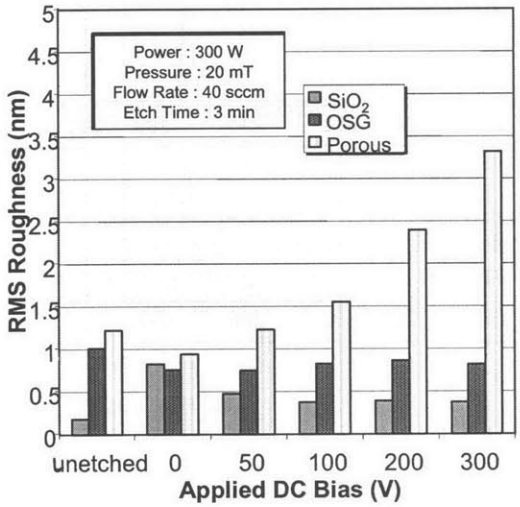

Figure 6.17 - RMS roughness of thermal oxide, OSG, and PLK in C_2F_6 plasma. The solid films do not show roughening at any condition. The porous film, however, shows the same trend as observed previously (increasing roughness with increasing ion bombardment) due to polymer micromask formation. The lower roughness magnitude in C_2F_6 is attributed to the fact that etch rates in C_2F_6 are lower than in C_4F_8 / Ar.

In contrast, the PLK film shows exactly the same trend as seen when etching in 10% C_4F_8/Ar. The surface roughens monotonically as ion bombardment is increased. "Peaks and valleys" are observed visually, indicating micromasking. However, the magnitude of the roughness is less than before, due to the slower etching rate of PLK in C_2F_6 vs. C_4F_8/Ar.

6.3.4. Surface Roughening in 10% C_4F_8 / 5% O_2 / Ar

Further evidence in support of micromask induced roughening was obtained by adding a small amount of O_2 to the highly polymerizing C_4F_8/Ar chemistry used previously. We hypothesized that oxygen might reduce polymerization during etch, preventing the formation of micromasks and leaving smooth surfaces. 5% O_2 was added to the gas feed (replacing an equivalent amount of Ar) giving a 10% C_4F_8 / 5% O_2 / 85% Ar mixture. Aside from the gas addition, all conditions were kept the same (20 mTorr, 40 sccm, 300 W top power, 3 minute etch), and surface roughness was determined.

Figure 6.18 shows AFM images of the solid films (oxide and OSG) after etching in the 10% C_4F_8 / 5% O_2 / 85% Ar plasma, while figure 6.19 shows a plot of the RMS surface roughness corresponding to these images. The surface roughness values without O_2 addition are included on the plot for reference purposes. The addition of O_2 has resulted in a dramatic effect, yielding extremely smooth surfaces. The prevention of gross polymerization during etch resulted in surface roughness improvements on oxide of 75% (from 2 nm to 0.5 nm RMS) at 150V, and improved roughness on OSG by an order of magnitude at 250V (from 8 nm to 0.8 nm RMS). Surface roughness on both films is essentially constant as a function of ion bombardment energy, indicating uniform, homogeneous etching. Therefore, we conclude that oxygen addition is effective in controlling polymerization on the solid dielectric films, eliminating the formation of micromasks and allowing uniform etching to proceed.

Unfortunately, the PLK films again prove difficult. Figure 6.20a shows images of PLK etched in 10% C_4F_8/Ar. These are the same images as in figure 8, but presented in a top-down view. Figure 6.20b shows equivalent PLK samples etched with 5% O_2 addition, also in top down view. Figure 6.21 shows a plot of the RMS surface roughness corresponding to these images. Interestingly, O_2 addition to the feedgas seems to increase

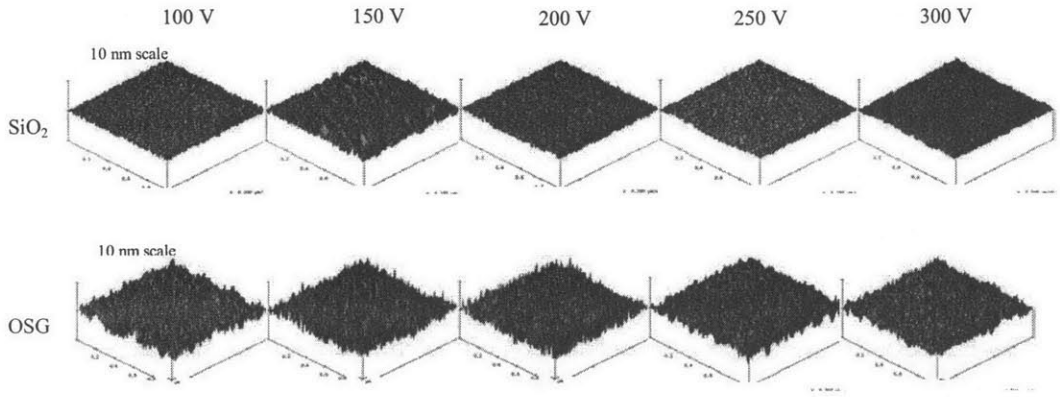

Figure 6.18 - AFM images of oxide and OSG after etching in 10% C_4F_8 / 5% O2 / Ar plasma. All images are on a 10 nm vertical scale. Addition of O_2 has allowed smooth etching to proceed, without the formation of polymer micromasks.

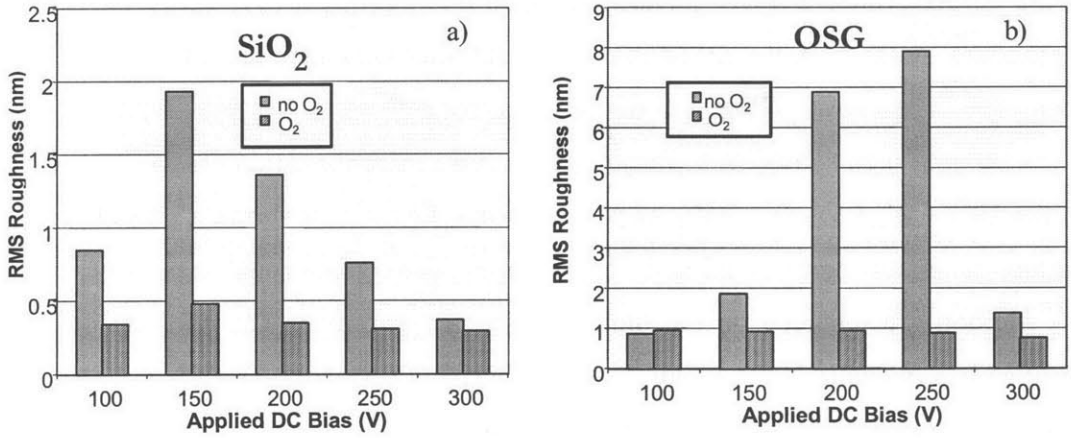

Figure 6.19 - Effect of O_2 addition to C_4F_8/Ar on surface roughness of a) oxide and b) OSG. Addition of O_2 has eliminated polymer micromasking, resulting in smooth surfaces. The effect is particularly dramatic on the OSG sample, with an improvement of 1 order of magnitude at 250 V DC bias.

roughness on PLK at lower bias voltages. The oxygen interferes with the conformal deposition of fluorocarbon polymer seen previously at 100 V bias without O_2, instead leaving a morphology characterized by small agglomerations grouped and separated by deep "crevices." (see figure 6.20b @ 100 V). This crevice morphology persists as ion bombardment energy is increased, eventually leading to uniformly separated peaks at 300V. However, the size and spacing of these peaks and valleys is smaller than when etching without O_2 (compare figures 18a and b @ 300 V). Looking at the plot in figure 6.21, this interference with uniform deposition at low ion bombardment roughens the

surface. As bias is increased, the roughness with and without O_2 looks comparable. At 300 V, however, the surface etched with O_2, at first glance, appears smoother. However, this is a bit deceiving. It seems smoother to the AFM because the narrower spacing between the peaks prevents the AFM tip from reaching deep into the crevices (i.e., the shape of the AFM tip is limiting the roughness measurement on this surface).

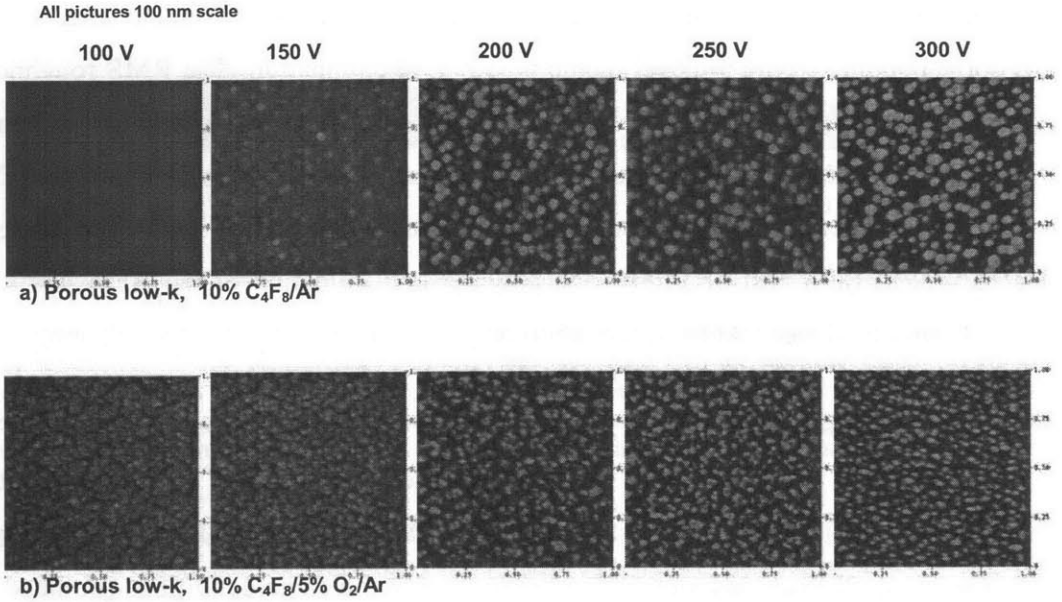

Figure 6.20 - AFM images of PLK films etched in 10% C_4F_8 / Ar a) without oxygen and b) with addition of 5% oxygen. Images are presented in top-down view to highlight morphology change that occurs with addition of O_2. At 100 V, O2 addition interferes with the uniform polymer deposition observed previously, actually making the surface rougher. As DC bias is increased, deep crevices develop, with a narrower spacing than before. The narrow crevices prevent the AFM tip from accessing the topography completely at 300 V, making the surface appear smoother than without O_2.

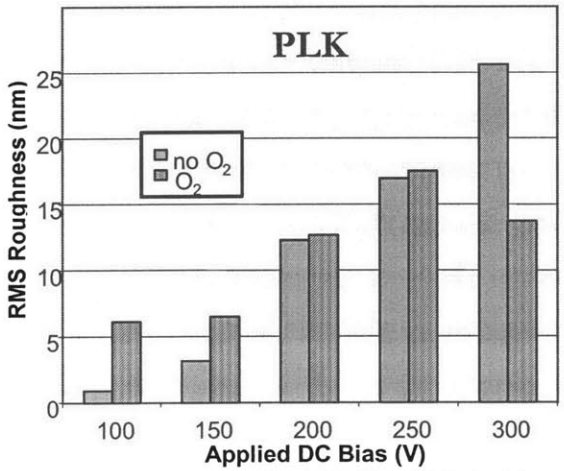

Figure 6.21 - RMS roughness of PLK films etched in 10% C_4F_8 / 5% O_2 / Ar, calculated from the above AFM images.

A higher aspect ratio tip (with a carbon nanotube) was tried as a way to mitigate this problem, but became contaminated with polymer after a few scans. In fact, tip contamination effects were seen on most samples etched in C_4F_8 with or without oxygen, showing up as a "smearing" or dragging on the surface. Standard AFM tips could be restored by repeated scanning on an unetched PLK sample. The image with a contaminated tip was blurry at first, with a sharp resolution improvement after a few scans corresponding to the removal of the polymer contamination. The RMS roughness of the surface and the visual appearance were used to gauge whether the tip was sharp enough for data collection (the blunter the tip, the smoother the measured surface). The nanotube tip, however, could not be restored in the same fashion, and was therefore rendered useless (at a cost of $400). The polymer contamination of the AFM tips was taken as further evidence that polymerization played a role in the surface roughening.

6.3.5. Surface Roughening by Pure Ion Bombardment

Finally, the three dielectric films were etched in Ar alone, to investigate the effects of pure ion bombardment with no fluorocarbon deposition. Figure 6.22 shows AFM images of all three films etched in Ar plasma at the same conditions (outlined in table 1) as the previous samples, at low ion bombardment (100V) and high ion bombardment (300V). Note the small particles on the SiO_2 sample etched at 100V; the effect of these particles was removed before the surface roughness was calculated. Figure 6.23 shows a plot of the RMS roughness of these surfaces. The oxide roughness remains relatively constant with increasing ion bombardment, while the OSG surface roughness decreases. The PLK roughness first drops at low ion bombardment, then roughens slightly as the bias is increased. Still, all three surfaces undergo a degree of smoothing using only ion bombardment, and no etched surfaces are rougher than the unetched samples. There is no evidence of a "peaks and valleys" morphology, and no evidence of micromasking. Thus, we conclude that ion bombardment alone does not give rise to elevated roughness levels, and that indeed, polymerization plays an important role.

6.4. Summary

We have characterized the etching and surface roughening of thermal oxide, OSG, and an MSQ porous low-k film is fluorocarbon plasma chemistries as a function of

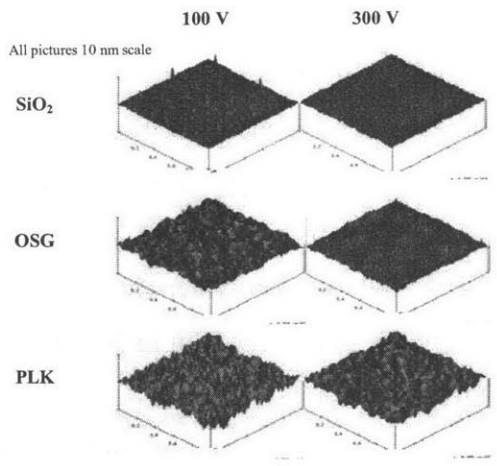

Figure 6.22 - AFM images of films after etching in Ar plasma to show the effect of pure ion bombardment without polymerization. Note the particles present on the oxide sample at 100V - these areas were removed before the roughness calculation was performed.

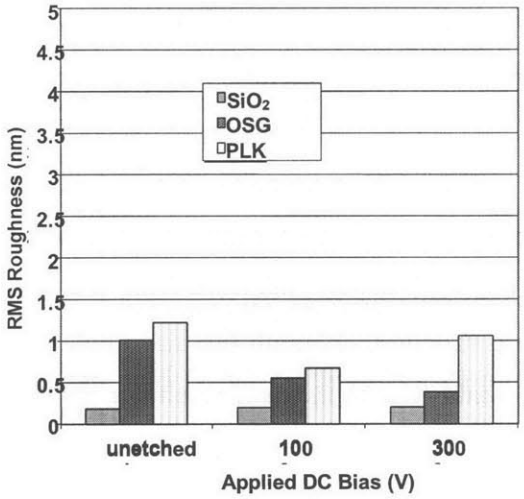

Figure 6.23 - RMS roughness of films after etching in pure Ar plasma. All etched films are smoother than the unetched films. No enhanced roughening is observed, further verifying that polymerization combined with ion bombardment is required to yield rough surfaces.

ion bombardment energy. $ER_{PLK} > ER_{OSG} > ER_{SiO2}$ in both 10% C_4F_8/Ar and C_2F_6. 10% C_4F_8/Ar showed a net deposition regime below 150 V DC bias. Porosity alone can explain the etching rate differences between OSG and PLK.

Surface roughening in fluorocarbon plasmas is controlled by a polymer – induced micromasking mechanism. At low ion bombardment energies, the surfaces of all three films were smooth when etching in 10% C_4F_8/Ar due to the thick uniform polymer deposition. As the ion bombardment energy is raised, however, the surface deposition becomes non-uniform, forming micromasks that cause surface roughness due to the selectivity difference between the fluorocarbon polymer and the underlying film. As the bias is increased, the surface roughness of the solid films goes through a maximum. Finally, when the ion bombardment energy is high enough, the formation of polymer micromasks is prevented, and the surfaces etch smoothly and uniformly.

The porous low-k film shows a different behavior due to the pore structure. The presence of pores seeds micromask formation due to fluorocarbon diffusion into the pore structure and the etching of the film. Once present, the polymer is difficult to remove even at high ion bombardment energy due to shielding of the polymer in the pore

structure. Therefore, as ion bombardment energy is increased, the surface roughness of the PLK increases monotonically, severely roughening at high DC bias.

Further evidence for the polymer-controlled roughening mechanism was obtained by etching in lower-polymerizing etch chemistries. Etching in C_2F_6 allowed smoother surfaces on all three films. No micromasking was seen on either oxide or OSG. As expected, however, micromasking was seen on PLK due to the polymer shielding in the pore structure, although the magnitude of the roughness was lower than in 10% C_4F_8/Ar (probably due to the lower etch rate and lower polymerization in C_2F_6).

Even more evidence was obtained by adding 5% O_2 to our 10% C_4F_8/Ar chemistry. Addition of oxygen completely eliminated micromask formation on both oxide and OSG, allowing fast, uniform etching. The surface roughness improvements approached an order of magnitude on OSG. On PLK however, O_2 addition did not help. In fact, adding O_2 interfered with the uniform polymer deposition at 100V seen previously without oxygen, leaving a surface morphology characterized by small agglomerations separated by deep crevices. As the ion bombardment energy was increased, the crevices etched deeper, yielding rough surfaces.

Finally, the films were etched in Ar alone to examine roughening without polymerization. As expected, all surfaces remained smooth in the absence of fluorocarbon, indicating that polymerization can indeed play an important role in surface roughening.

6.5. References

1 International Technology Roadmap for Semiconductors, Semiconductor Industry Association, San Jose, CA (2000).

2 L. Peters, Semiconductor International **23,** 108 (2000).

3 A. M. Padovani, L. Rhodes, L. Riester, G. Lohman, B. Tsuie, J. Conner, S. A. B. Allen, and P. A. Kohl, Electrochemical and Solid State Letters **4,** F25-F28 (2001).

4 C. M. Flannery, T. Wittkowski, K. Jung, B. Hillebrands, and M. R. Baklanov, Applied Physics Letters **80,** 4594-4596 (2002).

5 S. A. Vitale and H. H. Sawin, Journal of Vacuum Science & Technology A **20,** 651-660 (2002).

[6] T. E. F. M. Standaert, P. J. Matsuo, S. D. Allen, G. S. Oehrlein, and T. J. Dalton, Journal of Vacuum Science & Technology A **17,** 741-748 (1999).

[7] T. E. F. M. Standaert, E. A. Joseph, G. S. Oehrlein, A. Jain, W. N. Gill, P. C. Wayner, and J. L. Plawsky, Journal of Vacuum Science & Technology A **18,** 2742-2748 (2000).

[8] A. Sankaran and M. J. Kushner, Applied Physics Letters **82,** 1824-1826 (2003).

[9] J. N. Sun, Y. F. Hu, W. E. Frieze, W. Chen, and D. W. Gidley, Journal of the Electrochemical Society **150,** F97-F101 (2003).

[10] B. N. Chapman, *Glow Discharge Processes : Sputtering and Plasma Etching* (Wiley, New York, 1980).

[11] D. R. Wright, D. C. Hartman, U. C. Sridharan, M. Kent, T. Jasinski, and S. Kang, Journal of Vacuum Science & Technology A **10,** 1065-1070 (1992).

[12] G. H. Buabbud, N. M. Bashara, and J. A. Woollam, Thin Solid Films **138,** 27-41 (1986).

[13] G. S. Oehrlein, Y. Zhang, D. Vender, and M. Haverlag, Journal of Vacuum Science & Technology A **12,** 323-332 (1994).

[14] J. W. Coburn and H. F. Winters, Journal of Vacuum Science & Technology **16,** 391-403 (1979).

[15] T. Fukasawa, T. Hayashi, and Y. Horiike, Japanese Journal of Applied Physics Part 1 **42,** 6691-6697 (2003).

[16] H. Kawanishi, T. Morioka, A. Shimonaka, M. Taneya, and A. Suzuki, Japanese Journal of Applied Physics Part 2-Letters **35,** L880-L882 (1996).

[17] S. M. Kong, H. J. Choi, B. T. Lee, S. Y. Han, and J. L. Lee, Journal of Electronic Materials **31,** 209-213 (2002).

[18] K. Richter, M. Orfert, and H. Schuhrer, Surface & Coatings Technology **142,** 797-802 (2001).

[19] A. H. Perera and M. J. Satterfield, Ieee Transactions on Semiconductor Manufacturing **9,** 577-580 (1996).

[20] H. Schroder, E. Obermeier, and A. Steckenborn, Journal of Micromechanics and Microengineering **9,** 139-145 (1999).

[21] G. Franz, Materials Science in Semiconductor Processing **5,** 525-527 (2002).

[22] S. Turner, L. Kam, M. Isaacson, H. G. Craighead, W. Shain, and J. Turner, Journal of Vacuum Science & Technology B **15,** 2848-2854 (1997).

[23] H. G. Craighead, S. W. Turner, R. C. Davis, C. James, A. M. Perez, P. M. St. John, M. S. Isaacson, L. Kam, W. Shain, J. N. Turner, and G. Banker, Biomedical Microdevices **1,** 49 (1998).

[24] H. G. Craighead, C. D. James, and A. M. P. Turner, Current Opinion in Solid State & Materials Science **5,** 177-184 (2001).

[25] O. Kwon, Ph.D Thesis, Massachusetts Institute of Technology, 2004.

Chapter 7 – New Plasma Beam Apparatus for the Investigation of Striation Formation, with Application to Polysilicon Roughening in HBr - The Role of Surface Topography

7.0. Abstract and Introduction

Up to this point, I have described numerous examples of plasma induced sidewall and surface roughening on many industrially relevant systems, with discussions of mechanisms and suggested improvement strategies. However, a fundamental study of sidewall striation formation is still elusive, mainly because of the experimental difficulties associated with attempting such a study in a conventional plasma etcher. Our group has previously investigated etching kinetics and feature profile evolution[1-6], and determined how differences in angular etching yield, ion bombardment, and plasma chemistry can explain many commonly observed etching artifacts. We believe that sidewall striation formation is governed by the same physics; therefore, a fundamental study of sidewall roughness and striation development requires an apparatus with independent control of ion impingement angle to the sample, ion bombardment energy, and the plasma chemistry,

To this end, we have constructed a realistic plasma beam chamber that allows the required independent control. The source has a stage for mounting samples, quartz crystal microbalance (QCM) for etch rate measurements, ion energy analyzer to characterize the ion energy distribution function of the beam, and an ion flux analyzer to spatially map the beam uniformity. The sample stage and QCM are mounted on angularly adjustable vacuum stages to allow the variation of the ion impingement angle. To simulate a sidewall, the sample is rotated to a near – glancing angle The ion bombardment energy can be selected by DC biasing the plasma, which is isolated from the source chamber walls by a quartz or alumina ceramic liner.

After fully characterizing the ion energy and beam uniformity in the new source, it was used to conduct our first preliminary investigation into roughening of polysilicon in an HBr plasma beam. The effects of initial topography were examined by comparing polysilicon (with a rough grain structure) to similarly processed single crystal silicon samples which are smooth and flat. Additionally, the ion bombardment energy,

impingement angle, and ion fluence were varied, and the effects on the surface roughness observed.

7.1. Beam Systems

Beam systems have been widely used in the literature in order to decouple reactions occurring at the surface from those in the gas phase. Many of these systems employ "independent" beams, with a separate beam for each ion and neutral species. Butterbaugh et al[7] and Gray et al[8] used F, CF_2, and Ar^+ beams to elucidate the role of radical species and ion bombardment in the fluorocarbon etching of SiO_2. Vugts et al employed a system with separate radical, ion, electron, and photon beams to study spontaneous etching of Si in XeF_2[9], and as a function of ion/neutral flux and ion energy[10]. Chang et al used beams of Cl radicals, and Cl^+ and Ar^+ ions to measure Si etching yield as a function of ion bombardment and ion incident angle[1,11-13]. Kota et al measured etching yields of Si and $WSi_{1.66}$ in chlorine/oxygen neutral beams and Ar/oxygen ion beams[14]. Greer et al determined photoresist etching yields with independent ion and neutral beams[15,16], and measured abstraction probabilities of fluorine and deuterium radicals from surfaces[17]. Toyoda et al used mass – selected single species CF_x^+ beams to study Si and SiO_2 etching[18].

As attractive as these systems are, most real plasmas contain many more species than could ever be represented by a collection of separate beams. Therefore, more "realistic" plasma beams systems have been employed in which ion and neutral beams are directly sampled from the plasma of choice. Vitale et al used beams extracted from an inductively coupled plasma into a small side sample chamber to measure etching yields of benzocyclobutene (BCB) films in F_2/O_2 chemistry[19], and Si etching yields in halogen chemistries[20]. Kwon used a similar system to measure SiO_2 etching yields in fluorocarbon chemistries[21]. Finally, Jin et al constructed a realistic inductively coupled plasma beam source in which the plasma was struck in a small side chamber, and extracted into the main sample chamber (the opposite of Vitale's method), and used it to measure etching yields of Si in Cl_2 and HBr chemistries[22].

7.2. New Inductively Coupled Beam Apparatus

A new apparatus, modeled after that used by Jin, was constructed in order to investigate roughness formation. This second generation chamber has a number of improvements over Jin's version. First, Jin's plasma beam source was somewhat minuscule (6" OD tube). While designed to be inductively coupled, the coupling actually was mainly capacitive due to the small window to deposit the power[23]. The new source, built into a 10" OD tube, is indeed inductively coupled with the associated higher density. Secondly, Jin's source permitted only one item at a time to be placed within the main sample chamber (be it a sample holder, QCM, ion energy analyzer, or ion flux analyzer). The new source has all four items present at once, eliminating the need to bring the chamber up to atmosphere to change them out.

Figure 7.1 shows an external schematic of the new inductively coupled plasma beam source. The apparatus possesses four instruments for data collection : 1) a water cooled sample holder that can accept 1" x 1" chips of any desired film, 2) a water cooled quartz crystal microbalance (QCM) for sensitive etching rate measurements, 3) an ion energy analyzer (IEA) to determine the energy distribution of the extracted plasma beam ions, and 4) an ion flux analyzer (IFA) to measure the beam ion flux. All four instruments are mounted on either Z – axis stages or linear motion feedthroughs to allow placement in the beam, and withdrawal when not in use. This feature enables use of any instrument

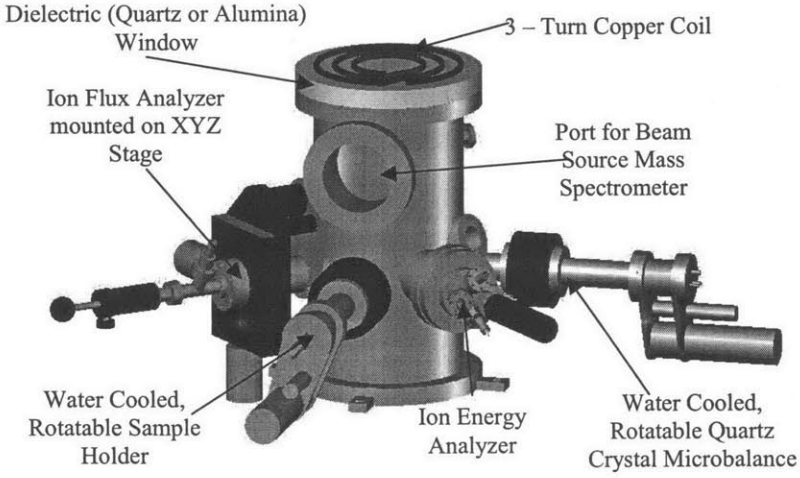

Figure 7.1 – External schematic of plasma beam apparatus. All four instruments (sample holder, QCM, ion energy analyzer, and ion flux analyzer) are mounted on either Z axis stages or linear motion feedthroughs to allow placement into the beam, and withdrawal when not in use. Additionally, the ion flux analyzer can be manipulated in XYZ to allow the collection of spatially resolved beam current maps. Finally, the sample holder and QCM are mounted on 360° rotatable axis stages to enable angularly resolved data collection.

without requiring the chamber to be opened. The IEA is mounted on an XY stage to enable collection of spatially resolved beam current maps. To allow angularly resolved data collection, the sample holder and QCM are placed on 360° rotatable stages.

Figure 7.2 shows an internal schematic of the plasma beam apparatus. It consists of an upper and lower chamber, both built into a 10" OD stainless steel vessel. The upper chamber is lined with a quartz or ceramic liner to isolate the plasma from the chamber wall. An inductively coupled plasma is struck in the upper chamber by RF powering a 3 – turn copper coil at 13.56 MHz (RF Plasma Products RF-10) through a matching network (RF Plasma Products AM-10). An anisotropic flux of ions is extracted through a grounded grid at the bottom of the upper chamber (Buckbee Mears # 514, 0.006" diameter holes, 0.005" thick, 27% open area). The ion bombardment energy is controlled

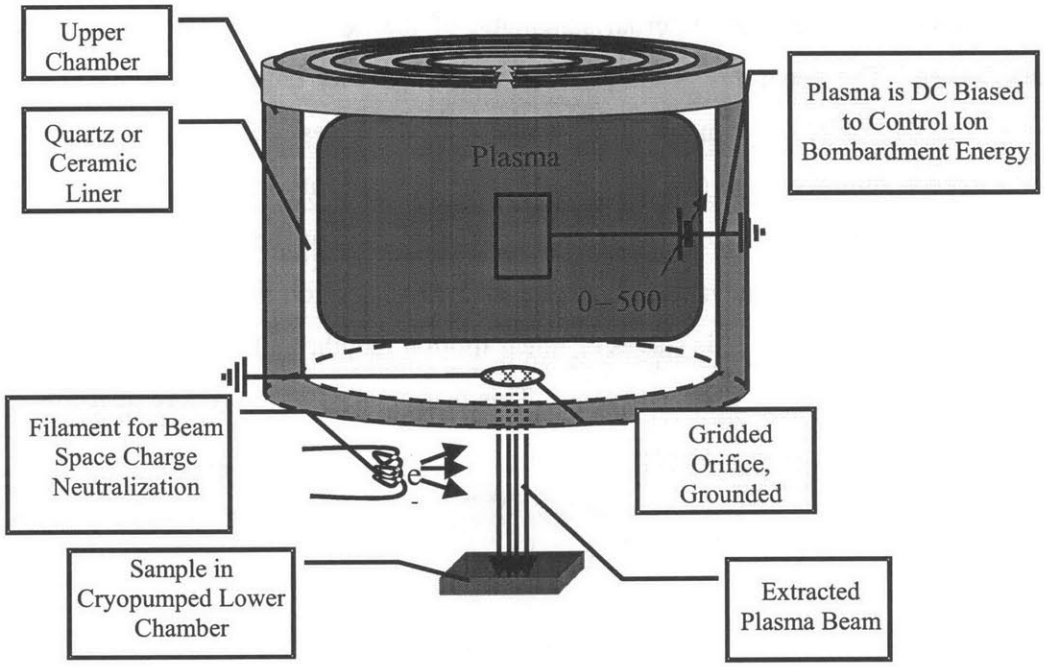

Figure 7.2 – Internal schematic of plasma beam apparatus. The upper chamber is lined with a quartz or ceramic liner, isolating the plasma from the chamber wall. The inductively coupled plasma is struck by powering a 3-turn copper coil at 13.56 Mhz through a matching network. The ion bombardment energy is controlled by placing a metal shim into the plasma, and DC biasing it. Since the plasma is isolated by the insulating liner, it will take up a potential 15 – 25 eV above the DC bias applied to the shim. An anisotropic flux of ions (with an isotropic neutral flux) is extracted via a grounded grid at the bottom of the upper chamber into the cryopumped lower chamber. Low energy electrons emitted by a filament neutralize the beam space charge to lessen beam spreading.

in a similar manner to that used by Jin[23] and Chang[24]. A stainless steel wire or shim placed in the plasma is connected to a DC power supply through a BNC connector. An RF choke is placed inline as a low-pass filter to block the RF signal to the DC supply. The wire or shim can be biased from 0 – 500 V by the supply, and the plasma (isolated from the chamber wall by the insulating liner) will take up a potential `~ 15 – 25 V above the biasing potential. Thus, the plasma potential above ground can be controlled. The ions are extracted anisotropically via the grounded extraction grid into the lower chamber. Obviously, an isotropic flux of neutrals is extracted as well. The source typically operates at a pressure of ~14 mT (for Ar) as measured by a capacitance manometer, with a gas flow rate of 2 sccm.

The lower chamber is pumped via a 4000 L/s cryopump (CTI Cryonics Cryotorr 8), and is maintained at a base pressure of ~$5x10^{-5}$ torr during operation. The mean free path at this pressure (for Ar at 20° C) is ~120 cm, much larger than the chamber characteristic dimension, so the beam can be considered collisionless. A tungsten filament can emit low energy electrons to neutralize the beam space charge and minimize any subsequent beam spreading (it also has the ability to neutralize charging that can develop on insulating samples).

7.2.1. Ion Energy Measurement

The gridded ion energy analyzer used here was described in detail in chapter 2. Briefly, it consists of 2 grids and a collector contained within a stainless steel can. The can has a ¼" orifice through which the ion flux is sampled. The first grid is biased slightly negative (-15 eV) to repel electrons. The voltage to the second grid is swept from 0 to + 500 V. This creates a potential "hill." Only ions with energy higher than the grid potential will make it through the second grid to be measured at the collector via a picoammeter (Keithly 480).

For a representative HBr plasma (225 W, 2 sccm, 12 mT source pressure), ion currents were measured at various plasma DC biasing, and differentiated to yield the ion energy distribution functions (IEDF). Figure 7.3 shows this result. It is clear that the ion energy control provided by the chamber setup is adequate, with the ions taking up a potential 15 – 25 eV above the plasma bias.

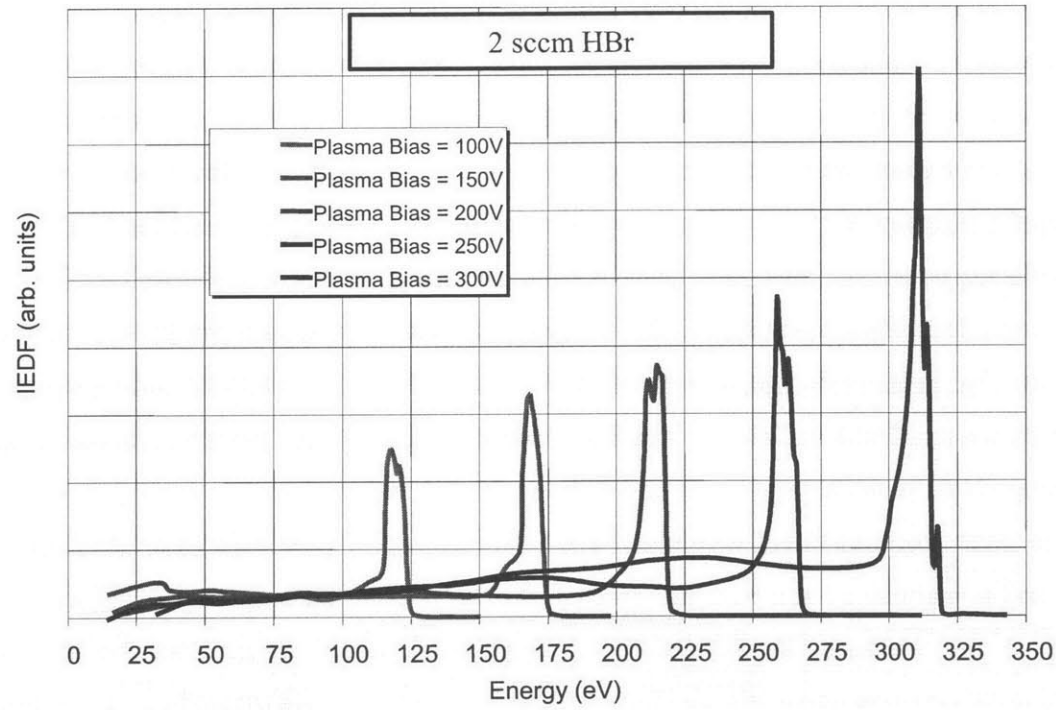

Figure 7.3 – Ion energy distribution functions (IEDF) for a representative HBr plasma beam (225 W, 2 sccm, 12 mT source pressure) at various plasma DC biasing. The data shows good ion energy control.

7.2.2. Neutral to Ion Flux Ratio Calculation

For ion enhanced etching (for example, Cl etching of polysilicon), the etch yield depends on the neutral to ion flux ratio (N/I^+) of the incoming beam. At low N/I^+, the surface reactions are limited by the neutral flux. At high N/I^+, however, the surface is saturated with neutrals (the so – called "saturation" regime). The reactions are limited by the ion flux, and the etching yield is relatively independent of N/I^+ [8,12,20]. While the effect of the N/I^+ ratio on surface roughness evolution is unknown, we would still like to calculate it for the beam apparatus.

The neutral flux can be estimated by the sum of the line of sight beam flux from the plasma Γ_{los}, and the background flux Γ_{bg}. These fluxes are given by[20]:

$$\Gamma = \frac{P}{\sqrt{2\pi m_{eff} k T_g}} \tag{7.1}$$

where m_{eff} = effective mass of neutrals (6.63×10^{-26} kg for Ar), k = boltzmann's constant (1.38×10^{-23} J/K), P = source pressure for Γ_{los} (14 mT) or chamber pressure for Γ_{bg} (5×10^{-2} mT), and T_g = gas temperature in the source for Γ_{los} (600 K) or the chamber for Γ_{bg} (300

K). Γ_{los} must further be corrected for the neutral beam spreading between the orifice and the sample[25], and for the grid open area:

$$\Gamma_{los} = \alpha \left(\frac{R^2}{R^2 + L^2} \right) \Gamma_{plasma} \tag{7.2}$$

where Γ_{plasma} = neutral flux calculated by equation 7.1, α = grid open area (27 %), R = radius of the orifice (0.355 in), and L = distance from the orifice to the sample plane (2.74 in). For the values given above for Ar at 300 W, $\Gamma_{plasma} = 3.2 \times 10^{18}$ $cm^{-2}s^{-1}$, $\Gamma_{los} = 1.4 \times 10^{16}$ $cm^{-2}s^{-1}$, and $\Gamma_{bg} = 1.6 \times 10^{16}$ $cm^{-2}s^{-1}$, so the total neutral flux $\Gamma_{total} = 3.0 \times 10^{16}$ $cm^{-2}s^{-1}$. The ion flux is directly measured with the ion flux analyzer. For Ar at 300 W, at the center of the beam the ion flux is ~ 50 $\mu A \cdot cm^{-2}$, equivalent to 3.1×10^{14} $cm^{-2}s^{-1}$. Therefore, the neutral to ion flux ratio under these conditions is approximately 97, which is adequate, if not spectacular. It should be noted that the error in the neutral flux calculation might be as high as a factor of 2, although the ion measurement is believed accurate within 20 %. Further improvement in the flux ratio can be obtained by operating the source at a lower power to reduce the ion current, at the cost of reducing the etching rate. A modification to the chamber that would move the orifice closer to the sample plane, reducing the effect of the neutral beam spreading, is also being considered (the rather large 2.74" spacing was necessitated by the spatial considerations of the chamber, but the resultant beam spreading reduces Γ_{los} by over 98% as a result).

7.2.3. Measurement and Modeling of Ion Flux

The ion flux analyzer (IFA) was described in detail in chapter 2. Briefly, ions traverse through a small (1 mm) orifice, to be measured by a collector connected to a picoammeter. The picoammeter (and thus, the collector) is floated at a slightly negative potential to repel electrons. The IFA is mounted on a linear motion and an XY stage, allowing the determination of spatially resolved beam current maps. This enables the uniformity of the ion current to be checked.

Figure 7.4 shows a contour plot of the spatially resolved beam current for Ar at 300 W and 2 sccm. The contours are labeled in units of $\mu A/cm^2$, with each contour corresponding to a 10% decrease in the maximum flux measured at the beam center (51 $\mu A/cm^2$). The beam uniformity is adequate for our purposes, with the contour line

corresponding to 80 % of the maximum flux (41.15 μA/cm^2 contour) describing an area approximately ½" in diameter. However, the degree of non – uniformity across the measured beam was, at first, rather surprising, as I expected a more anisotropic ion beam. Even though the uniformity is adequate, it is instructive to try to ascertain the cause of the observed flux variation.

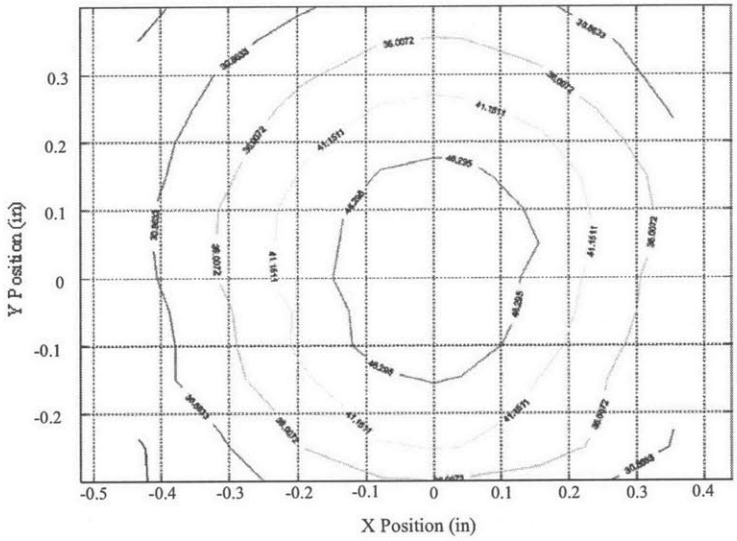

Figure 7.4 – Spatially resolved beam ion current for an Ar discharge at 300 W and 2 sccm. The contours are marked in increments of 10% of the maximum flux (ie, 90%, 80%, etc). The contour of 80% max ion flux (41.15 μA/cm2) describes an area approximately ½" in diameter, more than large enough to perform roughness measurements. Thus, we conclude the beam uniformity is adequate for our purposes.

An extremely simple model to describe what might be going on can be developed by assuming that the ion flux given off at any point on the orifice grid, rather than being perfectly anisotropic, instead has a gaussian angular distribution with standard deviation σ, i.e. :

$$I(d) \propto \exp\left(\frac{\theta^2}{2\sigma^2}\right) \tag{7.3}$$

where d represents the XY position on the sample. The flux to any position on the sample would thus contain a contribution from all points on the orifice, depending on the angular view factor. Figure 7.5 shows a schematic of the system in one dimension. The two characteristic lengths are the orifice grid diameter R and the grid/sample plane spacing L. At any position d along the sample plane, ion flux is received over a range of angles. Thus, to determine the total flux received at any point on the sample, we only need to

determine the angular range, and integrate the gaussian angular distribution over that range.

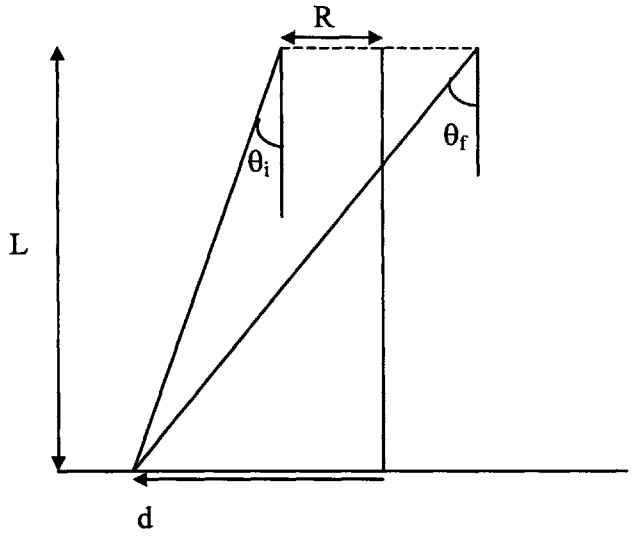

Figure 7.5 – Diagram of the flux received a any point x on the sample plane. Point x receives flux from all angles between θ_i and θ_f. By inspection, $\theta_i = \tan^{-1}[(d-R)/L]$, and $\theta_i = \tan^{-1}[(d+R)/L]$. Thus, to determine the total flux incident at position x, the flux angular distribution must simply be integrated from θ_i to θ_f.

By inspection of figure 7.5, $\theta_i = \tan^{-1}[(d-R)/L]$, and $\theta_i = \tan^{-1}[(d+R)/L]$. Additionally, since the flux is symmetric about the centerline and we will normalize the results, we can incorporate 2 dimensions by replacing d by $\sqrt{X^2+Y^2}$, where X and Y are the coordinates where the beam flux is measured. Therefore, by integrating equation 7.3 from θ_i to θ_f, the flux to any position on the sample is proportional to:

$$I(X,Y) \propto \left[\operatorname{erf}\left(\frac{\tan^{-1}\left(\frac{\sqrt{X^2+Y^2}+R}{L} \right)}{\sqrt{2}\sigma} \right) - \operatorname{erf}\left(\frac{\tan^{-1}\left(\frac{\sqrt{X^2+Y^2}-R}{L} \right)}{\sqrt{2}\sigma} \right) \right] \qquad (7.4)$$

This equation gives the correct functional form, reducing to a uniform flux for $\sqrt{X^2+Y^2} < R$ and zero flux for $\sqrt{X^2+Y^2} > R$, as either $L \rightarrow 0$ (i.e. very close to the orifice) or $\sigma \rightarrow 0$ (i.e. a highly directional ion beam).

The data in figure 7.4 was normalized by dividing each measurement by the maximum measured flux to obtain a flux map ranging from 0 to 1. The model in equation 7.4 (also normalized) was then fit to the measured data by least squares, with a single adjustable parameter (the angular dispersion σ). Figures 7.6 and 7.7 shows the result.

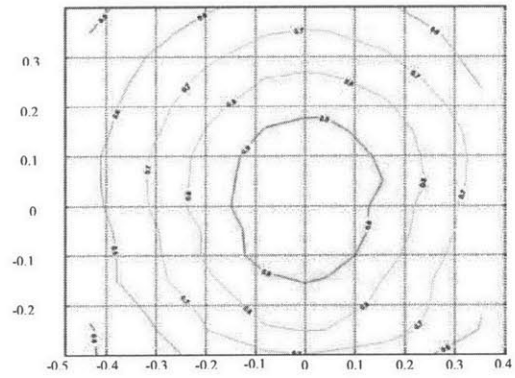

Figure 7.6 – Measured ion flux (the same data as shown in figure 7.4), normalized to range from 0 to 1.

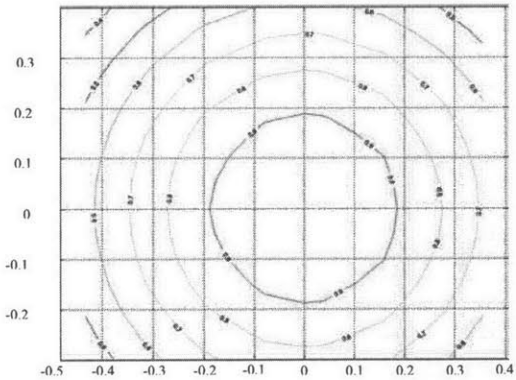

Figure 7.7 – Model results with σ = 7.2 ° as determined by a least squares fit to the data in figure 7.6. The extremely simple model gives a good representation of the measured data with only a single adjustable parameter.

By least squares fitting, σ = 7.2 °. This is in reasonable agreement with angular dispersions commonly used in profile simulators, which tend to be on the order of 4 – 5 degrees[23,26]. Thus, the observed ion flux dispersion can be explained via a very simple model containing only a single adjustable parameter, and as it is uniform within 20% over a ½" area as seen in figure 7.6, is adequate for our purposes.

Figure 7.8 shows the ion flux measured at the chamber center for both Ar and HBr plasma beams at 300 W source power, as a function of the plasma DC bias (and hence, the ion bombardment energy). The Ar ion flux is larger than the HBr ion flux as the ionization efficiency for Ar is higher. Both curves increase as the ion bombardment energy increases. This is because the ion extraction is dependent on the potential difference between the biased plasma and the grounded extraction grid. At higher potential, the extracted ions have a higher velocity, increasing the measured flux.

These curves can be used to normalize the total fluence received by a sample. By varying the etching time of samples etched at different ion bombardment energies, we can assure that each sample receives the same total ion fluence, enabling a more direct comparison between them.

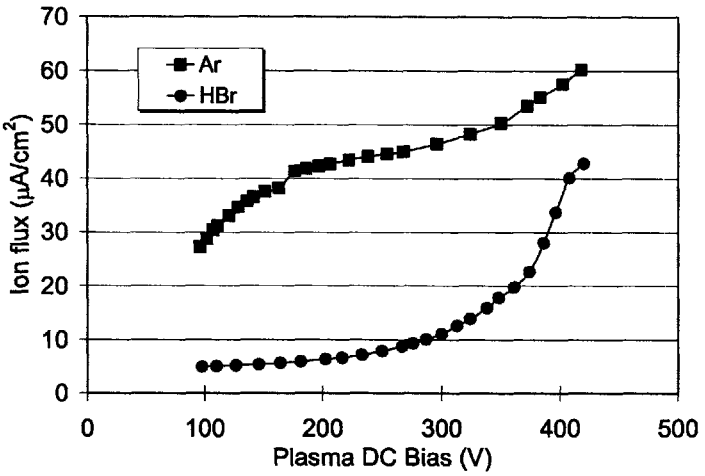

Figure 7.8 – Ion flux measured at the chamber center for both Ar and HBr plasma beams at 300 W source power.

7.3. Quantitative Beam Investigation of Polysilicon Roughening in HBr

Once the beam source was characterized, a set of "proof of concept" experiments was run. These investigations serve two purposes: 1) they verify that indeed, blanket samples at glancing angles can serve as models for sidewalls through the formation and observation of striations, and 2) they provide some preliminary insight into one potential mechanism for striation formation during etching.

7.3.1. Feature Profile Evolution

Previous work in our laboratory has focused on feature profile evolution based on measurement of angular etching yields in a variety of plasma chemistries, with incorporation into a profile simulator (the etch yield is a measure of how much "stuff" comes off a surface for every ion that strikes). In particular, Jin focused his work on the etching of polysilicon features in HBr and Cl_2 plasmas[23]. Figure 7.9 shows measurements by Jin of the etching yield as a function of ion impingement angle for polysilicon in both Cl_2 and HBr plasmas. The Cl_2 curve shows a shape characteristic of ion – induced chemical etching. It is flat up to an angle of ~ 45 °, and then drops off toward zero at 90 °. The HBr curve, on the other hand, drop off slowly but steadily to about 60 ° before dropping. In his simulator, Jin interprets these curves as a probability of either reacting an incoming ion with the surface, or scattering, with the curve itself representing the reaction probability. Therefore, at glancing angles the scattering probability is simply 1 – the value of the yield curve. By this interpretation, Cl_2 has a greater probability of high –

angle scattering, which leads to commonly observed etching artifacts such as microtrenching (figure 7.10). HBr, on the other hand, with a lower probability of high – angle scattering, leading to features with flatter bottoms (figure 7.11).

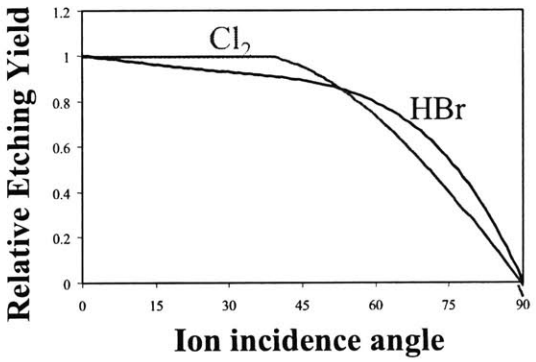

Figure 7.9 – Relative etching yield of polysilicon in Cl_2 and HBr plasmas as a function of incidence angle (based on data from ref 23). The curve can be interpreted as showing a probability of either reaction or scattering. The greater probability of high – angle scattering in Cl_2 vs HBr creates etching artifacts such as microtrenching (see figure 7.10)

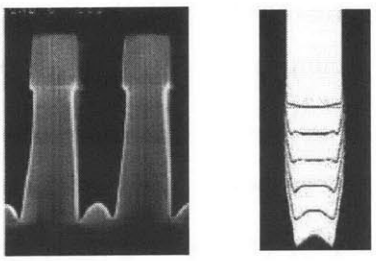

Cl_2

Figure 7.10 – Cross section of polysilicon trench etched in Cl_2 plasma, with corresponding feature profile simulation (reprinted from ref. 23). High angle scattering from the sidewall focuses ions at the foot of the sidewall, inducing microtrenching.

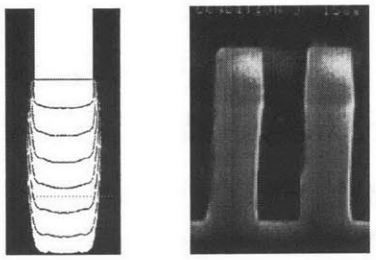

HBr

Figure 7.11 – Cross section of polysilicon trench etched in HBr plasma, with corresponding feature profile simulation (reprinted from ref. 23). The reduction in high angle scattering demonstrated on the angular etch yield curve creates a flatter trench profile.

7.3.2. Topography – Induced Striation Formation

Based on these types of results, one possible hypothesis for the formation of sidewall striations might be that similar physics is responsible. For example, the presence of microscale irregularities on the sidewall might "seed" the formation of a striation due ion reaction and scattering off of various angularly oriented surfaces. Once formed, the streak might propagate in a similar fashion as the feature profile evolution described above.

To investigate this possibility, both polysilicon and single crystal samples were placed in an HBr plasma beam at various incident angles and ion bombardment energies, and the resulting morphology changes were observed via AFM. The polysilicon / HBr system was chosen because 1) we understand the etching kinetics (yield curves, etc) quite well from Jin's previous work, 2) No deposition or other processes occur, allowing the impact of the etching process itself to be observed, and 3) both microscopically rough (polysilicon) and smooth (single crystal silicon) samples are available, allowing the contributions of the initial surface topography to be examined.

7.3.2.1. Experimental

150 nm undoped polysilicon was deposited via low – pressure chemical vapor deposition (LPCVD) onto 8 inch silicon substrates at the IBM ASTC in East Fishkill, NY. Additionally, 4 inch single crystal Si (100) wafers were obtained. All wafers were diced into approximately 1" x 1" pieces, and cleaned for 30 s with agitation in a 2% HF acid solution to remove native oxide. Once cleaned, the wafers were placed immediately into high vacuum at ~ 10^{-7} torr to prevent the formation of more native oxide. Typical time between cleaning and placement in vacuum was ~ 5 – 10 min.

For processing, each sample was transferred to the beam chamber. An HBr plasma at 300 W source power and 2 sccm flow rate was struck, and was DC biased as described previously to extract ions of a desired energy. At this flow rate the source pressure was approximately 30 mT. In the lower chamber, the samples were rotated to the desired angle, and etched. The total baseline fluence was fixed at $1x10^{17}$ ions/cm^2 by varying the total processing time, based on the measured flux at the chamber center.

Figures 7.12 and 7.13 show AFM images of the unetched polysilicon and single crystal silicon, respectively, from a top – down perspective. The images are 1 μm x 1 μm in size, with 256 linescans. The vertical scale for the polysilicon (corresponding to the range from the darkest to brightest pixel values) was 50 nm, while for the single crystal silicon, a scale of 5 nm was used. The grain structure of the polysilicon is clearly visible. This surface has an RMS roughness of ~ 3.5 nm. The surface of the single crystal Si, on the other hand, is perfectly smooth, with an RMS roughness of less than 2 angstroms.

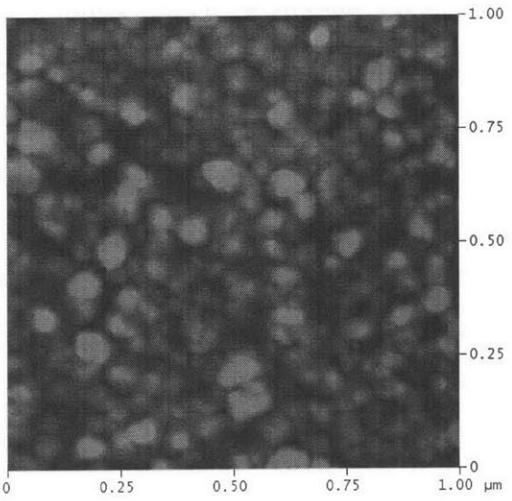

Figure 7.12 – Top – down AFM image of unetched polysilicon (50 nm vertical scale). The sample has an RMS roughness of 3.5 nm, with a clearly visible grain structure.

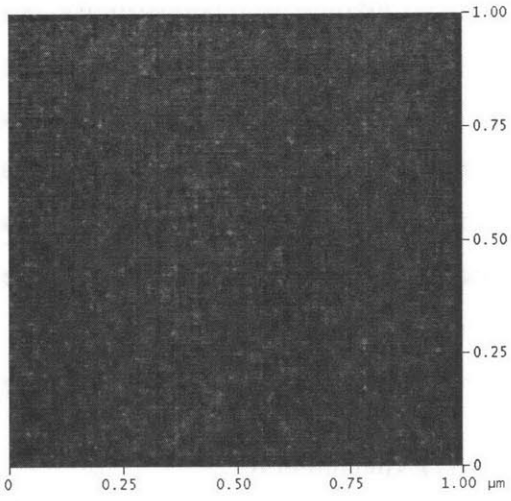

Figure 7.13 – Top – down AFM image of unetched single crystal silicon (5 nm vertical scale). The sample has an RMS roughness of 0.15 nm, and is visually smooth.

7.3.2.2. Results

Figure 7.14 and 7.15 show the effects of ion impingement angle on polysilicon roughening with a plasma DC bias of 100 V and 350 V, respectively. Images were taken at normal (0 °), near – normal (20 °), intermediate (50 °), and near – glancing (75 °) angles. Let us first examine the non – glancing results. We note evidence of smoothing at normal and near – normal incident angles (0° and 20°). This is consistent with the observations of Rauf[27], who noted that in etching processes high points tend to etch preferentially to low points due to ion bombardment of asperities coupled with the shadowing of neutral etchants in cavities. Samples etched with higher energy ions also appear smoother than those etched at lower energy. This is explained by the fact that the absolute etching yield increases approximately as the square root of the ion bombardment energy, so more etching of the high points takes place at 350 V plasma bias.

At 50°, however, there is no evident smoothing at either ion energy. We may be able to explain this trend through the etch yield curve for HBr shown in figure 7.9. Conceptually, there should be more scattering at 50° than at 0° or 20°. In fact, the scattering probability can be determined from the plot (it is equal to one minus the etch

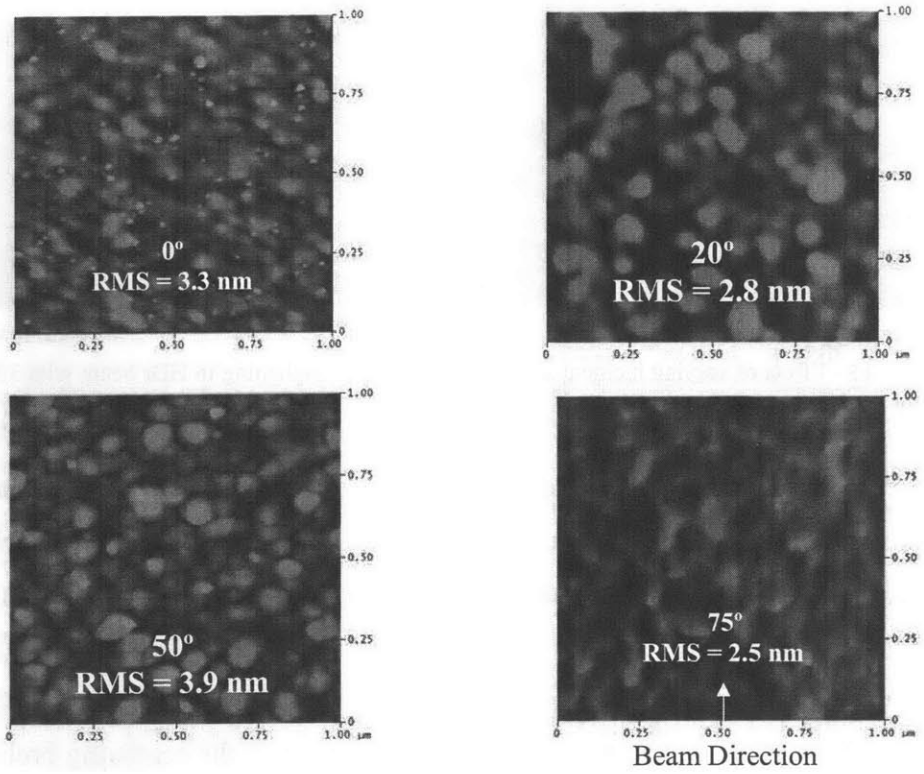

Figure 7.14 – Effect of varying incident angle at near – normal and intermediate incidence on polysilicon roughening in HBr beam with 100 V plasma DC bias.

yield). From the figure, scattering probabilities for 0°, 20°, and 50° are 0%, 5%, and 14%, respectively. Thus, we might expect that, at 50°, less etching is occurring, leading to less smoothing of the surfaces. We can model this very simply by considering a 1-D representative profile extracted from figure 7.12 (the unetched polysilicon). From this profile, I have calculated the local surface normal direction by taking the derivative of the profile (giving the local surface slope) and calculating the direction of a line perpendicular to it. Once the local surface normal is known along the profile, the interaction angle between the surface and a directional incoming ion is easily determined. Once this interaction angle is known, the local instantaneous etching yield can be calculated from figure 7.9. Finally, the local instantaneous scattering probability along the profile is determined (again, one minus the etch yield).

The results of this calculation for ions impinging on our representative surface profile at 0° (normal), 20°, 50°, and 75° are shown in figure 7.16. The surface profile is drawn to scale to give an accurate visual representation of the extent of the surface

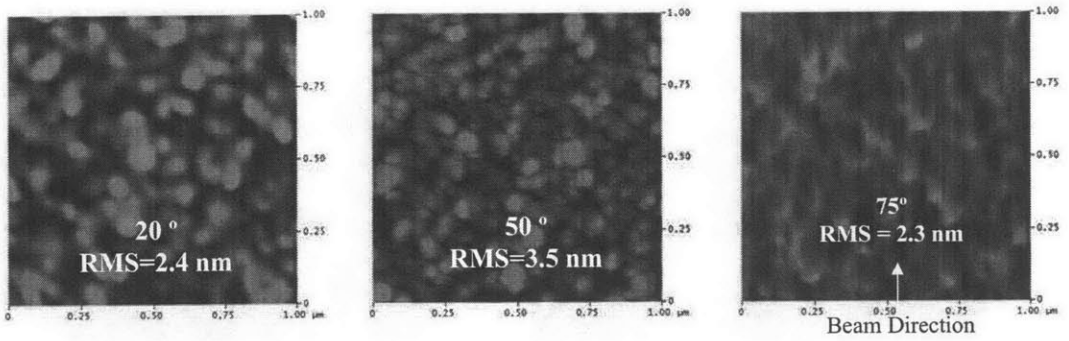

Figure 7.15 - Effect of varying incident angle on polysilicon roughening in HBr beam with 350 V plasma DC bias.

roughness. The arrow shows the direction of the incoming ions. We see that at both normal and near – normal incident angles (0° - 20°), the probability of scattering due to the surface topography is minimal (less than 10%). Therefore, the majority of ions striking the surface will etch, smoothing the features. At an incident angle of 50°, however, the results are interesting. From figure 7.9, the scattering probability for an ion striking a flat surface at this angle is about 14%. However, the scattering probability off the rough surface is enhanced due to the local surface topography. For this profile, the calculated average scattering probability is 17.1%, with several areas exceeding 40%. Since many of the ions scatter instead of etching, this might explain the lack of smoothing observed when etching the polysilicon surfaces at a 50° incident angle. Note that this simple model would predict similar roughness for samples etched at 0° and 20°. The apparent rougher surface for the sample etched at 0° as compared to 20° in figure 7.14 may be due to the presence of the particulate contamination visible on the surface.

Now, let's take a look at the glancing angle (75°) results. We can observe immediately that the structure of the roughness is markedly different from the other samples. While the polysilicon etched at non – glancing angles maintained an isotropic characteristic, the 75° samples have taken on anisotropy. Striations are clearly visible on the surface, propagating in the direction of the beam impingement (indicated in the figures). Additionally, a visual comparison of the etched sample with the unetched polysilicon indicates that the striation width seems comparable to the size of the initially present grains. The roughness magnitude on the surface is reduced, with an RMS roughness of 2.5 nm (100 V) and 2.3 nm (350 V).

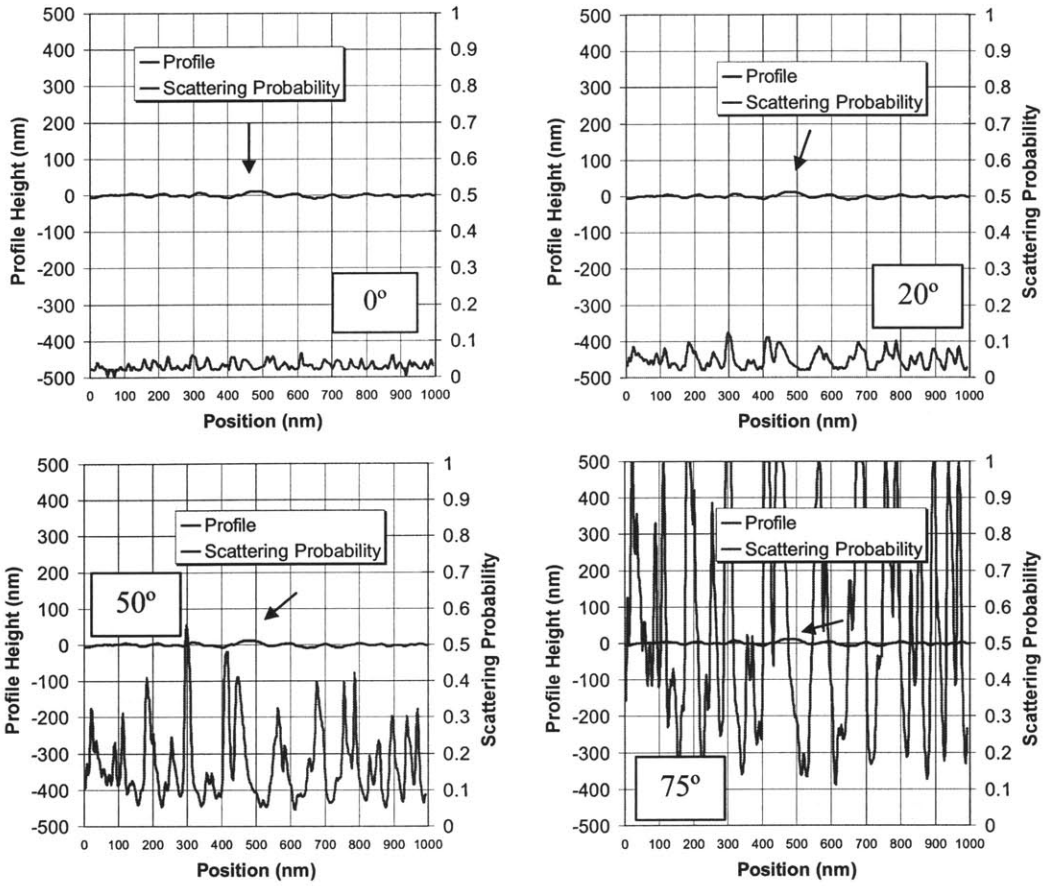

Figure 7.16 – Representative surface profile extracted from the unetched polysilicon image, with the calculated instantaneous scattering probability for ions incident at the indicated direction. For normal and near – normal incident angle (0° - 20°), the scattering probability is low at all positions along the profile, resulting in etching and smoothing. However, at 50° the scattering probability is much higher, explaining the larger roughness observed on this surface. At 75°, the surface is dominated by scattering, which may explain the observed striation formation.

Note that the surface smoothing is not captured by the interpretation of our simple model based on the etch yield curve, which would predict a rougher surface. However, the model at 75° does predict very enhanced scattering. Additionally, a glance at figure 7.16 shows several areas of the profile with a scattering probability equal to 100%. This corresponds to areas of the surface that due to the topography, are completely shadowed to the incoming ions (figure 7.17). Due to the very glancing angle formed by the beam ions, areas of the surface directly behind a protrusion receive no flux. Evidence of this phenomenon on the 75° etched sample can be seen by taking a representative profile of the surface, parallel to the beam direction (figure 7.18). The profile shows evidence of

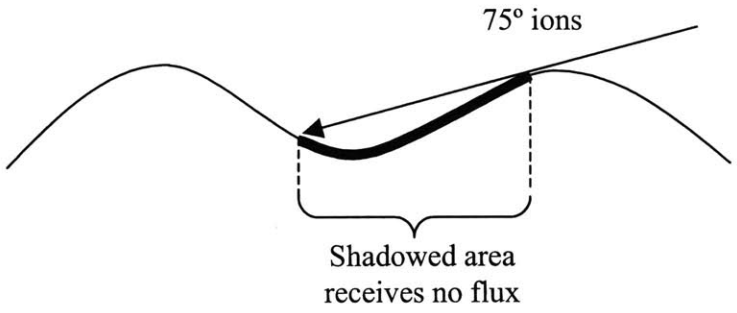

Figure 7.17 – Schematic representation of "shadowed" sample area with near – glancing ions at 75°. This occurs when the angle formed by the surface normal and incident ion direction exceeds 90°, corresponding to a relative etching yield of 0 (or a scattering probability of 1).

slanted "tails" beginning at a grain, and propagating backwards forming a ridge. These are due to the shadowing of ions on the back side of the grain, and scattering at the glancing incident angle.

Figure 7.19 shows the time evolution of the striation formation when etched at 350 V plasma bias and 75° incident angle. Samples were etched with total ion fluences of $1 \cdot 10^{16}$, $3 \cdot 10^{16}$, and $1 \cdot 10^{17}$ ions/cm^2. No significant surface change is noted at the lowest fluence (10^{16} ions/cm^2). However, as the fluence is increased, striations begin to form. At a fluence of $3 \cdot 10^{16}$ ions/cm^2 striations have begun to develop. Additionally, this image clearly illustrates that the grain structure initiates the streaks. At $1 \cdot 10^{17}$ ions/cm^2 the striations are fully developed. The surface roughness also seems to scale with the fluence,

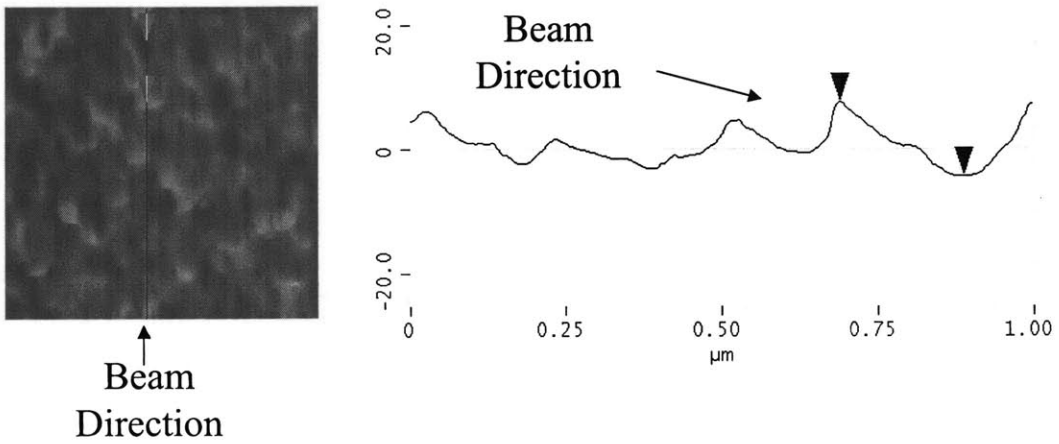

Figure 7.18 – Surface profile of polysilicon etched at 350 V, 75°, showing striation formation due to shadowing by the grain structure. The profile shows slanted "tails" beginning at the grain and propagating backwards caused by shadowing and scattering of the incoming ions, creating a ridge.

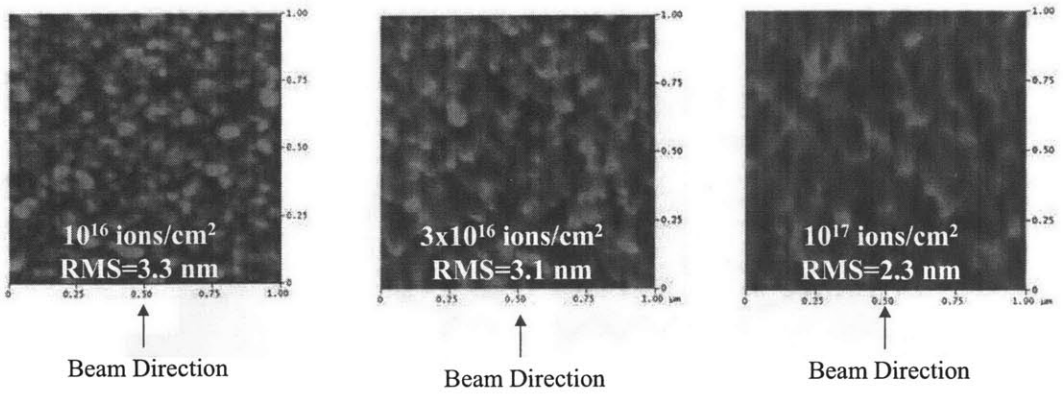

Figure 7.19 – Effect of ion fluence on striation formation in HBr plasma beam at 350 V plasma bias and 75° incident angle. At a fluence of 10^{16} ions/cm^2, no significant change in the surface structure is noted. However, as the fluence is increased, striations initiated by the surface topography begin to develop. The surface roughness scales with the fluence, with a larger flux resulting in a smoother surface.

with a larger fluence resulting in a smoother surface.

These results seem to suggest that striation formation on the rough polysilicon surface in the HBr plasma beam can be governed by specular scattering from the topography, whether propagating between the grains, or due to ridge formation from shadowing of the incoming ion flux. The striations seem to be initiated by the grain structure itself. As one further check, a different polysilicon sample (obtained from the MIT Microsystems Technology Laboratory) was etched at 350 V plasma bias and 75° incident angle with a fluence of 10^{17} ions/cm^2. This polysilicon sample had a larger grain structure than the first type. Therefore, if the striation formation is determined by the grain structure, the streaks should be larger as well.

Figure 7.20 shows both types of polysilicon samples, illustrating the surfaces before and after etching at the conditions described above. The difference in the etched surfaces is striking. In both cases, the streaks present after processing do indeed scale with the grain structure on the unetched surfaces. On the sample with large grains, wide ridges formed by shadowing are clearly visible propagating backward from the surface high points, indicative of the ion shadowing effect observed previously.

Finally, single crystal silicon samples were etched similarly to the polysilicon, The single crystal silicon etching kinetics are similar to the polysilicon, but there is no initial surface topography (as seen in figure 7.13, the surface is flat). Therefore, the absence of striation formation on similarly processed single crystal silicon should further

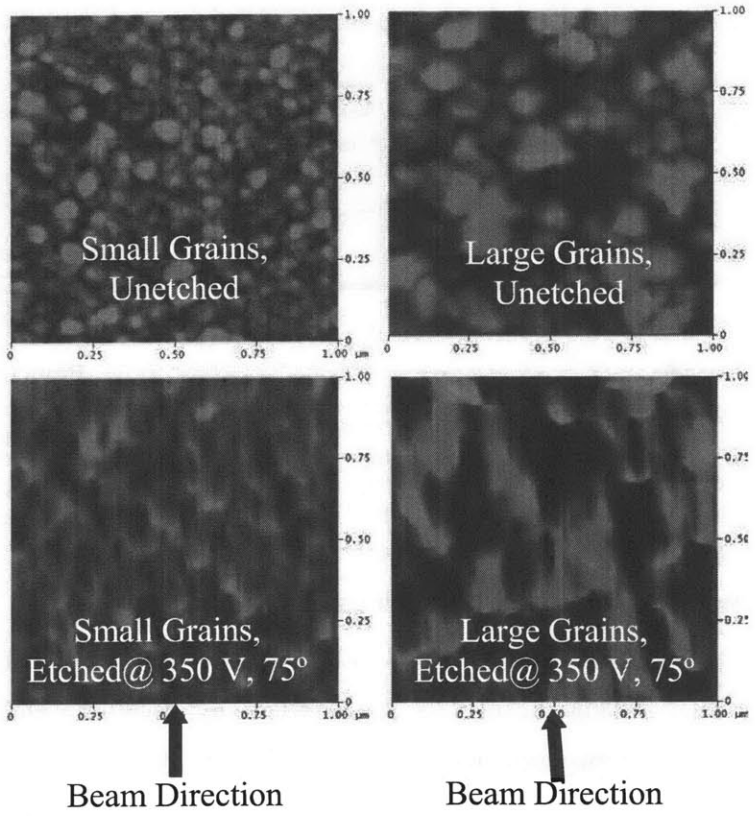

Figure 7.20 – Small – grained polysilicon and large – grained polysilicon samples were etched in the HBr plasma beam at 350 V plasma bias, 75° incidence angle, and 10^{17} ions/cm^2 fluence. Striations are present after etching on both samples. The streak width correlates with the grain size on the unetched surfaces, indicating that the striation formation results from the surface topography.

indicate the role of the surface topography, rather than some other process inherent in the sample material or etching mechanism.

Figure 7.21 shows AFM images of single crystal silicon at 100 V and 350 V plasma bias as a function of the ion incident angle. These images are on a 5 nm vertical scale (rather than the 50 nm vertical scale used for the polysilicon) as the single crystal silicon is much flatter. On the 100 V samples, some sort of particulate or other contamination is observable. However, it looks worse than it really is since the vertical range of the image pixels is so small. This can be seen by examining the RMS roughness of the surfaces, which even on the 75° sample is only ~ 4 angstroms. Since the contamination is not present on the 350 V samples, it is possible that it may have resulted from small amounts of native oxide that were either not removed completely, or developed before the samples were placed in vacuum. At 350 V, the ion bombardment energy may have been high enough to sputter it away. Of course, it is also possible that

the observed contamination is particles that adhered to the surfaces after they were removed from the vacuum system, and that the observed trend is coincidental.

Nevertheless, disregarding the particulate contamination it is immediately apparent that no striations of any kind have formed on the single crystal silicon, regardless of the incident angle or ion bombardment energy. Judging by the surface RMS

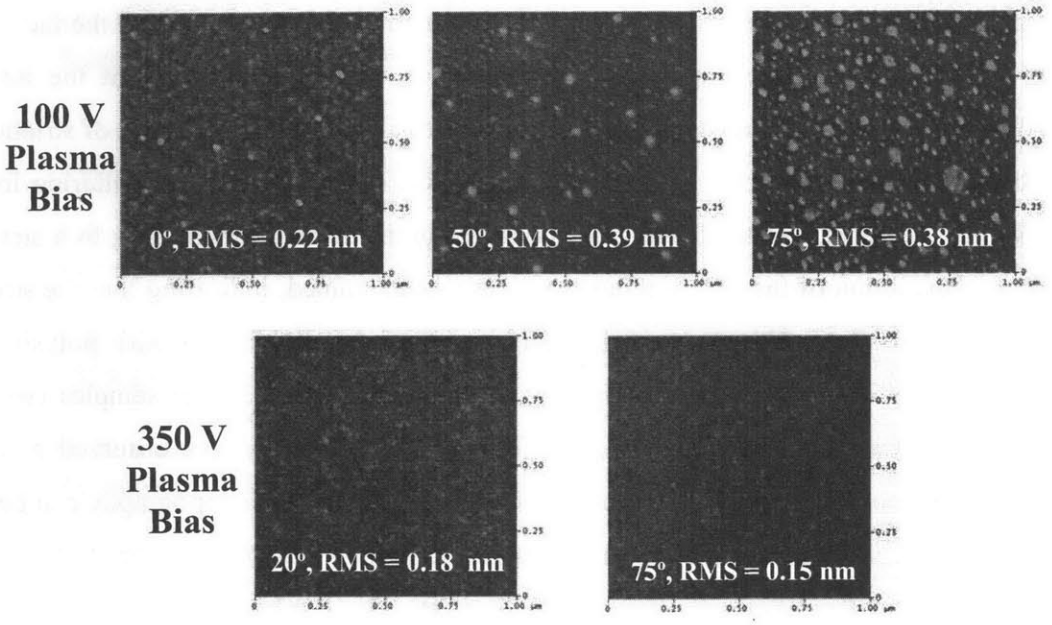

Figure 7.21 – Single crystal silicon etched in the HBr plasma beam at 100 V and 350 V plasma bias and 10^{17} ions/cm^2, as a function of the ion incident angle. Particulate contamination is observed on the samples etched at 100 V. Nevertheless, the surfaces show no sign of striation development, again providing evidence for the role of surface topography on the formation of anisotropic streaks.

roughness (and disregarding the particles) the single crystal silicon remains smooth at all etching conditions. The lack of striation development on the single crystal silicon as compared to the polysilicon gives further evidence for the role of surface topography on the formation of striations during etching.

7.4. Conclusions

A new plasma beam chamber was described that allows the independent control of the ion bombardment energy, ion incident angle, sample type, and plasma chemistry, essential for a fundamental study of striation and roughness development during etching processes. The chamber was fully characterized, demonstrating good ion energy control

and beam uniformity over a ½" diameter sample area. Additionally, a simple model that adequately explained the measured ion flux (by assuming a slight angular dispersion to the ions) represented the beam uniformity.

After characterizing, the beam source was used to perform our first fundamental studies into mechanisms behind striation development during etch. The polysilicon / HBr system was chosen because of previous work elucidating the etching kinetics in the system (typified by a determination of the relative angular etching yield), and the fact that both rough and smooth samples could be obtained. Results indicated that the initial surface topography can play a crucial role in the formation and development of striations on the surface. At a glancing incident angle, the ions undergo enhanced scattering from the surface features, and shadowing by the larger grains, eventually leading to a streak. The time evolution of the striation development was examined, indicating that the streak size might correlate with the initial grain size. Further experiments with polysilicon samples of differing grain sizes supported this. Finally, single crystal samples (which were smooth) were etched at similar conditions. No streaking was observed at any experimental condition, further supporting the idea that the surface topography can be an important source of striations observed during etching.

7.5. References

1 J. P. Chang, A. P. Mahorowala, and H. H. Sawin, Journal of Vacuum Science & Technology A **16,** 217-224 (1998).

2 A. P. Mahorowala and H. H. Sawin, Journal of Vacuum Science & Technology B **20,** 1064-1076 (2002).

3 A. P. Mahorowala and H. H. Sawin, Journal of Vacuum Science & Technology B **20,** 1077-1083 (2002).

4 A. P. Mahorowala and H. H. Sawin, Journal of Vacuum Science & Technology B **20,** 1084-1095 (2002).

5 W. Jin and H. H. Sawin, Journal of the Electrochemical Society **150,** G711-G717 (2003).

6 W. Jin and H. H. Sawin, Journal of Vacuum Science & Technology A **21,** 911-921 (2003).

[7] J. W. Butterbaugh, D. C. Gray, and H. H. Sawin, Journal of Vacuum Science & Technology B **9,** 1461-1470 (1991).

[8] D. C. Gray, I. Tepermeister, and H. H. Sawin, Journal of Vacuum Science & Technology B **11,** 1243-1257 (1993).

[9] M. J. M. Vugts, G. J. P. Joosten, A. Vanoosterum, H. A. J. Senhorst, and H. C. W. Beijerinck, Journal of Vacuum Science & Technology A **12,** 2999-3011 (1994).

[10] M. J. M. Vugts, L. J. F. Hermans, and H. C. W. Beijerinck, Journal of Vacuum Science & Technology A **14,** 2138-2150 (1996).

[11] J. P. Chang, J. C. Arnold, G. C. H. Zau, H. S. Shin, and H. H. Sawin, Journal of Vacuum Science & Technology A **15,** 1853-1863 (1997).

[12] J. P. Chang and H. H. Sawin, Journal of Vacuum Science & Technology A **15,** 610-615 (1997).

[13] J. P. Chang and H. H. Sawin, Journal of Vacuum Science & Technology B **19,** 1319-1327 (2001).

[14] G. P. Kota, J. W. Coburn, and D. B. Graves, Journal of Vacuum Science & Technology A **16,** 2215-2221 (1998).

[15] F. Greer, J. W. Coburn, and D. B. Graves, Journal of Vacuum Science & Technology A **18,** 2288-2294 (2000).

[16] F. Greer, L. Van, D. Fraser, J. W. Coburn, and D. B. Graves, Journal of Vacuum Science & Technology B **20,** 1901-1906 (2002).

[17] F. Greer, D. Fraser, J. W. Coburn, and D. B. Graves, Journal of Vacuum Science & Technology B **21,** 1391-1402 (2003).

[18] H. Toyoda, H. Morishima, R. Fukute, Y. Hori, I. Murakami, and H. Sugai, Journal of Applied Physics **95,** 5172-5179 (2004).

[19] S. A. Vitale, H. Chae, and H. H. Sawin, Journal of Vacuum Science & Technology A **18,** 2770-2778 (2000).

[20] S. A. Vitale, H. Chae, and H. H. Sawin, Journal of Vacuum Science & Technology A **19,** 2197-2206 (2001).

[21] O. Kwon, Ph.D. Thesis, Massachusetts Institute of Technology, 2004.

[22] W. Jin, S. A. Vitale, and H. H. Sawin, Journal of Vacuum Science & Technology A **20,** 2106-2114 (2002).

[23] W. Jin, Ph.D. Thesis, Massachusetts Institute of Technology, 2003.

[24] J. P. Chang, Ph.D. Thesis, Massachusetts Institute of Technology, 1999.

[25] J. W. Coburn and E. Kay, Journal of Vacuum Science & Technology **8,** 738-743 (1971).

[26] R. A. Gottscho, Journal of Vacuum Science & Technology B **11,** 1884-1889 (1993).

[27] S. Rauf, P. J. Stout, and J. Cobb, Journal of Vacuum Science & Technology B **21,** 655-659 (2003).

Chapter 8 – Conclusions and Future Work

8.0. Conclusions

For the patterning of sub 100 nm features, a clear understanding of the origin and control of line edge roughness (LER) is extremely desirable, both from a fundamental as well as a manufacturing perspective. Until recently, LER studies have focused on the analysis of top-down SEM micrographs of post-developed photoresist lines. However, the effect of plasma etch on sidewall roughness has not received sufficient attention. Plasma etching processes often roughen the feature sidewalls, leading to the formation of anisotropic striations. It is this post-etch sidewall roughness which will ultimately affect device performance.

In this thesis, I have attempted to provide a thorough investigation into sidewall roughness transfer occurring on a variety of industrially relevant systems and toolsets, and to identify potential mechanisms for improvement through processing and materials solutions. Additionally, more fundamental work was performed on blanket samples though the identification of a novel polymer – induced roughening mechanism on low – k dielectric films. Finally, a new apparatus was constructed and characterized that will allow the study of roughness and striation formation through a decoupling of plasma parameters that is impossible to achieve in a traditional plasma etcher.

In chapter 3, we observed via AFM sidewall roughness during the ARC / HM open and subsequent oxide etch for 248 nm and 193 nm systems, with a wide variety of organic ARCs, hardmasks, Si – containing ARCs, and bilayers. The initial 248 nm lithography sidewall morphology is isotropic in nature with a 3-5 nm 1-σ RMS roughness, and is relatively constant as a function of depth. After the ARC/hardmask etch, however, the sidewall morphology takes on an anisotropic characteristic, with striations created by ion bombardment. During a subsequent oxide etch, these striations transfer into the oxide sidewall, the anisotropic topography created during the ARC/hardmask etch casting the morphology of the oxide layer beneath. While all resist systems are about equivalent from a roughness standpoint after the ARC/hardmask etch, they show variation after oxide etch. On the 248 nm resist platforms, hardmask and Si containing ARC samples allow more roughness transfer during an aggressive oxide etch than organic ARC samples, perhaps due to the polymerizing nature of the Si ARC /

hardmask open chemistry, or to compositional differences between these films as compared to the organic ARC. On the 193 nm resist platforms, a less aggressive (higher pressure, lower ion bombardment) oxide etch was required due to the lower etch resistance versus 248 nm systems. However, this gentler oxide etch allowed the oxide to be opened relatively smoothly regardless of the resist type, leaving the post – etch oxide SWR comparable to that obtained with 248 nm organic resist/ARC. These results indicate that the SWR on the oxide substrate can be maintained within reasonable limits, as long as the increasing resist/ARC roughness does not extend to the oxide interface.

In Chapter 4, I identified how processing conditions (specifically the ARC open or hardmask open plasma chemistry) could be tuned to improve sidewall roughness transfer. It was found that, on the 248 nm organic ARC system from Chapter 3, opening the ARC in a Cl_2/O_2 plasma chemistry (or "chemical" ARC open) enabled an isotropic SWR to be maintained, at the cost of reduced selectivity to resist. A subsequent oxide etch resulted in smoother sidewalls than the samples with a "physical" N_2/H_2 ARC open, as no post ARC open striations were present to transfer into the oxide.

It was also possible to etch the hardmask material in a Cl_2/O_2 "chemical" HM open, again resulting in an isotropic sidewall. After a subsequent oxide etch, the sidewall roughness underwent a vast improvement over the hardmask samples opened with the "physical," highly depositing fluorocarbon chemistry described previously, with an RMS roughness decrease of ~60% at the top of the oxide line (from 8 nm to 3.3 nm RMS).

Finally, a similar methodology was applied to the post – etch roughness of polysilicon gate lines, patterned with a TEOS oxide hardmask. Varying the hardmask etch conditions highlighted a roughness improvement mechanism driven by polymerization during the hardmask open. Fluorocarbon polymer (formed on the gates during the hardmask etch) filled in imperfections in the gate line, allowing a smoother transfer to the underlying polysilicon. However again the roughness improvement came at a cost. The increased polymerization grew the width of the line during the hardmask open, creating a "fatter" mask that resulted in wider gates than originally patterned.

These results indicate several methods by which modulating the ARC/HM open chemistry can improve roughness transfer, and illustrates some of the tradeoffs (reduced selectivity, CD shift, etc) involved.

In Chapter 5, the impact of employing thin and/or fluorinated photoresists on the post etch line edge roughness transfer into oxide substrates was investigated. First, a non-fluorinated, very thin (130 nm) resist was investigated. It was found that almost half of the resist thickness was consumed during the ARC open, leaving inadequate masking material remaining to properly etch the oxide. At the feature edges, all the resist and ARC was consumed during a 0.6 μm oxide etch, leaving the substrate exposed and causing mousebite formation. Next, blanket etch rates of fluorinated 193 resists with varying fluorine content were measured in both halogen and fluorocarbon plasma chemistries. The dependence of the etching rate on resist fluorine content showed a "threshold" behavior in both chemistries. Resists with fluorine content below the threshold showed no significant etch rate enhancement. However, once the fluorine content of the resist increased beyond the threshold, etching rates increased monotonically. Sidewall roughness transfer was compared on 3 different resist systems: 1) non-fluorinated, 2) sub – threshold fluorine content, and 3) super-threshold fluorine content. Roughness transfer on the sub-threshold resist was only slightly higher than the control. However, the super-threshold system showed severe roughening during etch accompanied by extreme resist consumption, faceting at the resist corners, and large mousebites left on the oxide lines.

These results have important implications for the success of 157 nm lithography. Because 157 nm resists are expected to be heavily fluorinated and extremely thin, it may become impossible to pattern certain levels using the conventional single layer resist / organic ARC approach that works well for 248 and 193 nm systems. These levels will require the use of alterative patterning schemes such as hard mask and / or bilayer approaches, which are expected to gain importance as the industry migrates to sub-70 nm nodes.

In Chapter 6, roughening of low – k and porous low – k dielectrics in fluorocarbon plasma chemistries was investigated. Three dielectric films: 1) thermal oxide, 2) organosilicate glass (OSG), and 3) a methylsilsequioxane porous low-k film (PLK), were etched in various fluorocarbon plasma chemistries, while varying ion bombardment energy. Etch rates and surface roughnesses were measured. Polymer – induced micromasking was identified as a roughening mechanism. During the etching process, under certain conditions multiple surface steady states develop on the films,

creating regions with both net etching and net fluorocarbon polymer deposition. Once the dual regions form, etch selectivity between the low-k substrate and the polymer leads to the formation surface roughness.

On the solid films, the roughness formation shows a threshold behavior in relation to ion bombardment, with a transition from roughening to smooth etching as the ion bombardment energy is increased. Moreover, on the solid dielectrics roughness formation can be prevented through polymerization control, for example by the addition of oxygen to the etching gases. However, roughness formation on the porous films was greater due to fluorocarbon diffusion into the pore structure, which seeded the formation of micromasks at conditions at which they do not form on the solid films. Therefore, the successful integration of porous low-k dielectrics will require very careful control of polymerization to prevent unacceptable roughness formation during fluorocarbon etching.

In Chapter 7, I described a newly constructed realistic plasma beam chamber that allows the independent control of the ion bombardment energy, ion impingement angle, and plasma chemistry that will enable the study of roughness and striation formation from a fundamental perspective. The source has a stage for mounting samples, quartz crystal microbalance (QCM) for etch rate measurements, ion energy analyzer to characterize the ion energy distribution function of the beam, and an ion flux analyzer to spatially map the beam uniformity. The sample stage and QCM are mounted on angularly adjustable vacuum stages to allow the variation of the ion impingement angle. To simulate a sidewall, the sample is rotated to a near – glancing angle The ion bombardment energy can be selected by DC biasing the plasma, which is isolated from the source chamber walls by a quartz or alumina ceramic liner.

After fully characterizing the ion energy and beam uniformity in the new source, it was used to conduct our first preliminary investigation into roughening of polysilicon in an HBr plasma beam. The effects of initial topography were examined by comparing polysilicon (with a rough grain structure) to similarly processed single crystal silicon samples which were smooth and flat. At glancing incident angles, the topography of the polysilicon led to enhanced scattering and shadowing of the incoming ions, creating striations that propagated backwards from the grains. Additinally, the streak width

correlated with the initial grain size. Single crystal silicon etched at similar conditions exhibited no signs of streaking. These results indicated that the surface topography can be an important source of striation formation during etching.

8.1. Future Work

While it was my task to get the new beam chamber operational and characterized, and to demonstrate its feasibility for performing fundamental roughness investigations, we have obviously only scratched the surface. Future beam studies on silicon films should include the addition of amorphous silicon to the poly / single crystal studies and additional polysilicon plasma chemistries such as HBr / O_2 and HBr / Cl_2. Oxide and low – k roughening in fluorocarbon plasma beams are on the horizon as well. Specifically, it would be enlightening to examine whether or not the micromask – induced roughening observed on blanket films can lead to striation formation on sidewalls. Since so many new experiments suggest themselves, our lab is currently constructing a second beam chamber to ease the bottleneck. The existing chamber will be used for polysilicon – type experiments (ie, "front end"), while the new chamber will be used for oxide and low – k type experiments (ie, "back end").

A third type of experiment could involve the use of patterned lines / spaces to examine more closely the role of faceting at the pattern edge on striation initiation and propagation. Figure 8.1 shows a schematic of the basic concept behind this. An array of dense line / space patterns (which, as mentioned in Chapter 2, we have available on the DARPA mask) is rotated to a near – glancing angle and placed in the plasma beam. The beam will impinge on the pattern corner in a manner analogous to a traditional line / space experiment. Additionally, the AFM analysis on these samples can be performed in a top – down manner, greatly simplifying and accelerating the data collection process. A first possibility for experiments of this type might be to bake the patterned photoresist lines, causing a reflow of the resist and rounding the corners. The role of rounded corners vs sharp corners (which should facet more) could thus be examined.

Another avenue for exploration is modeling of the roughening process. For a number of years our group has investigated feature profile evolution during plasma etching, using a 2 ½ - D monte carlo simulation, with a good deal of success[1-5]. However,

while features can be simulated in 2-D (by assuming that the 3rd dimension is infinite), sidewall roughness is inherently a 3 dimensional problem. Thus, simulation of sidewall roughness formation will require a 3 – D simulator.

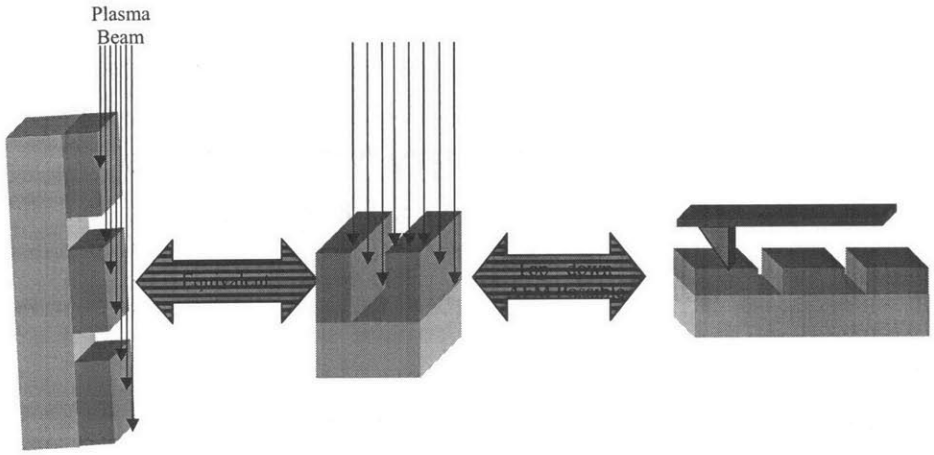

Figure 8.1 – A pattern of wide, dense lines / spaces is placed in the beam, and rotated to a near – glancing angle. This setup simulates a traditional line – space pattern, allowing the evaluation of corner faceting effects on striation formation. Additionally, top – down AFM analysis should be possible, greatly simplifying the data collection.

In his PhD thesis, Jin[6] began the construction of a 3 dimensional simulator for the purpose of examining roughness formation during etching. The work was preliminary, and is currently on – going in our laboratory. Once the simulator is operational, real images produced from the plasma beam chamber via AFM will be used to calibrate and verify the results produced by the simulator.

8.2. References

1 A. P. Mahorowala and H. H. Sawin, Journal of Vacuum Science & Technology B **20,** 1064-1076 (2002).

2 A. P. Mahorowala and H. H. Sawin, Journal of Vacuum Science & Technology B **20,** 1077-1083 (2002).

3 A. P. Mahorowala and H. H. Sawin, Journal of Vacuum Science & Technology B **20,** 1084-1095 (2002).

4 W. D. Jin and H. H. Sawin, Journal of Vacuum Science & Technology A **21,** 911-921 (2003).

[5] W. D. Jin and H. H. Sawin, Journal of the Electrochemical Society **150,** G711-G717 (2003).

[6] W. D. Jin, Ph.D. Thesis, Massachusetts Institute of Technology, 2003.